

**ENTHALPY RELATIONS BETWEEN DIFFERENT
PHASES IN REPRESENTATIVE WURTZITE
SEMICONDUCTORS: *AB INITIO* CALCULATIONS**

Kanoknan Sarasamak

**A Thesis Submitted in Partial Fulfillment of the Requirements for the
Degree of Doctor of Philosophy in Physics
Suranaree University of Technology
Academic Year 2008**

ความสัมพันธ์ระหว่างเอนทัลปีของเฟสที่แตกต่างกันในตัวแทนสารกึ่งตัวนำ
แบบเวรีตไซต์: การคำนวณแบบแอบ อินิซิโอ

นางสาวกนกนันทน์ สารสมัคร

วิทยานิพนธ์นี้เป็นส่วนหนึ่งของการศึกษาตามหลักสูตรปริญญาวิทยาศาสตรดุษฎีบัณฑิต
สาขาวิชาฟิสิกส์
มหาวิทยาลัยเทคโนโลยีสุรนารี
ปีการศึกษา 2551

**ENTHALPY RELATIONS BETWEEN DIFFERENT PHASES IN
REPRESENTATIVE WURTZITE SEMICONDUCTORS:
AB INITIO CALCULATIONS**

Suranaree University of Technology has approved this thesis submitted in partial fulfillment of the requirements for the Degree of Doctor of Philosophy.

Thesis Examining Committee

(Asst. Prof. Dr. Chinorat Kobdaj)

Chairperson

(Prof. Dr. Sukit Limpijumnong)

Member (Thesis Advisor)

(Prof. Dr. Walter R. L. Lambrecht)

Member

(Assoc. Prof. Dr. Vittaya Amornkitbamrung)

Member

(Dr. Saroj Rujirawat)

Member

(Prof. Dr. Pairote Sattayatham)

Vice Rector of Academic Affairs

(Assoc. Prof. Dr. Prapun Manyum)

Dean of Institute of Science

กนกนันท์ สารสมักร : ความสัมพันธ์ระหว่างเอนทัลปีของเฟสที่แตกต่างกันในตัวแทน
สารกึ่งตัวนำแบบเวิร์ตไซต์: การคำนวณแบบแอบ อินิซิโอ (ENTHALPY RELATIONS
BETWEEN DIFFERENT PHASES IN REPRESENTATIVE WURTZITE
SEMICONDUCTORS: *AB INITIO* CALCULATIONS)

อาจารย์ที่ปรึกษา : ศาสตราจารย์ ดร. ชูกิจ ลิ้มปิงานงค์, 180 หน้า.

ในวิทยานิพนธ์ฉบับนี้ได้มีการศึกษาคุณสมบัติเชิงกลบางอย่างของ SiC GaN InN ZnO และ CdSe โดยวิธีคำนวณแบบแอบ อินิซิโอ ภายใต้สภาวะปกติ พบว่า สารเหล่านี้มีโครงสร้างผลึกแบบเวิร์ตไซต์ ภายใต้สภาวะความดันสูงสารเหล่านี้สามารถเปลี่ยนโครงสร้างผลึกไปเป็นโครงสร้างผลึกแบบรอกซอลต์ได้ และได้คำนวณค่าความดันสมดุลสำหรับการเปลี่ยนโครงสร้างผลึกของสารประกอบเหล่านี้ นอกจากนั้นแล้วความเค้นแบบแกนเดียวยังสามารถทำให้ผลึกเวิร์ตไซต์ เปลี่ยนโครงสร้างไปเป็นผลึกเวิร์ตไซต์ที่มีระนาบผลึกไม่โค้งงอได้ โดยพบว่าความเค้นที่สามารถทำให้เกิดการเปลี่ยนโครงสร้างดังกล่าวคือความเค้นกดแบบแกนเดียวยตามทิศทาง [0001] และความเค้นดึงแบบแกนเดียวยตามทิศทาง [01 $\bar{1}$ 0] ซึ่งได้คำนวณค่าความเค้นวิกฤติสำหรับกรณีต่าง ๆ ไว้ด้วยแล้ว นอกจากนั้นยังพบอีกว่าความเค้นดึงแบบแกนเดียวยตามทิศทาง [0001] สามารถทำให้ ZnO เกิดการเปลี่ยนโครงสร้างผลึกไปเป็นผลึกแบบเตตระ โกนอลที่มีอะตอมอยู่ตรงกลาง (BCT-4) ซึ่งเป็นโครงสร้างใหม่ที่ยังไม่เคยมีการรายงานมาก่อนสำหรับ ZnO ความดันสมดุลหรือความเค้นสมดุลในการเปลี่ยนโครงสร้างที่คำนวณได้นี้สอดคล้องเป็นอย่างดีกับผลจากการคำนวณและการทดลองที่มีมาในอดีต ความเสถียรของแต่ละโครงสร้างนั้นศึกษาได้จากการวิเคราะห์ค่าเอนทัลปีเป็นฟังก์ชันของตัวแปรโครงสร้างผลึก c/a และ b/a ท้ายสุดยังมีการศึกษาพฤติกรรมของค่าคงที่ยืดหยุ่นที่เป็นฟังก์ชันของความดันของสารที่กล่าวข้างต้น โดยได้พบความสัมพันธ์กับการเปลี่ยนโครงสร้างผลึกจากแบบเวิร์ตไซต์ไปเป็นแบบรอกซอลต์ด้วย

สาขาวิชาฟิสิกส์
ปีการศึกษา 2551

ลายมือชื่อนักศึกษา _____
ลายมือชื่ออาจารย์ที่ปรึกษา _____
ลายมือชื่ออาจารย์ที่ปรึกษาร่วม _____

KANOKNAN SARASAMAK : ENTHALPY RELATIONS BETWEEN
DIFFERENT PHASES IN REPRESENTATIVE WURTZITE
SEMICONDUCTORS: *AB INITIO* CALCULATIONS. THESIS ADVISOR :
PROF. SUKIT LIMPIJUMNONG, Ph.D. 180 PP.

ENTHALPY/WURTZITE/SEMICONDUCTORS/*AB INITIO*

In this thesis, some mechanical properties of SiC, GaN, InN, ZnO, and CdSe are studied using *ab initio* calculations method. Under ambient conditions, these compounds have the wurtzite (WZ) structure. Under large hydrostatic pressure, the transformation into the rocksalt (RS) structure can take place. The equilibrium transformation pressures are calculated. Moreover, uniaxial stresses can cause the transformation into an unbuckled wurtzite structure (HX) under uniaxial compressive stress along the [0001] crystalline direction or uniaxial tensile stress along the $[0\bar{1}10]$ crystalline direction and the critical stresses are calculated. In addition, the novel structure, a body centered tetragonal (BCT-4) structure was predicted for ZnO under uniaxial tensile stress along [0001] direction. The predicted equilibrium transformation pressures and stresses are in good agreement with available theoretical and experimental results. The stability of each crystal structure is studied by analyzing enthalpy as a function of lattice parameters c/a and b/a . The behavior of the elastic constants as a function of pressure, which related to the WZ-to-RS phase transformation, is also studied for above compounds.

School of Physics

Student's Signature _____

Academic Year 2008

Advisor's Signature _____

Co-advisor's Signature _____

ACKNOWLEDGEMENTS

I would like to express the gratitude to my advisor Prof. Dr. Sukit Limpijumnong for, his guidance, his patience, his kind support, and his help in proofreading the thesis. I would like to express the appreciation to my co-advisor Prof. Dr. Walter R. L. Lambrecht for his warm hospitality, his advice and his kind assistance during my visit at the Department of Physics, Case Western Reserve University, Cleveland, Ohio, USA. I thank Assoc. Prof. Dr. Vittaya Amornkitbamrung, Asst. Prof. Dr. Chinorat Kobdaj, and Dr. Saroj Rujirawat for contributing as the thesis-examining committees. I thank Dr. Sirichok Jungthawan for his advices and his help with some parts of my thesis. Part of the work has been done during my visit at the department of Physics, Case Western Reserve University, Cleveland, Ohio, USA through the Royal Golden Jubilee Ph.D. Program (Grant No. PHD/0264/254). I appreciated the warm welcome and supports from my friends at Cleveland, especially from Adisak Boonchun. I acknowledge Synchrotron Light Research Institute, Thailand for the computation resources. I thank the faculties and friends at the School of Physics, Suranaree University of Technology for their guidances and friendships. I would like to thank my friends in the condensed matters physics group – Sutassana Na-Phattalung, Jiraroj T-Thienprasert, and Pakpoom Reunchan for their friendships and helpful discussions. Finally, I would like to express thanks to my parents, my sister, and my brother for their love, encouragement and support.

Kanoknan Sarasamak

CONTENTS

	Page
ABSTRACT IN THAI.....	IV
ABSTRACT IN ENGLISH.....	V
ACKNOWLEDGEMENTS.....	VI
CONTENTS.....	VII
LIST OF TABLES.....	X
LIST OF FIGURES.....	XII
LIST OF ABBREVIATIONS.....	XX
CHAPTER	
I INTRODUCTION.....	1
II THEORETICAL APPROACH.....	5
2.1 Density functional theory.....	5
2.1.1 The Hohenberg and Kohn Theorem.....	5
2.1.2 Kohn and Sham equation.....	6
2.1.3 The local density approximation (LDA).....	7
2.1.4 The generalized gradient approximation (GGA).....	9
2.2 Plane waves.....	10
2.3 Pseudopotentials.....	11
2.3.1 Norm-conserving pseudopotentials.....	13
2.3.2 Ultrasoft pseudopotentials.....	15
2.3.3 Projector augmented waves.....	15

CONTENTS (Continued)

	Page
2.4 Full potential linear muffin tin orbital (FP-LMTO) method.....	16
2.5 The Vienna <i>Ab initio</i> Simulation (VASP) Package.....	18
III CRYSTALS PROPERTIES.....	19
3.1 Crystal structure.....	19
3.2 The stability of the crystal structures.....	29
3.3 Thermodynamic stability.....	31
3.4 Mechanical properties.....	32
3.4.1 Phase transition under pressure.....	32
3.4.2 Elasticity.....	34
3.4.3 Elastic energy.....	38
IV STABILITY OF WURTZITE, UNBUCKLED WURTZITE, AND ROCKSALT PHASES OF SiC, GaN, InN, ZnO, AND CdSe UNDER LOADING OF DIFFERENT DIRECTIONS.....	40
4.1 Introduction.....	40
4.2 Computational method.....	42
4.3 Results and discussions.....	45
4.3.1 Ambient conditions (stress-free state).....	45
4.3.2 Hydrostatic compression.....	52
4.3.3 Uniaxial compression along [0001] direction.....	60
4.3.4 Uniaxial compression along $[01\bar{1}0]$ direction.....	66
4.6 Conclusions.....	69

CONTENTS (Continued)

	Page
V FIRST PRINCIPLES STUDY OF ZnO POLYMORPHS.....	71
5.1 Introduction.....	71
5.2 Computational method.....	72
5.3 Results and discussions.....	74
5.4 Conclusions.....	80
VI CONCLUSIONS AND FUTURE RESEARCH.....	81
REFERENCES.....	93
APPENDIX.....	106
CURRICULUM VITAE.....	159

LIST OF TABLES

Table		Page
3.1	Ideal lattice parameters for WZ, HX and RS crystalline structures.....	20
3.2	Lattice parameters for WZ, HX and RS SiC under their equilibrium loading conditions. Values in parentheses are taken from literature.....	24
3.3	Lattice parameters for WZ, HX and RS GaN under their equilibrium loading conditions. Values in parentheses are taken from literature.....	25
3.4	Lattice parameters for WZ, HX, DHX, and RS InN under their equilibrium loading conditions. Values in parentheses are taken from literature.....	26
3.5	Lattice parameters for WZ, HX, DHX, and RS ZnO under their equilibrium loading conditions. Values in parentheses are taken from literature.....	27
3.6	Lattice parameters for WZ, HX, DHX, and RS CdSe under their equilibrium loading conditions. Values in parentheses are taken from literature.....	28
4.1	Energy difference (eV per 2 pairs) between HX (or RS) and the WZ structure. The Phillips ionicity parameters (f_i) are also listed. (Phillips, 1970).....	48
4.2	Percentage changes in V (volume), lattice parameters b and c as the crystal structure changed from WZ to HX and WZ to RS for all five compounds. The conditions that stabilize each phase are given in parentheses.....	50

LIST OF TABLES (Continued)

Table	Page
4.3 Equilibrium pressure, transformation barrier, and stresses for SiC, GaN, InN, ZnO and CdSe for the WZ→RS and WZ→HX (WZ→DHX) transformations. p^{eq} is the hydrostatic pressure that establishes the equilibrium between the WZ and RS structures and $p_t(\text{exp})$ is the corresponding experimental value. $-\sigma_c^{\text{eq}}$ (σ_b^{eq}) is the value of the compressive (tensile) force per unit area along the c -direction (b -direction) at which the WZ and HX (DHX) structures are in equilibrium. For CdSe, although $-\sigma_c^{\text{eq}} = 3.8$ GPa provides equilibrium between the WZ and HX phases, the RS phase has lower enthalpy (hence more stable) under this condition. The transformation enthalpy barrier in eV/2-pairs between the WZ and RS phases at a given equilibrium pressure are given in square brackets following p^{eq} in the same column.....	57
5.1 Lattice parameters for WZ and BCT-4 ZnO under tensile loading along [0001] direction for $\sigma_c = 0, 4, 7$ and 10 GPa.....	76
6.1 The bulk modulus (B_0) and the elastic constants (C_{ij}) in unit of GPa, of WZ – SiC, GaN, InN, ZnO, and CdSe at $P = 0$ GPa.....	85
6.2 The calculated lattice constant a , bulk modulus B , and pressure derivation of the bulk modulus B' , and equilibrium volume V_0 , for γ -LiAlO ₂ , and δ -LiAlO ₂	91

LIST OF FIGURES

Figure	Page
2.1 Illustrations of the pseudopotential and pseudo wavefunction. The dash lines show the real wavefunction, $\psi(\vec{r})$, and real potential, $V(\vec{r})$. The solid lines show the corresponding pseudo wavefuncions, $\psi^{\text{PS}}(\vec{r})$, based on the pseudopotential, $V^{\text{PS}}(\vec{r})$. The cutoff radius r_c represents a radius at which the all electron and pseudo quantities match. (The figure is reproduced from Ref. (Wolfram Quester Source, www, 2006)).....	12
3.1 Crystal model of the WZ structure: small spheres represent anions and large spheres represent cations. The top figure shows the perspective view. The middle and bottom figures show top view and side view, respectively. The distances described by crystal parameters a , b , c , u , and v are indicated...	21
3.2 Crystal model of the HX structure: small spheres represent anions and large spheres represent cations. The top figure shows the perspective view. The middle and bottom figures show top view and side view, respectively. The distances described by crystal parameters a , b , c , u , and v are indicated.....	22
3.3 Crystal model of the RS structures: small spheres represent anions and large spheres represent cations. The top figure shows the perspective view. The middle and bottom figures show top view and side view, respectively. The distances described by crystal parameters a , b , c , u , and v are indicated...	23

LIST OF FIGURES (Continued)

Figure	Page
3.4 Total energy as a function of the volume for WZ, RS, HX, and DHX structures (black, red, green and blue curves represent WZ, RS , HX, and DHX structure, respectively) for (a) SiC, (b) GaN, (c) InN, (d) ZnO, and (e) CdSe with LDA calculations	30
3.5 Energy versus volume for four ZnO structure. The transition pressure is given by the slope of the common tangent lines between the two phases. For example, the dashed line shows the common tangent line between the WZ- and RS- structures. The slope of the line gives the equilibrium transition pressure of 8.22 GPa (Sarasamak <i>et al.</i> , 2008).....	34
3.6 Representation of (a) uniform compression resulting from a purely hydrostatic compressive stress and (b) pure shear deformation (Figure is reproduced from Ref. (Elliott, 1998)).....	37
4.1 Energy (solid curve) and enthalpy (dashed curve) as functions of volume for wurtzite ($c/a = 1.61$ and $b/a = 1.73$) ZnO. At hydrostatic pressure $p_1=8.22$ GPa, the volume that minimizes enthalpy (V_1) is smaller than the volume at ambient pressure (V_0). (The figure is a reproduction of Figure 2 in our published paper (Sarasamak <i>et al.</i> , 2008)).....	44

LIST OF FIGURES (Continued)

Figure	Page
<p>4.2 (a) Energy (E) landscape for ZnO (in eV per wurtzite unit cell which contains 2 cation-anion pairs or 2 f.u.). Each point on the surface represents the minimum energy for a given combination of c/a and b/a. To obtain each minimum energy, u, v, and V are allowed to relax while c/a and b/a are kept constant. Energy levels above -20.5 eV are truncated as they are not of interest in the discussions here. (b) 2-D sections of the energy surface for $b/a = 1.73$ (solid line) and 1.00 (dashed line).....</p>	46
<p>4.3 Energy surface map (in eV/2 pairs) for a wurtzite unit cell of (a) SiC, (b), GaN, (c) InN and (d) CdSe. Each point on the surface represents the minimum energy for a given combination of c/a and b/a. To obtain each minimum energy, u, v, and V are allowed to relax while c/a and b/a are kept constant. Energy levels above a certain value for each plot are truncated as they are not of interest in the discussions.....</p>	47
<p>4.4 2-D sections of (a) SiC, (b) GaN, (c) InN, (d) CdSe energy surfaces for $b/a = 1.73$ (solid lines) and 1.00 (dashed lines).....</p>	48
<p>4.5 Correlation between the formation energy differences (ΔE) and the ionicity as quantified by Phillips' f_i for SiC, GaN, InN, ZnO and CdSe. $\Delta E^{\text{RS-WZ}}$ is shown with the solid line and $\Delta E^{\text{HX-WZ}}$ is shown with the dashed line. For all compounds, WZ has the lowest energy and RS has the highest energy, except for CdSe whose RS phase has a slightly lower energy than HX phase.....</p>	49

LIST OF FIGURES (Continued)

Figure	Page
<p>4.6 Schematic illustrations of the WZ, HX, and RS structures: small spheres represent anions and large spheres represent cations. The middle and bottom rows show top view and side view, respectively. Parameters a, b, c, u, and v are indicated. For realistic rendering, the images shown are drawn to scale using parameters for ZnO at equilibrium conditions, i.e., ambient pressure for WZ, $\sigma = -\sigma_c^{\text{eq}}$ for HX and $p = p^{\text{eq}}$ for RS. ΔV, Δb, and Δc are the percentage changes in V (volume), b and c relative to the same quantities for WZ. (The figure is a reproduction of Figure 1 in our published paper (Sarasamak <i>et al.</i>, 2008)).....</p>	51
<p>4.7 Enthalpy differences (ΔH), in the unit of eV/2-pairs, between RS and WZ (solid line) and between HX¹ and WZ (dashed line) as a function of hydrostatic pressure for (a) SiC, (b) GaN, (c) InN, (d) ZnO and (e) CdSe. As the pressure reaches the equilibrium point (p^{eq}, indicated by solid dots), the enthalpies for RS and WZ become equal. Above p^{eq}, RS turn to be more stable. Note that HX is never stable under hydrostatic loading.....</p>	53
<p>4.8 Enthalpy surface maps (in eV/2 pairs) for a wurtzite unit cell of (a) SiC, (b) GaN, (c) InN, (d) ZnO and (e) CdSe at their respective RS-WZ equilibrium pressures (p^{eq}).....</p>	54
<p>4.9 2-D sections of the enthalpy surface maps in Figure 4.8 for $b/a = 1.73$ (solid lines) and 1.00 (dashed lines).....</p>	55

LIST OF FIGURES (Continued)

Figure	Page
<p>4.10 Correlation between equilibrium hydrostatic pressure (p^{eq}) and the difference in energy (ΔE) between the RS and WZ phases of the five compounds. p^{eq} is the pressure at which the WZ and RS structures are in equilibrium as illustrated in Figure 4.7 and tabulated in Table 4.2. The energy difference $\Delta E = E^{\text{RS}} - E^{\text{WZ}}$ is calculated under the conditions of zero external loading and is tabulated in Table 4.1.....</p>	59
<p>4.11 Enthalpy differences (ΔH) between the RS and WZ (solid line) and HX and WZ (dashed line) as a function of c-direction stress ($-\sigma_c$) for (a) SiC, (b) GaN, (c) InN, (d) ZnO and (e) CdSe. As the magnitude of the stress reaches the equilibrium value ($-\sigma_c^{\text{eq}}$, indicated by solid dots), enthalpies of the HX and WZ structures become comparable. At stresses above $-\sigma_c^{\text{eq}}$, the HX phase is more stable.....</p>	61
<p>4.12 Enthalpy surface maps (in eV/2 pairs) for a wurtzite unit cell of (a) SiC, (b) GaN, (c) InN, (d) ZnO and (e) CdSe at their respective HX-WZ equilibrium c-direction stresses ($-\sigma_c^{\text{eq}}$).....</p>	62
<p>4.13 2-D sections of the enthalpy surface maps in Figure 4.12 for $b/a = 1.73$ (solid lines) and 1.00 (dashed lines).....</p>	63

LIST OF FIGURES (Continued)

Figure	Page
<p>4.14 Correlation between equilibrium stresses ($-\sigma_c^{\text{eq}}$ and σ_b^{eq}) and the difference in energy (ΔE) between the HX and WZ phases for the five compounds. $-\sigma_c^{\text{eq}}$ (σ_b^{eq}) is the equilibrium value of the c-direction compressive stress (b-direction tensile stress) for the HX (DHX) and RS structures (see Table 4.2). The energy difference $\Delta E = E^{\text{HX}} - E^{\text{WZ}}$ is calculated under conditions of zero external loading and is tabulated in Table 4.1.....</p>	65
<p>4.15 Enthalpy surface maps (in eV/2 pairs) for a wurtzite unit cell of (a) InN, (b) ZnO and (c) CdSe at their respective DHX-WZ equilibrium stresses along b-direction (σ_b^{eq}).....</p>	67
<p>4.16 2-D sections of the enthalpy surface maps in Figure 4.15 for two b/a values that cut through the DHX and WZ structures.....</p>	67
<p>4.17 Enthalpy differences (ΔH) between the DHX and WZ phases of (a) InN, (b) ZnO and (c) CdSe as a function of b-direction stress (σ_b). As the applied stress reaches the equilibrium point (σ_b^{eq}, indicated by solid dots), the enthalpy of HX equals that of WZ. At stresses above σ_b^{eq}, the DHX phase is more stable</p>	68
<p>4.18 Enthalpy surface maps (in eV/2 pairs) for (a) SiC and (b) GaN at the tensile stress along b-direction (σ_b) of 60 GPa and 30 GPa, respectively</p>	69

LIST OF FIGURES (Continued)

Figure	Page
5.1 (a) Crystallographic transition through breaking and formation of bonds and differences in bond angles between the wurtzite (WZ) and body-centered-tetragonal (BCT-4) structures and (b) WZ and BCT-4 structures. The red dash box lines show the cell size with 8 atoms (four Zn-O pairs), for the WZ and BCT-4 structures used for the calculations.....	73
5.2 Crystal model of the BCT-4 structure: small spheres represent anions and large spheres represent cations. The top figure shows the perspective view. The middle and bottom rows show top view and side view, respectively. The distances described by crystal parameters a , b , and c are indicated.....	77
5.3 Enthalpy (eV/ 4 Zn-O pairs) as a function of c/a obtained from first principles calculations for $b/a = 1.73$ at tensile stresses of (a) $\sigma_c = 0$ GPa, (b) $\sigma_c = 4$ GPa, (c) $\sigma_c = 7$ GPa and (d) $\sigma_c = 10$ GPa. The minimum enthalpy curve for each plot is shown with the thick solid green line.....	78
6.1 The elastic constant as function of pressure in WZ-SiC, GaN, InN, ZnO, and CdSe. The black, red, blue, and green color represented C_{11} , C_{33} , C_{44} , and C_{66} , respectively.....	86
6.2 Schematic illustration of the γ -LiAlO ₂ and δ -LiAlO ₂ structures: The middle row and the bottom row show the side view and top view, respectively. The crystal parameters a and c are indicated.....	89

LIST OF FIGURES (Continued)

Figure	Page
6.3 Unit cells of γ -LiAlO ₂ and δ -LiAlO ₂ used in the calculations.....	90
6.4 The total energy as a function of volume for γ - and δ -phase and the common tangent construction.....	90

LIST OF ABBREVIATIONS

ADX	= Angle Dispersive X-ray diffraction
ASA	= Atomic Sphere Approximation
AE	= All electron
BCT-4	= Body center tetragonal
BZ	= Brillouin Zone
CN	= Coordination Number
DFT	= Density Functional Theory
EDXD	= Energy Dispersive X-ray Diffraction
EPMD	= Empirical Potential based Molecular Dynamic
EXAFS	= Extended X-ray Absorption Fine Structure
FP-LMTO	= Full Potential Linear Muffin Tin Orbitals
GGA	= Generalized Gradient Approximation
HX	= unbuckled wurtzite
KS	= Kohn-Sham
LDA	= Local Density Approximation
LMTO	= Linear Muffin Tin Orbitals
MCFC	= Molten Carbonate Fuel Cells
MD	= Molecular Dynamics
PP	= Pseudo Potential
PAW	= Projector Augmented Wave

LIST OF ABBREVIATIONS (Continued)

RS	=	Rocksalt
USPP	=	Ultra Soft Pseudo Potential
UTS	=	Ultimate Tensile Strengths
VASP	=	Vienna Ab-initio Simulation Package
WZ	=	Wurtzite
XC	=	Exchange-Correlation
XRD	=	X-Ray Diffraction
ZB	=	Zincblende

CHAPTER I

INTRODUCTION

One-to-one binary compounds that obey the octet rule, i.e., I-VII, II-VI, III-V, or IV-IV materials, are generally semiconductors or insulators. Although these AB compounds have the same chemical formula units, their crystal structures under ambient conditions can be vary different, depending on their bond ionicities. While highly ionic compounds, such as CsCl (I-VII), prefer dense crystal structures with a coordination number of 8 (C.N.= 8), compounds with lower degrees of ionicity, such as NaCl (also I-VII), gravitate toward the rocksalt structure (RS, $Fm\bar{3}m$ space group) with C.N.= 6. As the degree of ionicity decreases (shifting toward the covalent bonding character), compounds, such as ZnO (II-VI), GaN (III-V) and SiC (IV-IV), stabilize in wurtzite (WZ, $P6_3mc$) or zincblende (ZB, $F\bar{4}3m$) structures with C.N.= 4. In wurtzite (or zincblende), the valence electron counting is satisfied, i.e., each bond contains two electrons. However, in compounds with higher degrees of ionicity such as CsCl and NaCl, the strong cation-anion attractions lead to the formation of the structures with higher C.N. Nevertheless, bond is not the only factor that determines the crystalline structure. The intrinsic factors such as band structures, valence electrons, bonding states and structural symmetries also play their rules. Extrinsic factors such as loading and temperature also play significant roles.

Calculations and experiments have been carried out to study the structural stabilities of materials. Over two decades ago, first principles calculations have been used to evaluate the formation energies of different crystalline structures (see for e.g., Chan *et al.*, 1986 and Fahy *et al.*, 1986). X-ray diffraction experiment is the main tool to determine the natural occurring structures. The stable crystalline structures under ambient conditions are well established. For a comprehensive review, see Mujica *et al.*, 2003. Furthermore, advances in experimental techniques, such as the use of intense and tunable x-ray from synchrotron radiation, also allowed x-ray diffraction analyses under external loadings. For hydrostatic compression, it is observed that most materials with low C.N. (e.g., WZ and ZB) transform into a more compressed crystalline form with higher C.N. structures (e.g., RS) (Bates *et al.*, 1962; Cline and Stephens, 1965; Xia *et al.*, 1993; Yoshida *et al.*, 1993; Ueno *et al.*, 1994; Xia *et al.*, 1994; Desgreniers, 1998; Kusaba *et al.*, 1999; Jiang *et al.*, 2000; Mujica *et al.*, 2003; Wu *et al.*, 2005). First principles and empirical potential calculations have yielded phase equilibrium pressures that are comparable but almost always lower than the transformation pressures measured from experiments (Jaffe and Hess, 1993; Christensen and Gorczyca, 1994; Karch *et al.*, 1996; Côté *et al.*, 1997; Jaffe *et al.*, 2000; Limpijumnong and Lambrecht, 2001a; 2001b; Zaoui and Sekkal, 2002; Mujica *et al.*, 2003; Limpijumnong and Jungthawan, 2004; Serrano *et al.*, 2004). The higher experimental values are attributed to the existence of an energy barrier between the phases for each transformation. This finding is supported by, for example, the observation that critical pressure for the upward WZ→RS transformation is higher than the critical pressure for the downward RS→WZ transformation (Mujica *et al.*, 2003; Limpijumnong and Jungthawan, 2004) or the trapping of nanocrystallite ZnO in the RS phase under ambient condition after a high heat-high pressure treatment

(Decremps *et al.*, 2002). If there was no transformation barrier, the upward and downward transformations would occur at the same point and there should be no trapping of the meta-stable high pressure phase. The study of strain is also important because many electronic devices use epitaxial growth film. It is well known that, at the thin film interfaces, lattice mismatched is inevitable and it degrades the devices' properties. It is necessary to study the behaviors of crystals under strain deformations. These properties have been partially studied in both theoretical side, for e.g., the first principles full-potential linear muffin-tin orbital calculations of elastic constants and related properties in BN, AlN, GaN, and InN (Kim *et al.*, 1996) and experimental side, for e.g., the study of strain in InN thin film by Raman measurements (Wang *et al.*, 2006) or the study of the lattice parameters of GaN epitaxial layers on different substrates by X-ray-diffraction measurements (Shan *et al.*, 1996).

This thesis employed first principle (also known as *ab initio*) method to study mechanical properties of some semiconductors in group IV (SiC), group III-V (GaN and InN), and group II-VI (ZnO and CdSe). We will first give a brief description of the calculation methods used (Chapter II). Then the calculated structural parameters under ambient conditions in comparison with available experimental results are reported and the brief description for the phase stability (in thermodynamics picture), phase transition under pressure, elastic constants are also presented as well (Chapter III). The calculated results of this work are constituted as follow, In Chapter IV, the relative phase stabilities between the wurtzite (WZ), unbuckled wurtzite (HX), and rocksalt (RS) phases of these compounds under different loading conditions will be presented. For ZnO, the novel structure was found and named as body center tetragonal (BCT-4) phase. In Chapter V, the relationship between the previous phases

for ZnO (from Chapter IV) with this new structure is summarized. Finally, the continuations work about the study of elastic constants under pressure (up to the transition pressure) of above mentioned five compounds and future works of interest are presented (Chapter VI). Note that the conclusions of Chapter IV – V are located at the end of each chapter.

CHAPTER II

THEORETICAL APPROACH

One often models solid by starting from an ideal crystal at zero temperature. A unit cell of a crystal may contain several atoms (at specific crystallography positions). To model a realistic crystal, the unit cell is repeated with periodic boundary conditions. Then the electronics structure of the entire crystal is solved quantum mechanically. In addition to electronically properties the electronic structure is also responsible for other properties such as relative stability, relaxation of atoms and phase transitions, etc. In this chapter, we will briefly discuss about the theories approximations, methods, and software used in this work. Details information can be found in the respective literatures provided throughout the chapter.

2.1 Density Functional Theory

2.1.1 The Hohenberg and Kohn Theorem

The basic principle of density functional theory (DFT) is to describe the complicated many-body electron wavefunction, Ψ , with a simple quantity, that is the electron density, $n(\vec{r})$ (Parr and Yang, 1989). Hohenberg and Kohn (Hohenberg and Kohn 1964) proposed that, the ground-state energy and all electron properties of the many electron wavefunction in the presence of an external potential can determined from the electron density, $n(\vec{r})$. They showed that for Coulomb-interacting particles moving in an external potential $V_{ext}(\vec{r})$, the ground state energy can be obtained by

minimizing the energy functional. The ground-state energy of a many electron wavefunction is written as (Hohenberg and Kohn, 1964),

$$E[n(\vec{r})] = \int V_{ext}(\vec{r})n(\vec{r})d^3r + F[n(\vec{r})], \quad (2.1)$$

where $V_{ext}(\vec{r})$ is the “external” potential generated by the nuclei acting on the electrons. $F[n(\vec{r})]$ is a universal functional of the electron density, independent of the external potential $V_{ext}(\vec{r})$. The functional $F[n(\vec{r})]$ includes all kinetic energy and electron-electron interaction terms (Parr and Yang, 1989).

2.1.2 Kohn and Sham Equation

Kohn and Sham (Kohn and Sham, 1965) proposed that the Hohenberg and Kohn expression in Eq. 2.1 can be written as,

$$E[n(\vec{r})] = \int V_{ext}(\vec{r})n(\vec{r})d^3r + \frac{e^2}{2} \iint \frac{n(\vec{r})n(\vec{r}')}{|\vec{r} - \vec{r}'|} d^3r d^3r' + T_s[n(\vec{r})] + E_{xc}[n(\vec{r})] \quad (2.2)$$

where $\frac{e^2}{2} \iint \frac{n(\vec{r})n(\vec{r}')}{|\vec{r} - \vec{r}'|} d^3r d^3r'$ is the electron-electron Coulomb energy, also called

Hartree energy. $T_s[n(\vec{r})]$ is the kinetic energy of a non-interacting system with the same density. Note that, $T_s[n(\vec{r})]$ is not the exact kinetic energy functional ($T[n(\vec{r})]$).

Kohn and Sham proposed that, the difference between $T[n(\vec{r})]$ and $T_s[n(\vec{r})]$ is generally small and can be included in exchange-correlation energy, $E_{xc}[n(\vec{r})]$ (Parr and Yang, 1989). E_{xc} is the exchange-correlation energy.

Thus the Kohn-Sham (KS) - effective potential can be written as,

$$V_{eff}(\vec{r}) = V_{ext}(\vec{r}) + e^2 \int \frac{n(\vec{r}')}{|\vec{r} - \vec{r}'|} d^3r' + \frac{\delta E_{xc}[n(\vec{r})]}{\delta n}. \quad (2.3)$$

Hence, the one-particle Schrödinger equation or Kohn-Sham (KS) equation (Kohn and Sham, 1965) can be written as,

$$\left[-\frac{\hbar^2}{2m} \nabla^2 + V_{eff}(\vec{r}) \right] \psi_i(\vec{r}) = \varepsilon_i \psi_i(\vec{r}). \quad (2.4)$$

The electron density for this system of electrons is given by (Kohn and Sham, 1965),

$$n(\vec{r}) = \sum_{i=1}^N |\psi_i(\vec{r})|^2, \quad (2.5)$$

where N is the number of electrons.

Equation 2.4 has to be solved self-consistently. Initially, a guess of $n(\vec{r})$ is used to construct V_{eff} , which is used as input quantities to solve Eq. 2.4 for the ψ_i . Then an improved $n(\vec{r})$ is calculated from ψ_i based on Eq. 2.5. The new $n(\vec{r})$ is then used instead of the guessing $n(\vec{r})$ to construct V_{eff} . This routine is repeated until convergence is reached, that mean the new $n(\vec{r})$ as output is equal to the old $n(\vec{r})$ as the input.

2.1.3 The local density approximation (LDA)

Out of three terms in the effective potential (V_{eff}), Eq. 2.3, only the exchange-correlation energy $E_{xc}[n(\vec{r})]$ is not exactly known. To solve the one-particle Schrödinger equation (Eq. 2.4), $E_{xc}[n(\vec{r})]$ must be approximated. The most popular approximation for approximating $E_{xc}[n(\vec{r})]$ is the local density approximation (LDA).

Under LDA, $E_{xc}[n(\vec{r})]$ depends solely on the value of electron density at each point in space. The most successful local approximation to $E_{xc}[n(\vec{r})]$ is the one derived from homogeneous electron gas model which was first formulated by Kohn

and Sham (Kohn and Sham, 1965) The local density approximation for exchange correlation energy can be written as (Parr and Yang, 1989; Kohn, 1999),

$$E_{xc}^{LDA}[n(\vec{r})] = \int n(\vec{r}) \varepsilon_{xc}[n(\vec{r})] d^3r, \quad (2.6)$$

where $\varepsilon_{xc}[n(\vec{r})]$ is the exchange correlation energy per particle of a homogeneous electron gas with the density $n(\vec{r})$. The $\varepsilon_{xc}[n(\vec{r})]$ can be written in the combination form between exchange and correlation energy as (Parr and Yang, 1989),

$$\varepsilon_{xc}[n(\vec{r})] = \varepsilon_x[n(\vec{r})] + \varepsilon_c[n(\vec{r})], \quad (2.7)$$

where the exchange energy term, $\varepsilon_x[n(\vec{r})]$ are known from an analytic form of homogeneous electron gas as proposed by Dirac (Dirac, 1930) and can be written as (Parr and Yang, 1989),

$$\varepsilon_x[n(\vec{r})] = -C_x n(\vec{r})^{1/3}, C_x = \frac{3}{4} \left(\frac{3}{\pi} \right)^{1/3}. \quad (2.8)$$

For the correlation energy term, $\varepsilon_c[n(\vec{r})]$ was first calculated by Wigner (Wigner, 1938). However, an analytic form of this energy is known only under the high (Gell-Mann and Brueckner, 1957; Carr and Maradudin, 1964) and low (Carr, 1961; Nozieres and Pines, 1966) density limit (Parr and Yang, 1989). There is the correlation energy values obtained from a quantum Monte Carlo method by Ceperley and Alder (Ceperley and Alder, 1980). Then, Vosko, Wilk, and Nusair (Vosko *et al.*, 1980) presented the analytic form of $\varepsilon_c[n(\vec{r})]$ by interpolating the values from Ceperley and Alder. In addition, there are other forms of $\varepsilon_c[n(\vec{r})]$ that can be used for $\varepsilon_{xc}[n(\vec{r})]$ (von Barth and Hedin, 1972; Perdew and Zunger, 1981; Perdew and Wang, 1992).

The LDA work well for the system with slowly varying in density. Some of successes and failures to use LDA to approximate $E_{xc}[n(\vec{r})]$ have been discussed by Jones and Gunnarsson (Jones and Gunnarsson, 1989).

2.1.4 The generalized gradient approximation (GGA)

The generalized gradient approximation (GGA) is introduced to take into account the variation of electron density in space. Under GGA, the exchange-correlation energy E_{xc} is a functional of the local electron densities, $n(\vec{r})$ and their gradients, $|\nabla n(\vec{r})|$ (Kohn, 1999),

$$E_{xc}^{GGA}[n(\vec{r})] = \int f[n(\vec{r}), \nabla n(\vec{r})] n(\vec{r}) d^3r. \quad (2.9)$$

The GGA improve the ground state properties, it reduces errors in energy of light atoms in small molecules. In general it tends to produce larger equilibrium lattice parameters than those obtained from LDA. The improvement of GGA with respect to LDA is not clear in the applications of solid. Sometimes the GGA overcorrect the LDA results. The comparison of GGA and LDA for some semiconductors can be found in Ref. (Filippi *et al.*, 1994; Khein *et al.*, 1995). There are many forms of GGA functional for the exchange correlation energy, $E_{xc}^{GGA}[n(\vec{r})]$. The most widely used are proposed by Becke (Becke, 1988), which is known as B88, Perdew and Wang (Perdew and Wang, 1992), which is known as PW91 and Perdew, Burke, and Enzerhof (Perdew *et al.*, 1996), which is known as PBE.

2.2 Plane waves

In this thesis, plane waves (PWs) are employed as a basis set, for the solutions of the KS equation (Eq.2.4). The starting point for PWs calculation is an expression of the wave functions in terms $e^{i\vec{k}\cdot\vec{r}}$, time a function of periodic function, $u_{n\vec{k}}(\vec{r})$ (Kittel, 1996),

$$\psi_{n\vec{k}}(\vec{r}) = e^{i\vec{k}\cdot\vec{r}} u_{n\vec{k}}(\vec{r}) \quad (2.10)$$

where

$$u_{n\vec{k}}(\vec{r} + \vec{R}) = u_{n\vec{k}}(\vec{r}). \quad (2.11)$$

Equation 2.10 and 2.11 are known as Bloch's theorem, where \vec{r} is the position in the crystal, \vec{R} is the lattice translation vector in the crystal, \vec{k} is the wave vector, n is the band index representing the different solutions that have the same wave vector, \vec{k} . $u_{n\vec{k}}(\vec{r})$ has the same periodicity as the potential. Using the Fourier transform of a periodic function to reciprocal space, the wave function in Eq. 2.10 can also be written in the sum of PWs in the following form (Kittel, 1996),

$$\psi_{n\vec{k}}(\vec{r}) = \sum_{\vec{G}} u_{n\vec{k}}(\vec{G}) e^{i(\vec{k}+\vec{G})\cdot\vec{r}} \quad (2.12)$$

where \vec{G} is the reciprocal lattice vector. This allows the calculations to be done in the reciprocal space. In practice, the numbers of \vec{G} vectors used in the sum are limited. The kinetic energy of PWs used in the calculations have to be smaller than the cutoff energy, E_{cutoff} , (Martin, 2004),

$$\frac{\hbar^2}{2m} |k + G|^2 < E_{cutoff}. \quad (2.13)$$

From the Bloch's theorem, the wavefunction of an infinite number of wave vectors, \vec{k} in the first Brillouin zone (BZ) need to be solved (Martin, 2004). In

practice, it is impossible to do the calculations with the infinite number of k-points. However, the wavefunctions are quite similar for k-points in the same vicinity. Therefore, it is possible to sampling a limited number of k-points to represent the entire BZ. There are various sampling methods to calculate the set of k-points see for e.g., (Monkhorst and Pack, 1976). The set of “special” k-points chosen to appropriately describe the BZ employed in this work is based on the Monkhorst-Pack method (Monkhorst and Pack, 1976).

2.3 Pseudopotentials

In materials, electrons can be divided into two types: core electrons and valence electrons. Core electrons are strongly localized in the inner atomic shell. Valence electrons are electrons in the outer shell, participating in bondings. PWs with a limited E_{cutoff} are not suitable for describing the core region. Since a large number of PWs would be required to accurately describe the fast oscillation wavefunctions in the core regions (Heine, 1970). To solve the problem, the strongly core potential is replaced by a smooth pseudopotential ($V^{PS}(\vec{r})$) as shown in Figure 2.1. This effectively removes the core electrons from the calculations. It does not seriously affect the results because the core electrons remain almost unchanged. The corresponding set of pseudo wavefunctions $\psi^{PS}(\vec{r})$ and the all electron wave functions $\psi(\vec{r})$ are matched outside a selected core radius r_c . Inside r_c , $\psi^{PS}(\vec{r})$ does not have the fast oscillation features that required high energy cutoff. The pseudo wavefunctions vary smoothly inside r_c , as shown in Figure 2.1.

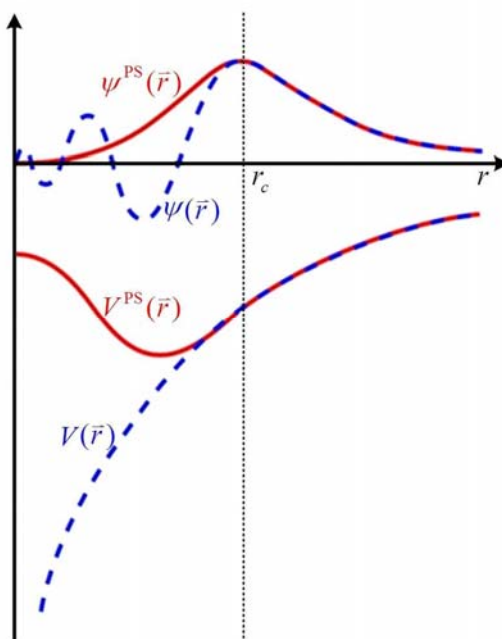


Figure 2.1 Illustrations of the pseudopotential and pseudo wavefunction. The dash lines show the real wavefunction, $\psi(\vec{r})$, and real potential, $V(\vec{r})$. The solid lines show the corresponding pseudo wavefunctions, $\psi^{\text{PS}}(\vec{r})$, based on the pseudopotential, $V^{\text{PS}}(\vec{r})$. The cutoff radius r_c represents a radius at which the all electron and pseudo quantities match. (The figure is reproduced from Ref. (Wolfram Quester Source, www, 2006))

2.3.1 Norm-conserving pseudopotentials

Pseudopotentials used in the electronic structure calculations are generated based on all electron KS calculations of isolated atoms. The radial KS equation is used because isolated atoms have the spherical symmetry. The pseudopotential should be nodeless (Martin, 2004; Beyer, 2006).

One important requirement is that the pseudopotentials have to meet the norm-conserving conditions. This is to ensure that the integration of pseudo and all electron (real) charges within the core radius are equal (Hamann *et al.*, 1979). The norm-conserving pseudopotentials are defined from the following list of conditions (Martin, 2004; Beyer, 2006; Carlsson, www, 2009)

1. All electron and pseudo wavefunctions (should be smooth and nodeless) are matched outside the cut-off radius, r_c , i.e.,

$$\psi_l^{AE}(r) = \psi_l^{PS}(r), \quad r > r_c. \quad (2.14)$$

2. The eigenvalues should be conserved.

$$\varepsilon_l^{AE} = \varepsilon_l^{PS} \quad (2.15)$$

3. Inside the core, the integration of pseudo charge density is equal to that of all electron charge density. This condition is the norm-conservation criteria, i.e.

$$\int_0^{r_c} |\psi_l^{AE}(r)|^2 dr = \int_0^{r_c} |\psi_l^{PS}(r)|^2 dr. \quad (2.16)$$

4. The logarithmic derivatives of all electrons and pseudo wavefunctions and their first energy derivatives agree at r_c .

The logarithmic derivative for an angular momentum l , can be written as

$$D_l(\varepsilon) = \frac{d}{dr} \ln \psi_l(r; \varepsilon) \Big|_{r_c} = \frac{\psi_l'(r_c; \varepsilon)}{\psi_l(r_c; \varepsilon)}, \quad (2.17)$$

where $\psi_l(r; \varepsilon)$ is a solution of the radial KS equation for a fix potential and fixed energy ε .

The pseudopotential generation steps can be presented as follow. First, the all electron wavefunction ψ^{AE} is replaced by an arbitrary smooth nodeless wavefunction $\psi^{PS}(r)$ which satisfied the conditions mentioned above. Based on the pseudo wavefunction $\psi^{PS}(r)$ and its corresponding energy $\varepsilon_l^{PS} = \varepsilon_l^{AE}$, the norm-conserving pseudo potential is obtained by solving the radial KS equation.

The norm-conserving pseudopotentials, V^{PS} can be separated into a local potential, $V_{loc}^{PS}(r)$ and a nonlocal potential, $V_{nl}^{PS}(r) = \sum_l |\beta_l\rangle V_l \langle \beta_l|$ (Kleinman and Bylander, 1982),

$$V^{PS} = V_{loc}^{PS}(r) + V_{nl}^{PS}(r) = V_{loc}^{PS}(r) + \sum_l |\beta_l\rangle V_l \langle \beta_l|. \quad (2.18)$$

The nonlocal part is the deviation from the all electron potential and is confined inside r_c . The projector, $|\beta_l\rangle$, acts only on the wavefunctions with angular momentum (l), which is localized within r_c .

Accuracy and transferability generally lead to the choice of a small cutoff radius (r_c) and “hard” potentials. This is to give the wavefunction as accurate as possible in the region near the atom. However, to benefit from the pseudopotential, one needs soft potentials that result in the smooth wavefunctions. The smoothness of the pseudopotentials generally leads to the choice of a large cutoff radius (r_c). (Martin, 2004).

2.3.2 Ultrasoft pseudopotentials

The elements with $2p$ and $3d$ valence electrons are difficult to treat within pseudopotentials scheme (Meyer, 2006). These valence electrons are strongly localized near the ionic core region. Many plane waves are required to represent the accurate wave functions, which is not an efficient way to perform in the calculations. To solve this problem, ultrasoft pseudopotentials (USPP) is introduced (Vanderbilt, 1990).

The norm conserving requirements has been relaxed in USPP, to obtain smoother wave functions. Instead of using the plane waves to describe the full valence wave function, only a small portion of the wave function is calculated within the USPP scheme. This allows one to reduce substantially the plane wave cutoff energy in the calculations (Meyer, 2006).

2.3.3 Projector augmented waves

The projector augmented waves (PAW) method is proposed by Blöchl (Blöchl, 1994). In this method a smooth wavefunction ($\tilde{\psi}$) is created. There exists a linear transformation which relates the all electron wave function (ψ) to this smooth wavefunction ($\tilde{\psi}$) by the transformation operator τ through the relationship:

$$|\psi\rangle = \tau |\tilde{\psi}\rangle. \quad (2.19)$$

Utilizing the linear transformation of PAW method, the all electron wavefunction (ψ) can be written as

$$|\psi\rangle = |\tilde{\psi}\rangle + \sum_m (|\psi_m\rangle - |\tilde{\psi}_m\rangle) \langle \tilde{p}_m | \tilde{\psi}\rangle, \quad (2.20)$$

where ψ_m is a localized all electron partial wave for state m , $\tilde{\psi}_m$ is a localized smooth partial wave for state m , and $\langle \tilde{p}_m |$ is the localized projection operator. The transformation operator τ can be written as

$$\tau = 1 + \sum_m (|\psi_m\rangle - |\tilde{\psi}_m\rangle) \langle \tilde{p}_m|. \quad (2.21)$$

From Eq. 2.21 the transformation operator τ can be used to add back the core potential of the all electron wavefunctions to the smoothed wavefunctions. Moreover, Eq. 2.21 can be applied equally well to core and valence states so that all electron results can be derived by applying Eq. 2.21 to all electron states (Martin, 2004).

2.4 The Full Potential Linear Muffin Tin Orbital Method

In full potential linear muffin tin orbital (FP-LMTO) method, the unit cell is divided into atom centered muffin tin spheres and an interstitial region outside these spheres. Inside the muffin tin spheres, the potentials can be solved numerically by means of expansions in spherical harmonics (Methfessel, 1988). In the interstitial region, the potential is calculated by using numerical integration which results in the matrix elements (Methfessel *et al.*, 2000),

$$V_{ij}^{(IR)} = \int_{IR} H_i^*(\vec{r}) V(\vec{r}) H_j(\vec{r}) d\vec{r} \quad (2.22)$$

where $V_{ij}^{(IR)}$ is the matrix element potential in the interstitial region, the functions $H_i(\vec{r})$ (or $H_j(\vec{r})$) is the envelop functions, which are augmented inside the muffin tin sphere to obtain the final basis function, $V(\vec{r})$ is the interstitial potential and IR denoted the interstitial region. The results also depend on how the suitable interstitial region is chosen. The general way in obtaining the interstitial region is presented as follow. The basis functions and the interstitial potential are smoothly extended through

the atomic sphere in some manner. Then these smooth functions are replaced into Eq. 2.22 to integrate for the potential of the interstitial region. Finally, the unwanted contributions inside the spheres are subtracted in conjunction with the augmentation step. In FP-LMTO, the smooth extension must be built for the sphere on which the function is centered by matching an analytical expression (i.e. a polynomial) at the sphere radius (Methfessel *et al.*, 2000). Alternatively, Hankel functions can be used to represent interstitial quantities. These functions make basis function quite similar to the real basis functions. Moreover, a smoothed Hankel functions that are bended more than normal Hankel functions near the muffin tin sphere, is introduced. This smoothed Hankel functions lead to the smaller basis functions. A different approach (to the interstitial potential matrix elements) is to re-expand the product of any two envelopes as a sum of an auxiliary atom-centered basis function. The matrix element in Eq. 2.22 then reduces to a linear combination of integrals of the auxiliary atom-centered basis function times the interstitial potential. In this way the three-center integrals in Eq. 2.22 can be reduced to a sum of two-center integrals (Methfessel *et al.*, 1988). The expansion can be obtained approximately by using Gauss's theorem to fit on the surfaces of the muffin-tin spheres (Methfessel *et al.*, 1988; Methfessel *et al.*, 2000). For further details, see Ref. (Methfessel *et al.*, 2000).

2.5 The Vienna *Ab initio* Simulation (VASP) Package

The calculations are performed with the Vienna *Ab initio* Simulation Package (VASP), developed by Kresse, Hafner, and Furthmüller (Kresse and Hafner, 1994; Kresse and Furthmüller, 1996a; 1996b). VASP uses planewaves (PWs) as a basis set to describe electron wavefunctions. The ultrasoft pseudopotentials (USPP) (Vanderbilt, 1990) and PAW (Blöchl, 1994) potentials needed for the calculations are included in the package. In this thesis, the ultrasoft pseudopotentials are mainly employed. So the fewer plane waves are needed in comparison to traditional pseudopotential methods. The k-point samplings are based on the Monkhorst-Pack approach (Monkhorst and Pack, 1976). The main computational part for solving the KS-equation self-consistently is obtained by using an iterative matrix-diagonalization scheme such as, a conjugate gradient scheme (Teter *et al.*, 1989; Bylander *et al.*, 1990) and block Davidson scheme (Davidson, 1983). The Broyden/Pulay mixing scheme (Pulay, 1980; Jonhson, 1988) is used for calculating of charge density. There are two main loops in VASP calculations. The charge density is optimized in the outer loop. In the inner loop, the wave functions are optimized by solving KS equation in a self consistent algorithm (Kresse and Furthmüller, 1996a; 1996b).

CHAPTER III

CRYSTAL PROPERTIES

3.1. Crystal structure

The natural form of all five materials studied is wurtzite, as shown in Figure 3.1 with the top view and side view in the middle and bottom row, respectively. This structure is quantified customarily by the lattice constant a , the c/a ratio, and the internal parameter u which specifies the relative distance ratio along the c -axis between the two hexagonal close-packed cation and anion sublattices. To describe the unbuckled-wurtzite (HX) (Figure 3.2) and the rocksalt (RS) structures (Figure 3.3) and the transformation from WZ to each of these phases, an extra lattice parameter b and an internal parameter v are introduced (Limpijumnong and Lambrecht, 2001a; 2001b). The parameter v defines the relative horizontal distance along the b -axis between the cation and anion sublattices. Out of five parameters (a , b , c , u , and v) illustrated in Figure 3.1, only three external ones (a , b , and c) can be directly manipulated by applying external stresses. The two internal parameters (u and v) cannot be directly controlled. These two internal parameters are determined such that, for any given configuration, the net forces on all atoms in the unit cell vanish. It is found that u depends mainly with c/a and v with b/a . An analysis of the variations of u with c/a and v with b/a can be found in Ref. (Limpijumnong and Lambrecht, 2001a; 2001b). The three crystal structures are significantly different, with $c/a \approx 1.63$ and $b/a \approx 1.73$ for WZ, $c/a \approx 1.20$ and $b/a \approx 1.73$ for HX and $c/a \approx 1.00$ and $b/a \approx 1.00$ for RS.

The ideal values of c/a , b/a , u , and v for WZ, HX, and RS under no load and zero temperature are listed in Table 3.1. All parameters are determined from the geometry of each structure, for instant, perfect tetrahedral coordination for WZ and perfect cubic for RS. This is with an exception of the c/a value for HX, which is obtained via enthalpy minimization and the approximated value is listed. Actual values of these parameters can deviate from those in Table 3.1, depending on the material, loading conditions and temperature. The calculations values of lattice parameters compare with other calculations and experimental results are shown in Table 3.2, 3.3, 3.4, 3.5, and 3.6 for SiC, GaN, InN, ZnO, and CdSe, respectively. These values are in good agreement with the experimental data and other theoretical values from the literature (see Table 3.2 – 3.6).

Table 3.1 Ideal lattice parameters for WZ, HX and RS crystalline structures.

Parameters	WZ	HX	RS
c/a	$\sqrt{8/3} \approx 1.63$	1.20	1.00
u	$3/8 \approx 0.37$	0.50	0.50
b/a	$\sqrt{3} \approx 1.73$	$\sqrt{3} \approx 1.73$	1.00
v	$1/3 \approx 0.33$	$1/3 \approx 0.33$	0.50

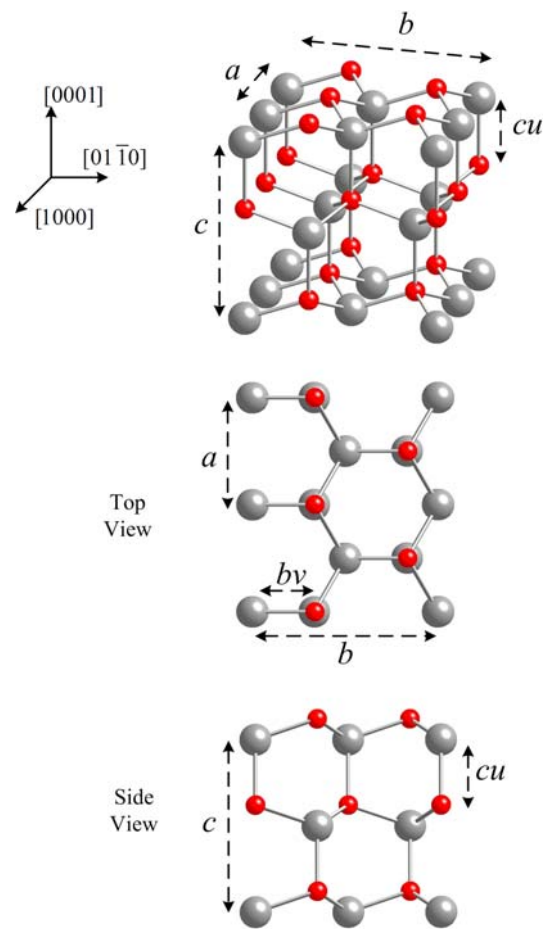


Figure 3.1 Crystal model of the WZ structure: small spheres represent anions and large spheres represent cations. The top figure shows the perspective view. The middle and bottom figures show top view and side view, respectively. The distances described by crystal parameters a , b , c , u , and v are indicated.

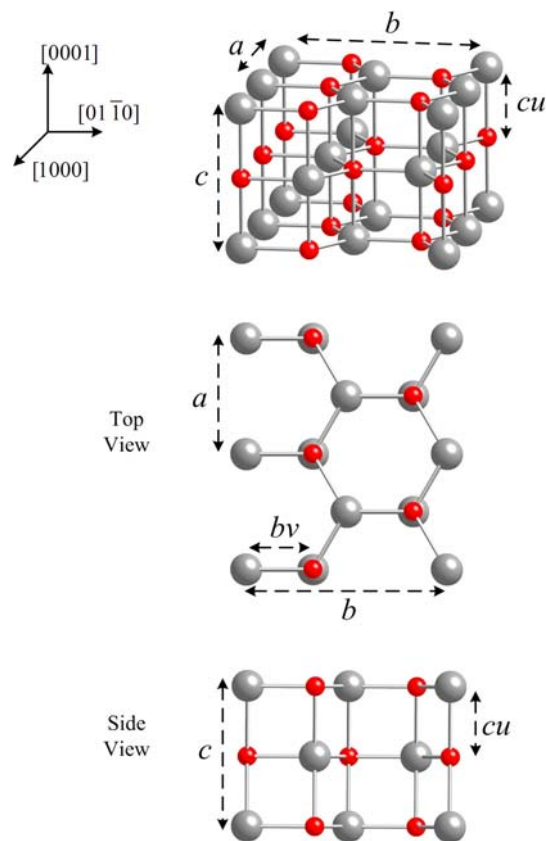


Figure 3.2 Crystal model of the HX structure: small spheres represent anions and large spheres represent cations. The top figure shows the perspective view. The middle and bottom figures show top view and side view, respectively. The distances described by crystal parameters a , b , c , u , and v are indicated.

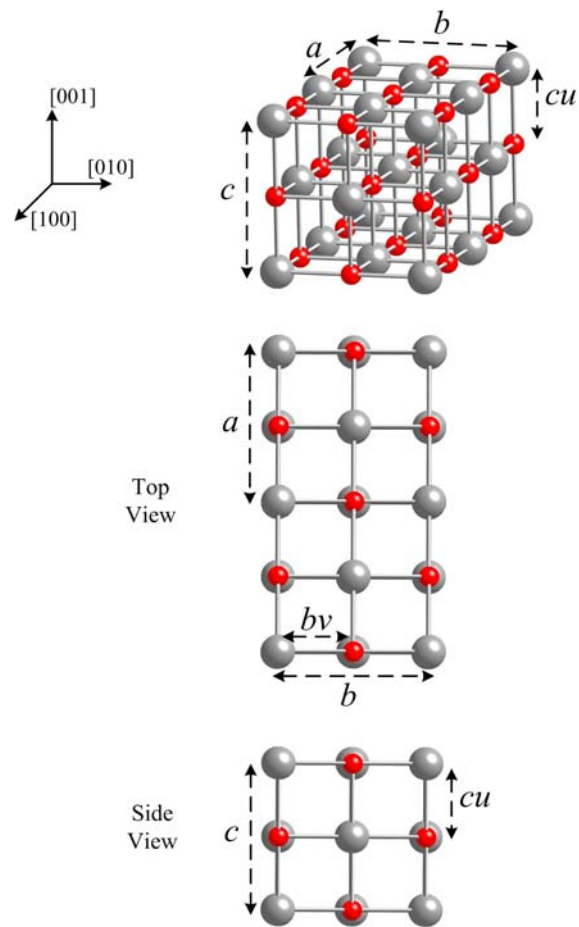


Figure 3.3 Crystal model of the RS structures: small spheres represent anions and large spheres represent cations. The top figure shows the perspective view. The middle and bottom figures show top view and side view, respectively. The distances described by crystal parameters a , b , c , u , and v are indicated.

Table 3.2 Lattice parameters for WZ, HX and RS SiC under their equilibrium loading conditions. Values in parentheses are taken from literature.

Parameters	WZ	HX	RS
	$p = 0$ GPa	$-\sigma_c^{\text{eq}} = 60.5$ GPa	$p^{\text{eq}} = 64.9$ GPa
a (Å)	3.05 (3.06, ^a 3.08 ^b)	3.32	4.00 (3.68, ^{a,b} 3.84 ^c)
b (Å)	5.28	5.74	4.00
c (Å)	4.97	3.98	4.00
$V = \frac{abc}{2}$ (Å ³)	40.0	37.9	32.0
c/a	1.63	1.20	1.00
b/a	1.73	1.73	1.00
u	0.38	0.50	0.50
v	0.35	0.33	0.50

^aDFT (LDA) calculations by Karch *et al.* (Karch *et al.*, 1996).

^bSynchrotron ADX by Yoshida *et al.* (Yoshida *et al.*, 1993).

^cDFT (LDA) calculations by Hatch *et al.* (Hatch *et al.*, 2005).

Table 3.3 Lattice parameters for WZ, HX and RS GaN under their equilibrium loading conditions. Values in parentheses are taken from literature.

Parameters	WZ	HX	RS
	$p = 0$ GPa	$-\sigma_c^{\text{eq}} = 30.5$ GPa	$p^{\text{eq}} = 44.1$ GPa
a (Å)	3.15 (3.19, ^a 3.16, ^{b,c} 3.10 ^d)	3.43	4.16 (4.01, ^a 4.10, ^b 4.07 ^e)
b (Å)	5.46	5.94	4.16
c (Å)	5.11	4.12	4.16
$V = \frac{abc}{2}$ (Å ³)	44.0	42.0	36.0
c/a	1.62	1.20	1.00
b/a	1.73	1.73	1.00
u	0.38	0.50	0.50
v	0.35	0.33	0.50

^aSynchrotron EDXD experiment by Xia *et al.* (Xia *et al.*, 1993).

^bXRD experiments by Xie *et al.* (Xie *et al.*, 1996).

^cDFT (LDA) calculations by Kim *et al.* (Kim *et al.*, 1996).

^dDFT (LDA) calculations by Yeh *et al.* (Yeh *et al.*, 1992).

^eXRD experiments by Lada *et al.* (Lada *et al.*, 2003).

Table 3.4 Lattice parameters for WZ, HX, DHX, and RS InN under their equilibrium loading conditions. Values in parentheses are taken from literature.

Parameters	WZ	HX	DHX	RS
	$p = 0$ GPa	$-\sigma_c^{\text{eq}} = 9.6$ GPa	$\sigma_b^{\text{eq}} = 14.7$ GPa	$p^{\text{eq}} = 12.2$ GPa
a (Å)	3.54 (3.53, ^a 3.54, ^{b,c} 3.52 ^d)	3.82	3.48	4.64 (4.67, ^e 4.62 ^d)
b (Å)	6.13	6.62	7.66	4.64
c (Å)	5.70	4.59	4.35	4.64
$V = \frac{abc}{2}$ (Å ³)	61.9	58.1	58.0	50.0
c/a	1.61	1.20	1.25	1.00
b/a	1.73	1.73	2.20	1.00
u	0.38	0.50	0.51	0.50
v	0.35	0.33	0.31	0.50

^aDFT (LDA) calculations by Kim *et al.* (Kim *et al.*, 1996).

^bDFT (LDA) calculations by Yeh *et al.* (Yeh *et al.*, 1992).

^cXRD calculations by Osamura *et al.* (Osamura *et al.*, 1975).

^dDFT (LDA) calculations by Furthmüller *et al.* (Furthmüller *et al.*, 2005).

^eADX experiments by Ueno *et al.* (Ueno *et al.*, 1994).

Table 3.5 Lattice parameters for WZ, HX, DHX, and RS ZnO under their equilibrium loading conditions. Values in parentheses are taken from literature.

Parameters	WZ	HX	DHX	RS
	$p = 0$ GPa	$-\sigma_c^{\text{eq}} = 6.0$ GPa	$\sigma_b^{\text{eq}} = 10.8$ GPa	$p^{\text{eq}} = 8.2$ GPa
a (Å)	3.21 (3.20, ^a 3.25, ^{b,c} 3.26 ^d)	3.49	3.24	4.24 (4.28, ^b 4.27 ^{c,e})
b (Å)	5.54	6.03	6.46	4.24
c (Å)	5.15 (5.17, ^a 5.22 ^d)	4.19	4.20	4.24
$V = \frac{abc}{2}$ (Å ³)	45.7 (46.69, ^e 47.24, ^f 47.98 ^d)	44.1	44.0	38.1 (39.03, ^e 38.16 ^f)
c/a	1.61 (1.59 ^f)	1.20	1.30	1.00
b/a	1.73	1.73	2.00	1.00
u	0.38 (0.38 ^{a,d,f})	0.50	0.50	0.50
v	0.33	0.33	0.31	0.50

^aDFT (LDA) calculations by Malashevich and Vanderbilt. (Malashevich and Vanderbilt, 2007).

^bSynchrotron EDX experiments by Desgrenier (Desgreniers, 1998).

^cXRD experiments by Karzel *et al.* (Karzel *et al.*, 1996).

^dEXAFS experiments by Decremps *et al.* (Decremps *et al.*, 2003).

^eDFT (GGA) calculations by Jaffe *et al.* (Jaffe *et al.*, 2000).

^fDFT (GGA) calculations by Ahuja *et al.* (Ahuja *et al.*, 1998).

Table 3.6 Lattice parameters for WZ, HX, DHX, and RS CdSe under their equilibrium loading conditions. Values in parentheses are taken from literature.

Parameters	WZ	HX	DHX	RS
	$p = 0$ GPa	$-\sigma_c^{\text{eq}} = 3.75$ GPa	$\sigma_b^{\text{eq}} = 5.8$ GPa	$p^{\text{eq}} = 2.2$ GPa
a (Å)	4.27 (4.30 ^a)	4.66	4.18	5.54 (5.58, ^a 5.71 ^b)
b (Å)	7.39	8.06	8.78	5.54
c (Å)	6.96	5.59	5.44	5.54
$V = \frac{abc}{2}$ (Å ³)	109.8	105.0	99.9	85.0
c/a	1.63	1.20	1.30	1.00
b/a	1.73	1.73	2.10	1.00
u	0.38	0.50	0.50	0.50
v	0.35	0.33	0.31	0.50

^aDFT calculations by Benkhetto *et al.* (Benkhetto *et al.*, 2004).

^bXRD experiments by Wickham *et al.* (Wickham *et al.*, 2000).

3.2 Stability of the crystal structures

Under ambient pressure, the natural form of all five materials studied is WZ structure which belongs to the $P6_3mc$ space group as shown in Figure 3.1. Under sufficiently large hydrostatic compressive RS is observed. HX can be stabilized under uniaxial compression loading along $[0001]$ direction and under uniaxial tensile loading along $[01\bar{1}0]$ direction particularly for InN, ZnO, and CdSe (Sarasamak *et al.*, 2008). Under uniaxial tensile loading along $[01\bar{1}0]$, the stabilized structure does not have hexagonal symmetry (the structure is elongated along b -direction). The structure will be referred to as distorted HX (DHX). Figure 3.4 shows the total energy as a function of volume at zero external loading for WZ, RS, HX and DHX structure for all five compounds. Since the HX and DHX structures are stable only under specific uniaxial loadings, the curves for them are produced based on two types of uniaxial stresses. (1) By keeping a uniaxial stress along $[0001]$ direction (fix $c/a = 1.2$ and $b/a = 1.73$ for all five compounds), green curves (corresponding to HX structures) are obtained. (2) By keeping a uniaxial tension along $[01\bar{1}0]$ direction (fix $c/a = 1.25$ and $b/a = 2.2$ for InN, fix $c/a = 1.3$ and $b/a = 2.0$ for ZnO, and fix $c/a = 1.3$ and $b/a = 2.1$ for CdSe), blue curves (corresponding to DHX structures) are obtained.

For each structure, the energies associated with at least four different unit cell volumes are calculated. The continuous energy-volume curves are obtained by a third-degree polynomial fit. As shown in Figure 3.4, WZ is the most stable structure with the lowest energy, HX has second highest energy, and RS has the highest energy (except for CdSe, where RS has a lower energy than HX). Figure 3.4 also shows that, HX, DHX, and RS are not stable under ambient conditions.

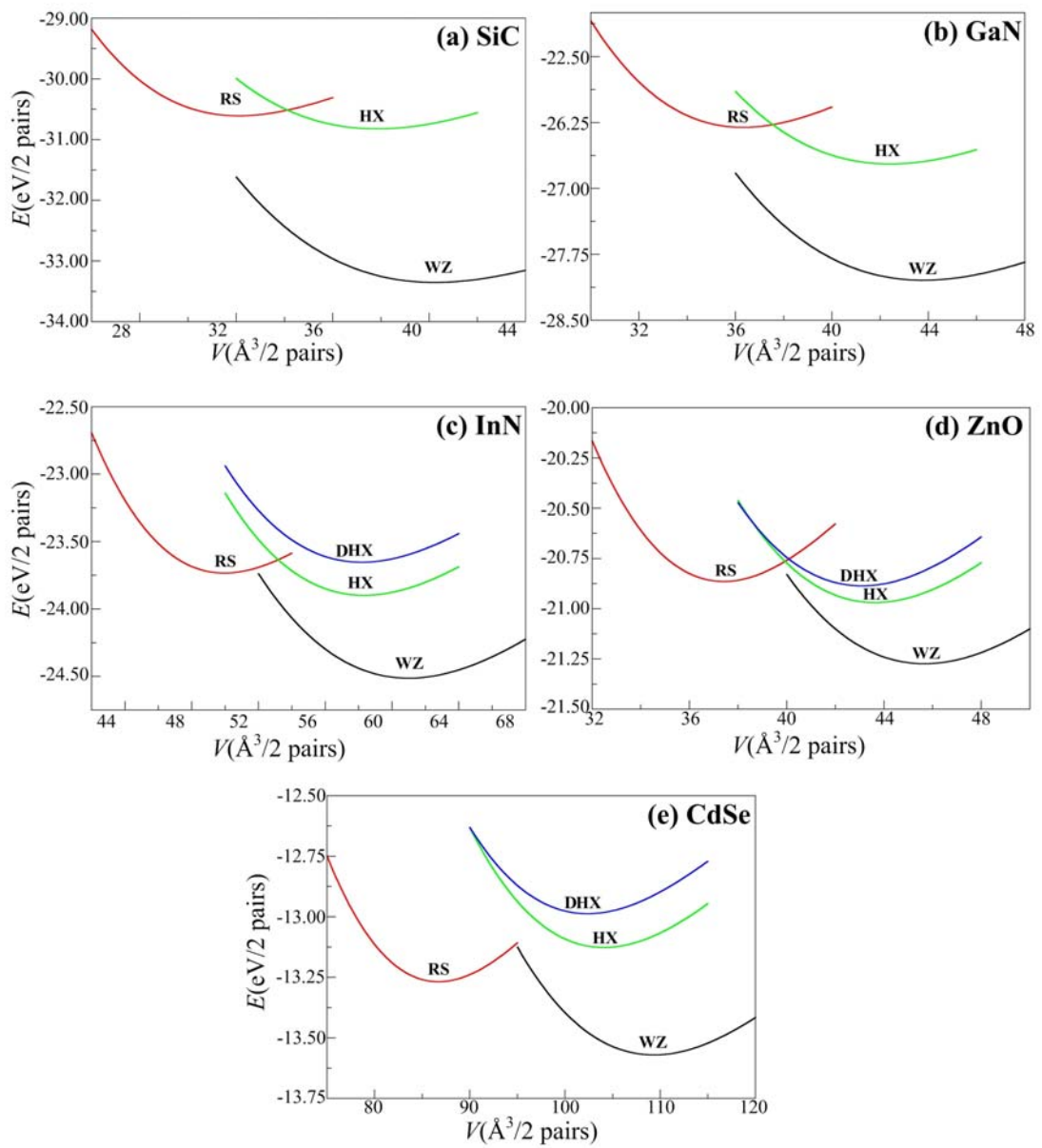


Figure 3.4 Total energy as a function of the volume for WZ, RS, HX and DHX structures (black, red, green, and blue curves represent WZ, RS, HX and DHX structure, respectively) for (a) SiC, (b) GaN, (c) InN, (d) ZnO, and (e) CdSe with LDA calculations.

3.3 Thermodynamic stability

Let us start with the fundamental quantities of materials: energy (E , in the unit of eV), pressure (P , in the unit of GPa), and bulk modulus (B , in the unit of GPa). The relationship between them can be written as (Martin, 2004),

$$\begin{aligned} E &= E(V), \\ P &= -\frac{dE}{dV}, \\ B &= -V \frac{dP}{dV} = V \frac{d^2E}{dV^2}. \end{aligned} \quad (3.1)$$

Because some quantities are macroscopic, they are determined for a fixed number of atoms, for e. g., in crystal, E is the energy per unit cell of volume $V = V_{\text{cell}}$ (V is in the unit of \AA^3).

The following steps are performed to determine the equilibrium volume V_0 , (for $P = 0$ and $T = 0$), and bulk modulus B of particular material with known crystal structure. First the energy (E) for several values of the volume (V) are calculated, and fit to an analytic form such as Murnaghan's equation of state (Murnaghan, 1944). For a sufficiently small range of volume, the E - V curve can be fitted by a simple 3rd degree polynomial. The minimum point gives the predicted volume V_0 and its total energy. The second derivative at that point is the bulk modulus (B).

When $P \neq 0$ and/or $T \neq 0$, the stable phase is the one with the lowest Gibbs free energy G . The Gibbs free energy is defined as (Martin, 2004)

$$G = E + PV - TS = H - TS, \quad (3.2)$$

where E is the internal energy (in the unit of eV), P is pressure (in the unit of GPa), V is volume (in the unit of \AA^3), T is temperature (in the unit of K), S is the entropy (in the unit of eV/ K), and H is the enthalpy (in the unit of eV).

The large pressure that can be obtained in high pressure experiments may cause volume reductions. Here, we focus on the $T = 0$ cases. The Gibbs free energy is the simply enthalpy H and given by

$$H = E + PV \quad (3.3)$$

At a given pressure, the thermodynamically stable phase is the one with the lowest enthalpy.

Although, the zero-temperature theory often results in a good agreement with experiment, the effects of finite temperature in some cases can be significant. For example, when the temperature is increased it becomes easier to overcome the energetic barriers of the transformation, so that the hysteresis is reduced (Mujica *et al.*, 2003).

3.4 Mechanical properties

3.4.1 Phase transition under pressure

Solid-solid phase transition driven by high pressure can be divided into (1) *reconstructive transitions*, which involve significant changes at the transition including the bond breakings and bond formations, and (2) *displacive transitions*, in which the positions of atoms changes by fairly small amounts at the transition (often accompanied by some strains) (Mujica *et al.*, 2003). Alternatively, phase transitions can be classified according to their thermodynamic “order”, which is the order of the derivative of Gibbs free energy ($G = E + PV - TS$). However, in this work, only pressure induced phase transitions is the main interest. In this case, Gibbs free energy is reduced to only the enthalpy term ($H = E + PV$). At $T = 0$, the stable structure (at constant pressure P) is the structure that gives the minimum enthalpy. The transition

pressure can be determined by calculating $E(V)$ and constructing the common tangent line between the $E(V)$ curves for two phases. The slope of the line is the transition pressure.

Figure 3.5 shows the energy versus volume for their crystal structures of ZnO that we obtained from *ab initio* DFT calculations (Sarasamak *et al.*, 2008). The local density approximation is used for the exchange correlation. The computation code (VASP) (Kresse and Hafner, 1994; Kresse and Furthmüller, 1996a; 1996b) is based on plane wave (ultrasoft) pseudopotential method. The stable structure at $P = 0$ is wurtzite structure, and ZnO is predicted to transform to the rocksalt structure at the pressure indicated by the slope of the tangent line, ≈ 8.22 GPa which is in a good agreement with other theoretical and experimental works (for e.g. , Ahuja *et al.*, 1998; Jaffe *et al.*, 2000). A five-fold coordinated *unbuckled wurtzite* phase which is found to be stable under uniaxial compression along the $[0001]$ crystalline direction (green curve which corresponding to HX structures) or uniaxial tension along the $[01\bar{1}0]$ crystalline direction (blue curve which corresponding to DHX structures) are also shown in this figure (more details for WZ to HX or DHX structure are given in Chapter IV).

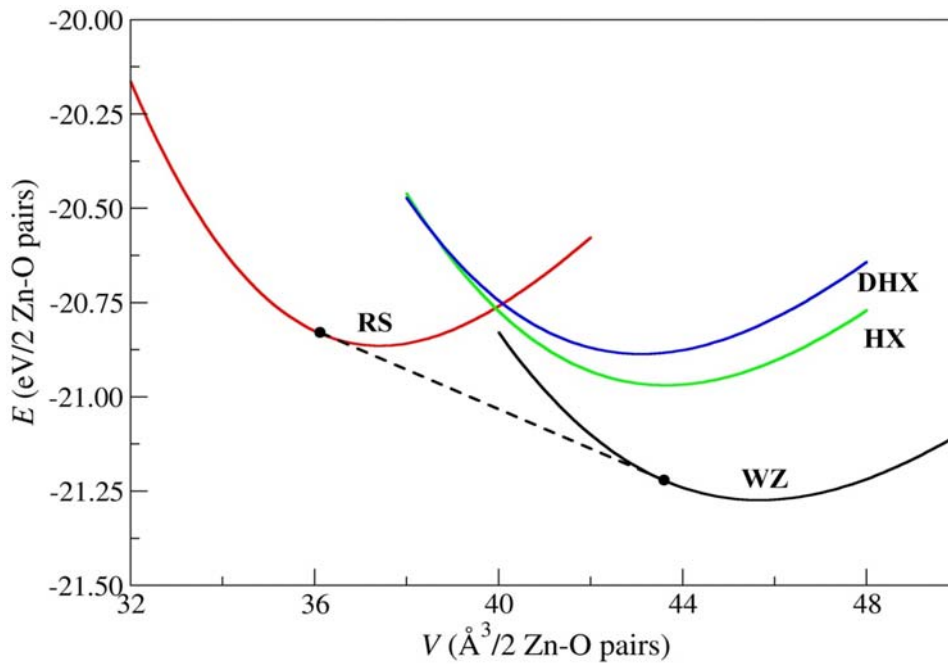


Figure 3.5 Energy versus volume for four ZnO structures. The transition pressure is given by the slope of the common tangent lines between the two phases. For example, the dashed line shows the common tangent line between the WZ- and RS- structures. The slope of the line gives the equilibrium transition pressure of 8.22 GPa (Sarasamak *et al.*, 2008).

3.4.2 Elasticity

Solids are generally deformed when subject to an applied mechanical stress. For small deformations, most solids behave in an elastic manner following Hooke's law which states that the stress, σ_{ij} ($i, j = x, y, z$), and strain, e_{ij} ($i, j = x, y, z$), are directly proportional to each other. The linearity in elastic response with an applied stress is applicable only in a limited range of deformation. For large deformations, the elastic response becomes non-linear. The non-linear response is a direct consequence of the anharmonicity of interatomic potentials that dominates at large displacements. The stress-strain relations are studied by applying external forces to the solid. The size or

shape of a solid can be changed under an applying external force since the stress defines the force acting on a unit area in the solid. The stress in the solids is expressed by a (3×3) matrix where the nine elements are the stress on various directions, σ_{ij} ($i, j = x, y, z$),

$$\sigma = \begin{pmatrix} \sigma_{xx} & \sigma_{xy} & \sigma_{xz} \\ \sigma_{yx} & \sigma_{yy} & \sigma_{yz} \\ \sigma_{zx} & \sigma_{zy} & \sigma_{zz} \end{pmatrix}. \quad (3.4)$$

Note that the subscript, i and j , in the stress component is used to indicate the direction of the force and the plane which the force is applied. For example, σ_{xx} means a force applied in the x direction to a unit area which its normal vector lies in the x direction (this type of stress is known as normal stress); σ_{xy} means a force applied in the x direction to a unit area which its normal vector lies in the y direction (this type of stress is known as shear stress). The nine components of stress are reduced to just six independent components because the constraint of zero totals torque (Kittel, 1996; Elliott, 1998) which gives,

$$\sigma_{xy} = \sigma_{yx}; \sigma_{yz} = \sigma_{zy}; \sigma_{zx} = \sigma_{xz}. \quad (3.5)$$

The general form of stress matrix in Eq. 3.4 can be transformed to the stress matrix which has only diagonal components (in a new set of coordinate x', y', z')

$$\sigma' = \begin{pmatrix} \sigma_{x'} & 0 & 0 \\ 0 & \sigma_{y'} & 0 \\ 0 & 0 & \sigma_{z'} \end{pmatrix}, \quad (3.6)$$

where $\sigma_{x'}$, $\sigma_{y'}$, and $\sigma_{z'}$, are the principal stresses. Furthermore the mean stress can be extracted from the principal stresses such that Eq. 3.6 can be written as (Elliott, 1998)

$$\begin{pmatrix} \sigma_x & 0 & 0 \\ 0 & \sigma_y & 0 \\ 0 & 0 & \sigma_z \end{pmatrix} = \begin{pmatrix} \sigma_0 & 0 & 0 \\ 0 & \sigma_0 & 0 \\ 0 & 0 & \sigma_0 \end{pmatrix} + \begin{pmatrix} (\sigma_x - \sigma_0) & 0 & 0 \\ 0 & (\sigma_y - \sigma_0) & 0 \\ 0 & 0 & (\sigma_z - \sigma_0) \end{pmatrix}, \quad (3.7)$$

where the mean stress, σ_0 , is given by

$$\sigma_0 = (\sigma_x + \sigma_y + \sigma_z)/3. \quad (3.8)$$

Eq. 3.7 shows that the stress tensor is the sum of a pure hydrostatic term which tends to change the volume and a pure shear or deviatoric stress term which tends to distort the shape (Elliott, 1998). The stress in the first term causes the solid to change volume but not the shape because the applying stresses (force per unit area) in all principal directions are equal in magnitude. Another term causes the solid to change the shape while the volume remains constant. The change in shape is the result from an unequal applying force among principal directions. The constant volume is the result from zero trace of shear stress tensor where as the sum of stress components is

$$(\sigma_x - \sigma_0) + (\sigma_y - \sigma_0) + (\sigma_z - \sigma_0) = 0. \quad (3.9)$$

In other words, the mean stress components are zero. Figure 3.6 shows the representation of the deformed solid shape under both types of stress.

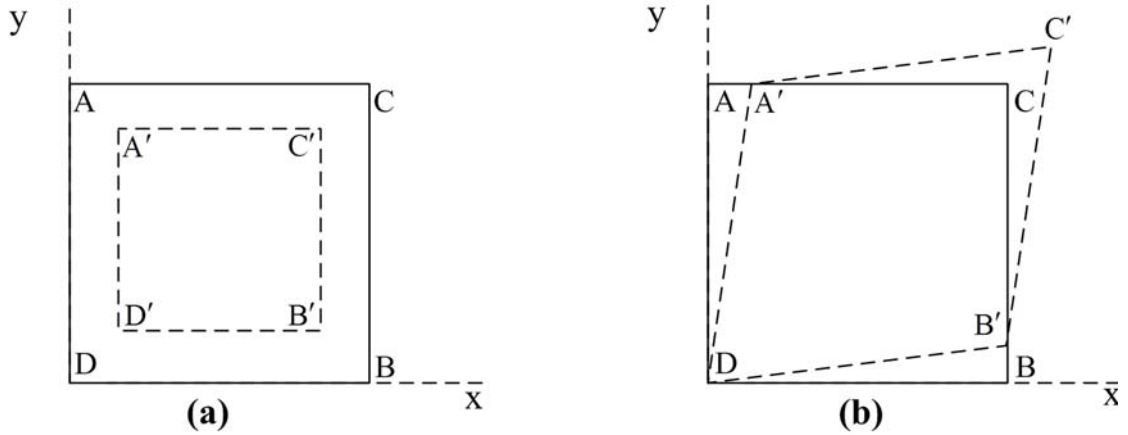


Figure 3.6 Representation of (a) uniform compression resulting from a purely hydrostatic compressive stress and (b) pure shear deformation (The figure is reproduced from Ref. (Elliott, 1998)).

By considering Hooke's law for the solids, within a small deformation limit, the stress components, σ_{ij} ($i, j = x, y, z$), can be expressed as linear combinations of the strain components, e_{ij} ($i, j = x, y, z$). The relationship between stress and strain can be written in the matrix form as (Elliott, 1998),

$$\begin{pmatrix} \sigma_{xx} \\ \sigma_{yy} \\ \sigma_{zz} \\ \sigma_{yz} \\ \sigma_{zx} \\ \sigma_{xy} \end{pmatrix} = \begin{pmatrix} C_{11} & C_{12} & C_{13} & C_{14} & C_{15} & C_{16} \\ C_{21} & C_{22} & C_{23} & C_{24} & C_{25} & C_{26} \\ C_{31} & C_{32} & C_{33} & C_{34} & C_{35} & C_{36} \\ C_{41} & C_{42} & C_{43} & C_{44} & C_{45} & C_{46} \\ C_{51} & C_{52} & C_{53} & C_{54} & C_{55} & C_{56} \\ C_{61} & C_{62} & C_{63} & C_{64} & C_{65} & C_{66} \end{pmatrix} \begin{pmatrix} e_{xx} \\ e_{yy} \\ e_{zz} \\ e_{yz} \\ e_{zx} \\ e_{xy} \end{pmatrix}, \quad (3.10)$$

where the proportional constant $C_{\lambda\alpha}$ ($\lambda, \alpha = 1, 2, 3, \dots, 6$) is elastic constants which are in the unit of GPa and the indices 1 to 6 are defined as (Kittel, 1996),

$$1 \equiv xx; 2 \equiv yy; 3 \equiv zz; 4 \equiv yz, zy; 5 \equiv zx, xz; 6 \equiv xy, yx. \quad (3.11)$$

Among 36 elastic constants in Eq. 3.10, there are only few constants that are independent when considering the symmetry of the crystal structure. For example, in the case of cubic crystal structure, there are 3 independent elastic constants, C_{11} , C_{12} , and C_{44} (for more details, see Ref. (Tinder, 2008)). In the hexagonal crystal structure (such as the wurtzite structure studied here), there are six independent elastic components which are C_{11} , C_{12} , C_{13} , C_{33} , C_{44} , and C_{66} , where $C_{66} = \frac{1}{2}(C_{11} - C_{12})$, the independent elastic constants for the wurtzite structure can be written in the matrix form as (Tinder, 2008),

$$\begin{pmatrix} C_{11} & C_{12} & C_{13} & 0 & 0 & 0 \\ C_{21} & C_{11} & C_{13} & 0 & 0 & 0 \\ C_{13} & C_{13} & C_{33} & 0 & 0 & 0 \\ 0 & 0 & 0 & C_{44} & 0 & 0 \\ 0 & 0 & 0 & 0 & C_{44} & 0 \\ 0 & 0 & 0 & 0 & 0 & C_{66} \end{pmatrix}. \quad (3.12)$$

3.4.3 Elastic energy

Under small distortions, the interatomic displacement is small and the interatomic potentials can be considered to be harmonic. The elastic energy is expressed as the quadratic function of the strains. The expression for the elastic energy per unit volume can be written as (Kittel, 1996),

$$U = \frac{1}{2} \sum_{\lambda=1}^6 \sum_{\alpha=1}^6 C_{\lambda\alpha} e_{\lambda} e_{\alpha} \quad (3.13)$$

where the number indices 1, 2, 3, ..., 6 are defined in the same way as Eq. 3.11. The elastic constants, $C_{\lambda\alpha}$ can be obtained from the derivative of U with respect to the associated strain components (Kittel, 1996).

In our work, the energy (E) is calculated for difference configurations of traceless (volume conserving) strain, $(e_{xx}, e_{yy}, e_{zz}, e_{zy}, e_{zx}, e_{xy})$. For each configuration, E is also calculated at a few values of the strains (e) (Wright, 1997; Prikhodko *et al.*, 2002). Then, the energy-strain curve for each strain configuration is obtained by fitting to a third-degree polynomial function. The second derivative of energy with respect to strain gives us the elastic constants.

For example, a traceless strain in a strain configuration $D_1 = (0, 0, e, 0, 0, 0)$ is introduced to calculate the elastic constant component C_{33} for a WZ structure. The elastic energy can be written in a matrix

$$U_1 = \frac{1}{2} \begin{pmatrix} 0 & 0 & e & 0 & 0 & 0 \end{pmatrix} \begin{pmatrix} C_{11} & C_{12} & C_{13} & 0 & 0 & 0 \\ C_{21} & C_{11} & C_{13} & 0 & 0 & 0 \\ C_{13} & C_{13} & C_{33} & 0 & 0 & 0 \\ 0 & 0 & 0 & C_{44} & 0 & 0 \\ 0 & 0 & 0 & 0 & C_{44} & 0 \\ 0 & 0 & 0 & 0 & 0 & C_{66} \end{pmatrix} \begin{pmatrix} 0 \\ 0 \\ e \\ 0 \\ 0 \\ 0 \end{pmatrix}. \quad (3.14)$$

The multiplication product of Eq. 3.14 gives the elastic energy for this strain configuration as $U_1 = \frac{1}{2} C_{33} e^2$. The energy is then calculated for several values of the strains (e). Then the energy-strain curve is fitted to a third-degree polynomial. The second derivative of the energy with respect to the strain gives us C_{33} . The other elastic components can be obtained by similar steps.

CHAPTER IV

STABILITY OF WURTZITE, UNBUCKLED WURTZITE, AND ROCKSALT PHASES OF SiC, GaN, InN, ZnO, AND CdSe UNDER LOADING OF DIFFERENT DIRECTIONS

4.1 Introduction

The recent synthesis of quasi-1D nanostructures such as nanowires, nanobelts and nanorods of GaN, ZnO and CdSe (see, for e.g., (Pan *et al.*, 2001; Bae *et al.*, 2002)) necessitates understanding the response of such compounds to external uniaxial loading. These nanostructures are mostly single-crystalline and nearly defect-free. Therefore, they are endowed with high strengths and the ability to undergo large deformations without failure. In addition, their high surface-to-volume ratios enhance atomic mobility and promote phase transformations under loading. We have computationally identified a novel five-fold coordinated *unbuckled wurtzite* phase (HX) within the $P6_3/mmc$ space group in $[01\bar{1}0]$ -oriented ZnO nanowires under uniaxial tensile loading (Kulkarni *et al.*, 2006; Kulkarni *et al.*, 2007). The stability of this novel phase and the stabilities of WZ and RS phases of ZnO under uniaxial tension along the $[01\bar{1}0]$ direction as well as hydrostatic compression were analyzed through enthalpy calculations. It is found that the HX structure can not be stabilized by applying hydrostatic pressure. Instead, first principles calculations showed that transformation into the HX structure can occur under either tensile loading along the

[01 $\bar{1}$ 0] direction or compressive loading along the [0001] direction of sufficient magnitude. For this WZ→HX transformation, the uniaxial stress deforms the crystal in only one direction. Since the unit cell of HX is significantly shorter than the unit cell of WZ in the c - or [0001] direction (details later), either compression along the c -direction or tension along the perpendicular [01 $\bar{1}$ 0] direction can cause the transformation. For compression along the c -direction, the corresponding contribution to enthalpy by mechanical work is linearly proportional to $-\sigma_c \Delta c$, with σ_c and Δc being the compressive stress and the change in unit cell size in the c -direction, respectively. For tension along the b -direction, the corresponding contribution to enthalpy by mechanical work is linearly proportional to $\sigma_b \Delta b$, with σ_b and Δb being the tensile stress and the change in unit cell size in the b -direction, respectively. For the WZ→RS transformation, the hydrostatic pressure uniformly compresses the WZ crystal in all directions and causes it to collapse into the RS phase which has a lower equilibrium unit cell volume. The mechanical work contribution to enthalpy is $p \Delta V$, with p and ΔV being the external pressure and volume reduction, respectively. The discovery of the novel HX phase has subsequently been confirmed in [0001]-oriented ZnO nanoplates (Zhang and Huang, 2006) and nanowires (Zhang and Huang, 2007).

To gain insight into the existence of the WZ, HX, and RS structures in binary compounds with different ionicities, we analyze here the energetic favorability of these phases for ZnO and CdSe (groups II-VI), GaN and InN (III-V) and SiC (IV-IV) under uniaxial loading along the [01 $\bar{1}$ 0] and [0001] crystalline axes as well as under hydrostatic compression (Sarasamak *et al.*, 2008). The possibility of transformations from WZ into HX or RS and the effort under loading of different directions on the transformations are analyzed.

4.2. Computational method

First principles calculations are carried out to evaluate the total energy of each compound in its natural and deformed states. The calculations are based on the density functional theory (DFT) with local density approximation (LDA) and ultrasoft pseudopotentials (Vanderbilt, 1990), as implemented in the VASP code (Kresse and Furthmüller, 1996). Here we are interested only in the energy differences between phases. Zinc $3d$, gallium $3d$, indium $4d$ and cadmium $4d$ electrons are treated as valence electrons. Cutoff energies for the plane wave expansion are 400 eV for ZnO, 180 eV for CdSe, 350 eV for nitrides and 300 eV for SiC. The k -point sampling set is based on a $7 \times 7 \times 7$ division of the reciprocal unit cell based on Monkhorst-Pack scheme (Monkhorst and Pack, 1976) with the Γ -point included, which gives approximately 100 inequivalent k -points.

The stability of each crystal structure and compound can be determined by analyzing enthalpy as a function of c/a and b/a . The enthalpy per a *wurtzite unit cell* under uniaxial loading is

$$H(c/a, b/a) = E(c, b, a, u, v) - A_{jk} \times \sigma_i q_i, \quad (4.1)$$

where E is the formation energy per (wurtzite) unit cell, σ_i is the stress along the i direction, q_i is the lattice parameter in the i direction, A_{jk} is the cross section area of the unit cell perpendicular to the stress direction, and $A_{jk} \times \sigma_i q_i$ (summation not implied) is external work. For tension along the b axis, $i = b$, $A_{ac} = ac/2$ and $q_b = b$, with σ_b being the tensile stress. For compression along the c axis, $i = c$, $A_{ab} = ab/2$, and $q_c = c$, with $-\sigma_c$ being the compressive stress.

For hydrostatic compression, the enthalpy is

$$H(c/a, b/a) = E(c, b, a, u, v) + pV, \quad (4.2)$$

where p and $V = abc/2$ are the pressure and unit cell volume, respectively. Under ambient pressure, the enthalpy is equal to the internal formation energy. Note that a wurtzite unit cell contains two cation-anion pairs and occupy the volume, $V = abc/2$.

For each c/a and b/a pair, the internal parameters u and v and the unit cell volume V are allowed to relax so that the configuration that yields the minimum H is obtained. For a given load condition, the minima on the enthalpy surface with c/a and b/a as the independent variables identifies the corresponding stable and metastable structures. For the analyses at hand, the parameter ranges used are [1.00, 1.63] for c/a and [1.00, 1.73] for b/a , with the increments of 0.05 for c/a and 0.10 for b/a . This meshing of the structural space results in approximately 170 strained configurations. For tensile loading along the b -direction, additional configurations with b/a up to 2.30 are also investigated, increasing the number of total configurations to 200. Out of these 170 or 200 configurations, those around $(c/a, b/a) \approx (1.63, 1.73)$, $(1.2, 1.73)$ and $(1.00, 1.00)$ are more carefully analyzed since these three parameter sets define the neighborhoods of WZ, HX and RS structures, respectively, for the given load condition.

For each strained configuration (each c/a - b/a pair), the energies associated with at least four different unit cell volumes (V) are calculated. An equation of state (energy-volume relation) is obtained by a 3rd-degree polynomial fit. Under loading, the volume that minimizes H is not the same as the volume that minimizes E . The equation of state allows the minimum enthalpy for each combination of c/a - b/a pair and loading condition to be obtained. As an illustration, the energy and enthalpy are shown in Figure 4.1 as functions of volume for WZ ZnO ($c/a = 1.61$ and $b/a = 1.73$)

under hydrostatic pressure. At ambient pressure ($p \approx 0$), the energy and enthalpy are equal and the minimum enthalpy is equal to $E(V_0)$, with V_0 being the equilibrium volume of WZ in a stress-free state. At $p = p_1$, the minimum enthalpy occurs at $V = V_1$ for which $dE/dV = -p_1$.

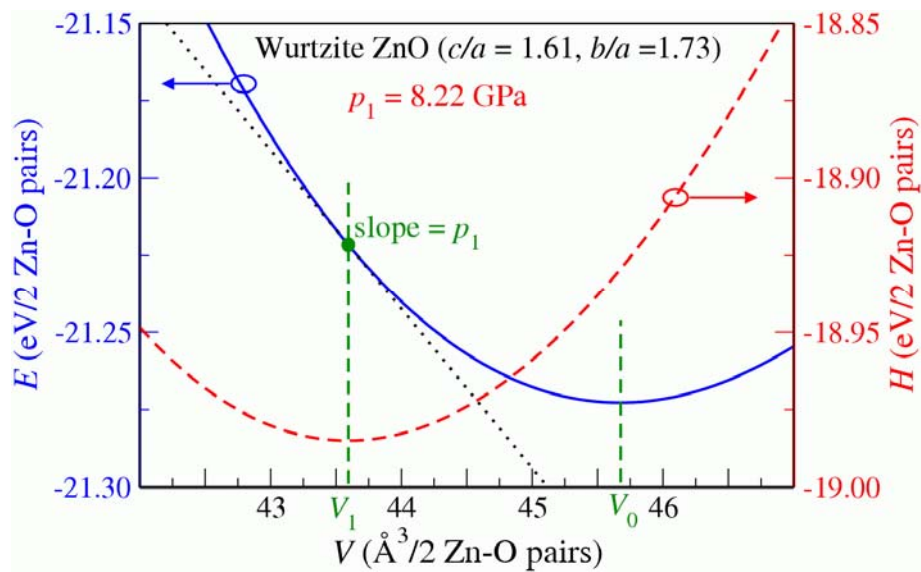


Figure 4.1 Energy (solid curve) and enthalpy (dashed curve) as functions of volume for wurtzite ($c/a = 1.61$ and $b/a = 1.73$) ZnO. At hydrostatic pressure $p_1=8.22$ GPa, the volume that minimizes enthalpy (V_1) is smaller than the volume at ambient pressure (V_0). (The figure is a reproduction of Figure 2 in our published paper (Sarasamak *et al.*, 2008).)

4.3 Results and discussions

4.3.1 Ambient conditions (stress-free state)

Figure 4.2(a) shows the energy (or enthalpy at zero external loading) landscape for ZnO. The global minimum occurs at the wurtzite structure with $(c/a, b/a) = (1.61, 1.73)$. The sections of the surface along $b/a = 1.73$ (solid line) and 1.00 (dash line) are shown in Figure 4.2(b). By virtue of symmetry, b/a is fixed at $\sqrt{3} \approx 1.73$ for WZ and HX and at 1.00 for RS. Clearly, in stress-free state, WZ is the most stable structure with the lowest energy, HX has higher energy and is not stable (no local minimum), and RS structure is metastable with high energy. For SiC, GaN, InN and CdSe, the shapes of the energy landscapes are similar to that of ZnO as shown in Figure 4.3(a), (b), (c), and (d), respectively and their 2-D sections at $b/a = 1.73$ and 1.00 are shown in Figure 4.4(a), (b), (c), and (d), respectively. The energy difference between HX and WZ ($\Delta E^{\text{HX-WZ}}$) and that between RS and WZ ($\Delta E^{\text{RS-WZ}}$) are tabulated in Table 4.1. For some low pressure or low stress conditions, the enthalpy surface might not have HX local minimum. In such cases, the c/a and b/a defining the HX phase is taken from the first metastable HX at higher pressure or stress. The energies of the three phases for all compounds except CdSe follow the order of $E^{\text{RS}} > E^{\text{HX}} > E^{\text{WZ}}$. For CdSe, $E^{\text{RS}} < E^{\text{HX}}$. This exception can be attributed to the fact that for compounds such as CdSe with high ionicity, the energy differences between RS, HX and WZ are relatively small. Therefore, other effects, such as energy cost for bond distortions, can affect the ordering in energies.

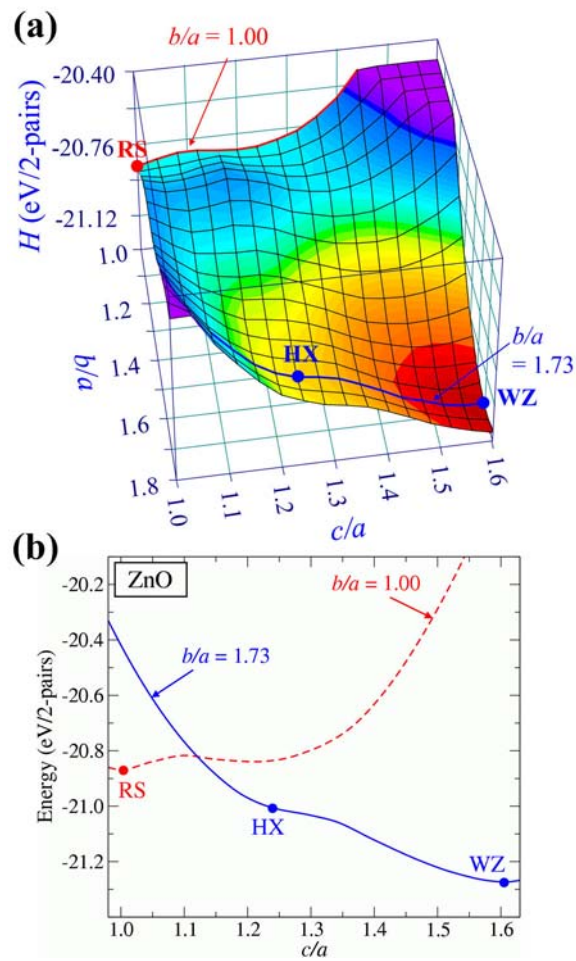


Figure 4.2 (a) Energy (E) landscape for ZnO (in eV per wurtzite unit cell which contains 2 cation-anion pairs). Each point on the surface represents the minimum energy for a given combination of c/a and b/a . To obtain each minimum energy, u , v , and V are allowed to relax while c/a and b/a are kept constant. Energy levels above -20.5 eV are truncated as they are not of interest in the discussions here. (b) 2-D sections of the energy surface for $b/a = 1.73$ (solid line) and 1.00 (dashed line).

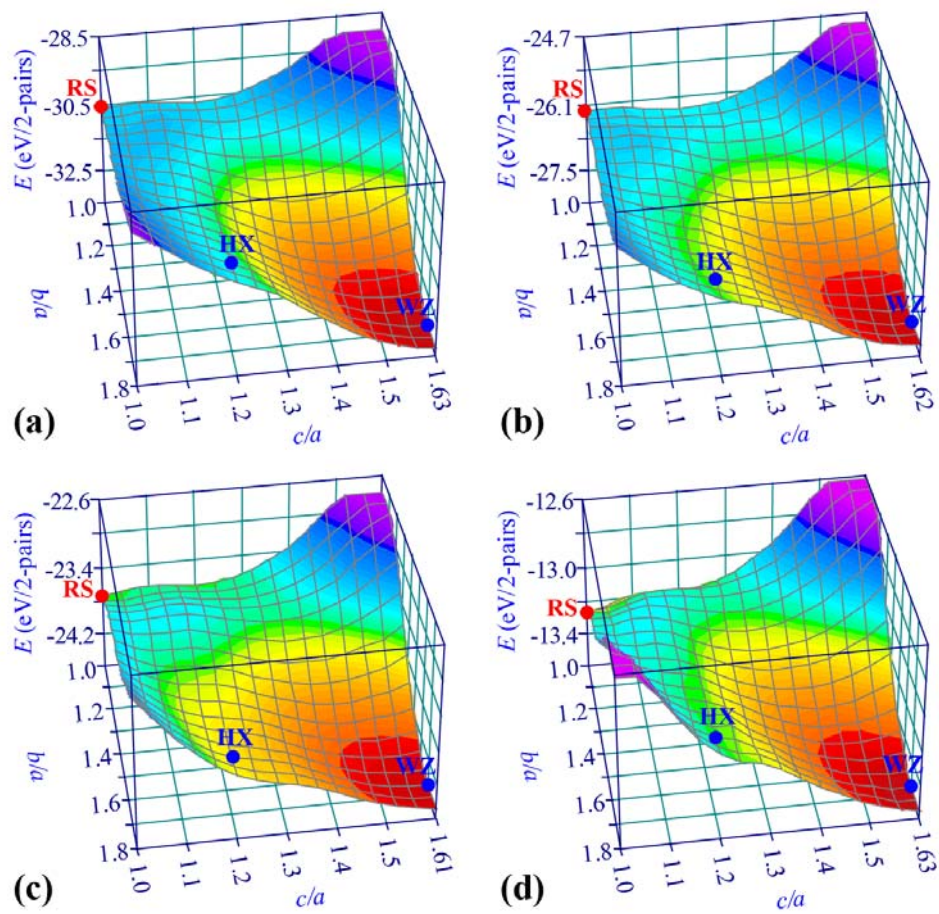


Figure 4.3 Energy surface map (in eV/2 pairs) for a wurtzite unit cell of (a) SiC, (b) GaN, (c) InN, and (d) CdSe. Each point on the surface represents the minimum energy for a given combination of c/a and b/a . To obtain each minimum energy, u , v , and V are allowed to relax while c/a and b/a are kept constant. Energy levels above a certain value for each plot are truncated as they are not of interest in the discussions.

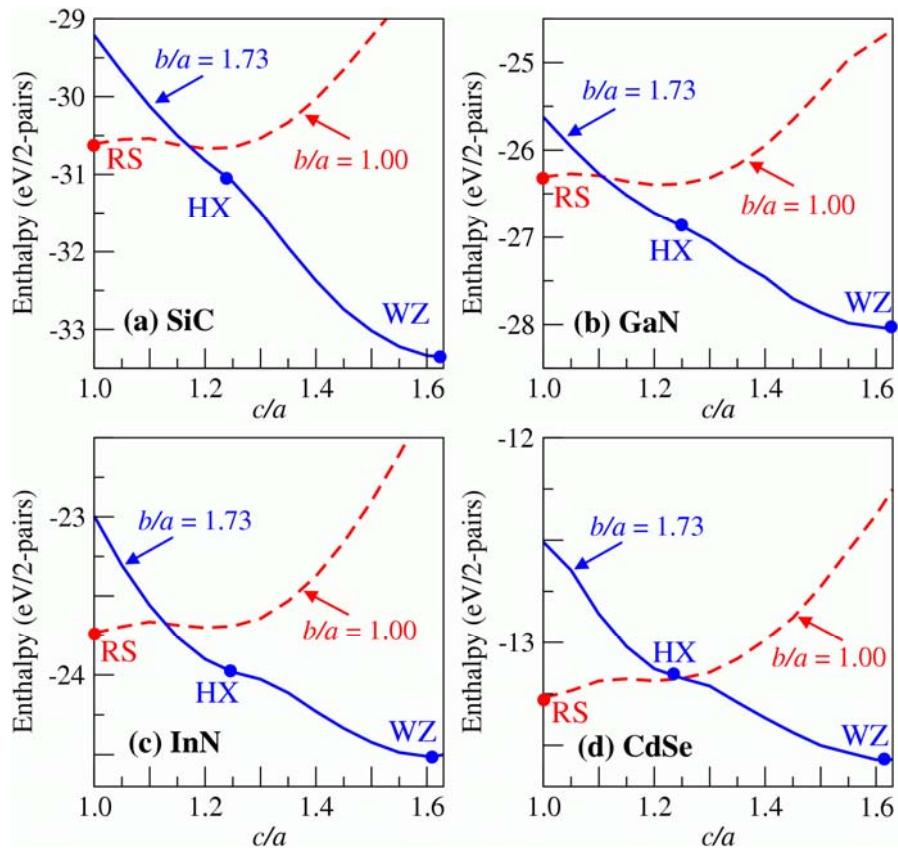


Figure 4.4 2-D sections of (a) SiC, (b) GaN, (c) InN, and (d) CdSe energy surfaces for $b/a = 1.73$ (solid lines) and 1.00 (dashed lines).

Table 4.1 Energy difference (eV per 2 pairs) between HX (or RS) and the WZ structure. The Phillips' ionicity parameters (f_i) are also listed. (Phillips, 1970)

Compounds	Phillips' f_i	$E^{\text{HX}}-E^{\text{WZ}}$ (eV)	$E^{\text{RS}}-E^{\text{WZ}}$ (eV)
SiC	0.177	2.53	2.74
GaN	0.500	1.32	1.74
InN	0.578	0.61	0.78
ZnO	0.616	0.26	0.41
CdSe	0.699	0.44	0.30

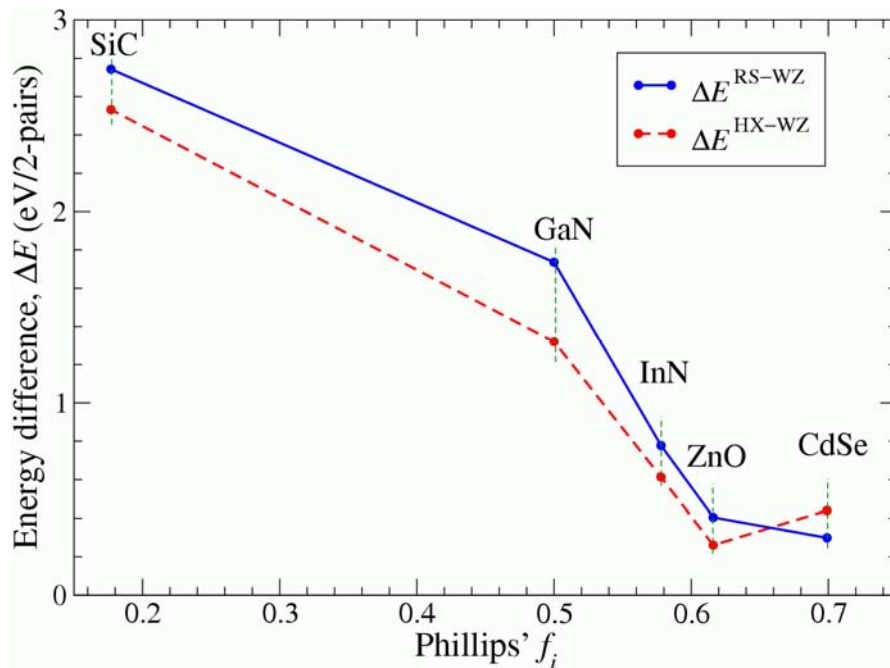


Figure 4.5 Correlation between the formation energy differences (ΔE) and the ionicity as quantified by Phillips' f_i for SiC, GaN, InN, ZnO and CdSe. $\Delta E^{\text{RS-WZ}}$ is shown with the solid line and $\Delta E^{\text{HX-WZ}}$ is shown with the dashed line. For all compounds, WZ has the lowest energy and RS has the highest energy, except for CdSe whose RS phase has a slightly lower energy than HX phase.

There are significant variations of $\Delta E^{\text{HX-WZ}}$ or $\Delta E^{\text{RS-WZ}}$ among the compounds, partly reflecting differences in the ionicity. Several indexes are available to describe the ionicity of materials. Phillips' ionic scale (f_i) (Phillips, 1970) which has the range between 0 (the least ionic) and 1 (the most ionic) is used here by choice. The values of f_i for the compounds studied here are listed in Table 4.1. (Phillips, 1970) The variations of $\Delta E^{\text{HX-WZ}}$ and $\Delta E^{\text{RS-WZ}}$ with f_i are shown in Figure 4.5. For RS, $\Delta E^{\text{RS-WZ}}$ (solid line) decreases monotonically as f_i increases. For HX, $\Delta E^{\text{HX-WZ}}$ (dashed line) decreases monotonically with f_i (except for CdSe). This is expected

because compounds with higher levels of ionicity can significantly lower their energies through increases in C.N. While ionicity is not the only factor that determines the relative stability of crystal structures, it clearly affects the stability of structures. For covalent compounds (e.g., SiC and GaN), the structure with four-fold coordination is highly favored, resulting in the large differences between the formation energies of RS (6-fold) and WZ (4-fold) and between HX (5-fold) and WZ. On the other hand, for a compound with higher level of ionicity, the differences in formation energies among RS, HX and WZ are lower. In this paper, only some ionic compounds that have four-fold coordinated structures (WZ) under ambient conditions are studied.

Table 4.2 Percentage changes in V (volume), lattice parameters b and c as the crystal structure changed from WZ to HX and WZ to RS for all five compounds. The conditions that stabilize each phase are given in parentheses.

Compounds	WZ ($\sigma = 0$) \rightarrow HX ($\sigma = -\sigma_c^{\text{eq}}$)			WZ ($p = 0$) \rightarrow RS ($p = p^{\text{eq}}$)		
	ΔV (%)	Δb (%)	Δc (%)	ΔV (%)	Δb (%)	Δc (%)
SiC	-5.0	8.7	-19.9	-20.0	-24.2	-19.5
GaN	-4.5	9.0	-19.4	-18.2	-23.8	-18.6
InN	-6.1	7.9	-19.5	-19.2	-24.3	-18.6
ZnO	-3.4	8.8	-18.6	-16.5	-23.5	-17.7
CdSe	-4.4	9.1	-19.7	-22.6	-25.0	-20.4

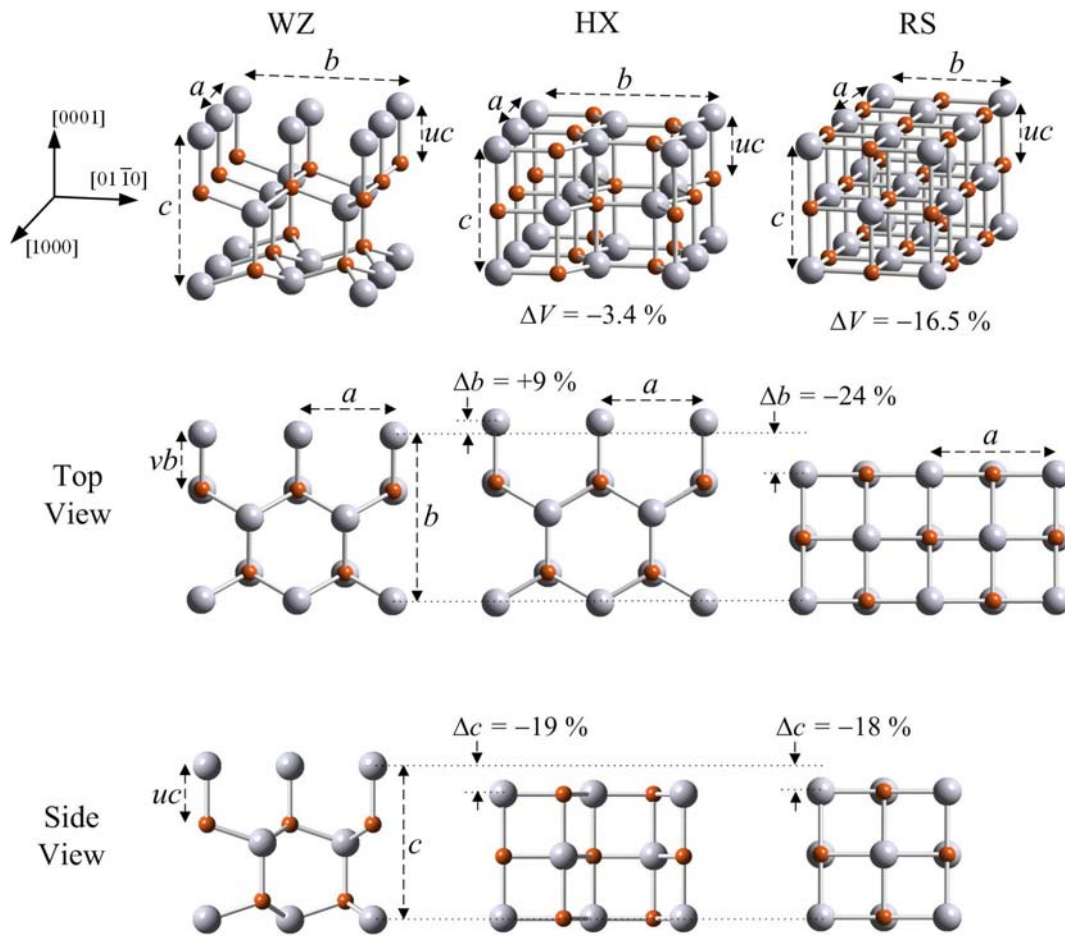


Figure 4.6 Schematic illustrations of the WZ, HX, and RS structures: small spheres represent anions and large spheres represent cations. The middle and bottom rows show top view and side view, respectively. Parameters a , b , c , u , and v are indicated. For realistic rendering, the images shown are drawn to scale using parameters for ZnO at equilibrium conditions, i.e., ambient pressure for WZ, $\sigma = -\sigma_c^{\text{eq}}$ for HX and $p = p^{\text{eq}}$ for RS. ΔV , Δb , and Δc are the percentage changes in V (volume), b and c relative to the same quantities for WZ. (The figure is a reproduction of Figure 1 in our published paper (Sarasamak *et al.*, 2008).)

4.3.2 Hydrostatic compression

Sufficiently high pressures can cause the WZ structure to collapse into the denser RS phase. As shown in Figure 4.6, the volume of the RS structure is $\sim 17\%$ smaller than the volume of the WZ structure ($\Delta V \approx -0.17V_0$, with V_0 being the equilibrium volume of WZ). Although, the figure uses ZnO as an illustrated case, other compounds show similar changes in the volume (see Table 4.2). For a given constant pressure p , the difference in contributions to enthalpy by mechanical work between RS and WZ is approximately $p\Delta V$ (neglecting the difference in bulk moduli of the two phases). If p is sufficiently high, mechanical work can overcome the formation energy difference, driving the transformation forward. Figure 4.7 shows $\Delta H^{\text{RS-WZ}} = H^{\text{RS}} - H^{\text{WZ}}$ and $\Delta H^{\text{HX-WZ}} = H^{\text{HX}} - H^{\text{WZ}}$ as the functions of p for the five compounds studied. The rather linear trends confirm that the bulk moduli of the WZ, HX, and RS phases are quite comparable. The slight deviation from linearity of $\Delta H^{\text{RS-WZ}}$ reflects the fact that the bulk modulus of RS is somewhat higher (approximately 25%) than that of WZ. Note that the slope of the $\Delta H^{\text{RS-WZ}}$ line is ~ 5 times that of the $\Delta H^{\text{HX-WZ}}$ line, consistent with the fact that the volume decrease associated with the WZ \rightarrow RS transformation (17%) is approximately 5 times of that associated with the WZ \rightarrow HX transformation (3.6%).

The equilibrium pressure p^{eq} between the WZ and RS structures (the pressure at which the enthalpies of RS and WZ become equal) can be obtained by examining the enthalpy surfaces at several pressures. This pressure is identified with the intercept of the enthalpy curve with the horizontal axis in Figure 4.7. From the figure, the $\Delta H^{\text{HX-WZ}}$ line does not intercept the horizontal axis for all five compounds over the

pressure range analyzed. Obviously, HX is not a thermodynamically stable structure under hydrostatic compression.

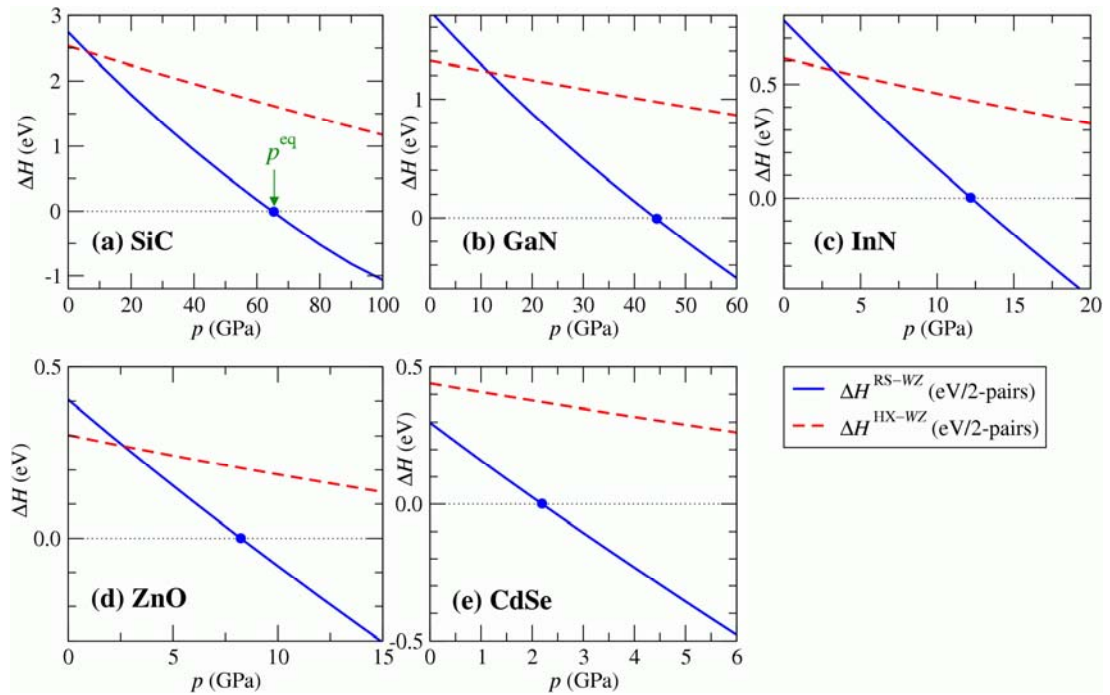


Figure 4.7 Enthalpy differences (ΔH), in the unit of eV/2-pairs, between RS and WZ (solid line) and between HX and WZ (dashed line) as a function of hydrostatic pressure for (a) SiC, (b) GaN, (c) InN, (d) ZnO and (e) CdSe. As the pressure reaches the equilibrium point (p^{eq} , indicated by solid dots), the enthalpies for RS and WZ become equal. Above p^{eq} , RS turn to be more stable. Note that HX is never stable under hydrostatic loading.

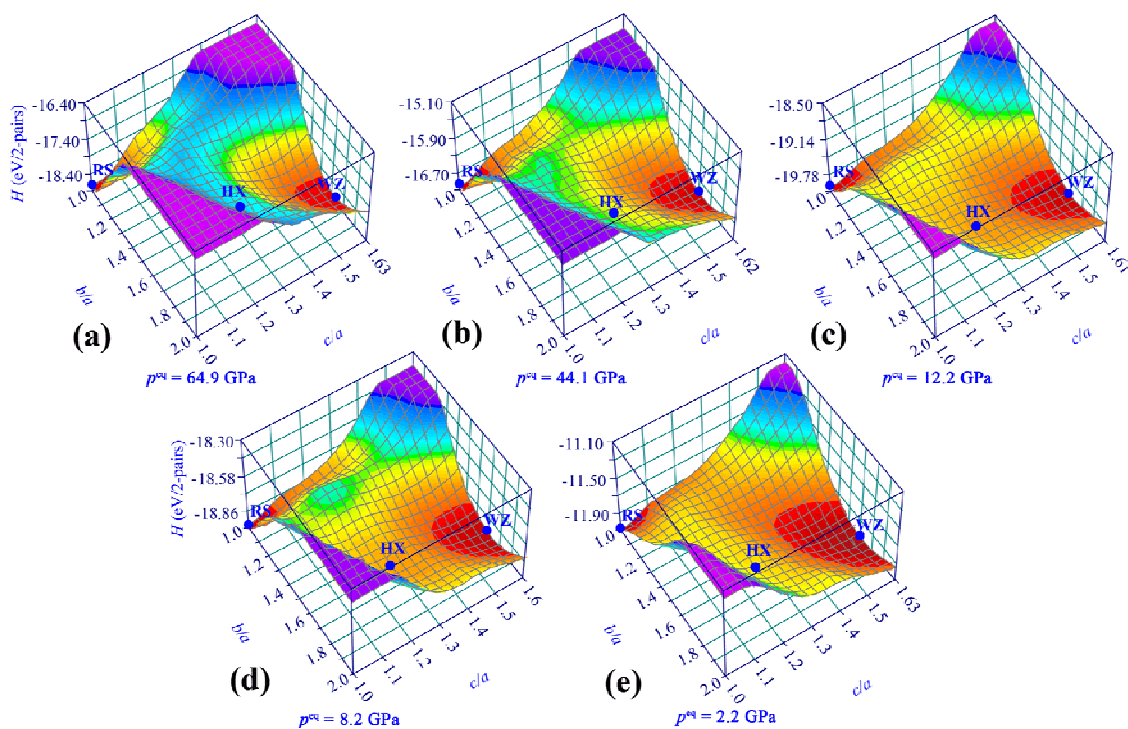


Figure 4.8 Enthalpy surface maps (in eV/2 pairs) for a wurtzite unit cell of (a) SiC, (b) GaN, (c) InN, (d) ZnO and (e) CdSe at their respective RS-WZ equilibrium pressures (p^{eq}).

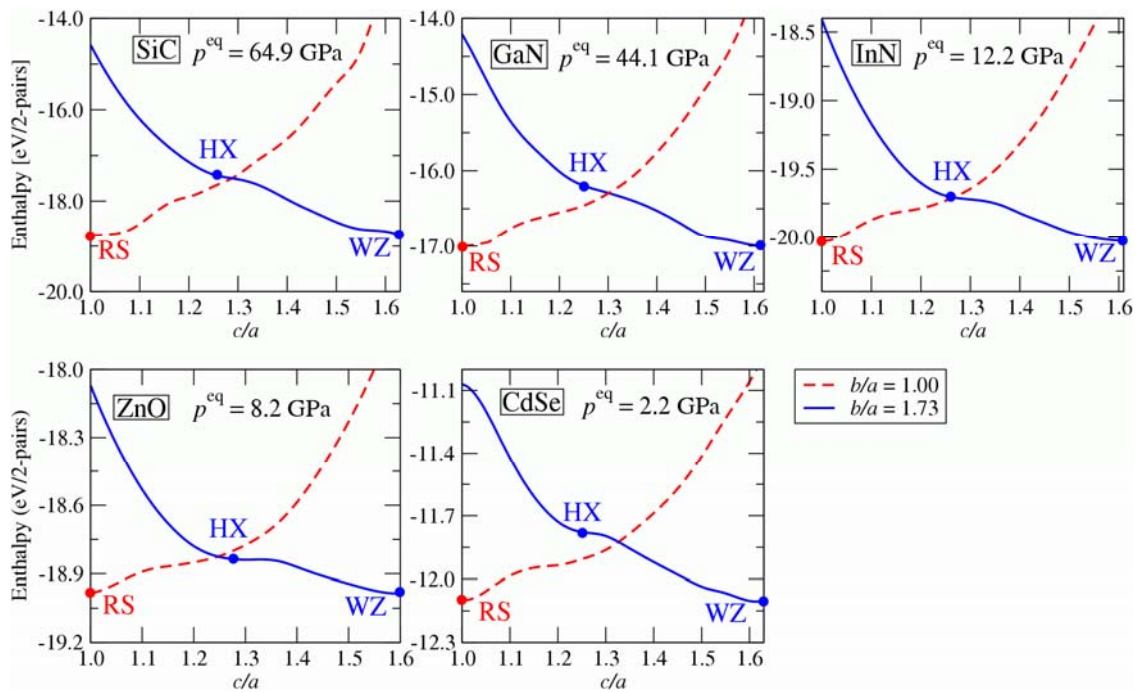


Figure 4.9 2-D sections of the enthalpy surface maps in Figure 4.8 for $b/a = 1.73$ (solid lines) and 1.00 (dashed lines).

The enthalpy surfaces of SiC, GaN, InN, ZnO and CdSe at their equilibrium pressure, p^{eq} , are shown in Figure 4.8 and their corresponding 2-D sections are shown in Figure 4.9. At $p < p^{\text{eq}}$, WZ has the lowest enthalpy. As p is increased above p^{eq} , RS has a lower enthalpy than WZ. p^{eq} depends strongly on the ionicity of the compound. This is expected because the initial energy difference between WZ and RS ($\Delta E^{\text{RS-WZ}} = E^{\text{RS}} - E^{\text{WZ}}$) depends on the ionicity of the compound (from $\Delta E^{\text{RS-WZ}} = 2.74$ eV for SiC to 0.30 eV for CdSe). SiC has the highest $\Delta E^{\text{RS-WZ}}$ and therefore the highest p^{eq} (64.9 GPa). CdSe has the lowest $\Delta E^{\text{RS-WZ}}$ and therefore the lowest p^{eq} (2.2 GPa). The equilibrium pressures of the five compounds are listed in Table 4.3. Our calculated equilibrium pressures are in good agreement with other calculated results in general. To compare with experiments, one should not directly compare the

calculated equilibrium pressure with either the critical pressures of the upward or downward WZ to RS transformations. This is because there is a transformation barrier between the two phases that causes the upward critical pressure to be higher (and the downward critical pressure to be lower) than the equilibrium pressure. (Mujica *et al.*, 2003; Limpijumnong and Jungthawan, 2004) The averages between the upward and downward critical pressures, shown as p_t in Table 4.3, are shown as an approximate experimental equilibrium pressures and are in good agreement with the corresponding calculated equilibrium pressures.

Table 4.3 Equilibrium pressure, transformation barrier, and stresses for SiC, GaN, InN, ZnO and CdSe for the WZ→RS and WZ→HX (WZ→DHX) transformations. p^{eq} is the hydrostatic pressure that establishes the equilibrium between the WZ and RS structures and p_t (exp) is the corresponding experimental value. $-\sigma_c^{\text{eq}}$ (σ_b^{eq}) is the value of the compressive (tensile) force per unit area along the c -direction (b -direction) at which the WZ and HX (DHX) structures are in equilibrium. For CdSe, although $-\sigma_c^{\text{eq}} = 3.8$ GPa provides equilibrium between the WZ and HX phases, the RS phase has lower enthalpy (hence more stable) under this condition. The transformation enthalpy barrier in eV/2-pairs between the WZ and RS phases at a given equilibrium pressure are given in square brackets following p^{eq} in the same column.

Compounds	RS			HX	DHX
	p^{eq} (GPa) (present)	p^{eq} (GPa) (other)	p_t (GPa) (exp)	$-\sigma_c^{\text{eq}}$ (GPa)	σ_b^{eq} (GPa)
SiC	64.9 [1.26]	60, ^a 66.6, ^b 66, ^c 92 ^d	67.5 ^e	60.5	-
GaN	44.1 [0.76]	51.8, ^f 42.9 ^g	52.2, ^h 31 ⁱ	30.5	-
InN	12.2 [0.51]	21.6, ^f 11.1 ^g	10, ^j 12.1 ^h	9.6	14.7
ZnO	8.2 [0.30]	6.6, ^k 9.3, ^l 8.0 ^m	5.5, ⁿ 8.5 ^o	6.0	10.8
CdSe	2.2 [0.40]	2.5 ^p	2.1 ^q	3.8	5.8

^aDFT (GGA) calculations by Miao and Lambrecht (Miao and Lambrecht, 2003).

^bDFT (LDA) calculations (of zincblende to RS) by Karch *et al.* (Karch *et al.*, 1996).

^cDFT (LDA) calculations (of zincblende to RS) by Chang and Cohen (Chang and Cohen, 1987).

^dDFT (B3LYP) calculations (of zincblende to RS) by Catti (Catti, 2001).

^eSynchrotron angle dispersive x-ray diffraction (ADX) experiment by Yoshida *et al.* (Yoshida *et al.*, 1993).

^fDFT(LDA) calculations by Christensen and Gorczyca (Christensen and Gorczyca, 1994).

^gDFT (LDA) calculations by Serrano *et al.* (Serrano *et al.*, 2000).

^hADX experiment by Ueno *et al.* (Ueno *et al.*, 1994).

ⁱSynchrotron energy-dispersive x-ray diffraction (EDX) by Xia *et al.* (Xia *et al.*, 1993).

^jSynchrotron EDX experiment by Xia *et al.* (Xia *et al.*, 1994).

^kDFT (LDA) calculations by Jaffe *et al.* (Jaffe *et al.*, 2000).

^lDFT (GGA) calculations by Jaffe *et al.* (Jaffe *et al.*, 2000).

^mDFT (GGA) calculations by Ahuja *et al.* (Ahuja *et al.*, 1998).

ⁿSynchrotron EDX experiment by Desgreniers. (Desgreniers, 1998).

^oSynchrotron EDX experiment by Recio *et al.* (Recio *et al.*, 1998).

^pDFT (LDA) calculations by Côté *et al.* (Côté *et al.*, 1997).

^qEDX experiment by Cline and Stephens (Cline and Stephens, 1965).

To gain insight on the transformation enthalpy barrier, we extracted the *homogeneous* transformation barrier (in the unit of eV/2-pairs) of these five compounds and tabulated in Table 4.3 inside the square brackets. The barrier for ZnO of 0.30 eV/2-pair is the same as previously reported value. (Limpijumnong and Jungthawan, 2004) The barrier for SiC and GaN of 1.26 and 0.76 eV/2-pairs are in good agreement with the calculated values reported by Miao and Lambrecht (Miao and Lambrecht, 2003) (for SiC) of 1.2 eV/2-pairs and by Limpijumnong and Lambrecht (Limpijumnong and Lambrecht, 2001a) (for GaN) of 0.9 eV/2-pairs. We can see that the magnitude of the barrier increases with the zero pressure energy difference between phases ($\Delta E^{\text{RS-WZ}}$), hence, the ionicity. The detail investigation of the barriers will be a subject of further study on more compounds in the future.

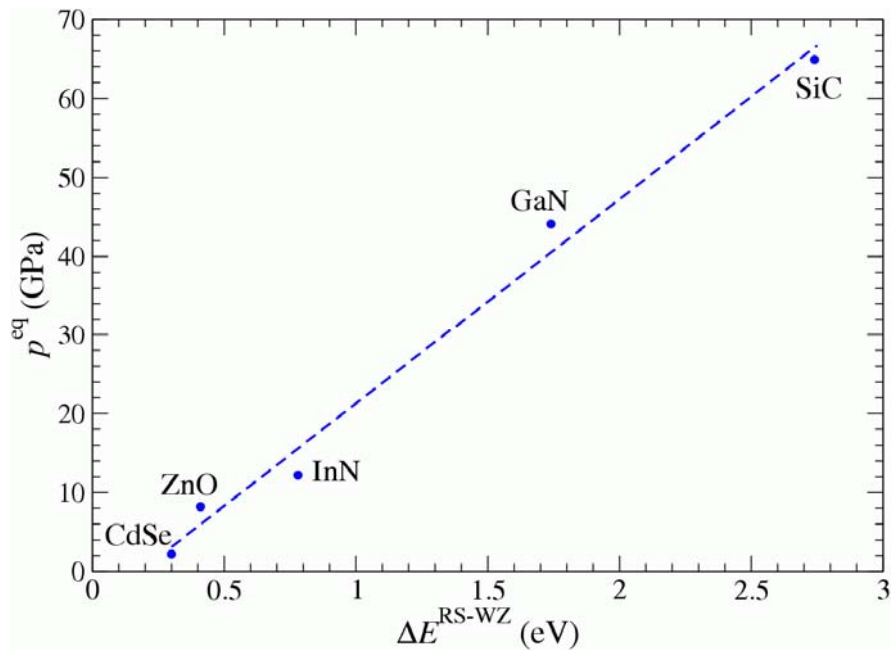


Figure 4.10 Correlation between equilibrium hydrostatic pressure (p^{eq}) and the difference in energy (ΔE) between the RS and WZ phases of the five compounds. p^{eq} is the pressure at which the WZ and RS structures are in equilibrium as illustrated in Figure 4.7 and tabulated in Table 4.3. The energy difference $\Delta E^{\text{RS-WZ}} = E^{\text{RS}} - E^{\text{WZ}}$ is calculated under the conditions of zero external loading and is tabulated in Table 4.1.

Figure 4.10 shows the relationship between equilibrium pressure and the initial energy difference. An approximately linear dependence of p^{eq} on $\Delta E^{\text{RS-WZ}}$ is seen. The linear fit gives

$$p^{\text{eq}} \approx 25.97(\Delta E^{\text{RS-WZ}}) - 4.68 \quad (4.3)$$

with the units of p^{eq} and $\Delta E^{\text{RS-WZ}}$ in GPa and eV/2-pairs, respectively. This approximate universal relationship can be used to estimate the difference in formation energy of the RS and WZ phases when the equilibrium pressure is known, or *vice versa*.

4.3.3 Uniaxial compression along the [0001] direction

HX has a lattice constant c significantly shorter ($\sim 19\%$) than that of WZ in the [0001] direction as illustrated in Figure 4.6. Although, the figure uses ZnO as an illustrated case, other compounds show similar changes in lattice constant c (see Table 4.2). This difference allows WZ to transform into HX *via* compression in the c -direction. Under constant compressive stress $-\sigma_c$ (negative sign indicates compression), the mechanical contribution to the enthalpy difference between WZ and HX is $-A_{ab} \times \sigma_c \Delta c$, where $\Delta c \approx -0.19c$. A sufficiently high $-\sigma_c$ would allow mechanical work to offset the energy difference between HX and WZ, leading to the transformation into the HX structure.

The stability of the HX phase can be analyzed through the enthalpy difference $\Delta H^{\text{HX-WZ}} = H^{\text{HX}} - H^{\text{WZ}}$ as a function of the compressive stress along the c -direction (dashed lines in Figure 4.11). If the elastic moduli of HX and WZ along the c -direction are assumed to be equal, ΔH would vary linearly with $-\sigma_c$ with an approximate slope of $A_{ab} \Delta c \approx -0.19 (abc/2) \approx -0.19V$. Figure 4.11 also shows the enthalpy difference between RS and WZ, $\Delta H^{\text{RS-WZ}} = H^{\text{RS}} - H^{\text{WZ}}$ (solid lines). Note that $\Delta H^{\text{HX-WZ}}$ and $\Delta H^{\text{RS-WZ}}$ show similar trends, with similar slopes. This is because for the WZ \rightarrow RS transformation $\Delta c/c \approx 18\%$, while for the WZ \rightarrow HX transformation $\Delta c/c \approx 19\%$.

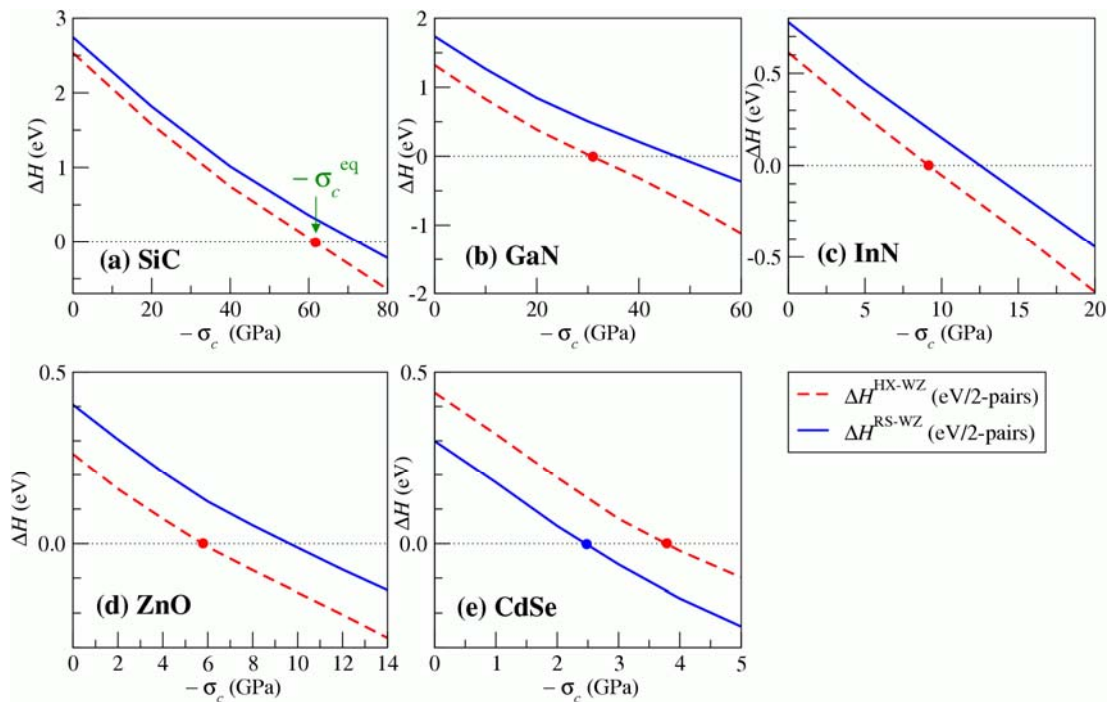


Figure 4.11 Enthalpy differences (ΔH) between the RS and WZ (solid line) and HX and WZ (dashed line) as a function of c -direction stress ($-\sigma_c$) for (a) SiC, (b) GaN, (c) InN, (d) ZnO and (e) CdSe. As the magnitude of the stress reaches the equilibrium value ($-\sigma_c^{\text{eq}}$, indicated by solid dots), enthalpies of the HX and WZ structures become comparable. At stresses above $-\sigma_c^{\text{eq}}$, the HX phase is more stable.

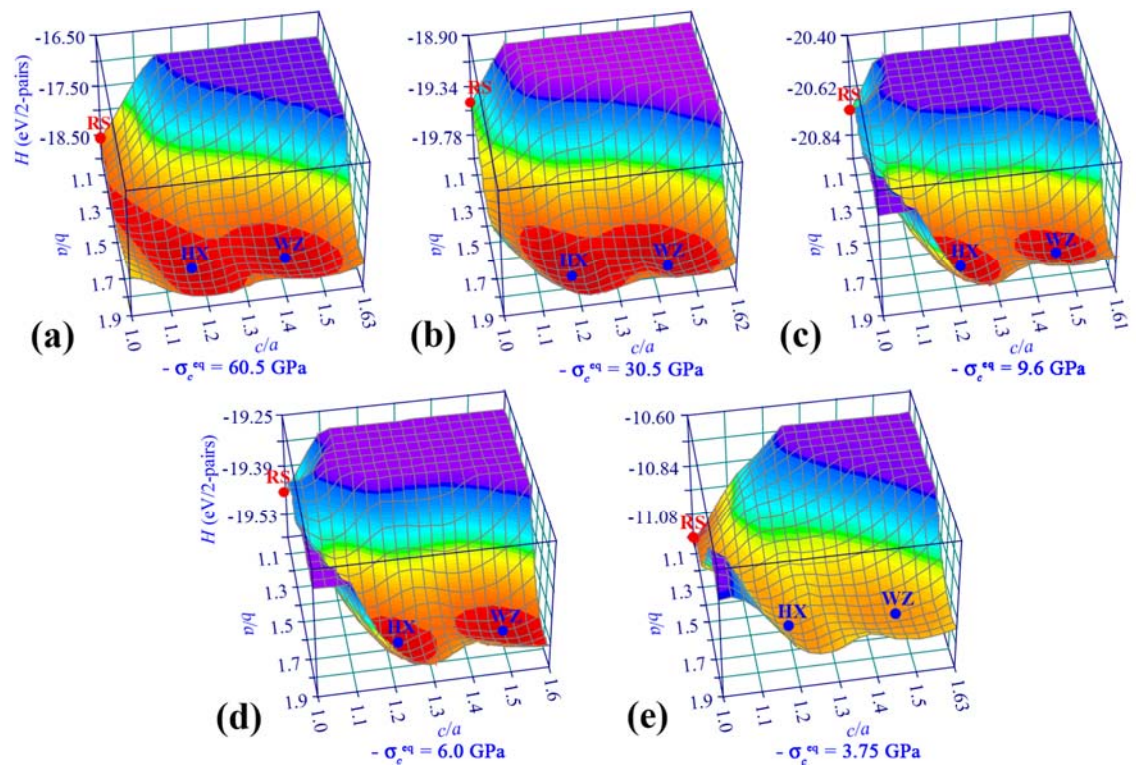


Figure 4.12 Enthalpy surface maps (in eV/2 pairs) for a wurtzite unit cell of (a) SiC, (b) GaN, (c) InN, (d) ZnO and (e) CdSe at their respective HX-WZ equilibrium c -direction stresses ($-\sigma_c^{\text{eq}}$).

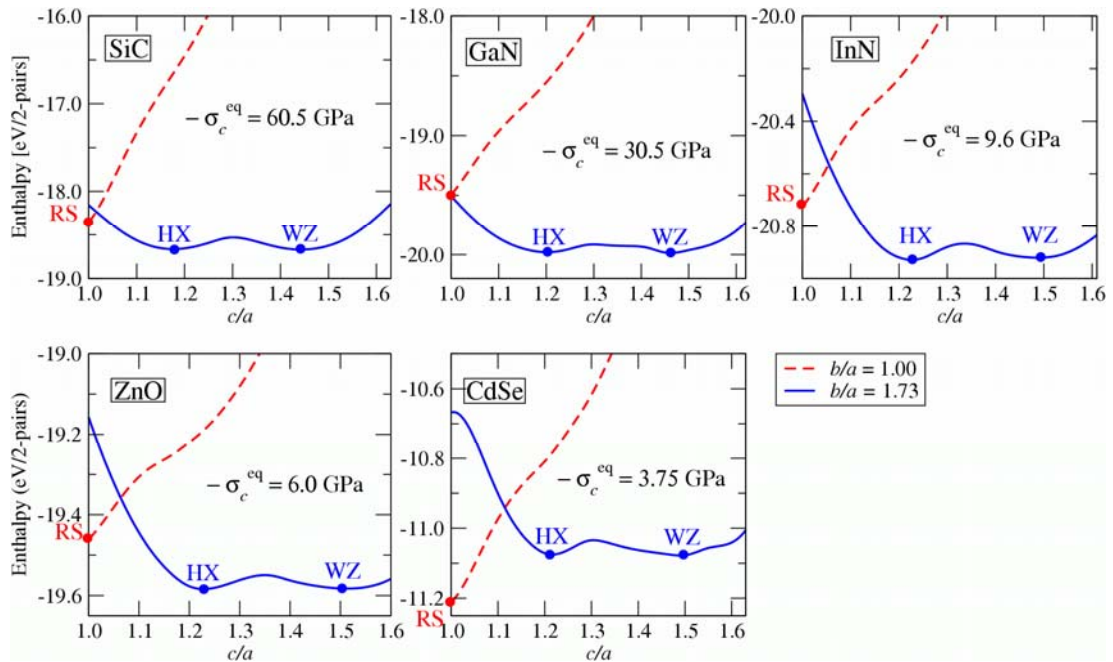


Figure 4.13 2-D sections of the enthalpy surface maps in Figure 4.12 for $b/a = 1.73$ (solid lines) and 1.00 (dashed lines).

The shapes of the enthalpy surfaces for SiC, GaN, InN, ZnO and CdSe at their respective equilibrium compressive stress $-\sigma_c^{\text{eq}}$ are shown in Figure 4.12 and their corresponding 2-D section are shown in Figure 4.13. For all compounds except CdSe, $\Delta H^{\text{HX-WZ}}$ is always lower than $\Delta H^{\text{RS-WZ}}$, indicating that HX is more stable than RS under compression in the c -direction. For CdSe, where initially (i.e., under no load condition) the RS phase has slightly lower energy than HX, $\Delta H^{\text{RS-WZ}}$ is always lower than $\Delta H^{\text{HX-WZ}}$, indicating that RS is the preferred structure over HX under uniaxial compression along the [0001] direction. As a result, the enthalpy surface at $-\sigma_c^{\text{eq}}$ of CdSe (Figure 4.12(e)) is qualitatively different from those of other four compounds, i.e. the RS phase has lower enthalpy. The equilibrium stress for the transformation ($-\sigma_c^{\text{eq}}$) of each compound is shown in Figure 4.12. At stresses

below $-\sigma_c^{\text{eq}}$, WZ phase is stable. At stresses above $-\sigma_c^{\text{eq}}$, HX is stable (RS for CdSe). The values of $-\sigma_c^{\text{eq}}$ depend on the initial energy difference (ΔE) between WZ and HX and are listed in Table 4.1. For SiC, $\Delta E = E^{\text{HX}} - E^{\text{WZ}} = 2.53$ eV, the stress required to cause the HX→WZ transformation is high ($-\sigma_c^{\text{eq}} = 60.5$ GPa). On the other hand, for ZnO, $\Delta E = 0.26$ eV and $-\sigma_c^{\text{eq}} = 6.0$ GPa which is only $1/10^{\text{th}}$ of the stress level required for SiC. This linear trend is clearly seen in Figure 4.14 which shows $-\sigma_c^{\text{eq}}$ as a function of ΔE for the compounds analyzed. The linear fit gives

$$-\sigma_c^{\text{eq}} \approx 25.72(\Delta E^{\text{HX-WZ}}) - 4.56. \quad (4.4)$$

The coefficients in the equation are based on the units of $-\sigma_c^{\text{eq}}$ and $\Delta E^{\text{HX-WZ}}$ in GPa and eV/2-pairs, respectively. The similarity in the numerical values of coefficients of Eq. 4.4 and Eq. 4.3 is fortuitous. Note that the WZ-HX homogeneous transformation enthalpy barrier is significantly lower than that of WZ-RS, i.e. always less than 0.1 eV/2-pairs for all compounds studied except SiC. (For SiC the barrier is only slightly higher, i.e. 0.13 eV/2-pairs.)

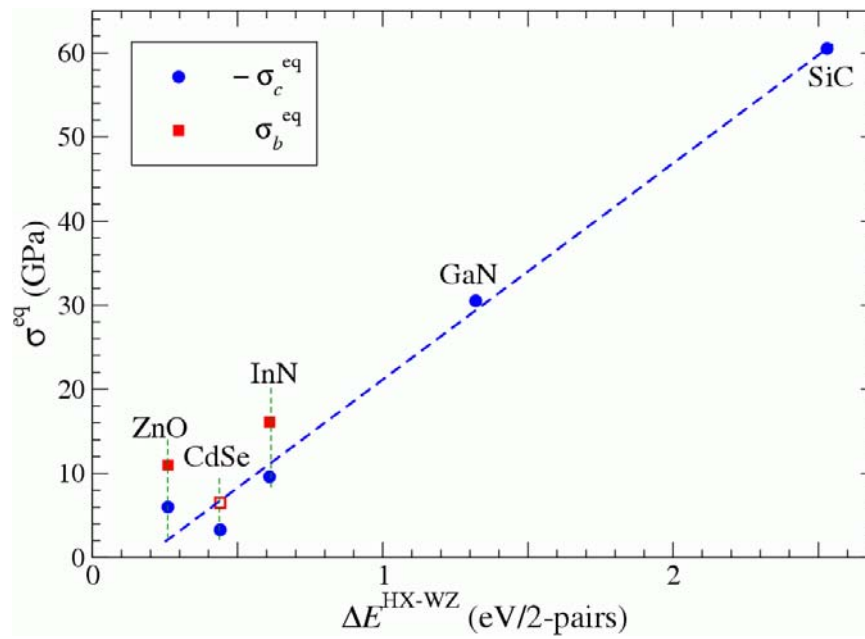


Figure 4.14 Correlation between equilibrium stresses ($-\sigma_c^{\text{eq}}$ and σ_b^{eq}) and the difference in energy (ΔE) between the HX and WZ phases for the five compounds. $-\sigma_c^{\text{eq}}$ (σ_b^{eq}) is the equilibrium value of the c -direction compressive stress (b -direction tensile stress) for the HX (DHX) and RS structures (see Table 4.3). The energy difference $\Delta E^{\text{HX-WZ}} = E^{\text{HX}} - E^{\text{WZ}}$ is calculated under conditions of zero external loading and is tabulated in Table 4.1.

4.3.4 Uniaxial tension along the $[0\bar{1}10]$ direction.

The HX structure has a longer dimension in the $[0\bar{1}10]$ direction compared to the WZ structure (longer by approximately 9%, see Figure 4.6 middle column). Although, the figure uses ZnO as an illustrated case, other compounds show similar changes in lattice constant b (see Table 4.2). This difference allows WZ to transform into DHX *via* tension in the b ($[0\bar{1}10]$) direction. Note that the difference in b between the two structures is only about half of the difference in c . Accordingly, the mechanical enthalpy contribution $A_{ac} \times \sigma_b \Delta b$ is roughly half of the case of c -compression for the comparable stress magnitude. Only three (InN, ZnO and CdSe) out of the five compounds studied have a local minimum corresponding to the DHX structure under tensile loading along the b direction. The enthalpy surfaces for these three compounds at their equilibrium tensile stresses σ_b^{eq} are shown in Figure 4.15 and their 2-D section plots are shown in Figure 4.16. The plot between the enthalpy differences $\Delta H^{\text{DHX-WZ}} = H^{\text{DHX}} - H^{\text{WZ}}$ as functions of tensile stress σ_b are shown in Figure 4.17. The equilibrium tensile stress σ_b^{eq} (14.7, 10.8 and 5.8 GPa for InN, ZnO and CdSe, respectively) is approximately twice the equilibrium compressive stress $-\sigma_c^{\text{eq}}$ for the c -direction. Empirical potential based molecular dynamic (EP-MD) simulations have shown that under tensile loading, $[0\bar{1}10]$ -oriented ZnO nanowires can indeed transform into the DHX structure under tensile loading (Kulkarni *et al.*, 2006). The nanowires can sustain tensile stresses up to 14 GPa before failure, which is well above the equilibrium stress σ_b^{eq} predicted here. The equilibrium transformation stress of $\sigma_b^{\text{eq}} = 5.8$ GPa for CdSe is the lowest among the compounds studied. For

nanostructures, other factors such as surface effects may contribute to facilitate the WZ→HX transformation (Grunwald *et al.*, 2006). As a result, HX can emerge as an intermediate phase during a WZ→RS transformation in CdSe nanorods (Grunwald *et al.*, 2006), even though it does not have the lowest enthalpy in the bulk calculations. The relationship between σ_b^{eq} and $\Delta E^{\text{DHX-WZ}} = E^{\text{DHX}} - E^{\text{WZ}}$ is shown Figure 4.14. Note that the tensile stress σ_b^{eq} of CdSe may be higher than its fracture strength.

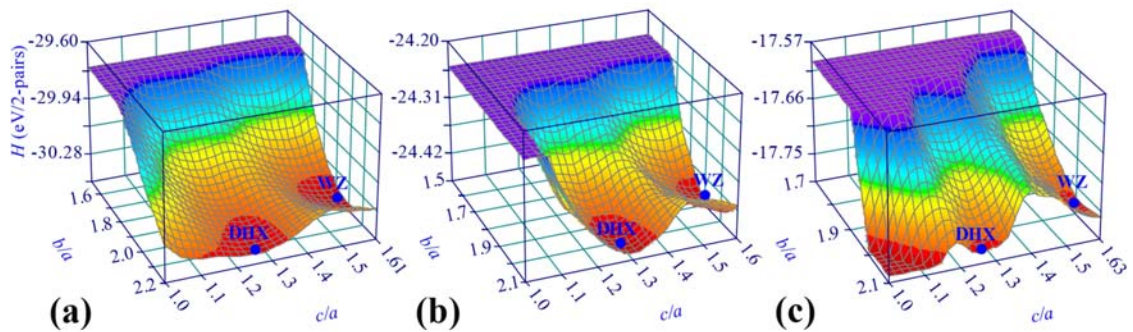


Figure 4.15 Enthalpy surface maps (in eV/2 pairs) for a wurtzite unit cell of (a) InN, (b) ZnO and (c) CdSe at their respective DHX-WZ equilibrium stresses along b -direction (σ_b^{eq}).

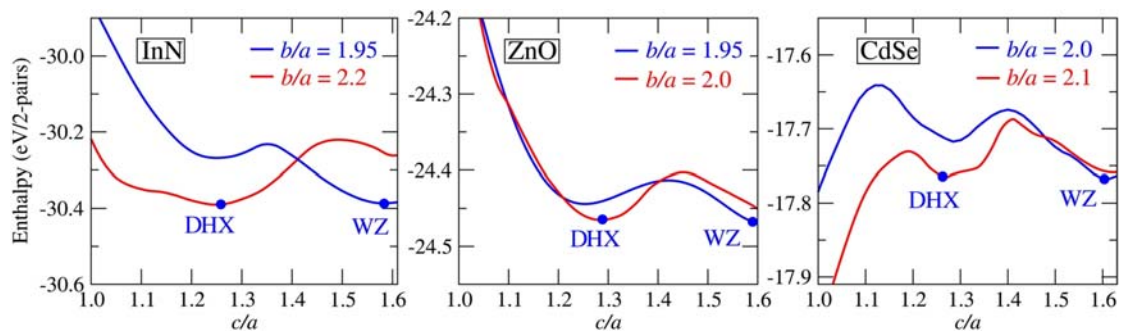


Figure 4.16 Sections of the enthalpy surface maps in Figure 4.15 for two b/a values that cut through the DHX and WZ structures.

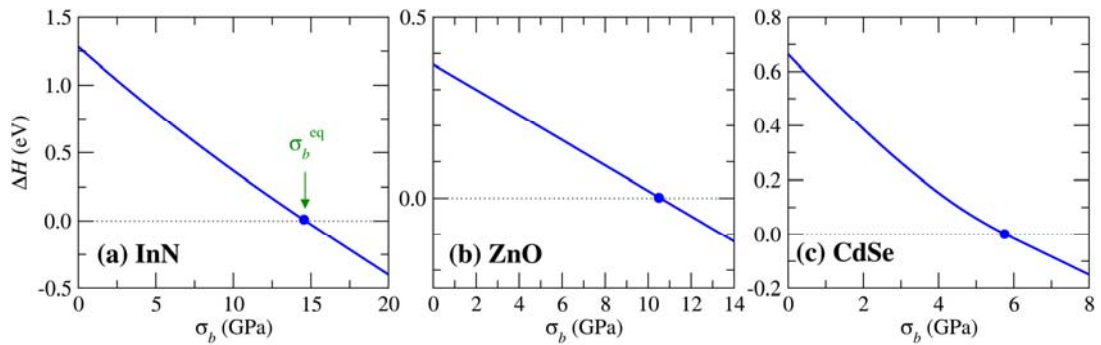


Figure 4.17 Enthalpy differences (ΔH) between the DHX and WZ phases of (a) InN, (b) ZnO and (c) CdSe as a function of b -direction stress (σ_b). As the applied stress reaches the equilibrium point (σ_b^{eq} , indicated by solid dots), the enthalpy of DHX equals that of WZ. At stresses above σ_b^{eq} , the DHX phase is more stable.

A local minimum for DHX is not observed in the enthalpy surfaces for SiC and GaN, even at extremely high theoretical levels of σ_b (60 GPa for SiC and 30 GPa for GaN). The enthalpy surfaces plots for SiC and GaN at their ultimate strengths, σ_{UTS} values (60 GPa for SiC and 30 GPa for GaN) are shown in Figure 4.18. The lack of transformation in these compounds can be attributed to the fact that their equilibrium transformation stresses are higher than their respective ultimate tensile strengths ($\sigma_b^{\text{eq}} \gg \sigma_{UTS}$). Indeed, EP-MD simulations have shown that for GaN nanowires $\sigma_{UTS} \approx 30$ GPa, (Wang *et al.*, 2007) only a fraction of the rough estimation of equilibrium stress of $\sigma_b^{\text{eq}} \geq 60$ GPa. The σ_b^{eq} of SiC is even higher since it has a higher energy difference between WZ and HX, making it more likely to have fractured before reaching its theoretical equilibrium stress of $\sigma_b^{\text{eq}} \geq 120$ GPa.

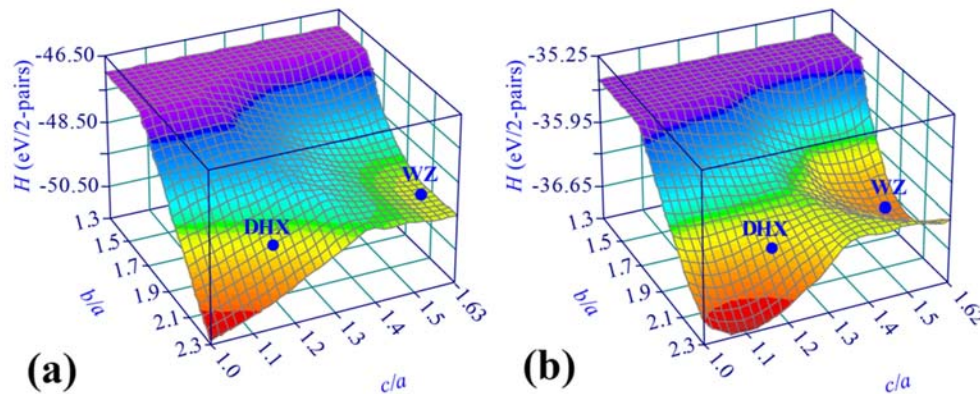


Figure 4.18 Enthalpy surface maps (in eV/2 pairs) for (a) SiC and (b) GaN at the tensile stress along b -direction (σ_b) of 60 GPa and 30 GPa, respectively.

4.4 Conclusions

First principles calculations are carried out to study the stability of the wurtzite (WZ), rocksalt (RS) and unbuckled wurtzite (HX) phases of SiC, GaN, InN, ZnO, and CdSe under loading of different directions. The relative energies between phases of the compounds correlate with their ionicity. At ambient conditions, WZ has the lowest energy, HX has the second highest energy and RS has the highest energy (with the exception of CdSe whose RS phase has a lower energy than its HX phase). All five compounds have the four-fold *wurtzite* structure as their stable and naturally occurring phase. Under hydrostatic compression, the compounds can transform into the six-fold coordinated *rocksalt* (RS) structure. Under uniaxial compression along the $[0001]$ direction and uniaxial tension along the $[01\bar{1}0]$ direction, the compounds can transform into the five-fold coordinated *unbuckled wurtzite* (HX) structure. The equilibrium conditions for the transformations are outlined.

For the WZ→RS transformation, the equilibrium hydrostatic pressure (p^{eq}) is predicted to be 64.9, 44.1, 12.2, 8.2 and 2.2 GPa for SiC, GaN, InN, ZnO, and CdSe, respectively. These values are in good agreement with other theoretical calculations and experimental measurements. For the WZ→HX transformation under uniaxial compression along the [0001] direction, the equilibrium stress ($-\sigma_c^{\text{eq}}$) is 60.5, 30.5, 9.6 and 6.0 GPa for SiC, GaN, InN and ZnO, respectively. For CdSe, uniaxial compression along the [0001] direction induces a WZ→RS transformation at a stress of 2.4 GPa instead of the WZ→HX transformation because the formation energy of RS is lower than HX for CdSe. For the WZ→DHX transformation under uniaxial tension along the $[01\bar{1}0]$ direction, the equilibrium transformation stress (σ_b^{eq}) is 14.7, 10.8, and 5.8 GPa for InN, ZnO and CdSe, respectively. The stress level for CdSe is close to its fracture limit. No transformation is observed for SiC and GaN under tension along the $[01\bar{1}0]$ direction due to the fact that their theoretical equilibrium transformation stresses are well above their respective ultimate fracture strengths. The magnitudes of p^{eq} , $-\sigma_c^{\text{eq}}$, and σ_b^{eq} are approximately linearly dependent with the formation energy differences between the relevant phase of the compounds. Based on the calculations of five compounds, we established a general linear function between p^{eq} and RS-WZ energy difference that could be useful for predicting the difference in formation energy of the RS and WZ phases of other materials when the equilibrium pressure is known, or *vice versa*.

CHAPTER V

FIRST PRINCIPLES STUDY OF

ZnO POLYMORPHS

5.1 Introduction

There are three well known polymorphs of ZnO; including wurtzite (WZ), rocksalt (RS), and zincblende (ZB) structures. (Ozgur *et al.*, 2005) WZ structure is the natural state under ambient conditions. RS structure is stable under high hydrostatic pressures. ZB structure can only be grown on certain crystalline surfaces of cubic crystals. So far, the existence of polymorphs other than WZ, RS, and ZB under various loading conditions has not been extensively studied. Recently, HX structure in $[01\bar{1}0]$ -orientated nanowires (Heussinger and Frey, 2006) and a body-centered-tetragonal phase (hereafter referred to as BCT-4) in $[0001]$ -oriented nanowires (Wang *et al.*, 2007) under uniaxial tensile loading are observed. The similar structures (to BCT-4) have been reported for carbon (Schultz and Stechel, 1998) and lithium aluminum oxide (Marezio, 1965). However, for a binary compound this structure is first studied by us (Wang *et al.*, 2007; Kulkarni *et al.*, 2008). In Chapter IV, the phase transformation from the WZ-to-RS and the WZ-to-HX(DHX) structure in ZnO has been reported. This chapter is devoted to the phase transformations from WZ - to - BCT-4. Based on first principles calculations, the BCT-4 ZnO is stable under uniaxial

tensile stress along [0001] direction. This chapter focused on the crystallographic changes and critical loading condition for the WZ-to-BCT-4 transformation.

5.2 Computational Method

First principles calculations are carried out to evaluate the total energy of ZnO in the WZ, BCT-4, and their deformed structures. The calculations are based on the density functional theory (DFT) within the local density approximations (LDA) and ultrasoft pseudopotentials (Vanderbilt, 1990), as implemented in the VASP code (Kresse and Furthmüller, 1996). Zinc *3d* electrons are treated as valence electrons. Cutoff energy for the plane wave expansion is 400 eV. The *k*-point sampling set is based on a $7 \times 7 \times 7$ division of the reciprocal unit cell according to Monkhorst-Pack scheme (Monkhorst and Pack, 1976) with the Γ -point included, which gives approximately 100 inequivalent *k*-points.

The stability of each crystal structure can be determined by analyzing enthalpy as a function of *c/a* and *b/a*. The enthalpy per a wurtzite unit cell under uniaxial loading is defined as (Sarasamak *et al.*, 2008)

$$H(c/a, b/a) = E(c, b, a, u, v) - A_{jk} \times \sigma_i q_i, \quad (5.1)$$

where *E* is the formation energy per wurtzite unit cell, σ_i is the stress along the *i* direction, q_i is the lattice parameter in the *i* direction, and A_{jk} is the cross section area of the unit cell perpendicular to the stress direction. Therefore, $A_{jk} \times \sigma_i q_i$ is external work. For tension along *c* axis, $i = c$, $A_{ab} = ab$, and $q_c = c$, with σ_c being the tensile stress. Note that, in the WZ-to-BCT-4 transformation, a unit contains 8 atoms or 4 Zn-O pairs ($V = abc$) is used for the calculations.

For each c/a and b/a pair, the internal parameters u and v and the unit cell volume V are allowed to relax so that the configuration that yields the minimum H is obtained. For a given load condition, the minima on the enthalpy surface with c/a and b/a as the independent variables identifies the corresponding stable structures. However, for WZ-to-BCT-4 transformation, b/a is fixed at 1.73. This is because both WZ and BCT-4 share the same $b/a = 1.73$. Therefore, only c/a is varied in the range from 1.4 – 2.0.

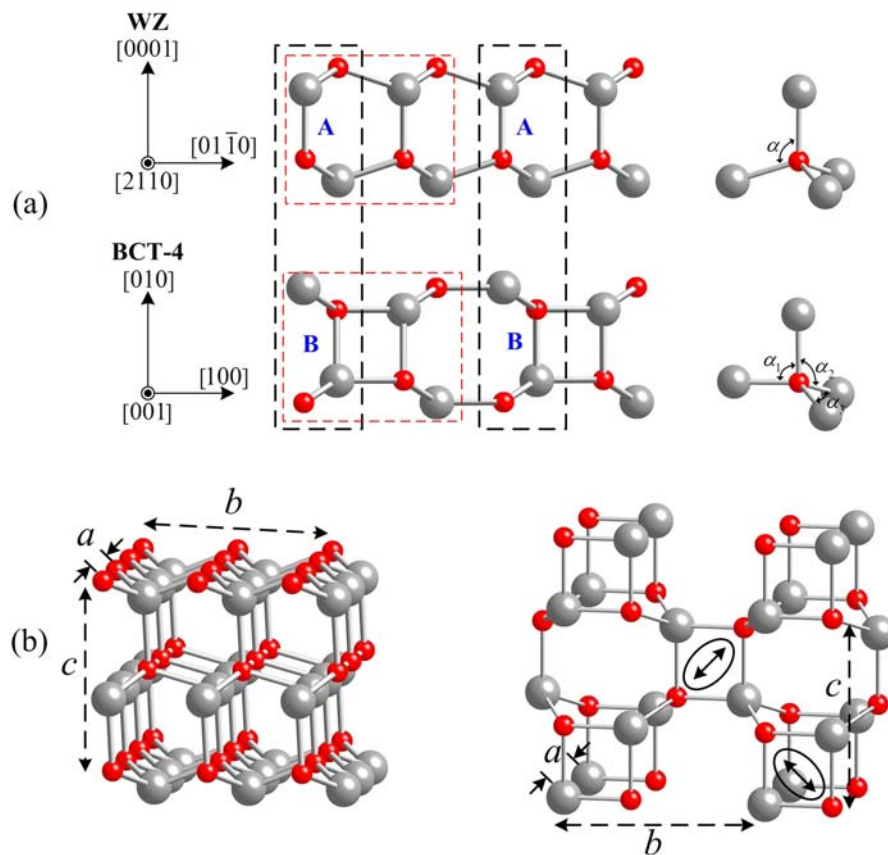


Figure 5.1 (a) Crystallographic transition through breaking and formation of bonds and differences in bond angles between the wurtzite (WZ) and body-centered-tetragonal (BCT-4) structures and (b) WZ and BCT-4 structures. The red dash box lines show the cell size with 8 atoms (four Zn-O pairs), for the WZ and BCT-4 structures used for the calculations.

5.3 Results and discussions

The WZ to BCT-4 transformation occurs through a combination of: (1) The breaking of every other Zn-O bonds along the [0001] direction (bonds labeled with A in Figure 5.1(a)) and (2) The formation of an equal number of Zn-O bonds next to the broken bonds along the same direction (bonds labeled with B in Figure 5.1(a)).

This bond-breaking and bond-formation process repeats on alternate planes along the $[01\bar{1}0]$ direction. The transformed phase keeps the tetrahedral coordination with each Zn/O atom at the center and 4 O/Zn atoms are at the vertices of a tetrahedron. The geometry of the tetrahedron can be characterized through the O-Zn-O bond angles (α_i , $i = 1-6$), as shown in Figure 5.1(a). For WZ, all bond angles are approximately equal ($\alpha_i \approx 109^\circ$). For BCT-4, however, the formation of 4-atom rings results in three distinct bond angles ($\alpha_1 \approx 90^\circ$, $\alpha_2 \approx 114^\circ$, and $\alpha_3 \approx 112^\circ$).

As can be seen from Figure 5.1(b), the transformed phase consists of 4-atoms (2 Zn and 2 O) rings one arranged at the center (of the figure) and another ring at the corner rotated by 90° relative to the first ring. In each 8-atom, BCT-4 unit cell, there are two 4-atom-ring clusters (one of each orientation) positioned in a simple tetragonal primitive lattice. The corresponding cell of 8 atoms for the WZ is shown for a direct comparison with the BCT-4 cell as well. Figure 5.1(b) shows the lattice parameters a , b , and c for the WZ and BCT-4 structures.

Their respective values as obtained from the first principles calculations at various stress levels are listed in Table 5.1 along with the corresponding cell volumes. For WZ, the c/a and b/a ratio are 1.61 and 1.73, respectively. Throughout the transformation, the b/a ratio remains at its initial value of 1.73, reflecting the symmetries of the loading and the lattice. By increasing tensile stress along the c -axis σ_c , the c/a ratio increases. The stability of the BCT-4 structure under the tensile loading along [0001] direction can be explained by its higher c/a ratio compares to that of WZ. Table 5.1 shows the equilibrium unit cell volume = 91.4 \AA^3 and 95.2 \AA^3 (per 4 Zn-O pairs) for the WZ and BCT-4 structure, respectively. The unit cell volume of the BCT-4 is 4.2% larger than that of the WZ, with the elongation along the [0001] direction being the primary reason for this volume difference. The ideal BCT-4 structure with lattice parameters a , b , and c is presented in Figure 5.2.

Table 5.1 Lattice parameters for WZ and BCT-4 ZnO under tensile loading along [0001] direction for $\sigma_c = 0, 4, 7$ and 10 GPa.

Parameters	WZ	BCT-4			
	$p = 0$ GPa	$\sigma_c = 0$ GPa	$\sigma_c = 4$ GPa	$\sigma_c = 7$ GPa	$\sigma_c = 10$ GPa
a (Å)	3.21 (3.20, ^d 3.25, ^{b,c} 3.26, ^f 3.29 ^g)	3.17 (3.24 ^g)	3.13	3.09	3.06
b (Å)	5.54 (5.67 ^g)	5.48 (5.58 ^g)	5.42	5.35	5.32
c (Å)	5.15 (5.17, ^d 5.22, ^f 5.17 ^g)	5.48 (5.52 ^g)	5.71	5.87	5.98
$V=abc$ (Å ³)	91.4 (93.4, ^a 94.5, ^e 96.0, ^f 96.4 ^g)	95.2 (99.8 ^g)	96.9	97.0	97.3
c/a	1.61 (1.59 ^e)	1.73 (1.71 ^g)	1.82	1.90	1.95
b/a	1.73 (1.73 ^g)	1.73 (1.72 ^g)	1.73	1.73	1.73

^aDFT (GGA) calculations by Jaffe *et al.* (Jaffe *et al.*, 2000).

^bSynchrotron EDXD experiments by Desgreniers. (Desgreniers, 1998).

^cXRD experiments by Karzel *et al.* (Karzel *et al.*, 1996).

^dDFT (LDA) calculations by Malashevich and Vanderbilt (Malashevich and Vanderbilt, 2007).

^eDFT (GGA) calculations by Ahuja *et al.* (Ahuja *et al.*, 1998).

^fEXAFS experiments by Decrempe *et al.* (Decrempe *et al.*, 2003).

^gMD simulation by Wang *et al.* (Wang *et al.*, 2007).

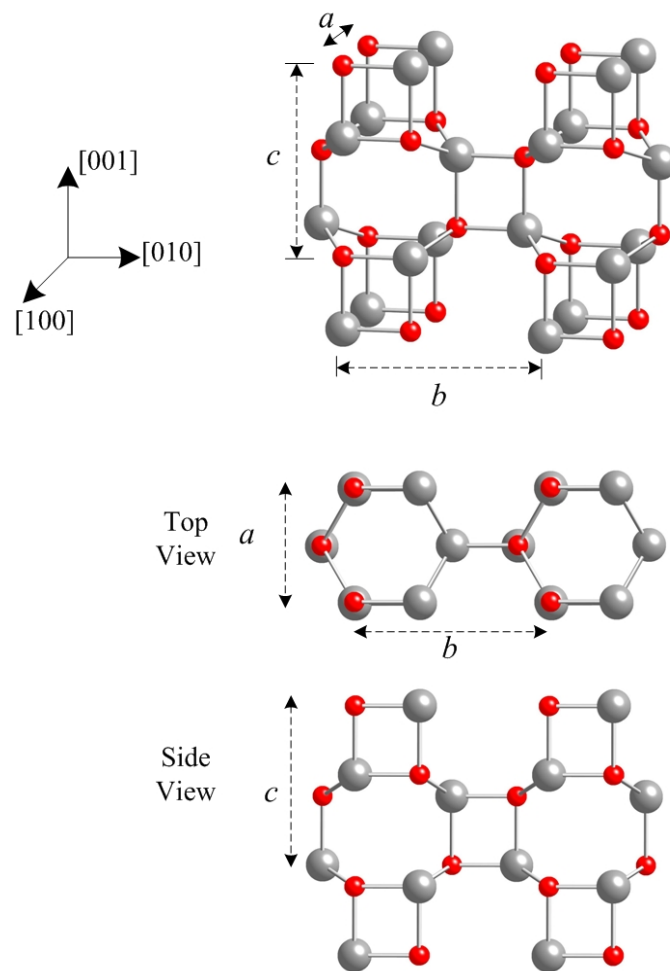


Figure 5.2 Crystal model of the BCT-4 structure: small spheres represent anions and large spheres represent cations. The top figure shows the perspective view. The middle and bottom rows show top view and side view, respectively. The distances described by crystal parameters a , b , and c are indicated.

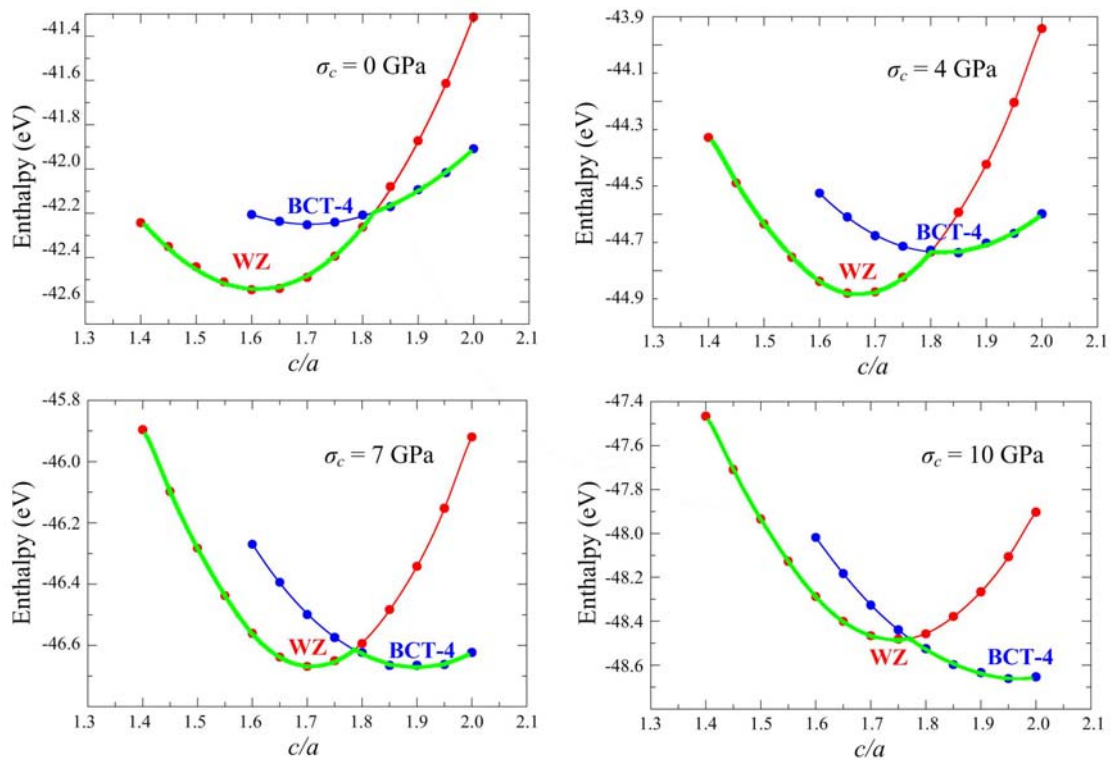


Figure 5.3 Enthalpy (eV/ 4 Zn-O pairs) as a function of c/a obtained from first principles calculations for $b/a = 1.73$ at tensile stresses of (a) $\sigma_c = 0$ GPa, (b) $\sigma_c = 4$ GPa, (c) $\sigma_c = 7$ GPa and (d) $\sigma_c = 10$ GPa. The minimum enthalpy curve for each plot is shown with the thick solid green line.

The relative favorability of the two structures is studied by calculating the enthalpies. Because both WZ and BCT-4 share the same b/a ratio at 1.73, it is not necessary to vary this parameter for the study of relative phase stability. The enthalpies are shown by the 2-D section plot at $b/a=1.73$. Figure 5.3 shows the enthalpy values for both the WZ and BCT-4 structure with $b/a = 1.73$ at the tensile stresses of $\sigma_c=0$ GPa, 4 GPa, 7 GPa and 10 GPa. At any stress level, each structure has its own enthalpy minimum. The first minimum (H_{\min}^{WZ}), at $\sigma_c=0$ GPa is in the vicinity of $c/a \approx 1.6$ which corresponds to the WZ structure and the second minimum ($H_{\min}^{\text{BCT-4}}$) is in the vicinity of $c/a \approx 1.7-1.9$ which corresponds to the BCT-4 structure. At zero stress, the WZ is stable crystal structure and its enthalpy is lower than that of the BCT-4 by 0.3 eV as shown in Figure 5.3(a). Because the two phases (WZ and BCT-4) are differed by the vertical bonds formations, the transformation from WZ-to-BCT-4 involves the bond-breaking and bond-formation that are the internal change inside the cell and are not directly affected by the changes in external parameter c/a . Varying c/a alone does not cause the spontaneous transformation from WZ to BCT-4. Therefore, in the calculations, both phases can be stabilized at the same c/a (for e.g. c/a in the range 1.6 – 1.8). In reality, there would be a transformation to the lower enthalpy phase, providing that the transformation barrier can be overcome. The minimum enthalpy curve for each plot in Figure 5.3 is shown with the thick solid green line. The kink is the expected transformation point. In reality, there might exist considerable hysteresis (the transformation occurs after the change in c/a passed the kink point in both forward and backward transformation) due to the large barrier associated with the bond-breaking/formation processes. As the stress is increased to 4 GPa (Figure 5.3(b)), the difference in enthalpies decreases, and at a stress of 7 GPa

(Figure 5.3(c)), the two minima, H_{\min}^{WZ} and $H_{\min}^{\text{BCT-4}}$ become comparable, indicating that the WZ and BCT-4 are equally favored. However, as mentioned above, there is a transformation barrier (expected to be large due to the bond breaking/formation) prohibiting the spontaneous transformation. This value of stress corresponds to the equilibrium transition stress for the two structures. At the stress of 10 GPa (Figure 5.3(d)), the enthalpy of the BCT-4 is lower, and this structure is clearly favored.

5.4 Conclusions

The first principles calculations are carried out to study the stability of the wurtzite (WZ), the rocksalt (RS), the unbuckled wurtzite (HX) and the BCT-4 phases of ZnO under different loading conditions. The stability of the RS and HX structures has been presented in Chapter IV. This chapter focused on the stabilities of WZ and BCT-4 structures. We found that the WZ to BCT-4 transformation can occur under uniaxial tension along the [0001] direction and estimated the equilibrium transition stress (σ_c^{eq}) to be about 7 GPa. A large hysteresis in the upward/downward transformation is expected due to a large barrier in bond breaking/formation during the transformation. The identification of the BCT-4 crystalline structures and the characterization of the WZ-to-BCT-4 phase transformations lead to a more complete understanding of the nature of polymorphism in ZnO.

CHAPTER VI

CONCLUSIONS AND FUTURE RESEARCH

In this thesis, some mechanical properties of some semiconductors in group-IV (SiC), group-III-V (GaN and InN), and group-II-VI (ZnO and CdSe) are calculated by utilizing the first principles (or *ab initio*) method. The crystal properties such as the phase stability and phase transformations under different loading conditions are calculated for the aforementioned materials. The results from our study are illustrated as following:

The stability of the wurtzite (WZ), rocksalt (RS), and unbuckled wurtzite (HX) phases of SiC, GaN, InN, ZnO, and CdSe under different loading directions is investigated. The phase transformations from WZ-to-RS structure and WZ-to-HX structure are systematically studied by considering the enthalpy surfaces and enthalpy barriers between the different structures. Under ambient conditions, the WZ-structure has the lowest energy for these compounds, the HX-structure has the second highest energy and the RS-structure has the highest energy. This is with the exception of CdSe, where the RS-structure has a lower energy than the HX-structure. Under sufficiently large hydrostatic compression, the WZ-structure can transform into the RS-structure. Under a uniaxial compression along the $[0001]$ crystalline direction or a uniaxial tension along $[0\bar{1}10]$ crystalline direction, the WZ-structure can transform into the HX or DHX structure.

Based on first principles calculations, the critical pressures of transformation are calculated and found to be in good agreement with available experimental results. The equilibrium conditions for the transformations are outlined.

For the WZ→RS transformation, the equilibrium hydrostatic pressures (p^{eq}) are predicted to be 64.9, 44.1, 12.2, 8.2 and 2.2 GPa for SiC, GaN, InN, ZnO, and CdSe, respectively. These values are in good agreement with other theoretical calculations and experimental measurements (Sarasamak *et al.*, 2008).

For the WZ→HX transformation under uniaxial compression along the [0001] direction, the equilibrium stresses ($-\sigma_c^{\text{eq}}$) are 60.5, 30.5, 9.6 and 6.0 GPa for SiC, GaN, InN and ZnO, respectively. For CdSe, uniaxial compression along the [0001] direction induces a WZ→RS transformation at a stress of 2.4 GPa instead of the WZ→HX transformation because the formation energy of RS is lower than HX in this particular compound.

For the WZ→DHX transformation under uniaxial tension along the $[0\bar{1}\bar{1}0]$ direction, the equilibrium transformation stresses (σ_b^{eq}) are 14.7, 10.8, and 5.8 GPa for InN, ZnO and CdSe, respectively. No transformation is observed for SiC and GaN under tension along the $[0\bar{1}\bar{1}0]$ direction due to the fact that their theoretical equilibrium transformation stresses are well above their respective ultimate fracture strengths (Wang *et al.*, 2007; Sarasamak *et al.*, 2008). The magnitudes of p^{eq} , $-\sigma_c^{\text{eq}}$, and σ_b^{eq} are linearly promotional with the formation energy differences between the relevant phases.

For ZnO, a novel structure, body-centered-tetragonal with 4 atoms ring (BCT-4) is predicted to be stable under tension along [0001] direction. This structure has never

been reported for a binary compound before. For the WZ→BCT-4 transformation under uniaxial tension along the [0001] direction, the equilibrium stress (σ_c^{eq}) is approximately 7 GPa. The identification of the BCT-4 structure and the characterization of the WZ-to-BCT-4 phase transformation lead to a more complete understanding of the nature of polymorphism in ZnO.

There is another ongoing project on the study of pressure dependences of the elastic constants in compounds with the WZ-structure. In our calculations, the elasticities under pressures are carried out by using the linear muffin tin orbital (LMTO) codes developed by M. Methfessel *et al.* (Methfessel *et al.*, 2000). The codes are based on the full potential linear muffin tin orbital method (FP-LMTO) in local density approximations. The energy as a function of various strains is calculated. Application of traceless (volume conserving) strains in the various directions provides the elastic constants. The six independent elastic constants for wurtzite structure are extracted. The calculations are repeated for varied unit cell volumes, and from the calculated pressure-volume relation, the elastic constants are obtained as a function of pressure (details in the elastic properties such as the stress-strain relation in WZ-structure can be seen in Chapter III).

The focus is on the behavior of the elastic moduli (C_{ij}) as a function of pressure. The two longitudinal modes, C_{11} and C_{33} , are increased with pressure as shown in Figure 6.1 (left column). For the shear modes, there is no common trend. The trends are varied depending on compounds as shown in Figure 6.1 (right column). Moreover, we observed that the high pressure crystal phase transformation from wurtzite to rocksalt relates to an orthorhombic strain with two components (1) a traceless compression along the [0001] axis corresponding to the longitudinal mode

and (2) a traceless compression along $[01\bar{1}0]$ direction corresponding to the shear mode.

To study the elastic constants under pressure, first we calculated six elastic constants in WZ-structure for each compound at the equilibrium volume. The agreement between the calculated value and experiment is satisfactory (Table 6.1). For the structures under pressures, the elastic constants are calculated at several reduced volumes, each of which corresponds to the system under pressure. The corresponding pressure is obtained from the slope of the energy-volume curve at each volume used for the calculation.

Table 6.1 The bulk modulus (B_0) and the elastic constants (C_{ij}) in unit of GPa, of WZ – SiC, GaN, InN, ZnO, and CdSe at $P = 0$ GPa.

Compounds	SiC	GaN	InN	ZnO	CdSe
B_0	229 (220 ^a)	207 (210, ^b 207, ^c 202 ^d)	151 (147, ^c 141 ^d)	162 (131.5, ^e 162.3, ^g 133.7 ^g)	60.1 (53.4 ⁱ)
C_{11}	541 (501 ^a)	367 (390, ^b 396, ^c 367 ^d)	232 (271, ^c 223 ^d)	228 (231, ^e 207 ^f)	80.5 (74.9, ^h 74.6 ⁱ)
C_{12}	117 (111 ^a)	135 (145, ^b 144, ^c 135 ^d)	115 (124, ^c 115 ^d)	133 (111, ^e 118 ^f)	47.2 (46.09, ^h 46 ⁱ)
C_{13}	61.1 (52 ^a)	98 (106, ^b 100, ^c 103 ^d)	95.8 (94, ^c 92 ^d)	118 (104, ^e 104 ^f)	39.9 (39.26, ^h 39 ⁱ)
C_{33}	586 (553 ^a)	409 (398, ^b 392, ^c 405 ^d)	239 (200, ^c 224 ^d)	232 (183, ^e 209 ^f)	91.9 (84.51, ^h 81 ⁱ)
C_{44}	162 (163 ^a)	97.9 (105, ^b 91, ^c 95 ^d)	52.4 (46, ^c 48 ^d)	40.0 (72, ^e 44.1 ^f)	14.9 (13.15, ^h 13 ⁱ)
C_{66}	212 (195 ^a)	116 (122.5, ^b 126, ^c 116 ^d)	58.8 (73.5, ^c 54 ^d)	47.1 (60, ^e 44.5 ^f)	16.7 (14.41, ^h 14 ⁱ)

^a(Kamitani *et al.*, 1997)

^b(Polian *et al.*, 1996)

^c(Kim *et al.*, 1994; Kim *et al.*, 1996)

^d(Wright, 1997)

^e(Zaoui and Sekkal, 2002)

^f(Carlotti *et al.*, 1995)

^g(Jaffe *et al.*, 2000)

^h(Cline *et al.*, 1967)

ⁱ(Rabani, 2002)

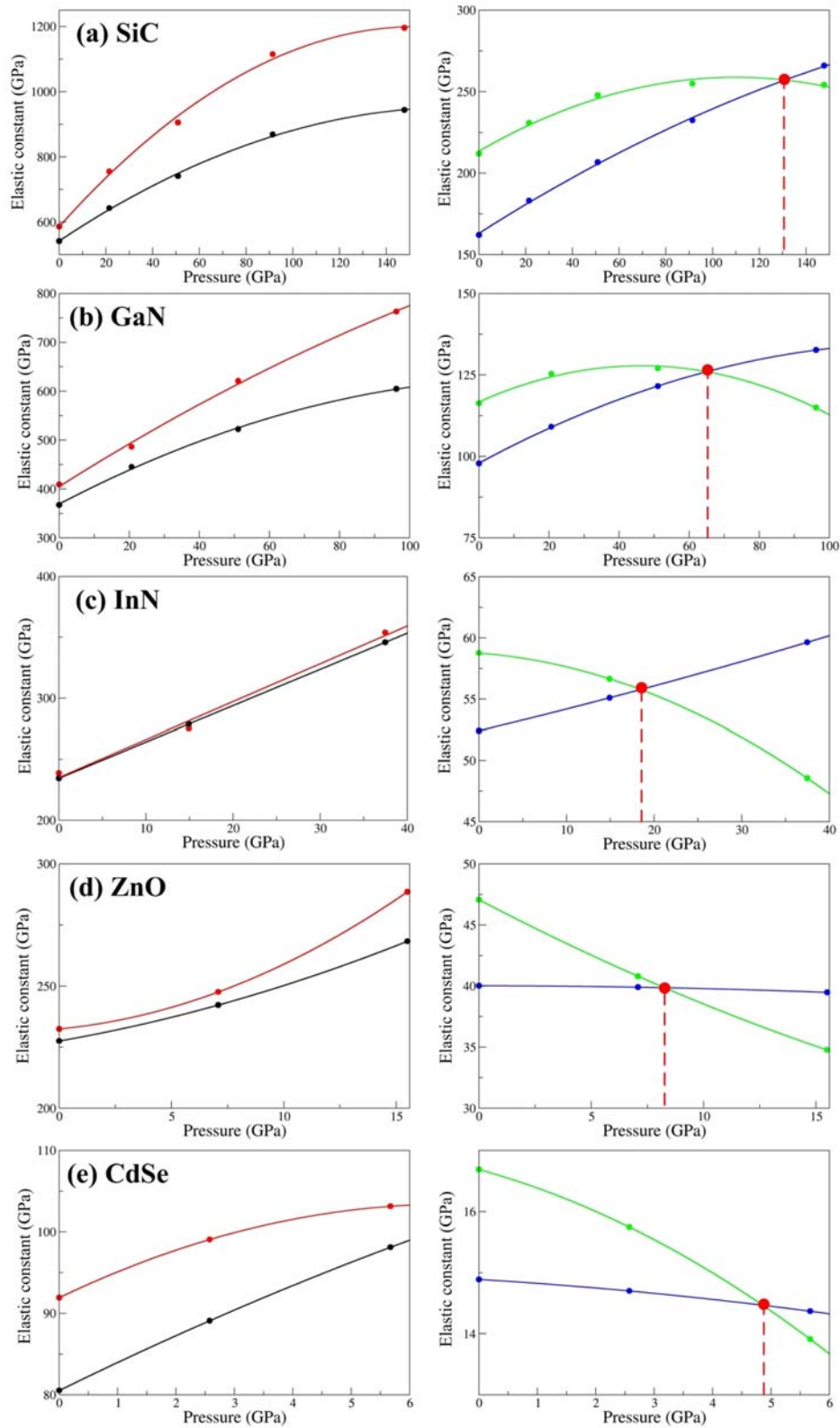


Figure 6.1 The elastic constant as function of pressure in WZ-SiC, GaN, InN, ZnO, and CdSe. The black, red, blue, and green color represented C_{11} , C_{33} , C_{44} , and C_{66} , respectively.

This work improves current understanding of the elastic constants under pressure. The results show that both of the longitudinal modes, C_{11} and C_{33} , increase with pressure for all compounds, as shown in the left side of Figure 6.1. For SiC, GaN, and InN, C_{44} monotonously increase with pressure. On the other hand, for ZnO and CdSe, C_{44} is slightly decreased with pressure. The depending with pressure of C_{66} is more complicated. For SiC and GaN, C_{66} increase with pressure at low pressure and drops at high pressures. For InN, ZnO, and CdSe, C_{66} tend to decrease with pressure. For all compounds studied, C_{44} and C_{66} curves are crossed (show with red solid dots in the right side of Figure 6.1). We observed that the crossing point of C_{44} and C_{66} occurs near the WZ-RS equilibrium transformation pressures but on the higher side. The crossing points are 130, 65, 18, 8.3, and 4.8 GPa, for SiC, GaN, InN, ZnO, and CdSe, respectively. These values are larger than the calculated equilibrium transition pressures, except for ZnO, where the value is comparable. However, for GaN, InN, ZnO, and CdSe the actual transformation pressures observed experimentally are generally higher than the calculated values (Ueno *et al.*, 1994; Kumar *et al.*, 2007; Wang *et al.*, 2007). This has been attributed to the transformation barrier (Mujica *et al.*, 2003). As a result, the experimental transformation pressures occur close to the C_{44} - C_{66} crossing point. In SiC, the crossing point is about two times larger than our calculated equilibrium transformation pressure. However, this value is quite close to the value from recent *ab-initio* study by Durandurdu (Durandurdu, 2007), where the pressure induce phase transition in WZ-to-RS is found to be 100 GPa. Since high quality WZ-SiC is difficult to grow, the WZ-RS phase transition has not been experimentally studied. However, there is some experimental studies in the pressure induce phase transition of SiC by x-ray diffraction measurements. For example,

Yoshida *et al.* found that SiC can transform from zincblende (ZB) to RS at the pressure ~ 100 GPa (Yoshida *et al.*, 1993).

There is another project being carried out on the investigation of the phase transformation in LiAlO₂. The total energies has been calculated by the projector augmented wave (PAW) method (Blöchl, 1994) as implemented in the VASP code (Kresse and Furthmüller, 1996; Kresse and Furthmüller, 1996; Kresse and Joubert, 1999). The codes are based on density functional theory within the generalized gradient approximation (GGA). This lithium compound has potential applications in the energy industry as lithium battery cathodes (Ceder *et al.*, 1998) and electrolyte tiles for molten carbonate fuel cells (MCFC) (Takizawa and Hagiwara, 2002). It has been reported that LiAlO₂ has at least four different types of crystal structures, the hexagonal α -phase (Marezio and Remeika, 1966), the monoclinic β - phase (Marezio and Remeika, 1966; Zou *et al.*, 2006), the tetragonal γ -phase (Marezio, 1965), and the tetragonal δ - phase (Li *et al.*, 2004). The γ - LiAlO₂ is a promising substrate for GaN-based laser diodes. This is because the lattice mismatch between LiAlO₂ and GaN is only 1.4% (Xu *et al.*, 1998). We investigate the γ - and δ - phases. The illustrations of both phases are shown in Figure 6.2. The unit cells used for the calculations are shown in Figure 6.3. The properties of both phases and the equilibrium transformation pressure between them are briefly summarized as follow.

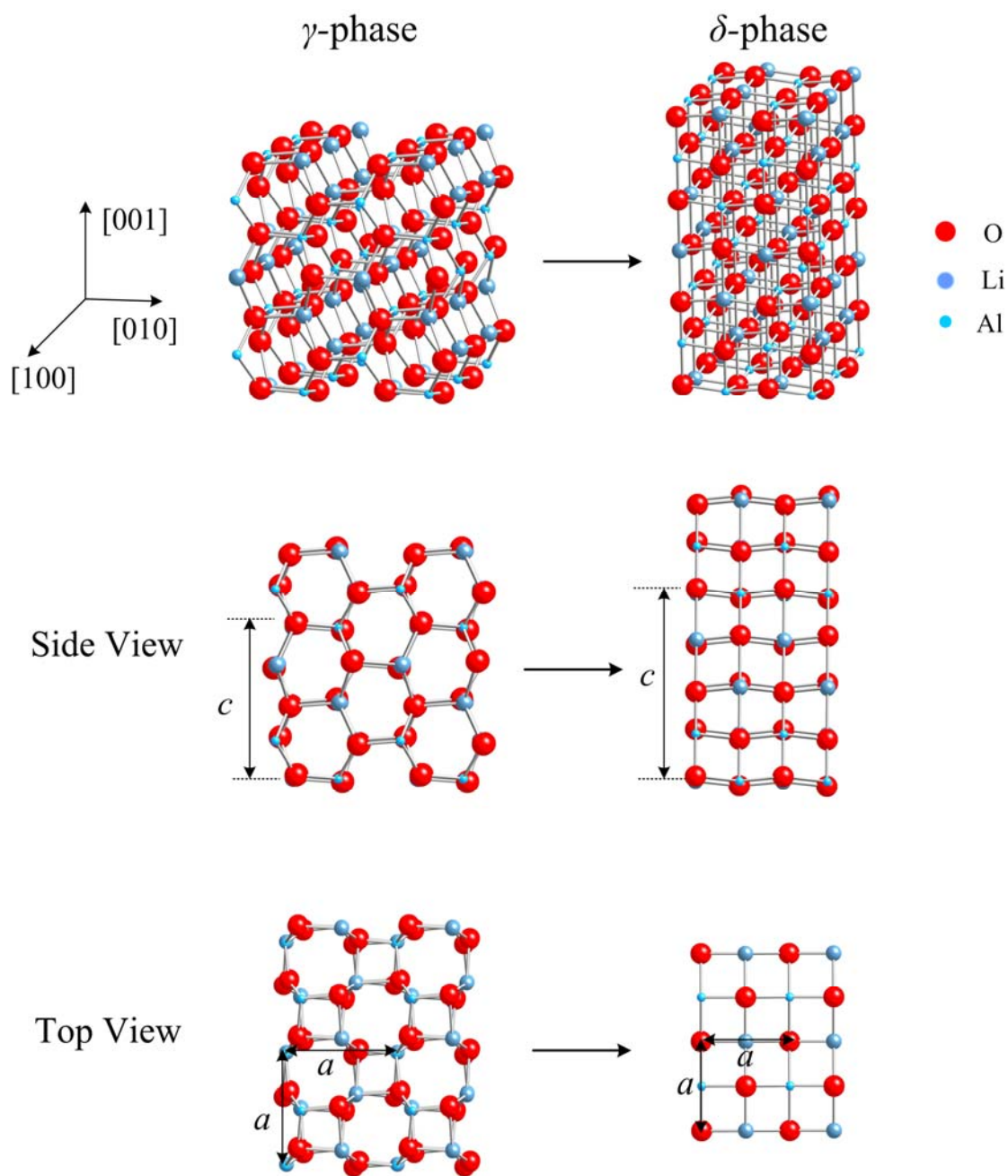


Figure 6.2 Schematic illustration of the γ - LiAlO_2 and δ - LiAlO_2 structures: The middle row and the bottom row show the side view and top view, respectively. The crystal parameters a and c are indicated.

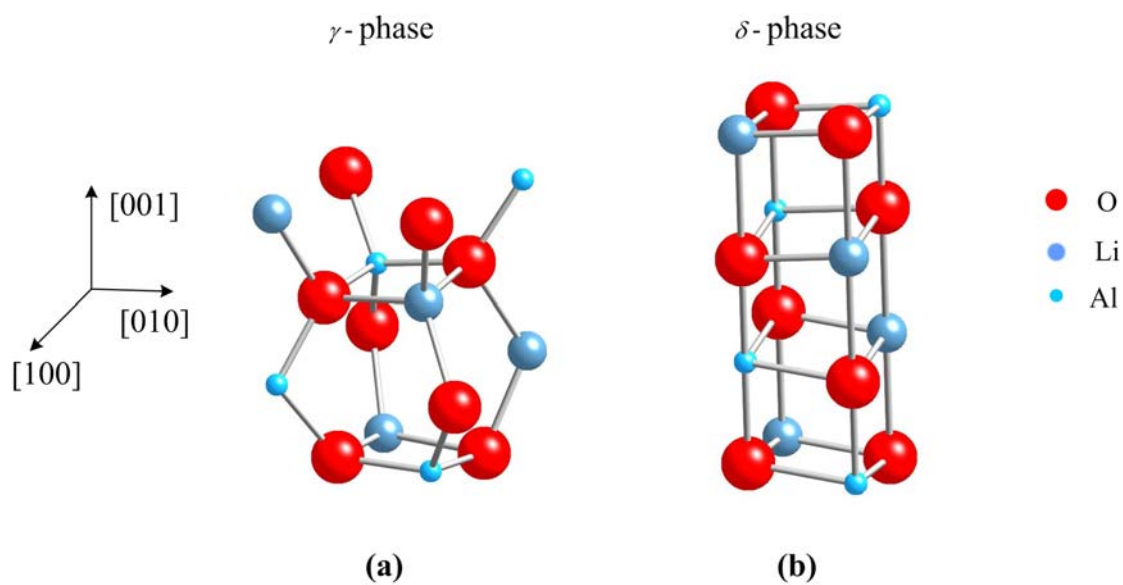


Figure 6.3 Unit cells of γ -LiAlO₂ and δ -LiAlO₂ used in the calculations

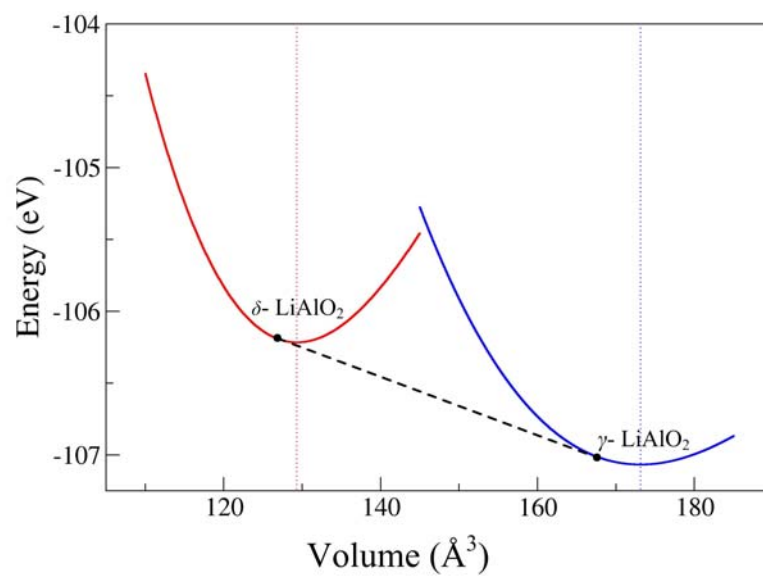


Figure 6.4 The total energy as a function of volume for γ - and δ -phase and the common tangent construction.

Table 6.2 The calculated lattice constant a , bulk modulus B , and pressure derivation of the bulk modulus B' , and equilibrium volume V_0 , for γ -LiAlO₂, and δ -LiAlO₂.

parameters	γ -LiAlO ₂	δ -LiAlO ₂
a (Å)	5.229 (5.169 ^a)	3.924 (3.887 ^b)
c (Å)	6.332 (6.268 ^a)	8.398 (8.300 ^b)
B (GPa)	92.2	156
B'	3.84	3.89
V_0 (Å ³)	173	129 (-25.3%)

^aXRD-experiment (Marezio, 1965)

^bA shock compression technique (Li *et al.*, 2004)

First, we present the results for γ - LiAlO₂ and δ - LiAlO₂, separately. In the calculations of both phases, c/a and volume are allowed to relax. The relaxed crystal parameters and the total energies are shown in Table 6.2. δ -LiAlO₂ has a smaller volume than the γ -phase. Under ambient conditions, the γ -phase is found to be lower in energy than the δ -phase. The calculated γ -LiAlO₂ crystal parameters are in agreement with the values by Marezio (Marezio, 1965). The energy-volume curve, i.e. the equation of states for each phase is calculated. The energy-volume curves for both phases are shown in Figure 6.4. Based on the equation of states, the bulk moduli, its derivative, and the equilibrium transformation pressure between the γ - and the δ - phase are calculated. The equilibrium transformation pressure is calculated from the common tangent between the two equation of states curves. The equilibrium transformation pressure is 3.3 GPa.

Our results agree quite well with the x-ray diffraction (XRD) study, where they estimated the minimum pressure required for the γ - to δ - phase transition to be

about 2 GPa under static compression. (Lei *et al.*, 2008). However, another experimental results from Li *et al.* (Li *et al.*, 2004), based on a shock recovery technique found a much higher transformation pressure, i.e. at pressures above 9 GPa. The larger pressure of the actual transformation compare to the equilibrium transformation pressure, especially for the shock wave experiment, is expected and can be attributed to the transformation barrier. Further experimental results can help to improve understands of the transformation

All of the results in this thesis show that the first principles calculation can be used to study many mechanical properties, such as the stability of different crystal phases, the equilibrium phase transformation pressures, and other properties such as the elastic constants. The approaches illustrated in this thesis can be applied to study other materials as well.

REFERENCES

REFERENCES

- Ahuja, R., Fast, L., Eriksson, O., Wills, J. M., and Johansson, B. (1998). Elastic and high pressure properties of ZnO. **J. Appl. Phys.** 83: 8065.
- Ashcroft, N. W. and Mermin, N. D. (1976). **Solid State Physics**. Philadelphia: Saunders Company.
- Bae, S. Y., Seo, H. W., Park, J., Yang, H., Park, J. C., and Lee, S. Y. (2002). Single-crystalline gallium nitride nanobelts. **Appl. Phys. Lett.** 81: 126.
- Bates, C. H., White, W. B., and Roy, R. (1962). New high-pressure polymorph of zinc oxide. **Science** 137: 993.
- Benkhattou, N., Rached, D., Soudini, B., and Driz, M. (2004). High-pressure stability and structural properties of CdS and CdSe. **Phys. Stat. Sol. (b)** 241: 101-107.
- Blöchl, P.E. (1994). Projector augmented-wave method. **Phys. Rev. B** 50: 17953.
- Cai, J. and Chen, N. (2007). First-principles study of the wurtzite-to-rocksalt phase transition in zinc oxide. **J. Phys.: Cond. Matter** 19: 266207.
- Carlsson, J. M. (2009). Pseudopotential from ultrahard to ultrasoft [On-line]. Available: http://www.tcm.phy.cam.ac.uk/castep/CASTEP_talks_07/carlsson2.pdf
- Carlotti, G., Fioretto, D., Socino, G., and Verona, E. (1995). Brillouin scattering determination of the whole set of elastic constants of a single transparent film of hexagonal symmetry. **J. Phys.: Cond. Matter** 7: 9147-9153.
- Carr, W.J., Jr. (1961). Energy, specific heat, and magnetic properties of the low-density electron gas. **Phys. Rev.** 122: 1437-1446.

- Carr, W.J. and Maradudin, A. A. (1964). Ground-state energy of a high-density electron gas. **Phys. Rev.** 133: A371-A374.
- Catti, M. (2001). Orthorhombic Intermediate State in the Zinc Blende to Rocksalt Transformation Path of SiC at High Pressure. **Phys. Rev. Lett.** 87: 035504.
- Ceder, G., Chiang, Y. M., Sadoway, D. R., Aydinol, M. K., Jang, Y. I., and Huang, B. (1998) Identification of cathode materials for lithium batteries guided by first-principles calculations. **Nature.** 392: 694 – 696.
- Ceperly, D. M. and Alder, B. J. (1980). Ground of the electron gas by a stochastic method. **Phys. Rev. Lett.** 45: 566-569.
- Chan, C. T., Vanderbilt, D., Louie, S. G., and Chelikowsky, J. R. (1986). Theoretical study of the cohesive and structural properties of Mo and W in BCC, FCC, and HCP structures. **Phys. Rev. B** 33: 7941.
- Chang, K. J. and Cohen, M. L. (1987). Ab initio pseudopotential study of structural and high-pressure properties of SiC. **Phys. Rev. B** 35: 8196.
- Christensen, N. E. and Gorczyca, I. (1994). Optical and structural properties of III-V nitrides under pressure. **Phys. Rev. B** 50: 4397.
- Cline, C. F. and Stephens, D. R. (1965). Volume compressibility of BeO and other II-VI compounds. **J. Appl. Phys.** 36: 2869.
- Cline, C. F., Dunegan, H. L., and Henderson, G. W. (1967). Elastic constants of hexagonal BeO, ZnS, and CdSe. **J. Appl. Phys.** 38: 1944-1948.
- Côté, M., Zakharov, O., Rubio, A., and Cohen, M. L. (1997). Ab initio calculations of the pressure-induced structural phase transitions for four II-VI compounds. **Phys. Rev. B** 55: 13025.

- Dal Corso, A., Pasquarello, A., Baldereschi, A., and Car, R. (1996). Generalized-gradient approximations to density-functional theory: A comparative study for atoms and solids. **Phys. Rev. B** 53: 1180.
- Decremps, F., Zhang, J., Li, B., and Liebermann, R. C. (2001). Pressure-induced softening of shear modes in ZnO. **Phys. Rev. B** 63: 224105.
- Decremps, F., Pellicer-Porres, J., Datchi, F., Itié, J. P., Polian, A., Baudelet, F., and Jiang, J. Z. (2002). Trapping of cubic ZnO nanocrystallites at ambient conditions. **Appl. Phys. Lett.** 81: 4820-4822.
- Decremps, F., Datchi, F., Saitta, A. M., Polian, A., Pascarelli, S., Di Cicco, A., Itié, J. P., and Baudelet, F. (2003). Local structure of condensed zinc oxide. **Phys. Rev. B** 68: 104101-104110.
- Desgreniers, S. (1998). High-density phases of ZnO: Structural and compressive parameters. **Phys. Rev. B** 58: 14102-14105.
- Durandurdu, M. (2007). Ab initio simulations of the structural phase transformation of 2H-SiC at high pressure. **Phys. Rev. B** 75: 235204-7.
- Elliott, S. (1998). **The Physics and Chemistry of Solids**. Chichester, England: John Wiley & Sons.
- Fahy, S., Louie, S. G., and Cohen, M. L. (1986). Pseudopotential total-energy study of the transition from rhombohedral graphite to diamond. **Phys. Rev. B** 34: 1191.
- Filippi, C., Singh, D. J., and Umrigar, C. J. (1994). All-electron local-density and generalized-gradient calculations of the structural properties of semiconductors. **Phys. Rev. B** 50: 14947.
- Furthmüller, J., Hahn, P. H., Fuchs, F., and Bechstedt, F. (2005). Band structures and optical spectra of InN polymorphs: Influence of quasiparticle and excitonic effects. **Phys. Rev. B** 72: 14.

- Gell-Mann, M. and Brueckner, K. A. (1957). Correlation energy of an electron gas at high density. **Phys. Rev.** 106: 364-368.
- Grunwald, M., Rabani, E., and Dellago, C. (2006). Mechanisms of the wurtzite to rocksalt transformation in CdSe nanocrystals. **Phys. Rev. Lett.** 96: 255701.
- Hatch, D. M., Stokes, H. T., Dong, J. J., Gunter, J., Wang, H., and Lewis, J. P. (2005). Bilayer sliding mechanism for the zinc-blende rocksalt transition in SiC. **Phys. Rev. B** 71: 9.
- Heussinger, C. and Frey, E. (2006). Floppy modes and nonaffine deformations in random fiber networks. **Phys. Rev. Lett.** 97: 105501-4.
- Hohenberg, P. and Kohn, W. (1964). Inhomogeneous electron gas. **Phys. Rev.** 136: B864.
- Jaffe, J. E. and Hess, A. C. (1993). Hartree-Fock study of phase changes in ZnO at high pressure. **Phys. Rev. B** 48: 7903-7909.
- Jaffe, J. E., Snyder, J. A., Lin, Z., and Hess, A. C. (2000). LDA and CGA calculations for high-pressure phase transition in ZnO and MgO. **Phys. Rev. B** 62: 1660-1665.
- Jiang, J. Z., Olsen, J. S., Gerward, L., Frost, D., Rubie, D., and Peyronneau, J. (2000). Structural stability in nanocrystalline ZnO. **Europhys. Lett.** 50: 48-53.
- Jones, R. O. and Gunnarsson, O. (1989). The density functional formalism, its applications and prospects. **Rev. Mod. Phys.** 61: 689.
- Kamitani, K., Grimsditch, M., Nipko, J. C., Loong, C. K., Okada, M., and Kimura, I. (1997). The elastic constants of silicon carbide: A Brillouin-scattering study of 4H and 6H SiC single crystals. **J. Appl. Phys.** 82: 3152-3154.
- Karch, K., Bechstedt, F., Pavone, P., and Strauch, D. (1996). Pressure-dependent properties of SiC polytypes. **Phys. Rev. B** 53: 13400.

- Karzel, H., Potzel, W., Köfferlein, M., Schiessl, W., Steiner, M., Hiller, U., Kalvius, G. M., Mitchell, D. W., Das, T. P., Blaha, P., Schwarz, K., and Pasternak, M. P. (1996). Lattice dynamics and hyperfine interactions in ZnO and ZnSe at high external pressures. **Phys. Rev. B** 53: 11425.
- Klein, A., Singh, D. J., and Umrigar, C. J. (1995). All-electron study of gradient corrections to the local-density functional in metallic systems. **Phys. Rev. B** 51: 4105.
- Kim, K., Lambrecht, W. R. L., and Segall, B. (1994). Electronic structure of GaN with strain and phonon distortions. **Phys. Rev. B** 50: 1502.
- Kim, K., Lambrecht, W. R. L., and Segall, B. (1996). Elastic constants and related properties of tetrahedrally bonded BN, AlN, GaN, and InN. **Phys. Rev. B** 53: 16310.
- Kittel, C. (1996). **Introduction to Solid State Physics**. United States of America: Cambridge University Press; John Wiley & Sons, Inc.
- Kleinman, L. and Bylander, D. M. (1982). Efficient form for model pseudopotentials. **Phys. Rev. Lett.** 48: 1425.
- Kohn, W. and Sham, L. J. (1965). Self-consistent equations including exchange and correlation effects. **Phys. Rev.** 140: A1133.
- Kresse, G. and Furthmüller, J. (1996a). Efficiency of ab-initio total energy calculations for metals and semiconductors using a plane-wave basis set. **Comp. Mater. Sci.** 6: 15-50.
- Kresse, G. and Furthmüller, J. (1996b). Efficient iterative schemes for ab-initio total energy calculations using a plane-wave basis set. **Phys. Rev. B** 54: 11169.

- Kresse, G. and Hafner, J. (1994). Norm-conserving and ultrasoft pseudopotentials for first row and transition elements. **J. Phys.: Cond. Matter** 6: 8245.
- Kulkarni, A. J., Zhou, M., Sarasamak, K., and Limpijumnong, S. (2006). Novel phase transformation in ZnO nanowires under tensile loading. **Phys. Rev. Lett.** 97: 105502-1-4.
- Kulkarni, A. J., Sarasamak, K., Limpijumnong, S., and Zhou, M. (2007). Characterization of novel pseudoelastic behavior of zinc oxide nanowires. **Phil. Mag.** 87: 2117-2134.
- Kumar, R. S., Cornelius, A. L., and Nicol, M. F. (2007). Structure of nanocrystalline ZnO up to 85 GPa. **Current Appl. Phys.** 7: 135.
- Kusaba, K., Syono, Y., and Kikegawa, T. (1999). Phase transition of ZnO under high pressure and temperature. **Proc. Japan Acad. Ser. B** 75: 1.
- Lada, M., Cullis, A. G., Parbrook, P. J., and Hopkinson, M. (2003). Metastable rocksalt phase in epitaxial GaN on sapphire. **Appl. Phys. Lett.** 83: 2808-2810.
- Lei, L., He, D., Zou, Y., Zhang, W., Wang, Z., Jiang, M., and Du, M. (2008). Phase transitions of LiAlO₂ at high pressure and high temperature. **J. Solid. State. Chem.** 181: 1810-1815.
- Li, X., Kobayashi, T., Zhang, F., Kimoto, K., and Sekine, T. (2004) A new high pressure phase of LiAlO₂. **J. Solid. State. Chem.** 177: 1939.
- Limpijumnong, S. and Lambrecht, W. R. L. (2001a). Homogeneous strain deformation path for the wurtzite to rocksalt high-pressure transition in GaN. **Phys. Rev. Lett.** 86: 91-94.
- Limpijumnong, S. and Lambrecht, W. R. L. (2001b). Theoretical study of the relative stability of wurtzite and rocksalt phases in MgO and GaN. **Phys. Rev. B** 63: 104103.

- Limpijumnong, S. and Jungthawan, S. (2004). First-principles study of the wurtzite-to-rocksalt homogeneous transformation in ZnO: A case of a low-transformation barrier. **Phys. Rev. B** 70: 054104.
- Malashevich, A. and Vanderbilt, D. (2007). First-principles study of polarization in $\text{Zn}_{1-x}\text{Mg}_x\text{O}$. **Phys. Rev. B** 75: 45106.
- Marezio, M. (1965). The crystal structure and anomalous dispersion of $\gamma\text{-LiAlO}_2$. **Acta Crystallographica** 19: 396.
- Marezio, M. and Remeika, J.P. (1966). Polymorphism of LiMO_2 compounds and high-pressure single-crystal synthesis of LiBO_2 . **J. Chem. Phys.** 44: 3348 – 3353.
- Martin, R. M. (2004). **Electronic Structure: Basic Theory and Practical Methods**. United Kingdom: Cambridge University Press.
- Methfessel, M. (1988). Elastic constants and phonon frequencies of Si calculated by a fast full-potential linear-muffin-tin-orbital method. **Phys. Rev. B** 38: 1537.
- Methfessel, M., Rodriguez, C. O., and Andersen, O. K. (1989). Fast full-potential calculations with a converged basis of atom-centered linear muffin-tin orbitals: Structural and dynamic properties of silicon. **Phys. Rev. B** 40: 2009.
- Methfessel, M., van Schilfgaarde, M., and Casali, R. (2000). A full-potential LMTO method based on smooth Hankel functions. **Electronic Structure and Physical Properties of Solids: the Uses of the LMTO Method**. edited by H. Dreyse, lecture notes in physics. 535.
- Meyer, B. (2006). The pseudo plane wave approach. **John von Neumann Institute for Computing**. 31, 71-83.

- Miao, M. S. and Lambrecht, W. R. L. (2003). Unified path for high-pressure transitions of SiC polytypes to the rocksalt structure. **Phys. Rev. B** 68: 092103.
- Monkhorst, H. J. and Pack, J. D. (1976). Special points for Brillouin-zone integrations. **Phys. Rev. B** 13: 5188.
- Mujica, A., Rubio, A., Muñoz, A., and Needs, R. J. (2003). High-pressure phases of group-IV, III-V, and II-VI compounds. **Rev. Mod. Phys.** 75: 863.
- Murnaghan, F. D. (1944). The compressibility of media under extreme pressures. *Proceedings of the National Academy of Sciences* 30: 4.
- Nozieres, P and Pines, D. (1966). **The Theory of Quantum Liquids. I**. New York: Benjamin.
- Ortiz, G. (1992). Gradient-corrected pseudopotential calculations in semiconductors. **Phys. Rev. B** 45: 11328.
- Osamura, K., Naka, S., and Murakami, Y. (1975). Preparation and optical properties of $\text{Ga}_{1-x}\text{In}_x\text{N}$ thin films. **J. Appl. Phys.** 46: 3432-3437.
- Ozgur, U., Alivov, Y. I., Liu, C., Teke, A., Reshchikov, M. A., Dogan, S., Avrutin, V., Cho, S. J., and Morkoc, H. (2005). A comprehensive review of ZnO materials and devices. **J. Appl. Phys.** 98: 041301-103.
- Pan, Z. W., Dai, Z. R., and Wang, Z. L. (2001). Nanobelts of semiconducting oxides. **Science** 291: 1947-1949.
- Parr. G.R. and Yang, W. (1989). **Density-Functional Theory of Atoms and Molecules**. The United States of America: Oxford University Press.
- Phillips, J. C. (1970). Ionicity of the chemical bond in crystals. **Rev. Mod. Phys.** 42: 317.

- Polian, A., Grimsditch, M., and Grzegory, I. (1996). Elastic constants of gallium nitride. **J. Appl. Phys.** 79: 3343-3344.
- Rabani, E. (2002). An interatomic pair potential for cadmium selenide. **J. Chem. Phys.** 116: 258-262.
- Recio, J. M., Blanco, M. A., and Luana, V. (1998). Compressibility of the high-pressure rocksalt phase of ZnO. **Phys. Rev. B** 58: 8949-8954.
- Sarasamak, K., Kulkarni, A. J., Zhou, M., and Limpijumnong, S. (2008). Stability of wurtzite, unbuckled wurtzite, and rocksalt phases of SiC, GaN, InN, ZnO, and CdSe under loading of different triaxialities. **Phys. Rev. B.** 77: 024104..
- Saitta, A. M. and Decremps, F. (2004). Unifying description of the wurtzite-to-rocksalt phase transition in wide-gap semiconductors: The effect of d electrons on the elastic constants. **Phys. Rev. B** 70: 035214.
- Schultz, P. A., and Stechel, E. B., (1998), Effects of basis set quality on the prediction of structures, energies, and properties of amorphous tetrahedral carbon. **Phys. Rev. B** 57: 3295.
- Serrano, J., Rubio, A., Hernandez, E., Munoz, A., and Mujica, A. (2000). Theoretical study of the relative stability of structural phases in group-III nitrides at high pressures. **Phys. Rev. B** 62: 16612-16623.
- Serrano, J., Romero, A. H., Manjon, F. J., Lauck, R., Cardona, M., and Rubio, A. (2004). Pressure dependence of the lattice dynamics of ZnO: an *ab initio* approach. **Phys. Rev. B** 69: 094306-1-14.
- Shan, W., Hauenstein, R. J., Fischer, A. J., Song, J. J., Perry, W. G., Bremser, M. D., Davis, R. F., and Goldenberg, B. (1996). Strain effects on excitonic transitions in GaN: deformation potentials. **Phys. Rev. B** 54: 13460.

- Takizawa, K. and Hagiwara, A. (2002). The transformation of LiAlO_2 crystal structure in molten Li/K carbonate. **J. Power Sources** 109: 127.
- Tinder, F. R. (2008). **Tensor Properties of Solids: Phenomenological Development of the Tensor Properties of Crystals**. Morgan & Claypool.
- Ueno, M., Yoshida, M., Onodera, A., Shimomura, O., and Takemura, K. (1994). Stability of the wurtzite-type structure under high pressure: GaN and InN. **Phys. Rev. B** 49: 14.
- Vanderbilt, D. (1990). Soft self-consistent pseudopotentials in generalized eigenvalue formalism. **Phys. Rev. B** 41: 7892.
- Wang, J., Kulkarni, A. J., Sarasamak, K., Limpijumnong, S., Ke, F. J., and Zhou, M. (2007). Molecular dynamics and density functional studies of a body-centered-tetragonal polymorph of ZnO. **Phys. Rev. B** 76: 172103.
- Wang, X., Che, S.-B., Ishitani, Y., and Yoshikawa, A. (2006). Experimental determination of strain-free Raman frequencies and deformation potentials for the E_2 high and $A_1(\text{LO})$ modes in hexagonal InN. **Appl. Phys. Lett.** 89: 171907.
- Wang, Y. L., Cui, H. L., Yu, B. R., and Chen, X. R. (2008). First-principle calculations of elastic properties of wurtzite-type aluminum nitride under pressure. **Commun. Theor. Phys.** 49: 4.
- Wang, Z., Finkelstein, K., Ma, C., and Wang, Z. L. (2007). Structure stability, fracture, and tuning mechanism of CdSe nanobelts. **Appl. Phys. Lett.** 90: 113115.
- Wang, Z., Zu, X., Yang, L., Gao, F., and Weber, W. J. (2007). Atomistic simulations of the size, orientation, and temperature dependence of tensile behavior in GaN nanowires. **Phys. Rev. B** 76: 045310-9.

- Wickham, J. N., Herhold, A. B., and Alivisatos, A. P. (2000). Shape change as an indicator of mechanism in the high-pressure structural transformations of CdSe nanocrystals. **Phys. Rev. Lett.** 84: 923.
- Wright, A. F. (1997). Elastic properties of zinc-blende and wurtzite AlN, GaN, and InN. **J. Appl. Phys.** 82: 2833-2839.
- Wolfram Quester Source [On-line] Available: <http://en.wikipedia.org/wiki/File:SketchPseudopotentials.png>
- Wu, X., Wu, Z., Guo, L., Liu, C., Liu, J., Li, X., and Xu, H. (2005). Pressure-induced phase transformation in controlled shape ZnO nanorods. **Solid State Comm.** 135: 780-784.
- Xia, H., Xia, O., and Ruoff, A. L. (1993). High-pressure structure of gallium nitride: Wurtzite-to-rocksalt phase transition. **Phys. Rev. B** 47: 12925.
- Xia, Q., Xia, H., and Ruoff, A. L. (1994). New crystal structure of indium nitride: a pressure-induced rocksalt phase. **Mod. Phys. Lett. B** 8: 345.
- Xie, Y., Qian, Y., Zhang, S., Wang, W., Liu, X., and Zhang, Y. (1996). Coexistence of wurtzite GaN with zinc blende and rocksalt studied by x-ray power diffraction and high-resolution transmission electron microscopy. **Appl. Phys. Lett.** 69: 334-336.
- Xu, K., Xu, J., Deng, P., Zhou, Y., Zhou, G., Qui, R., and Fang, Z. (1998). γ -LiAlO₂ single crystal: a novel substrate for GaN epitaxy. **J. Crystal. Growth.** 193: 127.
- Yoshida, M., Onodera, A., Ueno, M., Takemura, K., and Shimomura, O. (1993). Pressure-induced phase transition in SiC. **Phys. Rev. B** 48: 10587.
- Yeh, C.-Y., Lu, Z. W., Froyen, S., and Zunger, A. (1992). Zinc-blende-wurtzite polytypism in semiconductors. **Phys. Rev. B** 46: 10086.

- Zaoui, A. and Sekkal, W. (2002). Pressure-induced softening of shear modes in wurtzite ZnO: A theoretical study. **Phys. Rev. B** 66: 174106 1-6.
- Zhang, L. and Huang, H. (2006). Young's moduli of ZnO nanoplates: ab initio determinations. **Appl. Phys. Lett.** 89: 183111.
- Zhang, L. and Huang, H. (2007). Structural transformation of ZnO nanostructures. **Appl. Phys. Lett.** 90: 023115.
- Zaoui, A. and Sekkal, W. (2002). Pressure-induced softening of shear modes in wurtzite ZnO: A theoretical study. **Phys. Rev. B** 66: 174106.

APPENDIX

APPENDIX

PUBLICATIONS AND PRESENTATIONS

1. List of publications

Kulkarni, A. J., Zhou, M., Sarasamak, K., and Limpijumnong, S. (2006). Novel phase transformation in ZnO nanowires under tensile loading. **Phys. Rev. Lett.** 97: 105502.

Kulkarni, A. J., Sarasamak, K., Limpijumnong, S., and Zhou, M. (2007). Characterization of novel pseudoelastic behaviour of zinc oxide nanowires. **Philos. Mag.** 87: 2117.

Wang, J., Kulkarni, A. J., Sarasamak, K., Limpijumnong, S., Ke, F. J., and Zhou, M. (2007). Molecular dynamics and density functional studies of a body-centered-tetragonal polymorph of ZnO. **Phys. Rev. B** 76: 172203.

Sarasamak, K., Kulkarni, A. J., Zhou, M., and Limpijumnong, S. (2008). Stability of wurtzite, unbluckled wurtzite and rocksalt phases of SiC, GaN, InN, ZnO and CdSe under loading of different triaxialities. **Phys. Rev. B** 77: 024104.

Kulkarni, A. J., Sarasamak, K., Wang, J., Ke, F. J., Limpijumnong, S., and Zhou, M. (2008). Effect of load triaxiality on polymorphic transitions in zinc oxide, **Mech. Res. Commun.** 35: 73.

2. List of presentations (oral)

Sarasamak, K., Kulkarni, A. J., Zhou, M., and Limpijumnong, S. (March 2007). Novel phase of ZnO nanowires under tension. In **Siam Physics Congress 2007**. Nakhon Pathom: Thai Physics Society.

Sarasamak, K., Kulkarni, A. J., Zhou, M., and Limpijumnong, S. (March 2008) High stress phases of SiC, GaN, InN, ZnO and CdSe. In **APS March Meeting 2008**. New Orleans, Louisiana, USA: American Physical Society.

Sarasamak, K., Kulkarni, A. J., Wang, J., Ke, F. J., Limpijumnong, S. (April 2009). Stability of wurtzite, unbluckled wurtzite, rocksalt, and BCT-4 phases of ZnO under different loading conditions. In **RGJ Ph.D. Congress X**. Chonburi: The Thailand Research Fund.

3. List of presentation (poster)

Sarasamak, K., Kulkarni, A. J., Zhou, M., and Limpijumnong, S. (March 2007). Crystal structures of SiC, GaN, InN, ZnO, and CdSe under different stress directions. In **Siam Physics Congress 2009**. Phetchburi: Thai Physics Society.

Novel Phase Transformation in ZnO Nanowires under Tensile Loading

Ambarish J. Kulkarni,¹ Min Zhou,^{1,*} Kanoknan Sarasamak,² and Sukit Limpijumnong²¹The George W. Woodruff School of Mechanical Engineering, Georgia Institute of Technology, Atlanta, Georgia 30332-0405, USA²School of Physics, Suranaree University of Technology and National Synchrotron Research Center, Nakhon Ratchasima, Thailand
(Received 18 April 2006; revised manuscript received 18 June 2006; published 7 September 2006)

We predict a previously unknown phase transformation from wurtzite to a graphitelike ($P6_3/mmc$) hexagonal structure in $[0110]$ -oriented ZnO nanowires under uniaxial tensile loading. Molecular dynamics simulations and first principles calculations show that this structure corresponds to a distinct minimum on the enthalpy surfaces of ZnO for such loading conditions. This transformation is reversible with a low level of hysteretic dissipation of 0.16 J/m^3 and, along with elastic stretching, endows the nanowires with the ability to recover pseudoelastic strains up to 15%.

DOI: 10.1103/PhysRevLett.97.105502

PACS numbers: 61.50.Ks, 61.46.-w, 62.25.+g, 64.70.Nd

The assumption of crystal structures by a material reflects a complex interplay of intrinsic factors such as composition, band structure, valence electrons, bonding states, and structural symmetry and extrinsic factors such as temperature and loading. A change in any of these factors may trigger a transformation to a different structure, giving rise to polymorphism which is especially pronounced in compounds such as ZnO whose electronic bonding states show significant dependence on applied loading [1]. There are three hitherto well-known polymorphs of ZnO, including wurtzite (WZ, $P6_3mc$ space group), zinc blende (ZB, $F\bar{4}3m$) and rock salt (RS, $Fm\bar{3}m$) [2]. WZ is the most stable and commonly observed phase under ambient pressure. ZB can be obtained only on cubic surfaces under specific growth conditions. RS is the result of a transformation from WZ at pressures between 8–10 GPa [1,3–8]. This pressure-induced reversible transformation has received significant consideration primarily because hydrostatic compression is the most likely mode of loading for bulk ZnO. Recent work on GaN, MgO, and ZnO thin films has revealed a previously unknown unbuckled structure resulting from extensive surface reconstructions to suppress surface polarity [9–12]. So far, the existence of polymorphs other than WZ, ZB, and RS at various loading triaxialities has not been extensively studied.

Recent synthesis of quasi-1D nanostructures such as ZnO nanowires, nanobelts, and nanorods necessitates understanding of the response of ZnO to uniaxial tensile loading [13–15]. Since these nanostructures are single-crystalline and nearly defect-free, they are endowed with high strengths and the ability to undergo large deformations without failure. Also, their high surface-to-volume ratios enhance atomic mobility and promote phase transformations under loading along certain crystalline directions.

Here, we report a novel phase transformation from WZ to an unbuckled wurtzite phase (hexagonal, hereafter denoted as HX) within the $P6_3/mmc$ space group during uniaxial tensile loading of $[0110]$ -oriented ZnO nanowires [Fig. 1(a)]. This structure bears both resemblance to and distinction from the layered structure (LY) [9–12]; see

Fig. 1(c) which compares charge density distributions on the $(11\bar{2}0)$ planes of WZ, HX, and LY. The resemblance is in crystallography and the distinction is in coordination. Specifically, a strong bond along the $[0001]$ axis is seen in HX which occurs throughout the solid wires. In contrast, this interplanar bond is absent in LY, which extends only a few layers from the surface beneath which the structure is predominantly WZ. Therefore, despite the similar geomet-

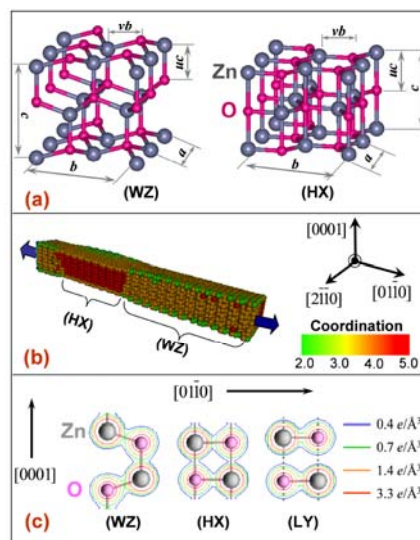


FIG. 1 (color online). (a) Wurtzite (WZ) and newly discovered hexagonal (HX) crystal structures, (b) nanowire with HX and WZ phases [transformation in progress under tensile loading (point C in Fig. 2 with a strain of 5.9%)]; and (c) charge density plots on the $(11\bar{2}0)$ planes of WZ, HX, and the layered structure (LY) reported in Refs. [9,10].

ric symmetries, HX has a higher coordination number (5) than LY (3). A similar HX phase has been reported as the natural state of boron nitride (*h*-BN) [16]. It has also been predicted as a metastable state of GaN during the WZ \rightarrow RS transformation at high pressures [17] and as a stable phase of MgO under hydrostatic tensile loading [18].

The deformation analysis here uses a quasistatic loading scheme within the molecular dynamics (MD) framework ([19]) and a Buckingham potential with charge interactions [20,21]. The parameters of the potential are the same as those in Ref. [22] and have been shown to accurately predict the lattice, elastic, and dielectric constants along with surface and defect properties of ZnO [20,22,23]. The nanowire considered has an initial WZ structure with [0110] growth orientation and (2110) and (0001) lateral surfaces. The lateral dimensions are 21.22×18.95 , 31.02×29.42 , or 40.81×39.89 Å. Under applied tensile stress (σ_b) along the wire axis, gradual transformation into the HX phase occurs. Figure 1(b) shows a partially transformed 21.22×18.95 Å wire containing both WZ and HX phases. To ascertain the relative energetic favorability of the two phases under loading, their enthalpies are independently determined using first principles calculations which are based on the density functional theory (DFT) as implemented in the VASP code [24], with local density approximation and ultrasoft pseudopotentials [25]. Computational parameters such as energy cutoff and sampling k points are the same as those in Ref. [7] which focused on the WZ \rightarrow RS transformation of ZnO and yielded lattice parameters, bulk modulus, and equilibrium transformation pressure that are in good agreement with experiments. For comparison, the emergence of HX as a stable phase under compressive loading (σ_c) along the [0001] axis is also shown.

We first characterize crystallographic changes associated with the transformation. As shown for the WZ lattice in Fig. 1(a), three parameters (a , c , and u) are typically used to define hexagonal structures, with uc denoting the offset between the Zn and O basal planes. Additional parameters b and v , with vb being the offset between Zn and O atoms along the [0110] axis, are introduced to

delineate the difference between the HX and RS structures [7,17]. a , b , and c are the dimensions of the hexagonal unit cell along the [2110], [0110], and [0001] directions, respectively. Table I lists the lattice constants for WZ, HX, and RS structures. Note that the parameters for relaxed wires deviate slightly from the values for ideal bulk WZ due to surface effects [19,26]. For HX, $c = 4.35$ Å and $u = 0.50$ are similar to those for RS; whereas $a = 3.34$ Å and $v = 0.32$ are similar to those for WZ. Since v remains unchanged, HX has the same hexagonal symmetry around the c axis as WZ. During the transformation, u changes from its initial value of 0.38 for WZ to a value of 0.5 for HX (Table I), implying the flattening of the buckled wurtzite basal plane (Zn and O atoms becoming coplanar). As a result, Zn atoms are at equal distances from O atoms along the [0001] axis and the structure acquires the additional symmetry of a mirror plane perpendicular to the [0001] axis. This process occurs while the orientation of the basal plane remains invariant. The in-plane coordination of the HX structure is threefold and the full 3D coordination is fivefold (as compared to the fourfold in WZ). The formation of additional bonds (therefore the increase in coordination) along the [0001] axis can also be seen in the charge density distributions on (1120) planes in Fig. 1(c). Obviously, an additional bond is formed between the Zn atom initially at the top left and the O atom initially at the bottom in the WZ structure. However, the charge density map for LY observed in [9,10] does not display such a strong intraplane molecular bond and the layers therein are only held together by Coulombic forces between Zn and O ions. Consequently, LY has a threefold in-plane coordination. The unusual fivefold coordination and uniform charge distribution around the atoms in HX and its crystallographic similarity to RS suggest that the WZ \rightarrow HX transformation observed here progresses toward an ionic bonding state with a higher coordination.

Figure 2 shows the tensile stress-strain (σ - ϵ) response of a nanowire with a 21.22×18.95 Å cross-section at 100 K. While only data for a particular wire size and temperature is shown here, the transformation and the characteristics of the σ - ϵ relation are the same for wires with lateral dimen-

TABLE I. Lattice parameters for WZ, HX, and RS under different loading conditions. Select values are highlighted in boldface for easy comparison across different structures.

Parameters	WZ					HX			RS
	DFT $\sigma_b = 0$ GPa	AP ^a $\sigma_b = 0$ GPa	EXP ^b $\sigma_b = 0$ GPa	DFT $\sigma_b = 10$ GPa	DFT $\sigma_c = -6$ GPa	AP ^a $\sigma_b = 10$ GPa	DFT $\sigma_b = 10$ GPa	DFT $\sigma_c = -6$ GPa	DFT $p = 8.22$ GPa
a (Å)	3.20	3.22	3.25	3.12	3.28	3.34	3.29	3.49	4.16
b (Å)	5.54	5.66	5.63	5.93	5.68	6.24	6.42	6.03	4.16
v	0.33	0.32	0.33	0.33	0.34	0.32	0.32	0.33	0.50
c (Å)	5.15	5.30	5.21	5.00	4.92	4.35	4.18	4.18	4.16
u	0.38	0.41	0.38	0.39	0.39	0.50	0.50	0.50	0.50
b/a	1.73	1.76	1.73	1.90	1.73	1.87	1.95	1.73	1.00
c/a	1.61	1.65	1.60	1.60	1.50	1.30	1.27	1.20	1.00

^aAnalytical Potential

^bExperiment [22]

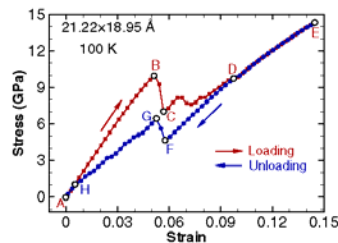


FIG. 2 (color online). Tensile stress-strain response of a $21.22 \times 18.95 \text{ \AA}$ nanowire at 100 K during loading-unloading. The hysteresis loop is relatively small.

sions between 18–40 Å and temperatures between 100–1200 K [27]. The region between *A* and *B* corresponds to elastic stretching of the WZ structure. Loading beyond *B* results in a stress drop from 10.02 to 6.98 GPa (*B* → *C*) at $\epsilon = 5.14\%$. This softening behavior corresponds to the nucleation of the HX phase. At this stage, *u* shows a precipitous change to 0.5 and the Zn and O basal planes become coplanar. As the deformation progresses, the transformed region sweeps through the entire wire length (*C* → *D*) and the transformation completes at $\epsilon = 9.71\%$ ($\sigma = 9.65 \text{ GPa}$). Further deformation occurs through the elastic stretching of the transformed structure (HX) and ultimate fracture occurs at $\epsilon = 16\%$ ($\sigma = 15.29 \text{ GPa}$, not shown) through cleavage along {1210} planes. Unloading from any strain prior to the initiation of failure, e.g., point *E* with $\epsilon = 14.5\%$, is first associated with the recovery of the elastic deformation within the HX structure (*E* → *F*). A reverse transformation from HX to WZ (*F* → *G* → *H*) initiates at $\epsilon = 5.77\%$ ($\sigma = 4.59 \text{ GPa}$, point *F*) and completes at $\epsilon = 0.6\%$ ($\sigma = 1.15 \text{ GPa}$, point *H*). Unloading beyond *H* occurs through elastic deformation within the WZ structure (*H* → *A*). Strains up to 14.5% can be recovered, highlighting a very unusual aspect of the behavior of ZnO which normally is quite brittle. Obviously, the large recoverable strains observed here are associated with a unique structural transformation process which occurs only in [0110] nanowires under uniaxial tensile loading. The energy dissipation associated with the stress-strain hysteresis loop is $\sim 0.16 \text{ J/m}^3$, much lower than that for the WZ → RS transformation in bulk ($\sim 1.38 \text{ J/m}^3$ with a maximum recoverable volumetric strain of 17% in compression) [3]. This low level of energy dissipation limits heat generation and heat-related damage, making the nanowires better suited for service under conditions of cyclic loading and large strains. It is important to point out that nanowires with other growth directions (e.g., [0001]) do not show such a phase transformation and are relatively brittle with failure strains not more than $\sim 7\%$.

To identify stable crystalline structures under uniaxial tensile loading along the [0110] direction, we obtained their enthalpy as a function of c/a and b/a for specific

values of stress using DFT calculations. Since the transformation proceeds with the Zn and O basal planes becoming coplanar and a corresponding reduction in c , we also explored the stability of the HX phase under compression along the [0001] axis. The enthalpy per unit cell (2 Zn-O pairs) under applied loading is given by

$$H(c/a, b/a) = E(c, b, a, u, v) - f_i q_i, \quad (1)$$

where E is the internal energy, $f_i q_i$ (summation not implied) is the external work, and f_i is the uniaxial force per unit cell. For tension along the b axis, $i = b$, $f_b = \sigma_b \times (ac)$, and $q_b = b$. For compression along the c axis, $i = c$, $f_c = \sigma_c \times (ab)$, and $q_c = c$. For each pair of c/a and b/a , u, v , and unit cell size a (thus the volume) are allowed to relax to minimize H . The minima of the $H(c/a, b/a)$ surface so obtained correspond to stable crystal structures under the applied stress.

Figure 3 shows the enthalpy surfaces (eV/unit cell) for $\sigma_b = 7, 10$, and 13 GPa (with $\sigma_c = 0 \text{ GPa}$) and $\sigma_c = -6 \text{ GPa}$ (with $\sigma_b = 0 \text{ GPa}$). In each case, there are two minima. For the tensile loading, the first minimum (${}^b H_{\text{min}}^{\text{WZ}}$) is in the vicinity of $c/a \approx 1.6$ and $b/a \approx 1.9$; for the compressive loading, the first minimum (${}^c H_{\text{min}}^{\text{WZ}}$) is in the vicinity of $c/a \approx 1.5$ and $b/a = 1.732$; each corresponding to a WZ structure with lattice parameters slightly different from those at zero stress (Table I). The second minimum in each of these plots corresponds to the HX phase. For the tensile loading, the second minimum (${}^b H_{\text{min}}^{\text{HX}}$) is in the vicinity of $c/a \approx 1.3$ and $b/a \approx 1.9$;

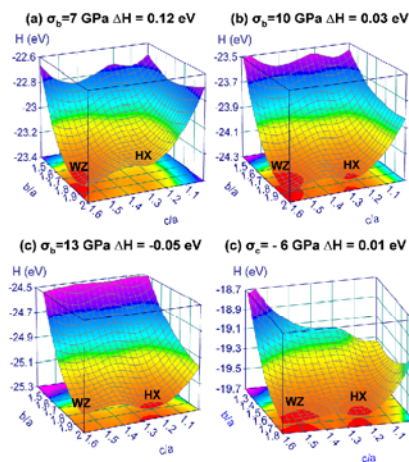


FIG. 3 (color online). Enthalpy surface maps from DFT calculations for uniaxial tensile stress of (a) $\sigma_b = 7 \text{ GPa}$, (b) $\sigma_b = 10 \text{ GPa}$ and (c) $\sigma_b = 13 \text{ GPa}$ along the b axis and uniaxial compressive stress of (d) $\sigma_c = -6 \text{ GPa}$ along the c axis.

for the compressive loading, the second minimum (${}^c H_{\min}^{\text{HX}}$) is in the vicinity of $c/a \approx 1.2$ and $b/a = 1.732$. The structure at ${}^b H_{\min}^{\text{HX}}$ is that observed in the MD simulations discussed earlier. The difference in lattice parameters obtained from the two modes of loading stems from the fact that the ratio b/a is locked at 1.732 by structural symmetry under compression along the [0001] axis.

At a tensile stress of 7 GPa [Fig. 3(a)], ${}^b H_{\min}^{\text{WZ}}$ is much lower than ${}^b H_{\min}^{\text{HX}}$ ($\Delta H^b = {}^b H_{\min}^{\text{HX}} - {}^b H_{\min}^{\text{WZ}} = 0.12$ eV), hence, no transformation takes place. As the stress is increased to 10 GPa, ${}^b H_{\min}^{\text{HX}}$ and ${}^b H_{\min}^{\text{WZ}}$ become comparable ($\Delta H^b = 0.03$ eV) and consequently both WZ and HX are equally favored. At an applied stress of 13 GPa [Fig. 3(c)], ${}^b H_{\min}^{\text{HX}}$ is lower than ${}^b H_{\min}^{\text{WZ}}$ ($\Delta H^b = -0.05$ eV), indicating that HX is more stable. The transformation barrier between the two phases of 0.06 eV (0.05 eV if calculated using the analytic potential) is quite low, compared with the barrier of ~ 0.15 eV for the high pressure WZ \rightarrow RS transformation [7]. A similar behavior is observed under uniaxial compression along the [0001] direction. The WZ and HX enthalpy wells are comparable at $\sigma_c = -6$ GPa [$\Delta H^c = 0.01$ eV, Fig. 3(d)]. At higher compressive stresses, ${}^c H_{\min}^{\text{HX}}$ is lower than ${}^c H_{\min}^{\text{WZ}}$, indicating the relative favorability of HX under such conditions. As the magnitude of either σ_c or σ_b is increased above the corresponding equilibrium transition value, HX becomes more stable and the transformation barrier becomes even lower, resulting in an even higher driving force for transformation. In summary, the distinct minima in the vicinities of the HX and WZ structures on the enthalpy maps obtained through DFT calculations confirm what is discovered in MD calculations by pointing out that (1) HX is energetically favored over WZ above a critical applied tensile stress value of $\sigma_b \approx 10$ GPa along the [0110] direction or a critical compressive stress value of $\sigma_c \approx -6$ GPa along the [0001] direction and (2) the barrier for the transformation decreases as applied stress increases.

HX can result from either uniaxial tension along the [0110] direction or uniaxial compression along the [0001] direction because both cause interatomic distances in Zn and O basal planes to increase, creating conditions favorable for the two types of atoms to be accommodated in a single plane. This process is similar to the fcc \rightarrow bcc Bain transformation [17]. Phenomenologically, the transformation can be explained by considering the effect of structural distortion on the nature of bonding. Specifically, under the external stresses discussed, lattice parameters change and the interatomic Coulombic interactions favor ionic states of bonding over covalent states of bonding [2]. For example, hydrostatic pressure can cause the progression of WZ (moderately ionic) toward RS (highly ionic), as shown by both experiments and theoretical analyses [1, 3–8].

Since HX and WZ can have very different properties, the stress-induced phase transformation may significantly alter the response of the nanowires. Examples include the

modulation of piezoelectric constant, Seebeck coefficient, and thermal conductivity [28]. Such effects provide mechanisms for tuning the response of nanocomponents in a variety of nano-electro-mechanical systems through the application of mechanical input.

Support from NSF (No. CMS9984298), NSFC (No. 10528205), NANOTEC (No. NN49-024) and TRF (No. BRG4880015 and No. PHD/0264/2545) is acknowledged. Computations are carried out at the NAVO and ASC MSRCs.

*To whom correspondence should be addressed.

Telephone: 404-894-3294.

Fax: 404-894-0186.

Email address: min.zhou@gatech.edu

- [1] C. H. Bates, W. B. White, and R. Roy, *Science* **137**, 993 (1962).
- [2] U. Ozgur *et al.*, *J. Appl. Phys.* **98**, 041301 (2005).
- [3] S. Desgreniers, *Phys. Rev. B* **58**, 14 102 (1998).
- [4] J. E. Jaffe and A. C. Hess, *Phys. Rev. B* **48**, 7903 (1993).
- [5] J. E. Jaffe *et al.*, *Phys. Rev. B* **62**, 1660 (2000).
- [6] H. Karzel *et al.*, *Phys. Rev. B* **53**, 11 425 (1996).
- [7] S. Limpijumnong and S. Jungthawan, *Phys. Rev. B* **70**, 054104 (2004).
- [8] J. Serrano *et al.*, *Phys. Rev. B* **69**, 094306 (2004).
- [9] F. Claeysens *et al.*, *J. Mater. Chem.* **15**, 139 (2005).
- [10] C. L. Freeman *et al.*, *Phys. Rev. Lett.* **96**, 066102 (2006).
- [11] J. Goniakowski, C. Noguera, and L. Giordano, *Phys. Rev. Lett.* **93**, 215702 (2004).
- [12] R. B. Capaz, H. Lim, and J. D. Joannopoulos, *Phys. Rev. B* **51**, 17 755 (1995).
- [13] C. Q. Chen *et al.*, *Phys. Rev. Lett.* **96**, 075505 (2006).
- [14] S. X. Mao, M. Zhao, and Z. L. Wang, *Appl. Phys. Lett.* **83**, 993 (2003).
- [15] Z. L. Wang, *J. Phys. Condens. Matter* **16**, R829 (2004).
- [16] R. M. Wentzcovitch *et al.*, *Phys. Rev. B* **38**, 6191 (1988).
- [17] S. Limpijumnong and W. R. L. Lambrecht, *Phys. Rev. Lett.* **86**, 91 (2001).
- [18] S. Limpijumnong and W. R. L. Lambrecht, *Phys. Rev. B* **63**, 104103 (2001).
- [19] A. J. Kulkarni, M. Zhou, and F. J. Ke, *Nanotechnology* **16**, 2749 (2005).
- [20] D. J. Binks and R. W. Grimes, *J. Am. Ceram. Soc.* **76**, 2370 (1993).
- [21] D. Wolf *et al.*, *J. Chem. Phys.* **110**, 8254 (1999).
- [22] D. J. Binks, Ph.D. thesis, University of Surrey, Harwell, 1994.
- [23] R. W. Grimes, D. J. Binks, and A. B. Lidiard, *Philos. Mag. A* **72**, 651 (1995).
- [24] G. Kresse and J. Furthmüller, *Comput. Mater. Sci.* **6**, 15 (1996).
- [25] D. Vanderbilt, *Phys. Rev. B* **41**, 7892 (1990).
- [26] A. J. Kulkarni and M. Zhou, *Acta Mechanica Sinica* **22**, 217 (2006).
- [27] A. J. Kulkarni *et al.* (unpublished).
- [28] A. J. Kulkarni and M. Zhou, *Appl. Phys. Lett.* **88**, 141921 (2006).

Characterization of novel pseudoelastic behaviour of zinc oxide nanowires

A. J. KULKARNI[†], K. SARASAMAK[‡],
S. LIMPIJUMNONG[‡] and M. ZHOU^{*†}

[†]The George W. Woodruff School of Mechanical Engineering, Georgia Institute of Technology, Atlanta, Georgia 30332-0405, USA

[‡]School of Physics, Suranaree University of Technology and National Synchrotron Research Center, Nakhon Ratchasima, Thailand

(Received 4 October 2006; in final form 17 December 2006)

We recently reported the discovery of a novel pseudoelastic behaviour resulting from a reversible phase transformation from wurtzite ($P6_3mc$) to a novel graphite-like hexagonal ($P6_3/mmc$) structure in $[01\bar{1}0]$ -oriented ZnO nanowires under uniaxial loading [Phys. Rev. Lett. **97** 105502 (2006)]. This previously unknown phenomenon is observed in nanowires and has not been reported for bulk ZnO. In this paper, molecular dynamics simulations are carried out to characterize the tensile behaviour dominated by this transformation of nanowires with lateral dimensions of 18–41 Å over the temperature range of 100–700 K. Significant size and temperature effects on the behaviour are observed. Specifically, the critical stress for the initiation of the phase transformation, the recoverable strains associated with the pseudoelasticity and the hysteretic energy dissipation are found to be both size and temperature dependent and can vary by as much as 59%, 32% and 57%, respectively. The large recoverable strains of 10–16% are unusual for the normally rather brittle ZnO ceramic and are due to both elastic stretch and the phase transformation in the slender one-dimensional nanowires. The hysteretic energy dissipation is in the range 0.05–0.14 GJ m⁻³ per cycle and such low levels are attributed to the relatively low energy barrier for the transformation. Unlike the pseudoelasticity in fcc metal nanowires of Cu, Ni and Au, which leads to a novel shape memory effect, the pseudoelasticity quantified here does not result in a shape memory of ZnO nanowires. The primary reason is the absence of an energy barrier for the phase transformation at zero stress.

1. Introduction

Pseudoelasticity and the shape memory effect (SME) are traditionally associated with shape memory alloys and elastomers [1]. Such effects have recently been discovered in single crystalline metal nanowires as a consequence of their nanoscale dimensionality [2–5]. We have recently reported a novel pseudoelastic behaviour in $[01\bar{1}0]$ -oriented ZnO nanowires which arises from a reversible phase transformation from a tetrahedrally coordinated wurtzite (herein denoted as WZ, $P6_3mc$ space group) phase to a newly discovered graphite-like phase (herein denoted as HX,

*Corresponding author. Email: min.zhou@gatech.edu.

$P6_3/mmc$ space group) [6]. This previously unknown five-fold coordinated polymorph of ZnO can result from either tensile loading along the $[01\bar{1}0]$ direction or compressive loading along the $[0001]$ direction. For $[01\bar{1}0]$ nanowires in tension, recoverable strains, which comprise of the elastic stretching of the WZ and HX phases and a contribution from the transformation, can be up to 16%. This is quite extraordinary since ionic compound semiconductors such as ZnO, GaN, InN and BN are known to be brittle under tensile loading. While the ability to undergo a phase transformation is the primary reason for the unusual pseudoelastic behaviour, the nearly defect-free nature of these nanowires and the large surface-to-volume ratios, which enhance atomic mobility, also contribute to the wires' ability to undergo deformation without fracture. The high strengths, large recoverable strains and property variations associated with transformation make these nanowires ideal candidates for nanocomponents in a variety of nano-electromechanical systems (NEMS), such as sensors, actuators and switches. Since this pseudoelastic behaviour has just been discovered in ZnO nanowires that have only been synthesized recently, a fundamental understanding of the overall constitutive behaviour, the nature of the phase transformation and the characteristics of the transformed phase is needed in order to unleash the potential of these nanowires.

In this paper, the pseudoelastic responses of $[01\bar{1}0]$ ZnO nanowires with lateral dimensions of 21.22×18.95 , 31.02×29.42 and $40.81 \times 39.89 \text{ \AA}^2$ under quasistatic tensile loading are characterized. The characterization accounts for temperatures between 100 and 700 K. The analysis focuses on the formation of the new HX crystalline structure and the transformation path from WZ to HX under uniaxial tensile loading. In particular, the atomic motions or lattice distortion resulting in the formation of the HX structure are quantified through the gradient of a continuum deformation map. The analysis lends itself to the quantification of the recoverable strains associated with the pseudoelastic behaviour of the nanowires, including contributions from the elastic stretching of the WZ and the HX phases and lattice size change due to the phase transformation. The size and temperature dependence of important parameters, including the critical stress for the initiation of phase transformation, maximum recoverable strain and hysteretic dissipation, are also quantified.

2. Computational framework

Molecular dynamics (MD) simulations using the Buckingham potential with charge interactions [7, 8] are carried out. The nanowires considered are single-crystalline and wurtzite-structured, with lattice constants $a = 3.249 \text{ \AA}$ and $c = 5.206 \text{ \AA}$ and a growth direction along the $[01\bar{1}0]$ axis [9–11]. The wire structure is generated by repeating a wurtzite unit cell along the $[2\bar{1}\bar{1}0]$, $[0001]$ and $[01\bar{1}0]$ directions (figure 1). Three different cross-sectional sizes (21.22×18.95 , 31.02×29.42 and $40.81 \times 39.89 \text{ \AA}^2$) are considered. The smallest cross-sectional size ($21.22 \times 18.95 \text{ \AA}^2$) is chosen such that the short-range cut-off distance in the Buckingham potential [7, 8] is smaller than the smallest wire dimension and long-range interactions are properly considered [12]. Periodic boundary conditions are specified in the axial direction. Calculations with

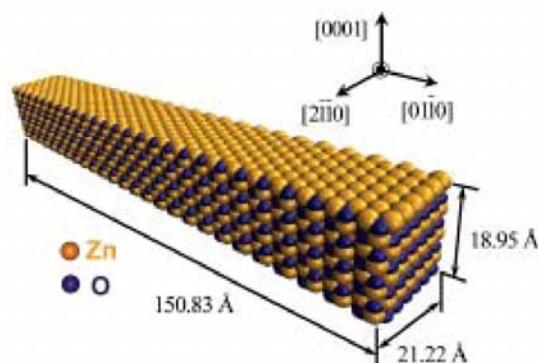


Figure 1. Configuration of a $[0\bar{1}10]$ nanowire with lateral dimensions of $21.22 \times 18.95 \text{ \AA}^2$ after geometric construction and before initial relaxation.

different computational cell sizes show that any length greater than 100 \AA , irrespective of the cross-section size, is sufficient to avoid image effects [13, 14]. Here, a periodic computational cell length of 150.83 \AA is used for all the cross-sections analyzed.

Since the crystallographically constructed nanowires may not be in equilibrium, preloading relaxations are carried out to obtain the wires' free-standing configurations. The relaxations occur at desired temperatures without external loading, until thermodynamic quantities (such as energy, stress, and temperature) indicate that statistical steady states have been reached. A relaxation time of 3 ps is found to be adequate for achieving equilibrium states for the ranges of wire size and temperature considered. During the relaxations, minimization of the wires' energy occurs through surface reconstruction and adjustment of the lattice spacing in the wire core. The surface reconstruction manifests in the forms of decreases in the interlayer spacing between outer surface layers and in-plane contractions of the surfaces [13]. Such morphological changes on surfaces and in the wires' cores are also monitored. This is especially important for nanostructures since their surface-to-volume ratios are high and extensive surface, and in some cases, core reconstructions may occur. For example, $[100]$ oriented fcc metal nanowires are known to reconstruct into $[110]$ orientations as a consequence of surface energy minimization [2, 4, 15, 16].

Following the initial relaxations, a quasistatic loading scheme is employed to effect tensile deformation and to obtain the mechanical response of the nanowires. Approximate quasistatic tensile loading in each deformation increment is achieved through successive loading and equilibration steps using a combination of algorithms for NPT and NVE ensembles [17]. Specifically in each deformation increment, stretching at a specified rate of 0.005 ps^{-1} is first carried out for 0.5 ps using a modified version of the NPT algorithm of Melchionna *et al.* [18, 19]. Subsequently, with the strain maintained constant, the nanowire is relaxed for 3 ps via an algorithm for NVE ensemble [17] at the specified temperature. This equilibration duration is chosen such that a statistically steady state is reached and no further structural

2120

A. J. Kulkarni et al.

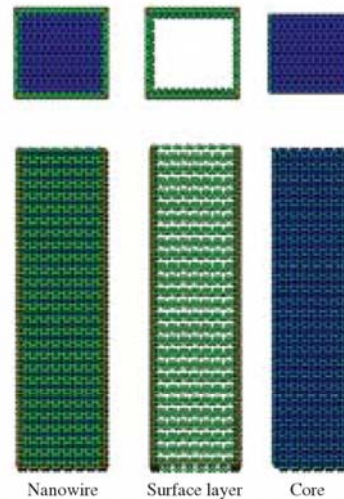


Figure 2. Decomposition of a nanowire into surface atoms and interior atoms using the coordination number (CN); the surface atoms have CNs below 4 and the core atoms have CNs equal to 4.

changes occur. It is possible that the magnitude of the strain increment in each step may affect the calculated stress-strain response. To minimize this error, calculations using series of strain increments between 0.35% and 0.1% were carried out. Based on the results, a strain increment of 0.25% and an equilibration period of 3 ps per loading step are found to minimize fluctuations in the calculated response and are used in the analysis reported. Since the loading proceeds in a series of equilibration steps, this process essentially simulates quasistatic loading of the specimen. Unloading is implemented in a similar manner with a reduction in strain for each unloading step. The virial formula is used to calculate the stress [20].

Changes in lattice structures are characterized using the average lattice constants and the radial distribution function (RDF) [21]. The average lattice constants are calculated at each strain increment by averaging local lattice constants over the bulk volume of the wire. Surface layers (figure 2) are not included in this calculation and the local lattice parameters are computed from coordinates of atoms in the wire core. The RDF describes how atoms in a system are radially packed around each other. It measures the density of atoms in a spherical shell of radius r and thickness dr surrounding an atom in the structure, i.e.

$$g(r) = \frac{n(r, r + dr)/V_S}{N/V}, \quad (1)$$

where $g(r)$ is the RDF, $n(r, r + dr)$ is the number of atoms in the spherical shell, $V_S = 4\pi r^2 dr$ is the volume of the spherical shell, N is the total number of atoms in the system and V is the volume of the structure. The RDFs are generated at the end

of the equilibration stage of a relevant strain increment when a steady state has been achieved. In particular, the RDFs for the WZ structure after initial relaxation and for the HX structure after transformation completion are studied to characterize the structural changes associated with the phase transformation.

3. Results and discussion

3.1. Loading response

Figure 3a shows the tensile stress–strain curve of a $40.81 \times 39.89 \text{ \AA}^2$ wire during loading and unloading at 100 K. The configurations of this wire at four different stages (three of which are during loading) of deformation along the curve are shown in figure 3b, with the atoms coloured by their coordination numbers. In the wurtzite structure [initial configuration, (i) in figure 3b], each atom has a coordination number of 4, typical for tetrahedral structures. Atoms on surfaces and edges have coordination numbers of 3 or less. In the HX phase [(ii) and (iii) in figure 3b], on the other hand, each atom has a coordination number of 5 due to an additional Zn–O bond along the [0001] axis as compared to the WZ phase. This five-fold coordination will be discussed later.

The loading response (figure 3a) consists of initial elastic stretching of the WZ wire (A \rightarrow B), structural transformation from WZ to HX (B \rightarrow D) and elastic stretching of the HX wire (D \rightarrow E), culminating in the eventual failure at E. The stress–strain relation in the elastic regime between A and B is essentially linear. Deformation beyond the elastic regime results in a stress drop from 11.31 to 10.45 GPa (B \rightarrow C). This relaxation event indicates the initiation of a phase transformation [22]. The HX phase nucleates near the wire's surface at a strain of 0.065 (figure 3a). As the deformation progresses, the transformed region sweeps through the whole specimen [C \rightarrow D and configuration (ii) in figure 3b] and the transformation is completed at a strain of 0.108 and a stress of 10.58 GPa (point D in figure 3a). Continued loading beyond point D causes elastic stretching of the transformed structure [D \rightarrow E in figure 3a and configuration (iii) in figure 3b] and the eventual failure at a strain of 0.162 and a stress of 12.28 GPa through cleavage along $(\bar{1}2\bar{1}0)$ type planes.

3.2. Crystallographic change

Figure 4 outlines the crystallographic characteristics of the initial WZ phase and the transformed HX phase. Following Limpijumnong and co-workers [23, 24], a common set of lattice parameters (a , b , c , uc and vb) for these two structures is used and illustrated in figure 4a. Additionally, two layers of atoms perpendicular to the $[01\bar{1}0]$ direction and two layers perpendicular to the $[2\bar{1}\bar{1}0]$ direction are shown in figures 4b and c, respectively, to delineate the atomic motions associated with the transformation. The figure shows that, as a result of the transformation, the (0001) Zn and O basal planes become coplanar and the HX structure acquires a new symmetry (mirror plane perpendicular to the [0001] axis). Consequently, an

2122

A. J. Kulkarni et al.

Downloaded By: [Zhou, M.] At: 06:30 24 May 2007

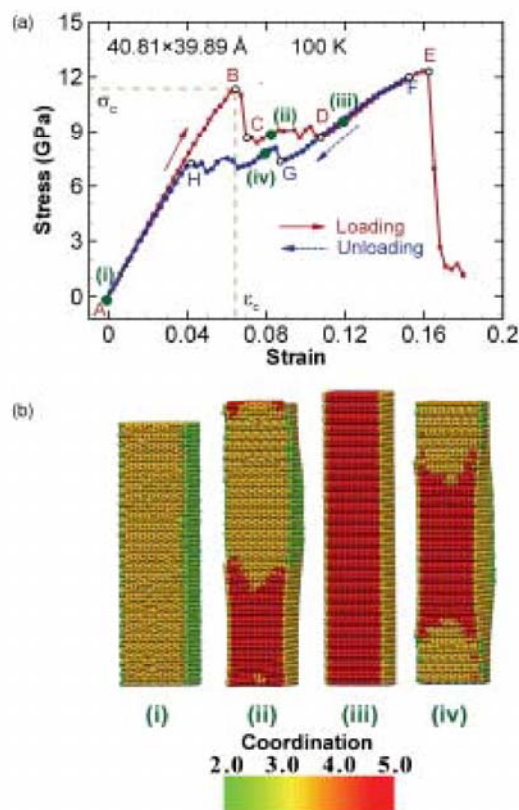


Figure 3. Tensile behaviour of a $40.81 \times 39.89 \text{ \AA}^2$ nanowire: (a) stress–strain curve under loading and unloading; (b) deformed configurations at different stages of loading and unloading.

additional Zn–O bond is formed along the [0001] axis (figures 4b and c), giving the HX phase a five-fold coordination. Table 1 lists the lattice parameters for the WZ and HX structures at several stress levels for the $40.81 \times 39.89 \text{ \AA}^2$ wire. During the deformation, $u = uc/c$ changes from its initial value of 0.4 for WZ to a value of 0.5 for HX, implying the flattening of buckled wurtzite basal planes. A similar unbuckled structure has been observed in GaN, MgO and ZnO thin films as a result of extensive surface reconstructions to suppress surface polarity [25–28].

Figure 5 shows the RDF profiles before loading is applied (point A, $\sigma = 0$ GPa) and upon completion of the WZ \rightarrow HX transformation (point D, $\sigma = 8.58$ GPa) for the nanowire in figure 3. The profile for the initial wire (WZ structure) has its first

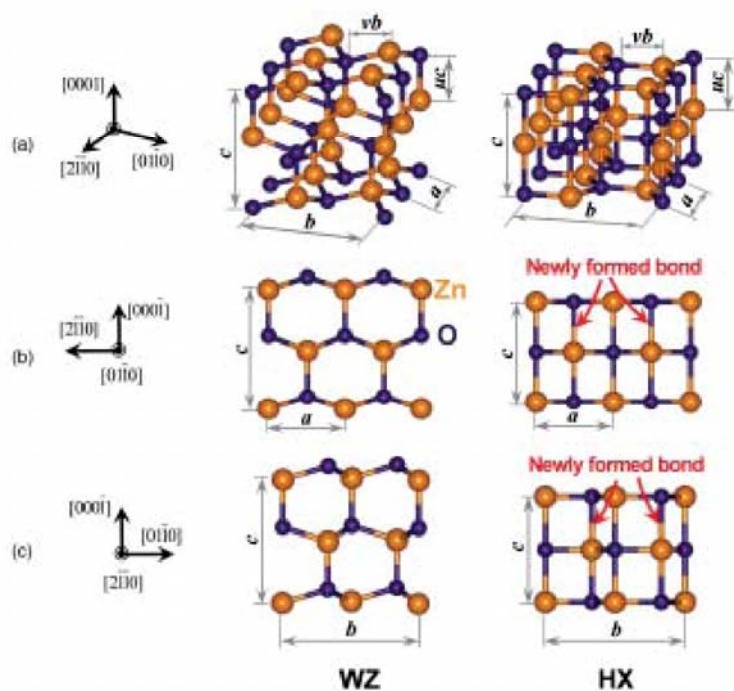


Figure 4. Illustrations of the WZ and HX structures involved in the phase transformation: (a) lattice structures of the WZ and HX phases; (b) atomic arrangement on $[01\bar{1}0]$ plane; (c) atomic arrangement on $[2\bar{1}10]$ plane.

Table 1. Lattice parameters for WZ, HX and RS under different loading conditions for a $40.81 \times 39.89 \text{ \AA}^2$ nanowire.

Parameter	WZ			HX	
	$\sigma = 0 \text{ GPa}$ $\varepsilon = 0^a$	$\sigma = 0 \text{ GPa}$ $\varepsilon = 0$	$\sigma = 11.39 \text{ GPa}$ $\varepsilon = 0.065$	$\sigma = 8.58 \text{ GPa}$ $\varepsilon = 0.108$	$\sigma = 12.29 \text{ GPa}$ $\varepsilon = 0.162$
\bar{a} (\AA)	3.25	3.26	3.23	3.38	3.40
\bar{b} (\AA)	5.63	5.62	6.05	6.22	6.62
\bar{v}	0.33	0.32	0.29	0.31	0.29
\bar{c} (\AA)	5.21	5.18	4.92	4.30	4.15
\bar{u}	0.38	0.41	0.46	0.50	0.49
\bar{b}/\bar{a}	1.73	1.74	1.87	1.84	1.95
\bar{c}/\bar{a}	1.60	1.57	1.53	1.27	1.22

^aExperiment [29].

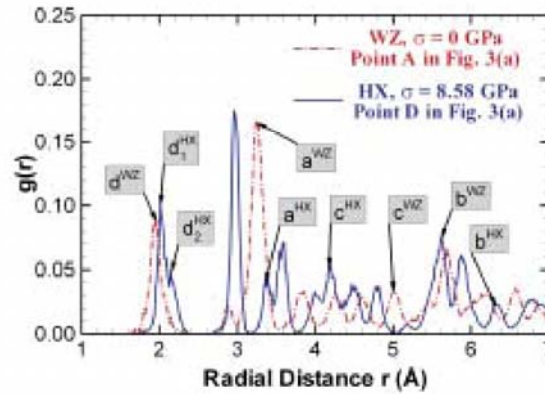


Figure 5. Radial distribution function profiles for a $40.81 \times 39.89 \text{ \AA}^2$ nanowire before loading (point A in figure 3a) and upon completion of phase transformation (point D in figure 3a).

peak at a radial distance of 1.93 \AA , indicating a Zn–O bond distance consistent with the experimental value of 1.95 \AA [29]. Upon completion of the WZ \rightarrow HX transformation at point D, this peak has split into two peaks with the primary peak at 1.98 \AA and the secondary peak at 2.20 \AA . The primary peak corresponds to Zn–O bonds in the basal ($\{0001\}$) plane of the HX structure, while the secondary peak is associated with the additional bonds formed along the $[0001]$ axis (see figure 4). Also seen in figure 5 are peaks corresponding to lattice constants a , b and c . Initially in the WZ phase, the ‘ a ’ peak is at 3.26 \AA and the ‘ c ’ peak is at 5.18 \AA . The transformation to HX results in the shift of the ‘ a ’ peak to 3.38 \AA and the shift of the ‘ c ’ peak to 4.30 \AA . These shifts indicate that the transformation to the HX structure involves both an expansion of the basal planes (increase in ‘ a ’) to accommodate the flattening of the buckled plane and a contraction in ‘ c ’ which results in the formation of the Zn–O bond along the $[0001]$ axis. The transformation is also associated with a shift of the ‘ b ’ peak from 5.60 \AA for WZ to 6.22 \AA for HX, consistent with the nature of the applied tensile loading. The values reported in table 1 also show a progressive increase in the lattice parameter b toward 6.22 \AA as the stress is increased towards the level of 8.58 GPa at the completion of the transformation. Further load increases are accompanied by increases in b with the associated RDF peak shifting toward a higher value (not shown).

3.3. Characterization of the deformation

The deformation can be quantified in a continuum sense through the deformation gradients F_i ($i=1, 2$, and 3) associated with the three stages of deformation, with $i=1$ denoting the first stage (elastic stretching of WZ, $A \rightarrow B$ in figure 3a), $i=2$ denoting the second stage (transformation from WZ to HX, $B \rightarrow D$ in figure 3a) and $i=3$ denoting the third stage (elastic stretching of HX, $D \rightarrow E$ in figure 3a). In such

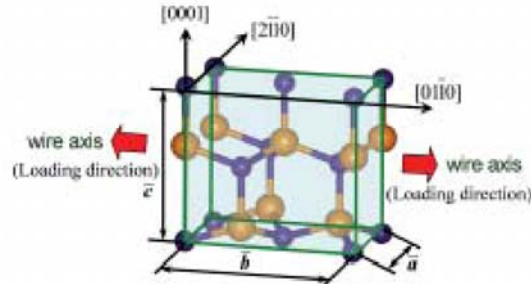


Figure 6. Representative volume defined in a unit cell of the wurtzite lattice for the purpose of deformation analysis.

an analysis, the deformation of a representative volume of $\Omega = \bar{a} \times \bar{b} \times \bar{c}$ (figure 6) is used, with dimensions \bar{a} , \bar{b} and \bar{c} being the average values of lattice constants a , b and c , respectively. Since the average values of the lattice parameters are used here, the deformed wire is regarded as a repetition of this representative volume. The deformation gradient for each stage can then be expressed as

$$\mathbf{F}_i = \begin{pmatrix} \bar{a}_i & 0 & 0 \\ \bar{a}_{i-1} & & \\ 0 & \bar{c}_i & 0 \\ & \bar{c}_{i-1} & \\ 0 & 0 & \bar{b}_i \\ & & \bar{b}_{i-1} \end{pmatrix}, \quad i = 1, 2, 3. \quad (2)$$

In the above expressions, \bar{a}_{i-1} , \bar{b}_{i-1} , and \bar{c}_{i-1} are the average lattice constants at the beginning of stage i and \bar{a}_i , \bar{b}_i , and \bar{c}_i are the average lattice constants at the end of stage i . Note that \bar{a}_0 , \bar{b}_0 , and \bar{c}_0 are the constants for the initial (undeformed, WZ) wire. The relative volume change associated with stage i is

$$\frac{\Omega_i}{\Omega_{i-1}} = \det(\mathbf{F}_i), \quad (3)$$

where Ω is the volume of the wire at the beginning and end of stage i , respectively.

For a $40.81 \times 39.89 \text{ \AA}^2$ wire at 100 K, the deformation gradient for the first stage (A \rightarrow B in figure 3a) is

$$\mathbf{F}_1 = \begin{pmatrix} 0.991 & 0 & 0 \\ 0 & 0.960 & 0 \\ 0 & 0 & 1.065 \end{pmatrix}. \quad (4)$$

The associated volume increase is 1.27% and the longitudinal (elastic) strain $\varepsilon_{33} = F_1^{33} - 1 = 0.065$ consistent with that seen from the stress-strain curve in figure 3.

During the second stage of deformation (phase transformation B → D in figure 3a), \bar{a} increases and \bar{c} decreases. The corresponding deformation gradient is

$$F_2 = \begin{pmatrix} 1.047 & 0 & 0 \\ 0 & 0.876 & 0 \\ 0 & 0 & 1.043 \end{pmatrix}. \quad (5)$$

The volume ratio associated with the transformation is $\Omega_2/\Omega_1 = 0.957$, indicating a slight decrease in volume of 4.3%. This decrease in volume under tensile loading is counterintuitive. It is a direct consequence of the discrete lattice structure and the structural transformation. Specifically, the uniaxial tensile stress in the $[01\bar{1}0]$ or 'b' direction causes the interatomic distances in the $[0001]$ Zn and O basal planes (a) to increase, causing the two types of basal planes to become coplanar and, therefore, the volume decrease.

The deformation gradient for the elastic deformation of the HX phase in the third stage (D → E in figure 3a) is

$$F_3 = \begin{pmatrix} 1.008 & 0 & 0 \\ 0 & 0.962 & 0 \\ 0 & 0 & 1.05 \end{pmatrix}. \quad (6)$$

Although the 'a' and 'b' directions are perpendicular to each other, a increases slightly (with a corresponding strain of $\varepsilon_{11} = 0.008$) under the tensile loading along the 'b' direction. This gives rise to a negative phenomenological Poisson's ratio of

$$\nu_{13} = -\frac{\varepsilon_{11}}{\varepsilon_{33}} = -0.16. \quad (7)$$

The total elastic strain of the wire beyond the completion of the phase transformation and before fracture (between D and F in figure 3a) is $\varepsilon_{33} = F_3^{33} - 1 = 0.05$. Here, the reference state of this strain is the length of the wire at the completion of transformation (point D). The corresponding volume increase is 1.68%.

Overall, the total strain of the wire between points A and E is $\varepsilon = F_1^{33} F_2^{33} F_3^{33} - 1 = 0.162$. Here, the reference length is the original length of the wire.

3.4. Unloading response

Unloading of an HX structured wire from any strain prior to wire fracture activates a novel pseudoelastic behaviour. Take the wire in figure 3 for example; unloading from a strain of 14.5% (point F) initially results in the recovery of the elastic straining of the HX structure embodied in F_3 and goes beyond the end point of the WZ → HX transformation during loading (point D). This elastic unloading within the HX structure continues until point G where a reverse transformation from HX to WZ initiates at a strain of 0.087 and a stress of 7.38 GPa. Further unloading results in the complete reversal of the HX → WZ transformation at H (with a strain of 0.039 and a stress of 7.04 GPa). Unloading between H and A follows the elastic trend of the WZ phase and the hysteresis loop is completed.

For the wire in figure 3, the total recoverable strain is ~16% which is significant since ZnO is a ceramic. The hysteretic energy dissipation in one loading and

unloading cycle is $\sim 0.14 \text{ GJ m}^{-3}$. This dissipation level is significantly lower than that observed for wurtzite to rock salt (WZ \rightarrow RS) transformations in bulk ZnO ($\sim 1.38 \text{ GJ m}^{-3}$ per cycle), therefore, limiting heat generation and heat-related damage and making the nanowires ideal for applications involving cyclic loading and unloading [30]. The low level of dissipation can be attributed to the fact that (i) the crystallographic transition between the WZ and HX structures, which does not require the formation of defects such as dislocations or twin boundaries, is smooth and (ii) the energy barrier for the transformation between the WZ and the HX structures is relatively low [6].

3.5. Effects of size and temperature

Temperature and lateral dimensions have significant effects on the pseudoelastic behaviour of the wires. Figures 7a–c show the loading part of the stress–strain curves over 100–700 K for the 21.22×18.95 , 31.02×29.42 and $40.81 \times 39.89 \text{ \AA}^2$ nanowires, respectively. The critical stress for the nucleation of the HX phase (σ_c) is marked by open circles in these figures. Figure 7d shows the variation of this critical stress as a function of size and temperature. Overall, the critical stress decreases as the wire size

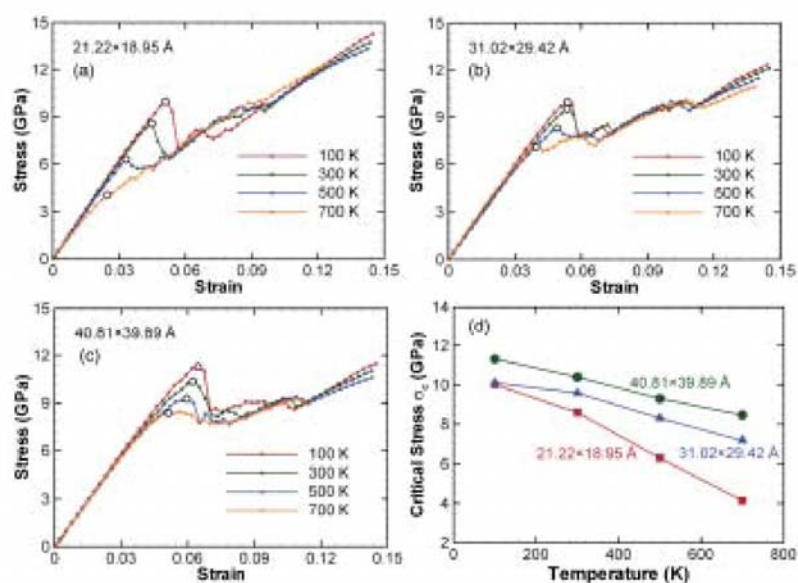


Figure 7. Stress–strain curves of (a) a $21.22 \times 18.95 \text{ \AA}^2$ wire, (b) a $31.02 \times 29.42 \text{ \AA}^2$ wire and (c) a $40.81 \times 39.89 \text{ \AA}^2$ wire at different temperatures. (d) The critical stress for the initiation of phase transform (σ_c) as a function of lateral dimensions and temperature.

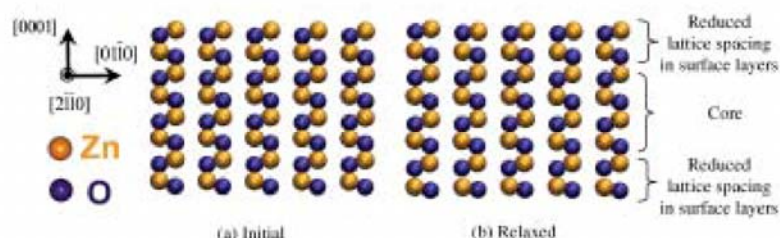


Figure 8. Surface reconstruction of a $21.22 \times 18.95 \text{ \AA}^2$ nanowire at 100 K relative to its configuration in bulk ZnO, the images correspond to the states of the wire after (a) geometric construction (before initial relaxation) and (b) after initial relaxation.

is reduced. The critical stress also decreases as temperature is increased. Over the temperature range analyzed, σ_c for the $31.02 \times 29.42 \text{ \AA}^2$ wire is up to 42% higher than that for the $21.22 \times 18.95 \text{ \AA}^2$ wire, whereas the values for the $40.81 \times 39.89 \text{ \AA}^2$ wire are approximately 11–15% higher than those for the $31.02 \times 29.42 \text{ \AA}^2$ wire. In contrast to the well-established trend that the stiffness of nanowires increases as wire size is reduced [13], σ_c decreases as the wire size is reduced. The higher surface-to-volume ratios at smaller wire sizes cause both effects. Note that, as the wire size is reduced from 50 \AA to 10 \AA , the surface-to-volume ratio increases by $\sim 35\%$. In particular, for polar (0001) surfaces (figure 1), the imbalance of charges results in extensive surface reconstruction.

Figure 8 shows the positions of atoms on layers perpendicular to the [0001] direction before and after the initial relaxation. Obviously, relative to the ideal bulk structure, the surface layers contract and the Zn and O basal planes become essentially coplanar, resulting in a layered surface structure (LY) which is crystallographically similar to the HX structure. This phenomenon has been predicted by first-principle calculations and observed in experiments on ZnO nanofilms [25, 26]. The reconstructed LY surfaces in the initial wire before loading play an important role because they can act as nucleation sites for and lower the energy barrier of the $\text{WZ} \rightarrow \text{HX}$ transformation due to the geometric similarities between the LY and HX structures. The smaller wire cores at smaller wire sizes facilitate the initiation of the phase transformation from the surfaces, resulting in the lower σ_c values.

As the temperature increases from 100 K to 700 K, a 25.2% decrease in σ_c is observed for the $40.81 \times 39.89 \text{ \AA}^2$ wire (figure 7d). This effect is attributed to thermal softening and the ability of the nanowire to overcome the energy barrier for the transformation at higher temperatures. Note that over the same range of temperature, the elastic modulus of the nanowire decreases by 24% [13]. Temperature changes also significantly affect hysteretic dissipation. To illustrate this effect, the stress-strain curves of the $40.81 \times 39.89 \text{ \AA}^2$ wire at 100 K, 300 K, 500 K and 700 K are shown in figure 9.

The corresponding dissipation during the loading–unloading cycle, along with those for the 21.22×18.95 and $31.02 \times 29.42 \text{ \AA}^2$ wires at these temperatures, is given

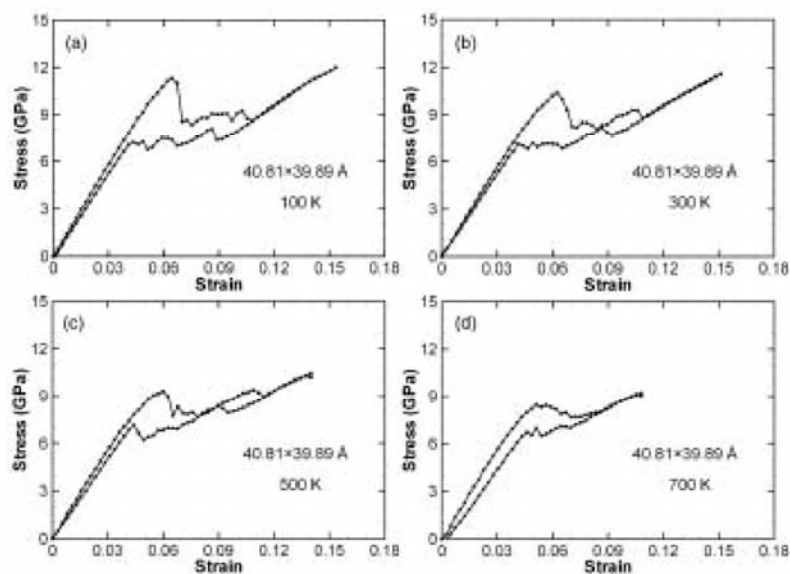


Figure 9. Stress-strain responses of a $40.81 \times 39.89 \text{ \AA}^2$ wire during one loading-unloading cycle at (a) 100 K, (b) 300 K, (c) 500 K and (d) 700 K.

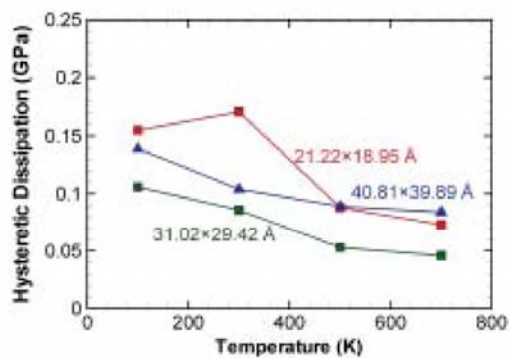


Figure 10. Hysteretic dissipation in one loading-unloading cycle as a function of lateral dimensions and temperature.

in figure 10. For the $40.81 \times 39.89 \text{ \AA}^2$ wire, the dissipation decreases by 39.6% as temperature is increased from 100 K to 700 K. A similar trend is seen for the 21.22×18.95 and $31.02 \times 29.42 \text{ \AA}^2$ wires which show decreases of 52.9% and 56.6%, respectively, over the same temperature range.

2130

A. J. Kulkarni et al.

Table 2. Size and temperature dependence of the stress–strain response of the nanowires.

Cross-section dimensions (\AA^2)	Temperature (K)	σ_c (GPa)	ϵ_c	Strain at completion of transformation	Maximum recoverable strain	Ultimate tensile strength (GPa)	Hysteretic dissipation (GJ m^{-3})
21.22×18.95	100	10.02	0.051	0.100	0.165	15.56	0.155
	300	8.59	0.045	0.096	0.155	14.50	0.171
	500	6.29	0.033	0.097	0.148	13.56	0.088
	700	4.15	0.027	0.091	0.127	12.34	0.073
31.02×29.42	100	10.10	0.053	0.110	0.155	13.05	0.106
	300	9.59	0.053	0.110	0.154	12.50	0.086
	500	8.31	0.049	0.098	0.140	11.44	0.053
	700	7.17	0.040	0.116	0.138	10.89	0.046
40.81×39.89	100	11.32	0.065	0.108	0.159	12.30	0.139
	300	10.40	0.063	0.109	0.162	11.68	0.104
	500	9.31	0.060	0.114	0.143	10.60	0.089
	700	8.47	0.051	0.086	0.108	9.21	0.084

Table 2 lists the values of several key parameters quantifying the pseudoelastic behaviour at various cross-sectional sizes and temperatures. In particular, note that the maximum recoverable strain decreases significantly as temperature is increased, while the strain at which the WZ \rightarrow HX transformation completes is essentially temperature-independent. The enhanced mobility of atoms at higher temperatures promotes the formation of defects and may be a factor contributing to the failure at lower strain levels.

3.6. Pseudoelasticity without shape memory

The pseudoelastic behaviour quantified here is reminiscent of a very similar pseudoelastic behaviour (which leads to a novel shape memory effect) in fcc metal nanowires discovered and analyzed by Liang *et al.* [3, 4]. This similarity in the pseudoelastic behaviours between nanowires of the two classes of materials naturally raises the question of whether a similar SME also exists in the ZnO nanowires analyzed here. To answer this question, we first note that the pseudoelasticity and the SME in the fcc metal nanowires are driven primarily by a surface-stress-induced lattice reorientation process which requires the formation of intermediate transitional structures involving partial dislocations. One attribute of that unique lattice reorientation process is that an energy barrier exists between the phases even at very low temperatures. Therefore, spontaneous relaxation occurs only at temperatures above a critical value. It is this temperature dependence that gives rise to the SME in the fcc metal wires.

To ascertain if a SME exists in the ZnO nanowires analyzed here, partially and fully transformed wires were cooled to various final temperatures, the lowest being 10 K. Subsequently, unloading is carried out at the low temperatures to determine if the HX phase can be retained without external stress. For all wire sizes considered and under all initial/final temperature combinations analyzed, the wires reverted

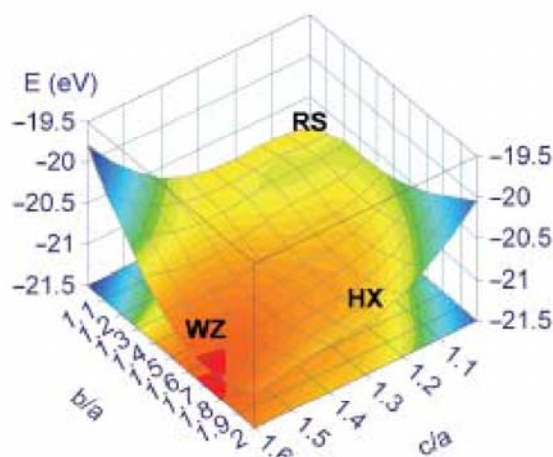


Figure 11. Potential energy map of ZnO with highlights of the WZ, RS and HX lattice structures.

fully back to the WZ structure. This result shows that there is no critical temperature below which either partially or fully HX-structured wires can exist without external loading. The absence of such a critical temperature and the lack of an HX structure at zero loading effectively rule out the possibility of a SME in the ZnO nanowires. This finding can be explained by the enthalpy surface for ZnO at 0 K and zero external loading. Figure 11 shows the potential energy profile of one ZnO unit cell at different structural configurations (when there is no external loading, the enthalpy is equal to the potential energy). This profile is obtained through first principle calculations, details of which are provided by Kulkarni *et al.* [6] and Limpijumng and Jungthawan [23]. Lattice structures corresponding to WZ, RS and HX are labelled in this figure. Note that only two local minima (energy wells) exist, one at the WZ structure and the other at the RS structure. A well is not seen at the HX structure. Obviously, WZ is the stable phase and any sample with the HX structure would spontaneously transform into the WZ structure. On the other hand, the RS structure is a metastable phase which may exist if temperature and load histories are carefully controlled. In contrast, it is not possible for HX to exist without loading since no energy well is seen for it on the energy surface. Of course, the enthalpy surface can be modified by appropriate external loading to include a local minimum (well) at the HX structure. Tensile loading of sufficient magnitude along the *b*-direction is such an example and has been shown to cause the WZ \rightarrow HX phase transformation [6]. Crystallographically, the two-way WZ \leftrightarrow HX transformation occurs through smooth lattice structure evolution without the formation of defects or intermediate structures. In particular, the process can be illustrated by a look at the buckling and unbuckling of the [0001] Zn and O basal planes.

Figure 12 shows the evolution of the 3-D O–Zn–O bond angle (α) at various stages of deformation. The strain values are associated with the loading process of

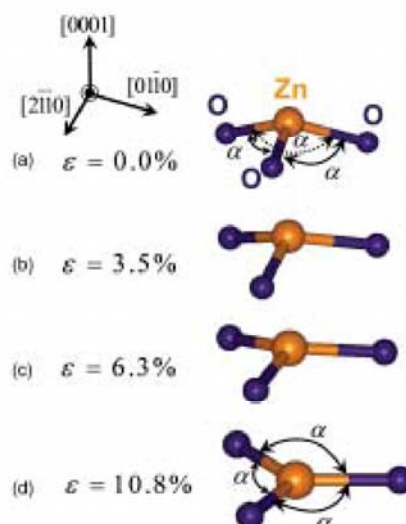


Figure 12. Increase in the O–Zn–O bond angle (α) between Zn and O atoms on [0001] basal planes at various levels of strain during tensile loading along the $[01\bar{1}0]$ wire axis.

the $40.81 \times 39.89 \text{ \AA}^2$ wire. The evolution of α during unloading is very similar except that the corresponding wire strain values are slightly different. For a perfect, undeformed WZ lattice, $\alpha \approx 108.2^\circ$ (figure 12a). As deformation progresses, α increases as loading is increased and the structure evolves (figures 12b and c). Upon full WZ \rightarrow HX transformation, the basal planes flatten out and α becomes 120° (figure 12d), at the same time, a new bond is formed along the [0001] axis (figures 4b and c). During unloading, the reverse process is seen, with α decreasing as the load is decreased. The lack of defect or intermediate structure formation in the process makes ZnO nanowires different from FCC metal nanowires such that the energy requirement for the nucleation of the WZ \leftrightarrow HX transformation is very low. Therefore, during the actual unloading of a HX wire, the barrier for the HX \rightarrow WZ transformation is primarily due to the breaking of the additional [0001] bond formed during the forward transformation. This barrier is relatively small [6] and is easily overcome by the strain energy stored in the HX structure. Consequently, spontaneous HZ \rightarrow WZ transformation occurs at all temperatures and no SME is observed in the ZnO nanowires.

4. Conclusions

A novel pseudoelastic behaviour we discovered recently in $[01\bar{1}0]$ -oriented ZnO nanowires over the temperature range 100–700 K has been characterized.

MD simulations of the uniaxial tensile loading and unloading of nanowires with lateral dimensions between 18 and 41 Å show that this behaviour results from a unique structural transformation from WZ to a previously unknown phase (herein referred to as HX). Crystallographically, this newly discovered polymorph of ZnO has a five-fold coordination, in contrast to the four-fold coordination of the initial WZ structure, implying that the transformation proceeds towards higher ionicity. The transformation is fully reversible upon unloading with recoverable strains up to 16%. The hysteretic dissipation associated with a loading-unloading cycle is 0.05–0.14 GJ m⁻³ and this value is significantly lower than the value for the reversible WZ–RS transformation in ZnO.

Significant temperature and size dependence of the pseudoelastic response is observed. In particular, the critical stress for the nucleation of the HX phase and the maximum recoverable strain decreases as temperature increases. In addition, the critical stress is lower at smaller wire sizes. Extensive surface reconstructions that minimize surface charge polarity and surface energy contribute to these temperature- and size-effects.

Unlike the pseudoelasticity in fcc metal nanowires, which was discovered recently by Liang *et al.* [2–4] and underlies a novel shape memory effect, the pseudoelasticity in the ZnO nanowires analyzed here does not lead to a SME. The primary reason for this lack of an SME is the absence of an energy barrier between the WZ and the HX lattice structures when no external loading is applied. The absence of an energy barrier between WZ and HX at zero stress can be regarded as a consequence of the smooth and continuous nature of the crystallographic transition which does not require the formation of defects such as dislocations and twin boundaries. The result is that stretched HX ZnO nanowires can spontaneously revert back to the WZ state at any temperature.

Acknowledgements

AJK and MZ acknowledge support through NSF grant no. CMS9984298 and NSFC grant no. 10528205. SL & KS are supported by NANOTEC through grant no. NN49-024 and TRF through grant nos. BRG4880015 & PHD/0264/2545. The computations are carried out at the NAVO, ARL and ASC MSRCs through AFOSR MURI no. D49620-02-1-0382. We thank Dr. Bill Smith for sharing the molecular dynamics code DL_POLY [31]. Images of deformation in this paper are created with the graphics package Visual Molecular Dynamics (VMD) [32].

References

- [1] K. Otsuka and C.M. Wayman, *Shape Memory Materials* (Cambridge University Press, New York, 1998).
- [2] W. Liang and M. Zhou, *J. Engng Mater. Technol.* **127** 123 (2005).
- [3] W. Liang and M. Zhou, *Phys. Rev. B* **73** 115409 (2006).

2134 *Characterization of novel pseudoelastic behaviour of zinc oxide nanowires*

- [4] W. Liang, M. Zhou and F.J. Ke, *Nano Lett.* **5** 2039 (2005).
 [5] H.S. Park, K. Gall and J.A. Zimmerman, *Phys. Rev. Lett.* **95** 255504 (2005).
 [6] A.J. Kulkarni, M. Zhou, K. Sarasamak, *et al.*, *Phys. Rev. Lett.* **97** 105502 (2006).
 [7] D.J. Binks and R.W. Grimes, *J. Amer. Ceram. Soc.* **76** 2370 (1993).
 [8] D. Wolf, P. Keblinski, S.R. Phillpot, *et al.*, *J. Chem. Phys.* **110** 8254 (1999).
 [9] Z.L. Wang, *J. Phys. Cond. Matt.* **16** R829 (2004).
 [10] Z.L. Wang, *Mater. Today* **7** 26 (2004).
 [11] Z.L. Wang, *Annu. Rev. Phys. Chem.* **55** 159 (2004).
 [12] A.J. Kulkarni, M. Zhou and F.J. Ke, *Nanotechnology* **16** 2749 (2005).
 [13] A.J. Kulkarni and M. Zhou, *Acta Mech. Sin.* **22** 217 (2006).
 [14] A.J. Kulkarni and M. Zhou, *Appl. Phys. Lett.* **88** 141921 (2006).
 [15] J. Diao, K. Gall and M.L. Dunn, *Nature Mater.* **2** 656 (2003).
 [16] J. Diao, K. Gall and M.L. Dunn, *Phys. Rev. B* **70** 075413 (2004).
 [17] J.M. Haile, *Molecular Dynamics Simulation* (Wiley-Interscience, New York, 1997).
 [18] S. Melchionna, G. Ciccotti and B.L. Holian, *Molec. Phys.* **78** 533 (1993).
 [19] D. Spearot, K. Jacob and D.M. McDowell, *Acta Mater.* **53** 3579 (2005).
 [20] M. Zhou, *Proc. R. Soc.* **459** 2347 (2003).
 [21] J.M.J.V. Leeuwen, J. Groeneveld and J.D. Boer, *Physica* **25** 792 (1959).
 [22] G.B. Olson and M. Cohen, *J. Phys., Paris* **43** 4 (1982).
 [23] S. Limpijumnong and S. Jungthawan, *Phys. Rev. B* **70** 054104 (2004).
 [24] S. Limpijumnong and W.R.L. Lambrecht, *Phys. Rev. Lett.* **86** 91 (2001).
 [25] F. Claeysens, C.L. Freeman, N.L. Allan, *et al.*, *J. Mater. Chem.* **15** 139 (2005).
 [26] C.L. Freeman, F. Claeysens, N.L. Allan, *et al.*, *Phys. Rev. Lett.* **96** 066102 (2006).
 [27] J. Goniakowski, C. Noguera and L. Giordano, *Phys. Rev. Lett.* **93** 215702 (2004).
 [28] R.B. Capaz, H. Lim and J.D. Joannopoulos, *Phys. Rev. B* **51** 17755 (1995).
 [29] D.J. Binks, *Computational modelling of zinc oxide and related oxide ceramics*. PhD thesis, University of Surrey (1994).
 [30] S. Desgreniers, *Phys. Rev. B* **58** 14102 (1998).
 [31] W. Smith and T.R. Forester, *DL_POLY – a Molecular Simulation Routine* (Central Laboratory of Research Councils, Daresbury, 1996).
 [32] W. Humphrey and A. Dalke, *J. Molec. Graphics* **14** 33 (1996).

PHYSICAL REVIEW B 76, 172103 (2007)

Molecular dynamics and density functional studies of a body-centered-tetragonal polymorph of ZnO

J. Wang,¹ A. J. Kulkarni,² K. Sarasamak,³ S. Limpijumnong,³ F. J. Ke,^{1,4} and M. Zhou^{2,*}¹Department of Physics, Beihang University, Beijing 100083, China²School of Mechanical Engineering, Georgia Institute of Technology, Atlanta, Georgia 30332-0405, USA³School of Physics, Suranaree University of Technology, Nakhon Ratchasima 30000, Thailand⁴Institute of Mechanics, Chinese Academy of Sciences, Beijing 100080, China

(Received 13 September 2007; published 13 November 2007)

We report a previously unknown body-centered-tetragonal structure for ZnO. This structure results from a phase transformation from wurtzite in [0001]-oriented nanorods during uniaxial tensile loading and is the most stable phase for ZnO when stress is above 7 GPa. The stress-induced phase transformation has important implications for the electronic, piezoelectric, mechanical, and thermal responses of ZnO. The discovery of this polymorph brings about a more complete understanding of the extent and nature of polymorphism in ZnO. A crystalline structure-load triaxiality map is developed to summarize the relationship between structure and loading.

DOI: 10.1103/PhysRevB.76.172103

PACS number(s): 61.50.Ks, 61.46.-w, 62.25.+g, 64.70.Nd

Natural selection of the lowest energy state determines the bonding state and atomic arrangement of a material under ambient conditions. Deviations from this natural state occur when external stimuli such as mechanical loading and temperature changes are provided, leading to failure through bond breaking or polymorphism due to atomic rearrangement. At the macroscopic scale, failure is dominant since atomic mobility is relatively low and defects are more prevalent. At the nanoscale, however, high surface-to-volume ratios and nearly defect-free structures lead to higher atomic motilities and more pronounced polymorphic transitions. Consequently, polymorphs previously unknown for bulk materials can be revealed. Recently, a fivefold coordinated hexagonal phase (referred to as HX) of ZnO was observed in [01 $\bar{1}$ 0]-oriented ZnO nanowires under uniaxial tensile loading.^{1,2} This discovery has subsequently been confirmed in [0001]-oriented ZnO nanoplates³ and nanowires.⁴ Here, we report yet another polymorph of ZnO with a body-centered-tetragonal structure with four-atom rings (referred to as BCT-4, space group $P4_2/mnm$), which occurs under uniaxial tensile loading along the [0001] crystalline axis of the wurtzite structure. While similar structures have been reported for carbon⁵ and lithium aluminum oxide,^{6,7} this polymorph has been reported here for a binary system. The results here show that the extent of polymorphism in ZnO (and perhaps in other groups IV, III-V, and II-VI materials such as GaN and CdSe) is much more pronounced than previously known. With the discovery of these phases, a more complete picture has emerged for the polymorphism of ZnO under the influence of mechanical loading with all realistic triaxialities. The recent fabrication and applications of defect-free, single-crystalline nanowires, nanobelts, and nanorings of materials such as ZnO, GaN, and CdSe highlights the need for understanding the extent of polymorphism. Characterization of the thermomechanical and electrical responses of the relevant phases is crucial since the performance and functionalities of these slender quasi-one-dimensional materials as components in ultrasensitive chemical and biological sensors, nanoresonators, field effect

transistors, and nanogenerators⁸⁻¹¹ are either significantly affected by or utilize the phase transitions.¹²⁻¹⁴

Our analyses include both molecular dynamics (MD) simulations and density functional theory (DFT) based first principles calculations. The MD simulations are performed to study the phase transformation and the associated mechanical response of ZnO nanorods with the [0001] growth direction under loading and subsequent unloading. The first principles calculations are carried out to determine the energetic favorability and the electronic band structures of the parent and transformed phases. The impact of this phase transformation on the thermal, mechanical, and electric responses of the nanorods is also evaluated.

The as-synthesized hexagonal ZnO nanorods have a wurtzite structure with a sixfold symmetry around the [0001] axis and six {01 $\bar{1}$ 0} lateral crystalline surfaces,^{15,16} as illustrated in Fig. 1(a). The lattice parameters (Ref. 16) are $a = 3.25$ Å, $u = 0.38$, and $c = 5.21$ Å as shown in Fig. 2(a). The

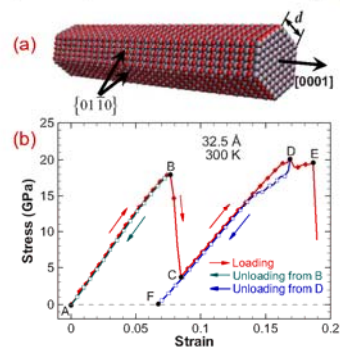


FIG. 1. (Color online) (a) [0001] nanorod with $d=32.5$ Å and (b) stress-strain curve of this nanorod at 300 K during loading and unloading.

BRIEF REPORTS

PHYSICAL REVIEW B 76, 172103 (2007)

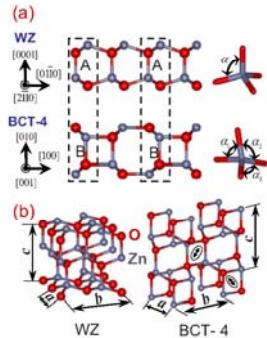


FIG. 2. (Color online) (a) Wurtzite (WZ) and body-centered-tetragonal with four-atom rings (BCT-4) structures and (b) crystallographic transition through breaking and formation of bonds and differences in bond angles between the WZ and the BCT-4 structures.

nanorods analyzed here have the same length of 145.8 Å and five different cross-sectional widths ($d=19.5, 26.0, 32.5, 39.0,$ and 45.5 Å). A Buckingham-type potential with charge interactions is used to define atomic interactions in the MD calculations.^{13,17,18} The analysis concerns quasistatic deformation at 300 K.¹

Figure 1(b) shows the stress-strain response of a nanorod with lateral dimension $d=32.5$ Å. Four distinct stages are observed. The first stage (A—B) corresponds to the elastic stretching of the wurtzite (WZ) structure up to a strain of 7.5%. Further deformation results in a precipitous stress drop (B—C) associated with the WZ to BCT-4 phase transformation. The transformation completes at a strain of 8.5%. Continued loading causes elastic stretching of the BCT-4 structure (C—D) and culminates in the eventual failure at a strain of 16.9% (point E). To analyze the stability of the parent and transformed structures, unloading is performed from states prior to transformation initiation (first peak tensile stress, point B) and failure initiation of the nanorod (second peak tensile stress, point D). The unloading path from B coincides with the loading path, confirming that the deformation from A to B is indeed the elastic response of the WZ-structured nanorod. Unloading from D also results in the elastic recovery of the BCT-4 structure, and continued unloading beyond the transformation completion strain (point C) does not result in a reverse transformation. Instead, the nanorod retains the BCT-4 structure when the stress is reduced to zero [F in Fig. 1(b)].

The WZ to BCT-4 transformation occurs through a combination of (1) the breaking of every other Zn-O bond along the [0001] direction [bond A in Fig. 2(a)] and (2) the formation of an equal number of Zn-O bonds along the same direction [bond B in Fig. 2(a)] next to the broken bonds. This process repeats on alternate planes along the [01 $\bar{1}$ 0] direction. The transformed structure retains the tetrahedral coordination with each Zn/O atom at the center and four O/Zn

TABLE I. Lattice constants for WZ and BCT-4 ZnO in tension along the c axis obtained via MD and DFT (in square brackets) calculations.

Parameters	WZ	BCT-4			
	$\sigma=0$	$\sigma=0$	$\sigma=4$	$\sigma=7$	$\sigma=10$
a (Å)	3.29 [3.20]	3.24 [3.17]	3.22 [3.13]	3.20 [3.09]	3.19 [3.06]
b (Å)	5.67 [5.55]	5.58 [5.48]	5.54 [5.42]	5.51 [5.35]	5.48 [5.32]
c (Å)	5.17 [5.13]	5.52 [5.48]	5.67 [5.71]	5.77 [5.87]	5.84 [5.98]
$V=abc$ (Å ³)	96.4 [91.1]	99.8 [95.2]	101.2 [96.9]	101.7 [97.0]	102.1 [97.3]
ΔV (Å ³)	0.0 [0.0]	3.4 [4.1]	4.8 [5.8]	5.3 [5.9]	5.7 [6.2]
c/a	1.57 [1.60]	1.71 [1.73]	1.76 [1.82]	1.80 [1.9]	1.83 [1.95]
b/a	1.72 [1.73]	1.72 [1.73]	1.72 [1.73]	1.72 [1.73]	1.71 [1.73]

atoms are at the vertices of a tetrahedron. The geometry of the tetrahedron can be characterized through the O-Zn-O bond angles ($\alpha_i, i=1-6$), as shown in Fig. 2(a). For WZ, all bond angles are approximately equal ($\alpha_i \approx 108^\circ$). For BCT-4, the formation of four-atom rings results in three distinct bond angles ($\alpha_1 \approx 90^\circ, \alpha_2 \approx 112.7^\circ,$ and $\alpha_3 \approx 113.7^\circ$).

As seen from Fig. 2(b), the transformed phase consists of four-atom (two Zn and two O) rings arranged in a BCT lattice. Note that the four-atom ring at the center is rotated by 90° relative to the rings at the corners of the tetragonal lattice cell. Strictly speaking, the unit cell consists of two-ring clusters (one of each orientation, total of eight atoms) positioned in a simple tetragonal primitive lattice. Figure 2(b) also shows the lattice parameters $a, b,$ and c for the WZ and BCT-4 structures. Their respective values as obtained from MD and DFT calculations (in square brackets) at various stress levels are listed in Table I along with unit cell volumes. For WZ, the ratios c/a and b/a are 1.60 and 1.73, respectively. Throughout the transformation, the b/a ratio remains at its initial value of 1.73 (± 0.02), reflecting the symmetries of the loading and the lattice. On the other hand, upon transformation to BCT-4 at a stress above 7 GPa, the c/a ratio increases to 1.8. Phenomenologically, the predilection for the BCT-4 phase over the WZ phase under the tensile loading conditions considered here can be explicated by its elongated configuration in the [0001] direction (higher c/a ratio) relative to that of the WZ structure. Upon unloading, the residual strain at F in Fig. 1(b) is 6.8% according to both MD and DFT. It reflects the dimensional difference between the unstressed WZ and BCT-4 structures in the [0001] direction. This unstressed BCT-4 structure corresponds to the “ideal” BCT-4 structure predicted by the DFT calculations with $b/a=c/a=1.73$ in Fig. 3(a).

The relative favorability of the two phases is studied by calculating the enthalpy (per four Zn-O pairs) using DFT calculations.^{2,19} The complete enthalpy surfaces (not shown

BRIEF REPORTS

PHYSICAL REVIEW B 76, 172103 (2007)

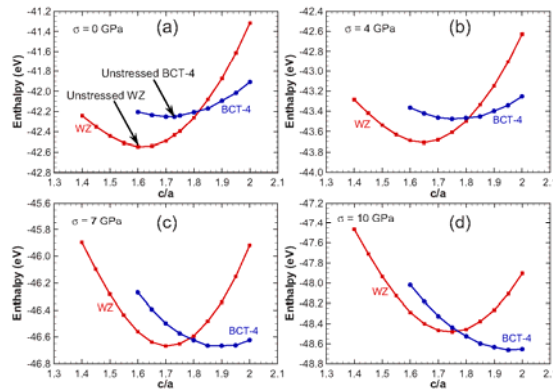


FIG. 3. (Color online) Enthalpy (per four Zn-O pairs) as a function of c/a obtained from DFT calculations for $b/a=1.73$ at tensile stresses of (a) $\sigma=0$ GPa, (b) $\sigma=4$ GPa, (c) $\sigma=7$ GPa, and (d) $\sigma=10$ GPa in the $[0001]$ direction.

due to space limitation) show that the BCT-4 structure has minimum enthalpy at $b/a=1.73$ for all values of tensile stress considered. For clarity without loss of generality, the discussions here use Fig. 3 which shows the enthalpy values (eV per four Zn-O pairs) for both structures for $b/a=1.73$ at $\sigma=0, 4, 7,$ and 10 GPa. At any stress level, each structure has its own enthalpy minimum. The first minimum is in the vicinity of $c/a \approx 1.6$ which corresponds to WZ with lattice parameters slightly different from those at zero stress, and the second minimum is in the vicinity of $c/a \approx 1.7-1.9$, which corresponds to BCT-4. At zero stress, WZ is the stable crystal structure and its enthalpy is lower than that of BCT-4 by 0.3 eV [Fig. 3(a)]. As the stress is increased to 4 GPa [Fig. 3(b)], the difference in enthalpies decreases, and at a stress of 7 GPa [Fig. 3(c)], the two minima become comparable indicating that WZ and BCT-4 are equally favored. This value of stress corresponds to the equilibrium transition stress for the two phases. Since an energy barrier (associated with intermediate transitional states) exists for the transformation, a stress level higher than the 7 GPa equilibrium stress is required to initiate the transformation. At a stress of 10 GPa [Fig. 3(d)], the enthalpy of BCT-4 is lower, and this structure is clearly favored. Further increases in stress result in the eventual initiation of the phase transformation. The specific stress level at which the transformation initiates depends on the rod size and temperature. For the particular nanorod in Fig. 1 at 300 K, the critical stress level is $\sigma = 17.9$ GPa. The gradual evolution of the local enthalpy minimum for the BCT-4 at $\sigma=0$ into a global minimum as stress increases confirms that the phase transformation observed in MD simulations is indeed energetically favored.

The phase transformation observed here alters the electrical, thermal, and mechanical responses of the nanorods. Recently, WZ-structured ZnO nanorods have been used to successfully generate direct electric current through mechanical bending.²⁰ The transformation from the piezoelectric WZ structure to the nonpiezoelectric BCT-4 structure establishes an upper bound for the maximum possible current generation and operational strain for this application. Specifically, the electric field output E_3 can be related to the longitudinal

strain e_3 through $E_3=e_3/d_{33}$, where $d_{33} \approx 20.5$ pm/V is the piezoelectric coefficient for the ZnO nanorods. Since the strain at the initiation of transformation [B in Fig. 1(b)] is approximately 7.5% for all rod sizes, the maximum electric field output is therefore 3.7 V/nm. The mechanical response of BCT-4 also differs significantly from that of WZ. In particular, the enthalpy curves for BCT-4 are flatter than those for WZ (Fig. 3), indicating that the elastic stiffness of BCT-4 is lower than that for WZ. Indeed, in Fig. 1(b), the slope of curve AB (228 GPa, which is the $[0001]$ elastic modulus of WZ) is higher than that of curve FD (167 GPa, which is the corresponding modulus of BCT-4). The thermal response of semiconductors such as ZnO is dominated by phonons and the interactions between phonons and surfaces.²¹ The WZ to BCT-4 phase transformation changes the atomic arrangement and hence the phonon spectrum, resulting in potentially large changes in thermal conductivity. The electronic band structures of WZ and BCT-4 are shown in Fig. 4. Note that the total number of bands for BCT-4 is twice that for WZ because the unit cell of BCT-4 has twice as many atoms as WZ. Both phases have direct band gaps at Γ . Although DFT calculations with local density approximations are known to underestimate band gaps and therefore are not normally used to predict absolute band gap values, they can provide valid

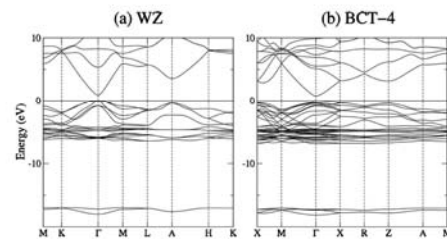


FIG. 4. Band structures of (a) WZ ZnO and (b) BCT-4 ZnO obtained by DFT calculations. The energy is relative to the top of the valence bands.

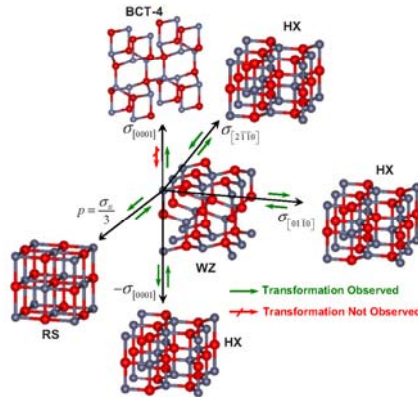


FIG. 5. (Color online) Crystalline structure-load triaxiality map summarizing the nature and much wider extent of polymorphism in ZnO than previously known; WZ is the natural state at ambient conditions, RS occurs under hydrostatic or near hydrostatic compression, HX occurs under tension along the $[2\bar{1}10]$ and $[01\bar{1}0]$ directions as well as compression along the $[0001]$ direction, and BCT-4 occurs under tension along the $[0001]$ direction. The green and red arrows indicate, respectively, possible and impossible transformation paths under relevant load direction reversals. ZB can only be grown epitaxially on certain crystalline planes of cubic crystals and cannot be obtained via a transformation from WZ under external loading; therefore, it is not included in this map.

relative comparisons between the two phases. The calculated band gap and average electron effective mass of BCT-4 are, respectively, 12% and 17% smaller than those of WZ, giving the nanorod a smaller band gap and potentially higher electron mobility after the WZ-to-BCT-4 transformation. These mechanically induced electrical property shifts may have applications in devices that depend on coupling between responses.

Most importantly, the identification of the BCT-4 structure leads to a more complete understanding of the nature and extent of polymorphism in ZnO and its dependence on load triaxiality. Joining wurtzite (WZ), zinc blende (ZB), rocksalt (RS), and HX, BCT-4 constitutes the fifth polymorph of ZnO discovered so far. It is now possible to construct a structure-load triaxiality map for ZnO, as shown in Fig. 5. Among the previously well known phases, WZ is the most stable and naturally occurring phase and RS is observed under hydrostatic compressive conditions. Both BCT-4 and HX are stabilized under uniaxial loading, with HX occurring under tension along the $[01\bar{1}0]$ and/or $[2\bar{1}10]$ directions as well as compression along the $[0001]$ direction and BCT-4 occurring under tension along the $[0001]$ direction. It is worthwhile to note that ZB grows epitaxially on specific surfaces of cubic crystals and cannot be obtained via a transformation from WZ under external loading; therefore, it is not included in this map.

Support from NSF (CMS9984298), NSFC (10772012, 10432050, and 10528205), NANOTEC (NN49-024), and TRF (BRG4880015 and PHD/0264/2545) is acknowledged. Computations are carried out at the NAVO, ARL, ASC MSRCs, NSRC, and the LSEC of the CAS.

*Author to whom correspondence should be addressed; FAX: 404-894-0186; min.zhou@gatech.edu

¹A. J. Kulkarni, K. Sarasamak, S. Limpijumnong, and M. Zhou, *Philos. Mag.* **87**, 2117 (2007).

²A. J. Kulkarni, M. Zhou, K. Sarasamak, and S. Limpijumnong, *Phys. Rev. Lett.* **97**, 105502 (2006).

³L. Zhang and H. Huang, *Appl. Phys. Lett.* **89**, 183111 (2006).

⁴L. Zhang and H. Huang, *Appl. Phys. Lett.* **90**, 023115 (2007).

⁵P. A. Schultz and E. B. Stechel, *Phys. Rev. B* **57**, 3295 (1998).

⁶M. Marezio, *Acta Crystallogr.* **19**, 396 (1965).

⁷M. Marezio and J. P. Remeika, *J. Chem. Phys.* **44**, 3348 (1966).

⁸M. S. Arnold, P. Avouris, Z. W. Pan, and Z. L. Wang, *J. Phys. Chem.* **107**, 659 (2003).

⁹X. D. Bai, P. X. Gao, Z. L. Wang, and W. G. Wang, *Appl. Phys. Lett.* **82**, 4806 (2003).

¹⁰E. Comini, G. Faglia, G. Sberveglieri, Z. W. Pan, and Z. L. Wang, *Appl. Phys. Lett.* **81**, 1869 (2002).

¹¹Z. L. Wang and J. Song, *Science* **312**, 242 (2006).

¹²J. Diao, K. Gall, and M. L. Dunn, *Phys. Rev. B* **70**, 075413 (2004).

¹³A. J. Kulkarni, M. Zhou, and F. J. Ke, *Nanotechnology* **16**, 2749 (2005).

¹⁴W. Liang and M. Zhou, *Phys. Rev. B* **73**, 115409 (2006).

¹⁵A. Umar, B. Karunakaran, E. K. Suh, and Y. B. Hahn, *Nanotechnology* **17**, 4072 (2006).

¹⁶A. Wei, X. W. Sun, C. X. Xu, Z. L. Dong, Y. Yang, S. T. Tan, and W. Huang, *Nanotechnology* **17**, 1740 (2006).

¹⁷D. J. Binks and R. W. Grimes, *J. Am. Ceram. Soc.* **76**, 2370 (1993).

¹⁸A. J. Kulkarni and M. Zhou, *Acta Mech. Sin.* **22**, 217 (2006).

¹⁹S. Limpijumnong and S. Jungthawan, *Phys. Rev. B* **70**, 054104 (2004).

²⁰M. H. Zhao, Z. L. Wang, and S. X. Mao, *Nano Lett.* **4**, 587 (2004).

²¹A. J. Kulkarni and M. Zhou, *Appl. Phys. Lett.* **88**, 141921 (2006).

Stability of wurtzite, unbuckled wurtzite, and rocksalt phases of SiC, GaN, InN, ZnO, and CdSe under loading of different triaxialities

K. Sarasamak,¹ A. J. Kulkarni,² M. Zhou,² and S. Limpijumnong¹

¹*School of Physics, Suranaree University of Technology and National Synchrotron Research Center, Nakhon Ratchasima 30000, Thailand*

²*The George W. Woodruff School of Mechanical Engineering, Georgia Institute of Technology, Atlanta, Georgia 30332-0405, USA*

(Received 29 August 2007; revised manuscript received 16 November 2007; published 7 January 2008)

First principles calculations are carried to study the structural stability of SiC, GaN, InN, ZnO, and CdSe which are found to transform from a fourfold coordinated *wurtzite* (WZ) structure under ambient conditions to two different crystalline structures under loading of different triaxialities. Under hydrostatic compression, transformation into a sixfold coordinated *rocksalt* (RS) structure occurs, and under uniaxial compression along the [0001] direction and uniaxial tension along the [01 $\bar{1}$ 0] crystalline direction (except SiC and GaN), transformation into a fivefold coordinated *unbuckled wurtzite* phase (HX) is observed. The lack of the WZ→HX transformation for SiC and GaN under uniaxial tension along the [01 $\bar{1}$ 0] direction is because for these two materials the tensile stress required for the enthalpy of HX to become lower than the enthalpy of WZ is higher than their corresponding ultimate tensile strength. Critical stress levels for the transformations are found to depend on the formation energies of the WZ, HX, and RS structures which in turn are related to the ionicity of each material. The transformations are a manifestation of the tension-compression response asymmetry of these materials.

DOI: 10.1103/PhysRevB.77.024104

PACS number(s): 61.50.Ks, 62.20.-x, 64.70.K-

I. INTRODUCTION

One-to-one binary compounds obeying the octet rule (i.e., I-VII, II-VI, III-V, or IV-IV materials) are generally semiconductors or insulators. Although these type *AB* compounds have the same chemical formula units, their crystal structures under ambient conditions show significant variations with bond ionicity. While highly ionic compounds such as CsCl (I-VII) prefer dense crystal structures with a coordination number of 8 (CN=8), compounds such as NaCl (also I-VII) with lower degrees of ionicity gravitate toward the rocksalt (RS) structure ($Fm\bar{3}m$ space group) with CN=6. As the degree of ionicity decreases (shifting toward covalent bonding states), compounds such as ZnO (II-VI), GaN (III-V), and SiC (IV-IV) stabilize in wurtzite (WZ) ($P6_3mc$) structures with CN=4. In such covalent compounds, the valence electron counting (two electrons in each bond) is satisfied through the formation of four bonds for each atom. However, in compounds with higher degrees of ionicity such as CsCl and NaCl, the gain in cation-anion attractions leads to the formation of structures with higher CN. Nevertheless, bond ionicity should not be considered as the only factor in determining crystalline structures in such compounds since the assumption of a particular structure also depends on intrinsic factors such as composition, band structure, valence electrons, bonding states, and structural symmetries. Extrinsic factors such as loading and temperature also play significant roles.

Calculations and experiments have been carried out to study the structural stabilities of these materials. Over two decades ago, first principles calculations have been used to evaluate the formation energies of different crystalline structures (see, e.g., Refs. 1 and 2). X-ray diffraction experiments have been used to determine the natural occurring structures. Consequently, the stable crystalline structures under ambient conditions are well established (for a comprehensive review,

see Ref. 3). Furthermore, advances in experimental techniques, such as the use of intense and tunable x ray from synchrotron radiation, have also allowed x-ray diffraction analyses under external loading. For hydrostatic compression, it is observed that most materials with low CN structures (e.g., WZ and ZB) transform into a more compressed crystalline form with higher CN structures (e.g., RS).³⁻¹³ First principles and empirical potential calculations have yielded phase equilibrium pressures that are comparable but always lower than the transformation pressures measured from experiments.^{3,14-23} The higher experimental values are attributed to the existence of an energy barrier between the phases for each transformation. This finding is supported by, for example, the observation that critical pressure for the upward WZ→RS transformation is higher than the critical pressure for the downward RS→WZ transformation^{3,18} or the trapping of nanocrystallite ZnO in the RS phase under ambient condition after a high heat-high pressure treatment.²⁴ If there was no transformation barrier, the upward and downward transformations would occur at the same pressure and there would be no trapping of the metastable high pressure phase.

The recent synthesis of quasi-one-dimensional nanostructures such as nanowires, nanobelts, and nanorods of GaN, ZnO, and CdSe (see, e.g., Refs. 25 and 26) necessitates understanding the response of such materials to uniaxial loading. These nanostructures are single crystalline and nearly defect-free and, therefore, are endowed with high strengths and the ability to undergo large deformations without failure. Also, their high surface-to-volume ratios enhance atomic mobility and promote phase transformations under loading. A novel fivefold coordinated *unbuckled wurtzite* phase (HX) within the $P6_3/mmc$ space group was observed in [01 $\bar{1}$ 0]-oriented ZnO nanowires under uniaxial tensile loading.^{27,28} The stability of this novel phase and the stabilities of WZ and RS phases of ZnO under uniaxial tension

SARASAMAK *et al.*

PHYSICAL REVIEW B 77, 024104 (2008)

along the $[01\bar{1}0]$ direction as well as hydrostatic compression were analyzed through enthalpy calculations. It is found that the HX structure cannot be stabilized by a hydrostatic pressure. Instead, both empirical potential based molecular dynamics (EP-MD) simulations and first principles calculations showed that transformation into the HX structure can occur under either tensile loading along the $[01\bar{1}0]$ direction or compressive loading along the $[0001]$ direction of sufficient magnitude. For this WZ→HX transformation, the uniaxial stress deforms the crystal in only one direction. Since the unit cell of HX is significantly shorter than the unit cell of WZ in the c or $[0001]$ direction (details later), either compression along the c direction or tension along the perpendicular $[01\bar{1}0]$ direction can cause the transformation. For compression along the c direction, the corresponding contribution to enthalpy by mechanical work is linearly proportional to $-\sigma_c \Delta c$, with σ_c and Δc being the compressive stress and the change in unit cell size in the c direction, respectively. For tension along the b direction, the corresponding contribution to enthalpy by mechanical work is linearly proportional to $-\sigma_b \Delta b$, with σ_b and Δb being the tensile stress and the change in unit cell size in the b direction, respectively. In contrast, for the WZ→RS transformation, the all around external pressure uniformly compresses the WZ crystal in all directions and causes it to collapse into the RS phase which has a lower equilibrium unit cell volume. The mechanical work contribution to enthalpy is $p\Delta V$, with p and ΔV being the external pressure and volume reduction, respectively. The discovery of the novel HX phase has subsequently been confirmed in $[0001]$ -oriented ZnO nanoplates²⁹ and nanowires.³⁰

To gain insight into the existence of the WZ, HX, and RS structures in materials with different ionicities, we analyze here the energetic favorability of these phases for ZnO and CdSe (groups II-VI), GaN and InN (III-V), and SiC (IV-IV) under uniaxial loading along the $[01\bar{1}0]$ and $[0001]$ crystal-line axes as well as under hydrostatic compression. The likelihood of transformations from WZ into HX or RS and the effort of load triaxialities on the transformations are analyzed.

II. CRYSTAL STRUCTURES

The natural form of the five materials studied is wurtzite, as shown in Fig. 1 (left column). This structure is quantified customarily by the lattice constant a , the c/a ratio, and the internal parameter u which specifies the relative distance along the c axis between the two hexagonal-close-packed cation and anion sublattices. To describe the HX and RS structures and the transformation from WZ to each of these phases, an extra lattice parameter b and an internal parameter v are introduced.^{19,20} v defines the horizontal distance along the b axis between the cation and anion sublattices. Out of the five parameters (a , b , c , u , and v) illustrated in Fig. 1, only the three external ones (a , b , and c) can be directly manipulated through applied loading. The two internal parameters (u and v) cannot be varied directly. These parameters are determined such that, for any given configuration,

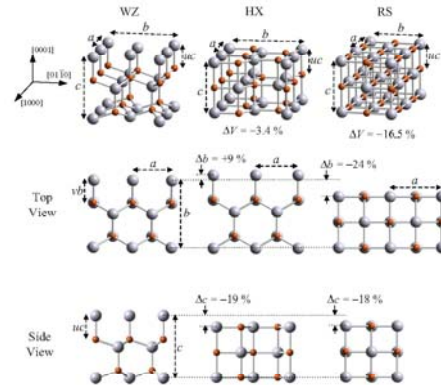


FIG. 1. (Color online) Schematic illustration of the WZ, HX, and RS structures: small spheres represent anions and large spheres represent cations. The middle and bottom rows show top view and side view, respectively. Parameters a , b , c , u , and v are indicated. For realistic rendering, the images shown are drawn to scale using parameters for ZnO at equilibrium conditions, i.e., ambient pressure for WZ, $\sigma = -\sigma_c^{\text{eq}}$ for HX, and $p = p^{\text{eq}}$ for RS. ΔV , Δb , and Δc are the percentage changes in V (volume), b , and c relative to the same quantities for WZ.

the net forces on all atoms in the unit cell vanish. An analysis of the variations of u with c/a and v with b/a can be found in Refs. 19 and 20. The three structures are significantly different, with $c/a \approx 1.63$ and $b/a \approx 1.73$ for WZ, $c/a \approx 1.20$ and $b/a \approx 1.73$ for HX, and $c/a \approx 1.00$ and $b/a \approx 1.00$ for RS. The ideal values of c/a , b/a , u , and v for WZ, HX, and RS under no load and zero temperature are listed in Table I. The c/a value for HX is obtained via enthalpy minimization. All other parameters are determined from the geometry of each structure, for instance, perfect tetrahedral coordination for WZ and perfect cubic for RS. Actual values of these parameters can deviate from those in the table, depending on the material, loading, and temperature.

III. COMPUTATIONAL METHOD

First principles calculations are carried out to evaluate the total energy of each material in its natural and deformed

TABLE I. Ideal lattice parameters for WZ, HX, and RS crystal-line structures.

Parameters	WZ	HX	RS
c/a	$\sqrt{8/3} = 1.63$	1.20	1.00
u	$3/8 = 0.37$	0.50	0.50
b/a	$\sqrt{3} = 1.73$	$\sqrt{3} = 1.73$	1.00
v	$1/3 = 0.33$	$1/3 = 0.33$	0.50

states. The calculations are based on the density functional theory (DFT) with local density approximation (LDA) and ultrasoft pseudopotentials,³¹ as implemented in the VASP code.³² Test calculations have shown that generalize gradient approximations (GGAs) give the results that are qualitatively the same as LDA.³³ Zinc 3*d*, gallium 3*d*, indium 4*d*, and cadmium 4*d* electrons are treated as valence electrons. Cut-off energies for the plane wave expansion are 400 eV for ZnO, 180 eV for CdSe, 350 eV for nitrides, and 300 eV for SiC. The *k*-point sampling set is based on a 7×7×7 division of the reciprocal unit cell based on the Monkhorst-Pack scheme³⁴ with the Γ point included, which gives approximately 100 inequivalent *k* points.

The stability of each crystal structure and compound can be determined by analyzing enthalpy as a function of *c/a* and *b/a*. The enthalpy per a wurtzite unit cell under uniaxial loading is

$$H(c/a, b/a) = E(c, b, a, u, v) - A_{jk}\sigma_j q_k, \quad (1)$$

where *E* is the formation energy per wurtzite unit cell, σ_i is the stress along the *i* direction, q_i is the lattice parameter in the *i* direction, A_{jk} is the cross section area of the unit cell perpendicular to the stress direction, and $A_{jk}\sigma_j q_k$ (summation not implied) is the external work. For tension along the *b* axis, $i=b$, $A_{ac}=ac/2$, and $q_b=b$, with σ_b being the tensile stress. For compression along the *c* axis, $i=c$, $A_{ab}=ab/2$, and $q_c=c$, with $-\sigma_c$ being the compressive stress. For hydrostatic compression, the enthalpy is

$$H(c/a, b/a) = E(c, b, a, u, v) + pV, \quad (2)$$

where *p* and $V=abc/2$ are the pressure and unit cell volume, respectively. Under ambient pressure, the enthalpy is equal to the internal formation energy. Note that a wurtzite unit cell contains two cation-anion pairs, i.e., 2 f.u. and occupy the volume $V=abc/2$.

For each *c/a* and *b/a* pair, the internal parameters *u* and *v* and the unit cell volume *V* are allowed to relax so that the configuration that yields the minimum *H* is obtained. For a given load condition, the minima on the enthalpy surface with *c/a* and *b/a* as the independent variables identify the corresponding stable and metastable structures. For the analyses at hand, the parameter ranges considered are [1.00, 1.63] for *c/a* and [1.00, 1.73] for *b/a*, with the increments of 0.05 for *c/a* and 0.10 for *b/a*. This meshing of the structural space results in approximately 170 strained configurations. For tensile loading along the *b* direction, additional configurations with *b/a* up to 2.30 are also investigated, increasing the number of total configurations to 200. Out of these 170 or 200 configurations, those around (*c/a*, *b/a*) \approx (1.63, 1.73), (1.2, 1.73), and (1.00, 1.00) are more carefully analyzed since these three parameter sets define the neighborhoods of stable WZ, HX, and RS structures, respectively, for the given load condition.

For each strained configuration (each *c/a-b/a* pair), the energies associated with at least four different unit cell volumes are calculated. An equation of state (energy-volume relation) is obtained by a third-degree polynomial fit. Under loading, the volume that minimizes *H* is not the same as the volume that minimizes *E*. The equation of state allows the

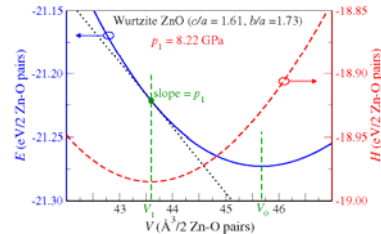


FIG. 2. (Color online) Energy (solid curve) and enthalpy (dashed curve) as functions of volume for wurtzite (*c/a*=1.61 and *b/a*=1.73) ZnO. At hydrostatic pressure $p_1=8.22$ GPa, the volume that minimizes enthalpy (V_1) is smaller than the volume at ambient pressure (V_0).

minimum enthalpy for each combination of *c/a-b/a* pair and loading condition to be obtained. As an illustration, the energy and enthalpy are shown in Fig. 2 as functions of volume for WZ ZnO (*c/a*=1.61 and *b/a*=1.73) under hydrostatic pressure. At ambient pressure ($p \approx 0$), the energy and enthalpy are equal and the minimum enthalpy is equal to $E(V_0)$, with V_0 being the equilibrium volume of WZ in a stress-free state. At $p=p_1$, the minimum enthalpy occurs at $V=V_1$ for which $dE/dV=-p_1$.

IV. RESULTS AND DISCUSSIONS

A. Ambient conditions (stress-free state)

Figure 3(a) shows the energy (or enthalpy at zero external loading) landscape for ZnO. The global minimum occurs at the wurtzite structure with (*c/a*, *b/a*)=(1.61, 1.73). The sections of the surface along *b/a*=1.73 (solid line) and 1.00 (dash line) are shown in Fig. 3(b). By virtue of symmetry, *b/a* is fixed at $\sqrt{3}(\approx 1.73)$ for WZ and HX and at 1.00 for RS. Clearly, in stress-free state, WZ is the most stable structure with the lowest energy, HX has higher energy and is not stable (no local minimum), and the RS structure is metastable with a high energy. For CdSe, GaN, InN, and SiC, the shapes of the energy landscapes (not shown but can be found online³⁵) are similar to that of ZnO. Their two-dimensional (2D) sections at *b/a*=1.73 and 1.00 are shown in Fig. 4. The energy difference (see Ref. 36) between HX and WZ ($\Delta E^{\text{HX-WZ}}$) and that between RS and WZ ($\Delta E^{\text{RS-WZ}}$) are tabulated in Table II. The energies of the three phases for all compounds except CdSe follow the order of $E^{\text{RS}} > E^{\text{HX}} > E^{\text{WZ}}$. For CdSe, $E^{\text{RS}} < E^{\text{HX}}$. This exception can be attributed to the fact that for compounds such as CdSe with high ionicity, the energy differences between RS, HX, and WZ are relatively small. Under this situation, other effects, such as energy cost for bond distortions, can affect the ordering in energies.

There are significant variations of $\Delta E^{\text{HX-WZ}}$ or $\Delta E^{\text{RS-WZ}}$ among the materials, partly reflecting differences in the ionicity. Several indices are available to describe the ionicity of materials. Although LDA calculation is sometimes believed

SARASAMAK *et al.*

PHYSICAL REVIEW B 77, 024104 (2008)

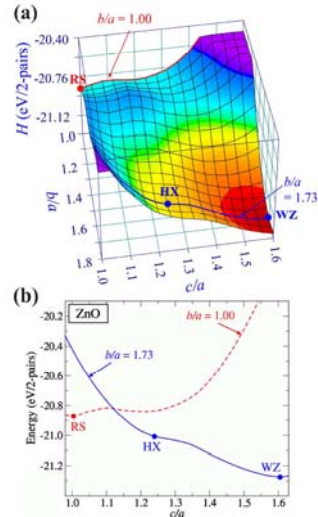


FIG. 3. (Color online) (a) Energy (E) (or enthalpy H under zero external loading) landscape for ZnO (in eV per wurtzite unit cell which contains two cation-anion pairs or 2 f.u.). Each point on the surface represents the minimum energy for a given combination of c/a and b/a . To arrive at the minimum, u , v , and V are allowed to relax while a , b , and c are kept constant. Energy levels above -20.50 eV are truncated as they are not of interest in the discussions here. (b) 2D sections of the energy surface for $b/a=1.73$ (solid line) and 1.00 (dashed line).

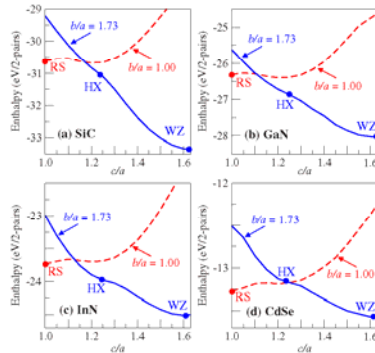


FIG. 4. (Color online) 2D sections of (a) SiC, (b) GaN, (c) InN, and (d) CdSe energy surfaces (Ref. 35) for $b/a=1.73$ (solid lines) and 1.00 (dashed lines).

TABLE II. Energy difference (eV/2 pairs) between HX (or RS) and the WZ structure. The Phillips ionicity parameters (f_i) are also listed. (Ref. 37).

Compounds	Phillips' f_i	$E^{\text{HX}} - E^{\text{WZ}}$ (eV)	$E^{\text{RS}} - E^{\text{WZ}}$ (eV)
SiC	0.177	2.53	2.74
GaN	0.500	1.32	1.74
InN	0.578	0.61	0.78
ZnO	0.616	0.26	0.41
CdSe	0.699	0.44	0.30

to slightly overestimate the ionicity in materials, the trend of ionicity between materials should be qualitatively correct. Therefore, Phillips' ionic scale (f_i),³⁷ which has the range between 0 (the least ionic) and 1 (the most ionic), is used here by choice. The values of f_i for the compounds studied here are listed in Table II.³⁷ The variations of $\Delta E^{\text{HX-WZ}}$ and $\Delta E^{\text{RS-WZ}}$ with f_i are shown in Fig. 5. For RS, $\Delta E^{\text{RS-WZ}}$ (solid line) decreases monotonically as f_i increases. For HX, $\Delta E^{\text{HX-WZ}}$ (dash line) decreases monotonically with f_i (except for CdSe). This is expected because compounds with higher levels of ionicity can significantly lower their energies through increases in CN. While ionicity is not the only factor that determines the relative stability of crystal structures, it clearly affects the stability of structures. For covalent compounds (e.g., SiC and GaN), the structure with fourfold coordination is highly favored, resulting in large differences between the formation energies of RS (sixfold) and WZ (fourfold) and between the formation energies of HX (fivefold) and WZ. On the other hand, for compounds with higher levels of ionicity, the differences in formation energies among RS, HX, and WZ are lower. In this paper, only ionic compounds that have fourfold coordinated structures (WZ) under ambient conditions are considered.

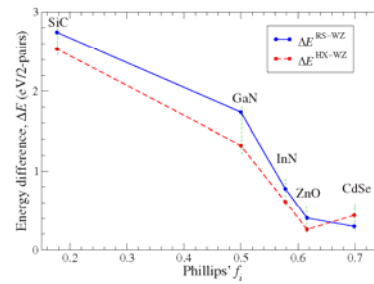


FIG. 5. (Color online) Correlation between the formation energy differences (ΔE) and the ionicity as quantified by Phillips' f_i for SiC, GaN, InN, ZnO, and CdSe. $\Delta E^{\text{RS-WZ}}$ is shown in solid line and $\Delta E^{\text{HX-WZ}}$ is shown in dash line. For all compounds, WZ has the lowest energy and RS has the highest energy, except for CdSe whose RS phase has a slightly lower energy than its HX phase.

024104-4

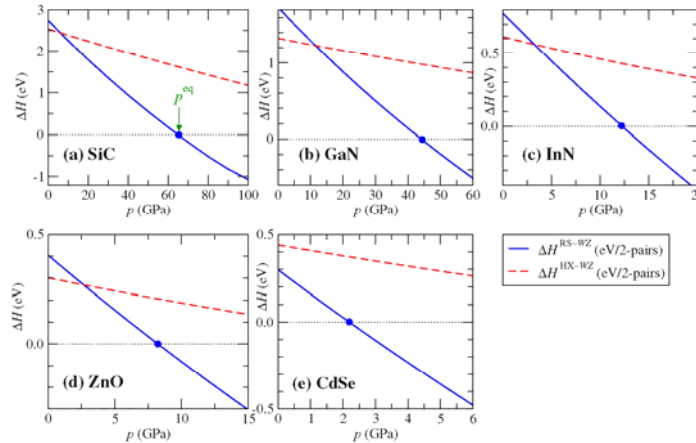


FIG. 6. (Color online) Enthalpy differences (ΔH), in the unit of eV/2 pairs, between RS and WZ (solid line) and HX and WZ (dashed line) as a function of hydrostatic pressure for (a) SiC, (b) GaN, (c) InN, (d) ZnO, and (e) CdSe. As the pressure reaches the equilibrium value (p^{eq} , indicated by solid dots), the enthalpies for RS and WZ become equal. Above p^{eq} , RS is more stable. Note that HX is never stable under hydrostatic loading.

B. Hydrostatic compression

Sufficiently high pressures can cause the WZ structure to collapse into the denser RS phase. As shown in Fig. 1, the volume of the RS structure is $\sim 17\%$ smaller than the volume of the WZ structure ($\Delta V \approx -0.17V_0$, with V_0 being the equilibrium volume of WZ). For a given constant pressure p , the difference in contributions to enthalpy by mechanical work between RS and WZ is approximately $p\Delta V$ (neglecting the difference in bulk moduli of the two phases). If p is sufficiently high, mechanical work can overcome the formation energy difference, driving the transformation forward. Figure 6 shows $\Delta H^{\text{RS-WZ}} = H^{\text{RS}} - H^{\text{WZ}}$ and $\Delta H^{\text{HX-WZ}} = H^{\text{HX}} - H^{\text{WZ}}$ as functions of p for the five compounds studied. The rather linear trends confirm that the bulk moduli of the WZ, HX, and RS phases are quite comparable. The slight deviation from linearity of $\Delta H^{\text{RS-WZ}}$ reflects the fact that the bulk modulus of RS is somewhat higher (approximately 25%) than that of WZ. Note that the slope of the $\Delta H^{\text{RS-WZ}}$ line is approximately five times that of the $\Delta H^{\text{HX-WZ}}$ line, consistent with the fact that the volume decrease associated with the WZ \rightarrow RS transformation (17%) is approximately five times of that associated with the WZ \rightarrow HX transformation (3.6%).

The equilibrium pressure p^{eq} between the WZ and RS structures (the pressure at which the enthalpies of RS and WZ become equal) can be obtained by examining the enthalpy surfaces at several pressures. This pressure is identified with the intercept of the enthalpy curve with the horizontal axis in Fig. 6. The enthalpy surfaces of all five materials at their equilibrium pressure p^{eq} are qualitatively the same (not shown here but can be found online³⁵). There-

fore, we choose to present only the enthalpy surface for InN in Fig. 7(a). The corresponding 2D section is shown in Fig. 7(b). At $p < p^{\text{eq}}$, WZ has the lowest enthalpy. As p is increased above p^{eq} , RS has a lower enthalpy than WZ. p^{eq} depends strongly on the ionicity of the compound. This is expected because the initial energy difference between WZ and RS ($\Delta E^{\text{RS-WZ}} = E^{\text{RS}} - E^{\text{WZ}}$) depends on the ionicity of the material (from $\Delta E^{\text{RS-WZ}} = 2.74$ eV for SiC to 0.30 eV for CdSe). SiC has the highest $\Delta E^{\text{RS-WZ}}$ and therefore the highest p^{eq} (64.9 GPa). CdSe has the lowest $\Delta E^{\text{RS-WZ}}$ and therefore the lowest p^{eq} (2.2 GPa). The equilibrium pressures of the five materials are listed in Table III. Our calculated equilibrium pressures are in good agreement with other calculated results in general (see Table III). To compare with experiments, one should not directly compare the calculated equilibrium pressure with either the critical pressures of the upward or downward WZ to RS transformations. This is because there is a transformation barrier between the two phases that causes the upward critical pressure to be higher (and the downward critical pressure to be lower) than the equilibrium pressure.^{3,18} The averages between the upward and downward critical pressures, shown as p_t in Table III, are shown as an approximate experimental equilibrium pressures and are in good agreement with the calculated equilibrium pressures.

To gain insight on the transformation enthalpy barrier, we extracted (from the plots) the *homogeneous* transformation barrier (in the unit of eV/2 pairs) of these five materials and tabulated in Table III using square brackets. The barrier for ZnO of 0.30 eV/2 pairs is the same as Limpijumnong and Jungthawan have previously reported.¹⁸ The barriers for SiC and GaN of 1.26 and 0.76 eV/2 pairs are in good agreement

SARASAMAK *et al.*

PHYSICAL REVIEW B 77, 024104 (2008)

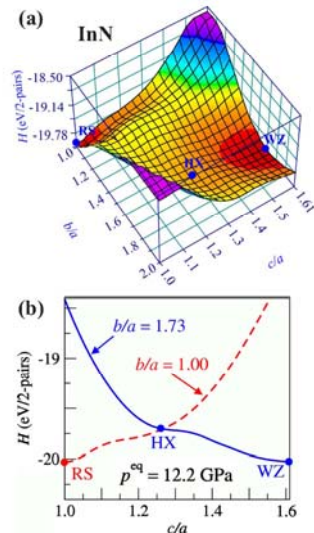


FIG. 7. (Color online) (a) Enthalpy surface maps (in eV/2 pairs) for InN at its RS-WZ equilibrium pressures, $p^{\text{eq}} = 12.2$ GPa. (b) 2D sections of the enthalpy surface for $b/a = 1.73$ (solid line) and 1.00 (dashed line).

with the calculated values reported by Miao and Lambrecht³⁸ (for SiC) of 1.2 eV/2 pairs and by Limpijumng and Lambrecht²⁰ (for GaN) of 0.9 eV/2 pairs. We can see that the magnitude of the barrier increases with the zero pressure energy difference between phases ($\Delta E^{\text{RS-WZ}}$), hence the ionicity. The detailed investigation of the barriers will be a subject of further study on more materials in the future.

Figure 8 shows the variation of equilibrium pressure with the initial energy difference. An approximately linear dependence of p^{eq} on $\Delta E^{\text{RS-WZ}}$ is seen. The linear fit gives

$$p^{\text{eq}} \approx 25.97(\Delta E^{\text{RS-WZ}}) - 4.68. \quad (3)$$

The units of p^{eq} and $\Delta E^{\text{RS-WZ}}$ are in GPa and eV/2 pairs, respectively. This approximate universal relationship can be used to estimate the difference in the formation energy of the RS and WZ phases when the equilibrium pressure is known or vice versa.

Figure 6 also shows that the $\Delta H^{\text{HX-WZ}}$ line never intercepts the horizontal axis for all five materials over the pressure range analyzed. Obviously, HX is not a thermodynamically stable structure under hydrostatic compression and the WZ \rightarrow HX transformation does not occur for such conditions.

C. Uniaxial compression along the [0001] direction

Figure 1 shows that HX has a lattice constant c significantly shorter ($\sim 19\%$) than that of WZ in the [0001] direc-

TABLE III. Equilibrium pressure, transformation barrier, and stresses for SiC, GaN, InN, ZnO, and CdSe for the WZ \rightarrow RS and WZ \rightarrow HX transformations. p^{eq} is the hydrostatic pressure that establishes the equilibrium between the WZ and RS structures and p_t (reported here as an average between the experimental upward and downward pressure of transformations) is the corresponding experimental value. $-\sigma_c^{\text{eq}}$ (σ_b^{eq}) is the value of the compressive (tensile) force per unit area along the c direction (b direction) at which the WZ and HX structures are in equilibrium. For CdSe, although $-\sigma_c^{\text{eq}} = 3.8$ GPa provides equilibrium between the WZ and HX phases, the RS phase has a lower enthalpy (hence more stable) under this condition. The transformation enthalpy barrier in eV/2 pairs are given in square brackets following p^{eq} in the same column.

Material	RS		HX		
	p^{eq} (GPa) (Present)	p^{eq} (GPa) (Other)	p_t (GPa) (Expt.)	$-\sigma_c^{\text{eq}}$ (GPa)	σ_b^{eq} (GPa)
SiC	64.9[1.26]	60, ^a 66.6, ^b 66, ^c 92 ^d	67.5 ^e	60.5	
GaN	44.1[0.76]	51.8, ^f 42.9 ^g	52.2, ^h 31 ⁱ	30.5	
InN	12.2[0.51]	21.6, ^f 11.1 ^g	10, ^j 12.1 ^h	9.6	14.7
ZnO	8.2[0.30]	6.6, ^k 9.3, ^l 8.0 ^m	5.5, ⁿ 8.5 ^o	6.0	10.8
CdSe	2.2[0.40]	2.5 ^p	2.1 ^q	3.8	5.8

^aDFT (GGA) calculations by Miao and Lambrecht (Ref. 41).

^bDFT (LDA) calculations (of zincblende to RS) by Karch *et al.* (Ref. 17).

^cDFT (LDA) calculations (of zincblende to RS) by Chang and Cohen (Ref. 42).

^dDFT (B3LYP) calculations (of zincblende to RS) by Catti (Ref. 43).

^eSynchrotron angle dispersive x-ray diffraction (ADX) experiment by Yoshida *et al.* (Ref. 10).

^fDFT (LDA) calculations by Christensen and Gorczyca (Ref. 14).

^gDFT (LDA) calculations by Serrano *et al.* (Ref. 44).

^hADX experiment by Ueno *et al.* (Ref. 6).

ⁱSynchrotron energy-dispersive x-ray diffraction (EDX) by Xia *et al.* (Ref. 8).

^jSynchrotron EDX experiment by Xia *et al.* (Ref. 9).

^kDFT (LDA) calculations by Jaffe *et al.* (Ref. 16).

^lDFT (GGA) calculations by Jaffe *et al.* (Ref. 16).

^mDFT (GGA) calculations by Ahuja *et al.* (Ref. 45).

ⁿSynchrotron EDX experiment by Desgreniers. (Ref. 5).

^oSynchrotron EDX experiment by Recio *et al.* (Ref. 46).

^pDFT (LDA) calculations by Côté *et al.* (Ref. 23).

^qEDX experiment by Cline and Stephens (Ref. 4).

tion. This difference allows WZ to transform into HX via compression in the c direction. Under constant compressive stress $-\sigma_c$ (negative sign indicates compression), the mechanical contribution to the enthalpy difference between WZ and HX is $-A_{\text{HX}}\sigma_c\Delta c$, where $\Delta c \approx -0.19c$. A sufficiently high $-\sigma_c$ would allow mechanical work to offset the energy difference between HX and WZ, affecting the transformation into the HX structure. The shapes of the enthalpy surfaces for SiC, GaN, InN, and ZnO at their respective equilibrium compressive stress $-\sigma_c^{\text{eq}}$ are qualitatively the same (not shown here but can be found online³⁵). Therefore, we choose

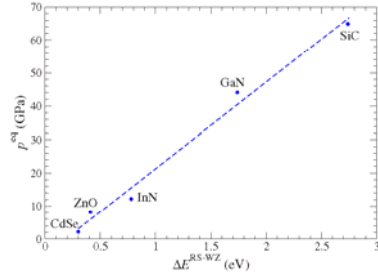


FIG. 8. (Color online) Correlation between equilibrium hydrostatic pressure (p^{eq}) and the difference in energy (ΔE) between the RS and WZ phases of the five materials. p^{eq} is the pressure at which the WZ and RS structures are in equilibrium, as illustrated in Fig. 6 and tabulated in Table III. The energy difference $\Delta E = E^{\text{RS}} - E^{\text{WZ}}$ is calculated under the conditions of zero external loading and is tabulated in Table II.

to present the enthalpy surface for InN with a 2D section plot in Fig. 9(a). The stability of the HX phase can be better analyzed through the enthalpy difference $\Delta H^{\text{HX-WZ}} = H^{\text{HX}} - H^{\text{WZ}}$ as a function of the compressive stress along the c direction (dashed lines, Fig. 10). If the elastic moduli of HX and WZ along the c direction are assumed to be equal, ΔH would vary linearly with $-\sigma_c$ with an approximate slope of $A_{ab}\Delta c \approx -0.19(abc/2) \approx -0.19V$. Figure 10 also shows the enthalpy difference between RS and WZ, $\Delta H^{\text{RS-WZ}} = H^{\text{RS}} - H^{\text{WZ}}$ (solid lines). Note that $\Delta H^{\text{HX-WZ}}$ and $\Delta H^{\text{RS-WZ}}$

show similar trends, with similar slopes. This is because for the WZ \rightarrow RS transformation, $\Delta c/c \approx 18\%$, while for the WZ \rightarrow HX transformation, $\Delta c/c \approx 19\%$.

For all materials except CdSe, $\Delta H^{\text{HX-WZ}}$ is always lower than $\Delta H^{\text{RS-WZ}}$, indicating that HX is more stable than RS under compression in the c direction. For CdSe, where initially (i.e., under no load condition) the RS phase has a slightly lower energy than HX, $\Delta H^{\text{RS-WZ}}$ is always lower than $\Delta H^{\text{HX-WZ}}$, indicating that RS is the preferred structure over HX under uniaxial compression along the $[0001]$ direction as well as under hydrostatic compression. As a result, the enthalpy surface at $-\sigma_c^{\text{eq}}$ of CdSe [Fig. 9(b)] is qualitatively different from those of the other four materials [represented by Fig. 9(a)], i.e., the RS phase has lower enthalpy. The equilibrium stress for the transformation ($-\sigma_c^{\text{eq}}$) of each material is shown in Fig. 10. Below $-\sigma_c^{\text{eq}}$, WZ phase is stable. Above $-\sigma_c^{\text{eq}}$, HX is stable (RS for CdSe). The values of $-\sigma_c^{\text{eq}}$ depend on the initial energy difference (ΔE) between WZ and HX and are listed in Table III. For SiC, $\Delta E = E^{\text{HX}} - E^{\text{WZ}} = 2.53$ eV, the stress required to cause the HX \rightarrow WZ transformation is high ($-\sigma_c^{\text{eq}} = 60.5$ GPa). On the other hand, for ZnO, $\Delta E = 0.26$ eV and $-\sigma_c^{\text{eq}} = 6.0$ GPa which is only 1/10 of the stress level required for SiC. This linear trend is clearly seen in Fig. 11 which shows $-\sigma_c^{\text{eq}}$ as a function of ΔE for the materials analyzed. The linear fit gives

$$-\sigma_c^{\text{eq}} \approx 25.72(\Delta E^{\text{HX-WZ}}) - 4.56. \quad (4)$$

The coefficients in the equation are based on the units of $-\sigma_c^{\text{eq}}$ and $\Delta E^{\text{HX-WZ}}$ in GPa and eV/2 pairs, respectively. The similarity in the numerical values of coefficients of Eqs. (4) and (3) is fortuitous. Note that the WZ-HX homogeneous transformation enthalpy barrier is significantly lower than that of WZ-RS, i.e., always less than 0.1 eV/2 pairs for all materials studied except SiC. However, for SiC, the barrier is only slightly higher, i.e., 0.13 eV/2 pairs.

D. Uniaxial tension along the $[01\bar{1}0]$ direction

The HX structure also has a longer dimension in the $[01\bar{1}0]$ direction compared to the WZ structure (longer by approximately 9%, see Fig. 1, middle column). This difference allows WZ to transform into HX via tension in the b ($[01\bar{1}0]$) direction. Note that the difference in b between the two structures is only about half of the difference in c . Accordingly, the mechanical enthalpy contribution $A_{ab}\sigma_b\Delta b$ is roughly half of the case of c compression for the comparable stress magnitude. Only three (InN, ZnO, and CdSe) out of the five materials studied have a local minimum corresponding to the HX structure under tensile loading along the b direction. We choose to present the enthalpy surfaces for InN (those for ZnO and CdSe can be found online³⁵) at the equilibrium tensile stress σ_b^{eq} [Fig. 12(a)] with its 2D section plot [Fig. 12(b)]. The plot³⁵ between the enthalpy differences $\Delta H^{\text{HX-WZ}} = H^{\text{HX}} - H^{\text{WZ}}$ as functions of tensile stress σ_b are similar to the compressive stress case. The equilibrium tensile stress σ_b^{eq} (14.7, 10.8, and 5.8 GPa for InN, ZnO, and CdSe, respectively) is approximately twice the equilibrium compressive stress $-\sigma_c^{\text{eq}}$ for the c direction. EP-MD simula-

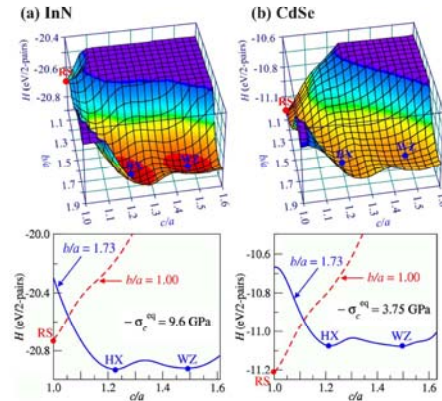


FIG. 9. (Color online) Enthalpy surface maps for (a) InN and (b) CdSe at their respective HX-WZ equilibrium c direction stress ($-\sigma_c^{\text{eq}}$). Their 2D sections for $b/a = 1.73$ (solid line) and 1.00 (dashed line) are also shown in the bottom panel. Note that, unlike other materials studied here, CdSe favors RS over HX phase under c -direction stress.

SARASAMAK *et al.*

PHYSICAL REVIEW B 77, 024104 (2008)

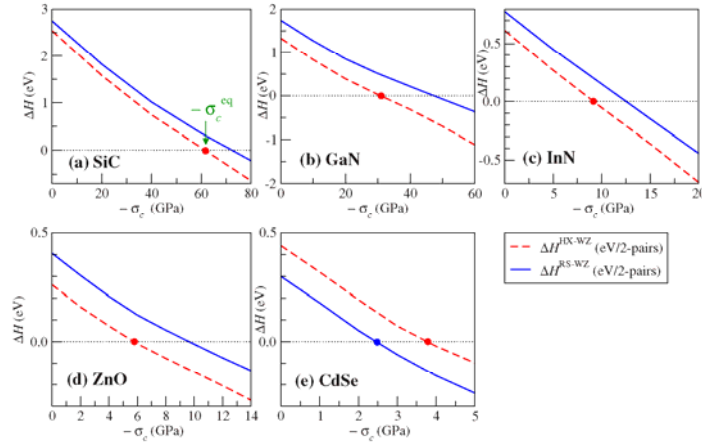


FIG. 10. (Color online) Enthalpy differences (ΔH) between the RS and WZ (solid line) and HX and WZ (dashed line) as a function of c -direction stress ($-\sigma_c$) for (a) SiC, (b) GaN, (c) InN, (d) ZnO, and (e) CdSe. As the magnitude of the stress reaches the equilibrium value ($-\sigma_c^{\text{eq}}$, indicated by solid dots), enthalpies of the HX and WZ structures become comparable. At stresses above $-\sigma_c^{\text{eq}}$, the HX phase is more stable.

tions have shown that under tensile loading, $[01\bar{1}0]$ -oriented ZnO nanowires can indeed transform into the HX structure under tensile loading.²⁸ The nanowires can sustain tensile stresses up to 14 GPa before failure, which is well above the equilibrium stress σ_b^{eq} predicted here. The equilibrium transformation stress of $\sigma_b^{\text{eq}}=5.8$ GPa for CdSe is the lowest among the materials studied. For nanostructures, other factors such as surface effects may contribute to facilitate the WZ \rightarrow HX transformation.³⁹ As a result, HX can emerge as

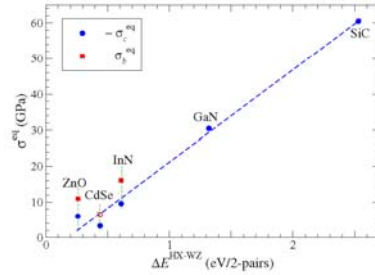


FIG. 11. (Color online) Correlation between equilibrium stresses ($-\sigma_c^{\text{eq}}$ and σ_b^{eq}) and the difference in energy (ΔE) between the HX and WZ phases for the five materials. $-\sigma_c^{\text{eq}}$ (σ_b^{eq}) is the equilibrium value of the c -direction compressive stress (b -direction tensile stress) for the HX and RS structures (see Table III). The energy difference $\Delta E=E^{\text{HX}}-E^{\text{WZ}}$ is calculated under conditions of zero external loading and is tabulated in Table II.

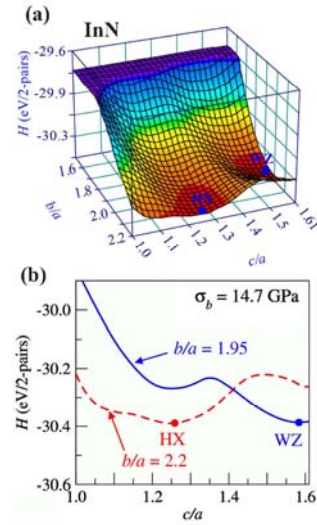


FIG. 12. (Color online) (a) Enthalpy surface maps (in eV/2 pairs) for InN at its HX-WZ stresses along the b direction, $\sigma_b^{\text{eq}}=14.7$ GPa. (b) 2D sections of the enthalpy surface for $b/a=1.95$ (solid line) and 2.20 (dashed line).

an intermediate phase during a WZ→RS transformation in CdSe nanorods,³⁹ even though it does not have the lowest enthalpy in the bulk calculations. The relationship between σ_b^{eq} and $\Delta E^{\text{HX-WZ}} = E^{\text{HX}} - E^{\text{WZ}}$ is shown Fig. 11. Note that the σ_b^{eq} of CdSe may be higher than its fracture strength.

A local minimum for HX is not observed in the enthalpy surfaces for SiC and GaN, even at extremely high theoretical levels of σ_b (60 GPa for SiC and 30 GPa for GaN).³⁵ The lack of transformation in these materials can be attributed to the fact that their equilibrium transformation stresses are higher than their respective ultimate tensile strengths ($\sigma_b^{\text{eq}} \gg \sigma_{\text{UTS}}$). Indeed, EP-MD simulations have shown that for GaN nanowires, $\sigma_{\text{UTS}} \approx 30$ GPa,⁴⁰ only a fraction of the rough estimation of equilibrium stress of $\sigma_c^{\text{eq}} \approx 60$ GPa. The σ_b^{eq} of SiC is even higher since it has a higher energy difference between WZ and HX, making it more likely to have fractured before reaching its theoretical equilibrium stress of $\sigma_c^{\text{eq}} \approx 120$ GPa.

V. CONCLUSIONS

First principles calculations are carried out to study the stability of the WZ, RS, and HX phases of SiC, GaN, InN, ZnO, and CdSe under loading of different triaxialities. The energy of the materials correlates with their ionicity. At ambient conditions, WZ has the lowest energy level, HX has the second highest energy level, and RS has the highest energy level (with the exception of CdSe whose RS phase has a lower energy level than its HX phase). All five materials have the fourfold *wurtzite* structure as their stable and naturally occurring phase. Under all around hydrostatic compression, the materials can transform into the sixfold coordinated RS structure. Under uniaxial compression along the [0001] direction and uniaxial tension along the [01 $\bar{1}$ 0] direction, the materials can transform into the fivefold coordinated *unbuckled wurtzite* structure. The equilibrium conditions for the transformations are outlined. For the WZ→RS transformation, the equilibrium hydrostatic pressures (p^{eq}) are predicted

to be 64.9, 44.1, 12.2, 8.2, and 2.2 GPa for SiC, GaN, InN, ZnO, and CdSe, respectively. These values are in good agreement with other theoretical calculations and experimental measurements. For the WZ→HX transformation under uniaxial compression along the [0001] direction, the equilibrium stresses ($-\sigma_c^{\text{eq}}$) are 60.5, 30.5, 9.6, and 6.0 GPa for SiC, GaN, InN, and ZnO, respectively. For CdSe, uniaxial compression along the [0001] direction induces a WZ→RS transformation at a stress of 2.4 GPa instead of the WZ→HX transformation because the formation energy of RS is lower than HX for CdSe. For the WZ→HX transformation under uniaxial tension along the [01 $\bar{1}$ 0] direction, the equilibrium transformation stresses (σ_b^{eq}) are 14.7, 10.8, and 5.8 GPa for InN, ZnO, and CdSe, respectively. The stress level for CdSe is close to its fracture limit. No transformation is observed for SiC and GaN under tension along the [01 $\bar{1}$ 0] direction due to the fact that their theoretical equilibrium transformation stresses are well above their respective ultimate fracture strengths. The magnitudes of p^{eq} , $-\sigma_c^{\text{eq}}$, and σ_b^{eq} are approximately linearly dependent with the formation energy differences between the relevant phase of the materials. Based on the calculations of five materials, we established a general linear function between p^{eq} and RS–WZ energy difference that could be useful for predicting the difference in formation energy of the RS and WZ phases of other materials when the equilibrium pressure is known or vice versa.

ACKNOWLEDGMENTS

This work was supported by NANOTEC (NN49-024) and Thailand Research Fund (BRG4880015 and PHD/0264/2545). A.J.K. and M.Z. are supported by NSF (CMS9984298) and NSFC (10528205). Computations are carried out at the National Synchrotron Research Center (Thailand) and at NAVO and ASC MSRCs through AFOSR MURI (D49620-02-1-0382).

APPENDIX

Tables IV–VIII.

TABLE IV. Lattice parameters for WZ, HX, and RS SiC under equilibrium loading conditions.

Parameters	WZ $p=0$ GPa	HX $-\sigma_c^{\text{eq}}=60.5$ GPa	RS $p^{\text{eq}}=64.9$ GPa
a (Å)	3.05 (3.06, ^a 3.08 ^b)	3.32	4.00 (3.68, ^{a,c} 3.84 ^d)
b (Å)	5.28	5.74	4.00
c (Å)	4.97	3.98	4.00
$V = \frac{abc}{2}$ (Å ³)	40.0	38.0	32.0
c/a	1.63	1.20	1.00
b/a	1.73	1.73	1.00
u	0.38	0.50	0.50
v	0.35	0.33	0.50

^aDFT (LDA) calculations by Karch *et al.* (Ref. 17).

^bXRD experiment by Schultz *et al.* (Ref. 47).

^cSynchrotron ADX by Yoshida *et al.* (Ref. 10).

^dDFT (LDA) calculations by Hatch *et al.* (Ref. 48).

TABLE V. Lattice parameters for WZ, HX, and RS GaN under equilibrium loading conditions.

Parameters	WZ	HX		RS
	$p=0$ GPa	$-\sigma_c^{\text{eq}}=30.5$ GPa	$\sigma_b^{\text{eq}}=14.7$ GPa	$p^{\text{eq}}=44.1$ GPa
a (Å)	3.15 (3.19, ^a 3.16, ^{b,c} 3.10 ^d)	3.43	3.48	4.16 (4.01, ^a 4.10, ^b 4.07 ^e)
b (Å)	5.46	5.94	6.46	4.16
c (Å)	5.11	4.12	4.20	4.16
$V=\frac{abc}{2}$ (Å ³)	44.0	42.0	44.0	36.0
c/a	1.62	1.20	1.30	1.00
b/a	1.73	1.73	2.00	1.00
u	0.38	0.50	0.50	0.50
v	0.35	0.33	0.31	0.50

^aSynchrotron EDX experiment by Xia *et al.* (Ref. 8).^bXRD experiment by Xie *et al.* (Ref. 49).^cDFT (LDA) calculations by Kim *et al.* (Ref. 50).^dDFT (LDA) calculations by Yeh *et al.* (Ref. 51).^eXRD experiment by Lada *et al.* (Ref. 52).

TABLE VI. Lattice parameters for WZ, HX, and RS InN under equilibrium loading conditions.

Parameters	WZ	HX		RS
	$p=0$ GPa	$-\sigma_c^{\text{eq}}=9.6$ GPa	$\sigma_b^{\text{eq}}=14.7$ GPa	$p^{\text{eq}}=12.2$ GPa
a (Å)	3.54 (3.53, ^a 3.54, ^{b,c} 3.52 ^d)	3.82	3.48	4.64 (4.67, ^e 4.62 ^d)
b (Å)	6.13	6.62	7.66	4.64
c (Å)	5.70	4.59	4.35	4.64
$V=\frac{abc}{2}$ (Å ³)	61.9	58.1	58.0	50.0
c/a	1.61	1.20	1.25	1.00
b/a	1.73	1.73	2.20	1.00
u	0.38	0.50	0.51	0.50
v	0.35	0.33	0.31	0.50

^aDFT (LDA) calculations by Kim *et al.* (Ref. 50).^bDFT (LDA) calculations by Yeh *et al.* (Ref. 51).^cXRD experiments by Osamura *et al.* (Ref. 53).^dDFT (LDA) calculations by Furthmüller *et al.* (Ref. 54).^eADX experiment by Ueno *et al.* (Ref. 6).

TABLE VII. Lattice parameters for WZ, HX, and RS ZnO under equilibrium loading conditions.

Parameters	WZ	HX		RS
	$p=0$ GPa	$-\sigma_c^{\text{eq}}=6.0$ GPa	$\sigma_b^{\text{eq}}=10.8$ GPa	$p^{\text{eq}}=8.2$ GPa
a (Å)	3.21 (3.20, ^a 3.25, ^{b,c} 3.26 ^d)	3.49	3.24	4.24 (4.28, ^b 4.27 ^{c,e})
b (Å)	5.54	6.03	6.46	4.24
c (Å)	5.15 (5.17, ^a 5.22 ^d)	4.19	4.20	4.24
$V=\frac{abc}{2}$ (Å ³)	45.7 (46.69, ^e 47.24, ^f 47.98 ^d)	44.1	44.0	38.1 (39.03, ^e 38.16 ^f)
c/a	1.61 (1.59 ^f)	1.20	1.30	1.00
b/a	1.73	1.73	2.00	1.00
u	0.38 (0.38 ^{a,d,f})	0.50	0.50	0.50
v	0.33	0.33	0.31	0.50

^aDFT (LDA) calculations by Malashevich and Vanderbilt (Ref. 56).^bSynchrotron EDX experiments by Desgrenier (Ref. 5).^cXRD experiments by Karzel *et al.* (Ref. 55).^dEXAFS experiments by Decremps *et al.* (Ref. 57).^eDFT (GGA) calculations by Jaffe *et al.* (Ref. 16).^fDFT (GGA) calculations by Ahuja *et al.* (Ref. 45).

Manuscript published in Physical Review B

STABILITY OF WURTZITE, UNBUCKLED WURTZITE...

PHYSICAL REVIEW B 77, 024104 (2008)

TABLE VIII. Lattice parameters for WZ, HX, and RS CdSe under equilibrium loading conditions.

Parameters	WZ	HX		RS
	$p=0$ GPa	$-\sigma_c^{\text{eq}}=3.75$ GPa	$\sigma_b^{\text{eq}}=5.8$ GPa	$p^{\text{eq}}=2.2$ GPa
a (Å)	4.27 (4.30 ^a)	4.66	4.18	5.54 (5.58, ^a 5.71 ^b)
b (Å)	7.39	8.06	8.78	5.54
c (Å)	6.96	5.59	5.44	5.54
$V=\frac{abc}{2}$ (Å ³)	109.8	105.0	99.9	85.0
c/a	1.63	1.20	1.30	1.00
b/a	1.73	1.73	2.10	1.00
u	0.38	0.50	0.50	0.50
v	0.35	0.33	0.31	0.50

^aDFT calculations by Benkhetou *et al.* (Ref. 58).^bXRD experiment by Wickham *et al.* (Ref. 59).

- ¹C. T. Chan, D. Vanderbilt, S. G. Louie, and J. R. Chelikowsky, Phys. Rev. B **33**, 7941 (1986).
- ²S. Fahy, S. G. Louie, and M. L. Cohen, Phys. Rev. B **34**, 1191 (1986).
- ³A. Mujica, A. Rubio, A. Muñoz, and R. J. Needs, Rev. Mod. Phys. **75**, 863 (2003).
- ⁴C. F. Cline and D. R. Stephens, J. Appl. Phys. **36**, 2869 (1965).
- ⁵S. Desgreniers, Phys. Rev. B **58**, 14102 (1998).
- ⁶M. Ueno, M. Yoshida, A. Onodera, O. Shimomura, and K. Takemura, Phys. Rev. B **49**, 14 (1994).
- ⁷X. Wu, Z. Wu, L. Guo, C. Liu, X. Li, and H. Xu, Solid State Commun. **135**, 780 (2005).
- ⁸H. Xia, Q. Xia, and A. L. Ruoff, Phys. Rev. B **47**, 12925 (1993).
- ⁹Q. Xia, H. Xia, and A. L. Ruoff, Mod. Phys. Lett. B **8**, 345 (1994).
- ¹⁰M. Yoshida, A. Onodera, M. Ueno, K. Takemura, and O. Shimomura, Phys. Rev. B **48**, 10587 (1993).
- ¹¹C. H. Bates, W. B. White, and R. Roy, Science **137**, 993 (1962).
- ¹²J. Z. Jiang, J. S. Olsen, L. Gerward, D. Frost, D. Rubie, and J. Peyronneau, Europhys. Lett. **50**, 48 (2000).
- ¹³K. Kusaba, Y. Syono, and T. Kikegawa, Proc. Jpn. Acad., Ser. B: Phys. Biol. Sci. **75**, 1 (1999).
- ¹⁴N. E. Christensen and I. Gorczyca, Phys. Rev. B **50**, 4397 (1994).
- ¹⁵J. E. Jaffe and A. C. Hess, Phys. Rev. B **48**, 7903 (1993).
- ¹⁶J. E. Jaffe, J. A. Snyder, Z. Lin, and A. C. Hess, Phys. Rev. B **62**, 1660 (2000).
- ¹⁷K. Karch, F. Bechstedt, P. Pavone, and D. Strauch, Phys. Rev. B **53**, 13400 (1996).
- ¹⁸S. Limpjumnong and S. Jungthawan, Phys. Rev. B **70**, 054104 (2004).
- ¹⁹S. Limpjumnong and W. R. L. Lambrecht, Phys. Rev. B **63**, 104103 (2001).
- ²⁰S. Limpjumnong and W. R. L. Lambrecht, Phys. Rev. Lett. **86**, 91 (2001).
- ²¹J. Serrano, A. H. Romero, F. J. Manjon, R. Lauck, M. Cardona, and A. Rubio, Phys. Rev. B **69**, 094306 (2004).
- ²²A. Zaoui and W. Sekkal, Phys. Rev. B **66**, 174106 (2002).
- ²³M. Côté, O. Zakharov, A. Rubio, and M. L. Cohen, Phys. Rev. B **55**, 13025 (1997).
- ²⁴F. Decremps, J. Pellicier-Porres, F. Datehi, J. P. Itie, A. Polian, F. Baudelet, and J. Z. Jiang, Appl. Phys. Lett. **81**, 4820 (2002).
- ²⁵S. Y. Bae, H. W. Seo, J. Park, H. Yang, J. C. Park, and S. Y. Lee, Appl. Phys. Lett. **81**, 126 (2002).
- ²⁶Z. W. Pan, Z. R. Dai, and Z. L. Wang, Science **291**, 1947 (2001).
- ²⁷A. J. Kulkarni, K. Sarasamak, S. Limpjumnong, and M. Zhou, Philos. Mag. **87**, 2117 (2007).
- ²⁸A. J. Kulkarni, M. Zhou, K. Sarasamak, and S. Limpjumnong, Phys. Rev. Lett. **97**, 105502 (2006).
- ²⁹L. Zhang and H. Huang, Appl. Phys. Lett. **89**, 183111 (2006).
- ³⁰L. Zhang and H. Huang, Appl. Phys. Lett. **90**, 023115 (2007).
- ³¹D. Vanderbilt, Phys. Rev. B **41**, 7892 (1990).
- ³²G. Kresse and J. Furthmüller, Comput. Mater. Sci. **6**, 15 (1996).
- ³³Here, we are interested only in the energy differences between phases. The calculations show that GGA consistently give slightly larger energy differences of between 0.1 and 0.4 eV/2 pairs (the largest case is for SiC which the energy difference by itself is large, i.e., 3 eV).
- ³⁴H. J. Monkhorst and J. D. Pack, Phys. Rev. B **13**, 5188 (1976).
- ³⁵See EPAPS Document No. E-PRBMDO-77-026802 for additional enthalpy surface maps. For more information on EPAPS, see <http://www.aip.org/pubservs/epaps.html>.
- ³⁶For some low pressure or low stress loading conditions, the enthalpy surface (or energy surface for the stress-free case) might not have a local minimum near the HX structure. In such cases, the c/a and b/a defining the enthalpy of the HX phase is taken from the first (meta)stable HX when the pressure and/or stress is increased.
- ³⁷J. C. Phillips, Rev. Mod. Phys. **42**, 317 (1970).
- ³⁸M. S. Miao and W. R. L. Lambrecht, Phys. Rev. B **68**, 092103 (2003).
- ³⁹M. Grunwald, E. Rabani, and C. Dellago, Phys. Rev. Lett. **96**, 255701 (2006).
- ⁴⁰Z. Wang, X. Zu, L. Yang, F. Gao, and W. J. Weber, Phys. Rev. B **76**, 045310 (2007).

Manuscript published in Physical Review B

SARASAMAK *et al.*PHYSICAL REVIEW B **77**, 024104 (2008)

- ⁴¹M. S. Miao and W. R. L. Lambrecht, *Phys. Rev. B* **68**, 092103 (2003).
- ⁴²K. J. Chang and M. L. Cohen, *Phys. Rev. B* **35**, 8196 (1987).
- ⁴³M. Catti, *Phys. Rev. Lett.* **87**, 035504 (2001).
- ⁴⁴J. Serrano, A. Rubio, E. Hernandez, A. Munoz, and A. Mujica, *Phys. Rev. B* **62**, 16612 (2000).
- ⁴⁵R. Ahuja, L. Fast, O. Eriksson, J. M. Wills, and B. Johansson, *J. Appl. Phys.* **83**, 8065 (1998).
- ⁴⁶J. M. Recio, M. A. Blanco, V. Luana, R. Pandey, L. Gerward, and J. S. Olsen, *Phys. Rev. B* **58**, 8949 (1998).
- ⁴⁷H. Schulz and K. H. Thiemann, *Solid State Commun.* **32**, 783 (1979).
- ⁴⁸D. Hatch, H. T. Stokes, J. Dong, J. Gunter, H. Wang, and J. Lewis, *Phys. Rev. B* **71**, 184109 (2005).
- ⁴⁹Y. Xie, Y. Qian, S. Zhang, W. Wang, X. Liu, and Y. Zhang, *Appl. Phys. Lett.* **69**, 334 (1996).
- ⁵⁰K. Kim, W. R. L. Lambrecht, and B. Segall, *Phys. Rev. B* **53**, 16310 (1996).
- ⁵¹C. Y. Yeh, Z. W. Lu, S. Froyen, and A. Zunger, *Phys. Rev. B* **46**, 10086 (1992).
- ⁵²M. Lada, A. G. Cullis, P. J. Parbrook, and M. Hopkinson, *Appl. Phys. Lett.* **83**, 2808 (2003).
- ⁵³K. Osamura, S. Naka, and Y. Murakami, *J. Appl. Phys.* **46**, 3432 (1975).
- ⁵⁴J. Furthmüller, P. H. Hahn, F. Fuchs, and F. Bechstedt, *Phys. Rev. B* **72**, 205106 (2005).
- ⁵⁵H. Karzel, W. Potzel, M. Kofferlein, W. Schiessl, M. Steiner, U. Hiller, G. M. Kalvius, D. W. Mitchell, T. P. Das, P. Blaha, K. Schwarz, and M. P. Pasternak, *Phys. Rev. B* **53**, 11425 (1996).
- ⁵⁶A. Malashevich and D. Vanderbilt, *Phys. Rev. B* **75**, 045106 (2007).
- ⁵⁷F. Decremps, F. Datchi, A. M. Saitta, A. Polian, S. Pascarelli, A. D. Cicco, J. P. Itie, and F. Baudlet, *Phys. Rev. B* **68**, 104101 (2003).
- ⁵⁸N. Benkhetou, D. Rached, B. Soudini, and M. Driz, *Phys. Status Solidi B* **241**, 101 (2004).
- ⁵⁹J. N. Wickham, A. B. Herhold, and A. P. Alivisatos, *Phys. Rev. Lett.* **84**, 923 (2000).

Available online at www.sciencedirect.com

Mechanics Research Communications 35 (2008) 73–80

MECHANICS
RESEARCH COMMUNICATIONSwww.elsevier.com/locate/mechrescom

Effect of load triaxiality on polymorphic transitions in zinc oxide

A.J. Kulkarni^a, K. Sarasamak^b, J. Wang^c, F.J. Ke^{c,d},
S. Limpijumngong^b, M. Zhou^{a,*}^a The George W. Woodruff School of Mechanical Engineering, Georgia Institute of Technology, Atlanta, GA 30332-0405, USA^b School of Physics, Suranaree University of Technology and National Synchrotron Research Center, Nakhon Ratchasima 30000, Thailand^c Department of Physics, Beihang University, Beijing 100083, China^d Institute of Mechanics, Chinese Academy of Sciences, Beijing 100080, China

Received 31 August 2007

Available online 21 September 2007

Abstract

Molecular dynamics (MD) simulations and first-principles calculations are carried out to analyze the stability of both newly discovered and previously known phases of ZnO under loading of various triaxialities. The analysis focuses on a graphite-like phase (HX) and a body-centered-tetragonal phase (BCT-4) that were observed recently in $[01\bar{1}0]$ - and $[0001]$ -oriented nanowires respectively under uniaxial tensile loading as well as the natural state of wurtzite (WZ) and the rocksalt (RS) phase which exists under hydrostatic pressure loading. Equilibrium critical stresses for the transformations are obtained. The WZ \rightarrow HX transformation is found to be energetically favorable above a critical tensile stress of 10 GPa in $[01\bar{1}0]$ nanowires. The BCT-4 phase can be stabilized at tensile stresses above 7 GPa in $[0001]$ nanowires. The RS phase is stable at hydrostatic pressures above 8.2 GPa. The identification and characterization of these phase transformations reveal a more extensive polymorphism of ZnO than previously known. A crystalline structure–load triaxiality map is developed to summarize the new understanding.

© 2007 Elsevier Ltd. All rights reserved.

Keywords: Phase transformations; Load triaxiality; Zinc oxide; Molecular dynamics; Density functional theory**1. Introduction**

Polymorphic transitions occur in materials with non-convex free energy landscapes or materials that display multiple local minima along with a global minimum under ambient conditions. The global minimum in free energy corresponds to a stable crystalline structure and is the natural state of the material. Each local minimum, on the other hand, represents a metastable lattice structure that the material can assume under external stimuli. Traditionally, external loading and temperature changes are used to transform materials from their stable structures to metastable states. Stress-induced phase transformations are widely observed in

* Corresponding author. Tel.: +1 404 894 3294; fax: +1 404 894 0186.
E-mail address: min.zhou@gatech.edu (M. Zhou).

groups IV, III-V and II-VI materials including ZnO, which have been predominantly studied through compressive loading (Mujica et al., 2003). Having a parent wurtzite (WZ, $P6_3mc$ space group) structure, these materials transform to a rocksalt (RS, $Fm\bar{3}m$ space group) structure under high hydrostatic pressures. The recent fabrication of defect-free, single-crystalline nanowires, nanobelts and nanorings of ZnO (IIB-VIA), GaN (IIIA-V) and CdSe (IIB-VIA) necessitates the analyses of responses to loading of various triaxialities, including bending and uniaxial tension since these materials have slender quasi one-dimensional geometries and are capable of undergoing significant elongations (Diao et al., 2004; Kulkarni et al., 2005; Liang and Zhou, 2006).

There are three hitherto known polymorphs of ZnO, including WZ, RS and zinc blende (ZB, $F\bar{4}3m$) (Ozgur et al., 2005). WZ is the natural state under ambient conditions. RS occurs under high hydrostatic pressures. ZB can only be grown on certain crystalline surfaces of cubic crystals. So far, the existence of polymorphs other than WZ, ZB and RS at various loading triaxialities has not been extensively studied. Recently, we observed a graphitic structure (hereafter referred to as HX) in $[01\bar{1}0]$ -orientated nanowires (Kulkarni et al., 2006) and a body-centered-tetragonal phase (hereafter referred to as BCT-4) in $[0001]$ -orientated nanowires under uniaxial tensile loading (Wang et al., accepted for publication). Here, we characterize the phase transformations from WZ that lead to these novel structures. For comparison and overall perspective, the WZ-to-RS transformation is also analyzed. Our analyses use first-principles calculations based on the density functional theory (DFT) and molecular dynamics (MD) simulations. Particular interest is on the crystallographic changes and critical loading condition for each transformation. A crystalline structure-load triaxiality map is developed to summarize the relationship between the structures and load condition.

2. Computational framework

The MD simulations use the Buckingham potential with charge interactions (Binks and Grimes, 1993; Wolf et al., 1999). The calculations concern the quasi-static uniaxial tension of nanowires with the $[01\bar{1}0]$ growth orientation and the hydrostatic compression of bulk ZnO. The initial structures considered are single-crystalline and wurtzite-structured with lattice constants $a = 3.249 \text{ \AA}$ and $c = 5.206 \text{ \AA}$, as illustrated in Fig. 1(a) (Wang, 2004). The computational cell for bulk structure is $29.24 \times 28.13 \times 31.24 \text{ \AA}$ in size and is created by repeating a unit wurtzite cell along the $[0001]$, $[01\bar{1}0]$ and $[2\bar{1}\bar{1}0]$ directions. Periodic boundary conditions (PBCs) are specified along the three directions to approximate infinite material extension. The $[01\bar{1}0]$ -orientated nanowires have rectangular cross-sections and $\{2\bar{1}\bar{1}0\}$ and $\{0001\}$ lateral surfaces and the computational cell size is $21.22 \times 18.95 \times 150.83 \text{ \AA}$. The $[0001]$ -orientated nanorods have hexagonal cross-sections with a six-fold symmetry around the $[0001]$ axis and six $\{01\bar{1}0\}$ lateral surfaces. The corresponding computational cell size is $28.14 \times 65.0 \times 145.8 \text{ \AA}$. PBCs are specified only along the axial directions for the nanowires.

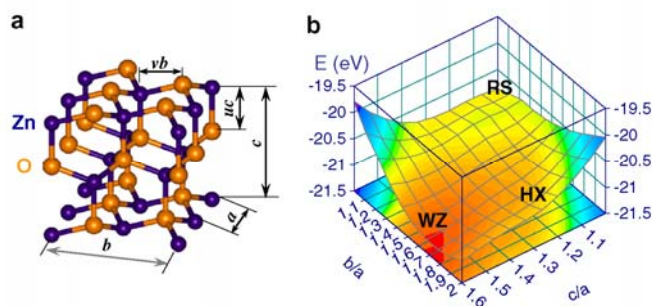


Fig. 1. (a) The wurtzite (WZ) crystal structure and (b) formation energy surface of ZnO with minima corresponding to the WZ, HX and RS structures.

Since the crystallographically constructed computational cells may not be in equilibrium, pre-loading relaxations are carried out to obtain their free standing configurations. Following this initial equilibration, approximate quasi-static tensile loading in each deformation increment is achieved through successive loading (at a specified rate of 0.005/ps) and equilibration steps (for 3 ps) using a combination of algorithms for NPT (Melchionna et al., 1993; Spearot et al., 2005) and NVE ensembles (Haile, 1997). The loading process results in a longitudinal strain increment of 0.25% (dilatation increment of $\sim 0.75\%$) per deformation increment. Unloading is implemented in a similar manner with a reduction in strain for each unloading step. The virial formula is used to calculate the stress (Zhou, 2003).

The DFT calculations use the VASP code (Kresse and Furthmüller, 1996) with local density approximation (LDA) and ultrasoft pseudopotentials (Vanderbilt, 1990) and focus on the evaluation of the total energy in the natural and deformed states. The stability of each crystal structure is determined by analyzing enthalpy as a function of lattice parameter ratios cla and b/a . The enthalpy per unit cell (2 Zn–O pairs) under uniaxial loading is defined as

$$H(c/a, b/a) = E(c, b, a, u, v) - \frac{1}{2} f_i q_i, \quad (1)$$

where E is the formation energy, f_i is the uniaxial force along the i direction, q_i is the lattice parameter in the i direction, and $f_i q_i$ (summation not implied) is external work per unit volume V . For tension along the $[01\bar{1}0]$ axis, $i = b$, $f_b = \sigma_b \times (ac)$ and $q_b = b$, with σ_b being the tensile stress. For tension along the c axis, $i = c$, $f_c = \sigma_c \times (ab)$, and $q_c = c$, with σ_c being the tensile stress. For hydrostatic compression, the enthalpy is

$$H(c/a, b/a) = E(c, b, a, u, v) + \frac{1}{2} pV, \quad (2)$$

where p is the pressure and $V = abc$ is the volume of two unit cells containing 4 Zn–O pairs. For each cla and b/a pair, the internal parameters u and v and the volume V are allowed to relax so that the configuration that yields minimum H is obtained. For a given load condition, the minima on the enthalpy surface with cla and b/a as the independent variables identify the corresponding stable and metastable structures.

3. Results and discussion

3.1. Stress-free state

Under ambient conditions, ZnO assumes the WZ structure which belongs to the $P6_3mc$ space group. As shown in Fig. 1a, this structure consists of two hexagonal close packed sublattices (one for Zn and the other for O) with an offset of ' uc ' along the $[0001]$ axis. The lattice parameters $a, b, c, u = uc/c, v = vb/b$ which completely define the structure are also indicated in the figure. Fig. 1b shows the formation energy (or enthalpy at zero external loading) landscape for ZnO. The structures corresponding to WZ, RS and HX are shown. The global minimum occurs at the WZ structure with $(cla, b/a) = (1.61, 1.73)$. Clearly, WZ is the most stable structure with the lowest energy; HX and RS have higher energies and are not stable under ambient conditions.

3.2. Uniaxial tension along the $[01\bar{1}0]$ orientation

Fig. 2a shows an intermediate configuration during the tensile loading of a $[01\bar{1}0]$ -oriented nanowire with the cross-sectional size of $21.22 \times 18.95 \text{ \AA}$ using MD simulations. The corresponding stress–strain (σ – ε) response is shown in Fig. 2b. The region between A and B corresponds to elastic stretching of the WZ structure. Loading beyond B results in a stress drop from 10.02 to 6.98 GPa (B \rightarrow C) at $\varepsilon = 5.14\%$. This softening behavior corresponds to the nucleation of the HX phase. At this stage, u changes from its initial value of 0.38 for WZ to a value of 0.5 for HX, implying the flattening of the buckled wurtzite basal plane (Zn and O atoms becoming co-planar) [Fig. 2c]. As a result, Zn atoms are at equal distances from O atoms along the $[0001]$ axis and the structure acquires the additional symmetry of a mirror plane perpendicular to the $[0001]$ axis. This process occurs while the orientation of the basal plane remains invariant. Since v remains unchanged, HX has the same hexagonal symmetry around the c -axis as WZ. As the deformation progresses, the transformed

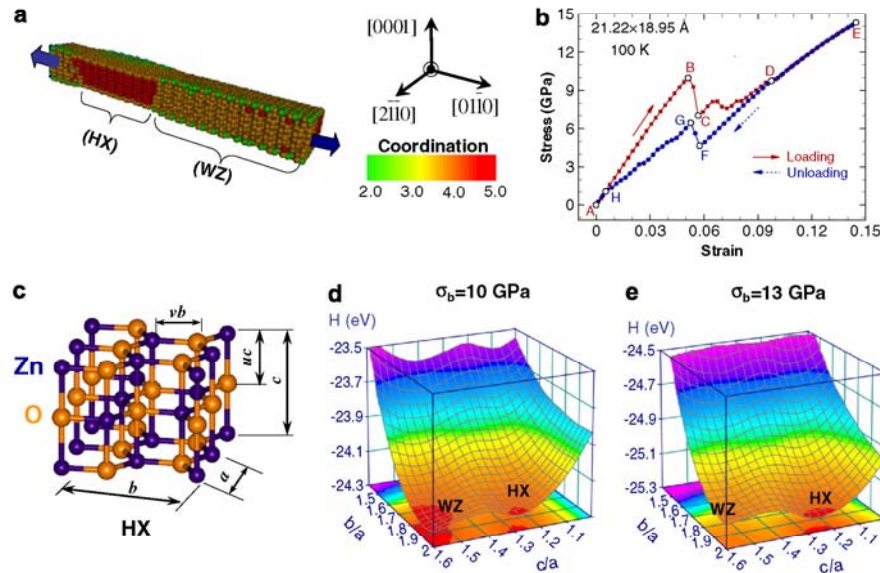


Fig. 2. (a) Nanowire with HX and WZ phases (transformation in progress under uniaxial tensile loading in the $[01\bar{1}0]$), (b) tensile stress-strain response of a 21.22×18.95 Å nanowire at 100 K during loading–unloading, (c) newly discovered hexagonal (HX) crystal structure, (d) enthalpy surface map obtained from DFT calculations with tensile stress $\sigma_b = 10$ GPa, and (e) enthalpy surface map with tensile stress $\sigma_b = 13$ GPa.

region sweeps through the entire wire length (C \rightarrow D) and the transformation completes at $\varepsilon = 9.71\%$ ($\sigma = 9.65$ GPa). Further deformation occurs through the elastic stretching of the transformed structure (HX) and ultimate fracture occurs at $\varepsilon = 16\%$ ($\sigma = 15.29$ GPa, not shown) through cleavage along $\{1\bar{2}10\}$ planes.

Unloading from any strain prior to the initiation of failure, e.g. point E with $\varepsilon = 14.5\%$, is first associated with the recovery of the elastic deformation within the HX structure (E \rightarrow F). A reverse transformation from HX to WZ (F \rightarrow G \rightarrow H) initiates at $\varepsilon = 5.77\%$ ($\sigma = 4.59$ GPa, point F) and completes at $\varepsilon = 0.6\%$ ($\sigma = 1.15$ GPa, point H). Unloading beyond H occurs through elastic deformation within the WZ structure (H \rightarrow A). Strains up to 14.5% can be recovered, highlighting a very unusual aspect of the behavior of ZnO which normally is quite brittle. Obviously, the large recoverable strains observed here are associated with the unique structural transformation process. The energy dissipation associated with the stress–strain hysteresis loop is ~ 0.16 GJ/m³, much lower than that for the WZ \leftrightarrow RS transformation in bulk (~ 1.38 GJ/m³ with a maximum recoverable volumetric strain of 17% in compression) (Desgreniers, 1998).

Fig. 2d and e shows the enthalpy surfaces (eV/unit cell) for $\sigma_b = 10$ and 13 GPa, respectively. In each case, there are two minima. The first minimum (H_{\min}^{WZ}) is in the vicinity of $cla \approx 1.6$ and $bla \approx 1.9$ corresponding to a WZ structure with lattice parameters slightly different from those at zero stress. The second minimum (H_{\min}^{HX}) is in the vicinity of $cla \approx 1.3$ and $bla \approx 1.9$ corresponds to the HX phase. At a stress value of 10 GPa, H_{\min}^{HX} and H_{\min}^{WZ} are comparable and consequently both WZ and HX are equally favored. At an applied stress of 13 GPa [Fig. 3e], H_{\min}^{HX} is lower than H_{\min}^{WZ} , indicating that HX is more stable. Obviously, the critical stress value for the WZ-to-HX transformation is $\sigma_b \approx 10$ GPa. As the magnitude of σ_b is increased above this equilibrium transition value, HX becomes more stable and simultaneously the transformation barrier is even lower, resulting in an increased driving force for transformation.

3.3. Uniaxial tension along the [0001] orientation

Fig. 3a shows the configuration of a [0001]-oriented nanorod with a lateral dimension of $d = 32.5 \text{ \AA}$. Fig. 3b shows the corresponding stress–strain response. Four distinct stages (A \rightarrow B, B \rightarrow C, C \rightarrow D and D \rightarrow E) are observed. The first stage (A \rightarrow B) corresponds to the elastic stretching of the WZ structure up to a strain of 7.5%. Further deformation results in a precipitous stress drop (B \rightarrow C) associated with the WZ to BCT-4 phase transformation which initiates in a local zone and propagates along the length of the nanorod. Crystallographic analysis reveals that the transformed phase consists of four-atom (2 Zn and 2 O) rings arranged in a BCT lattice [Fig. 3c]. The four-atom ring at the center has an orientation different (rotated by 90°) from that of the rings at the corners of the tetragonal lattice cell. The BCT-4 structure thus obtained preserves the initial tetrahedral coordination such that each Zn/O atom is at the center and four O/Zn atoms are at the vertices of a distorted tetrahedron. The distortion in the coordination tetrahedron can be analyzed through a quantification of the 3-D O–Zn–O bond angles (α_i , $i = 1..6$). For WZ, the bond angles are approximately equal ($\alpha_i \approx 108^\circ$). For BCT-4, the formation of 4-atom rings results in three distinct groups of bond angles ($\alpha_1 \approx 90^\circ$, $\alpha_2 \approx 112.7^\circ$ and $\alpha_3 \approx 113.7^\circ$). Throughout the transformation, the b/a ratio remains at its initial value of $1.73 (\pm 0.02)$, reflecting the symmetries of the loading and the lattice. The transformation completes at a strain of 8.5%. Further loading causes the elastic stretching of the BCT-4 structure (C \rightarrow D) and culminates in the eventual failure at a strain of 16.9% (point E).

To analyze the stability of the WZ and BCT-4 structures, unloading is performed from points B and D which correspond, respectively, to the states prior to the transformation initiation and failure initiation of the nanorod. The unloading path from B coincides with the loading path, confirming that the deformation from A to B is indeed the elastic response of the WZ structured nanorod. Unloading from D also results in the elastic recovery of the stretched BCT-4 structure and continued unloading beyond the transformation completion strain (point C) does not result in a reverse transformation back to WZ. Instead, the nanorod

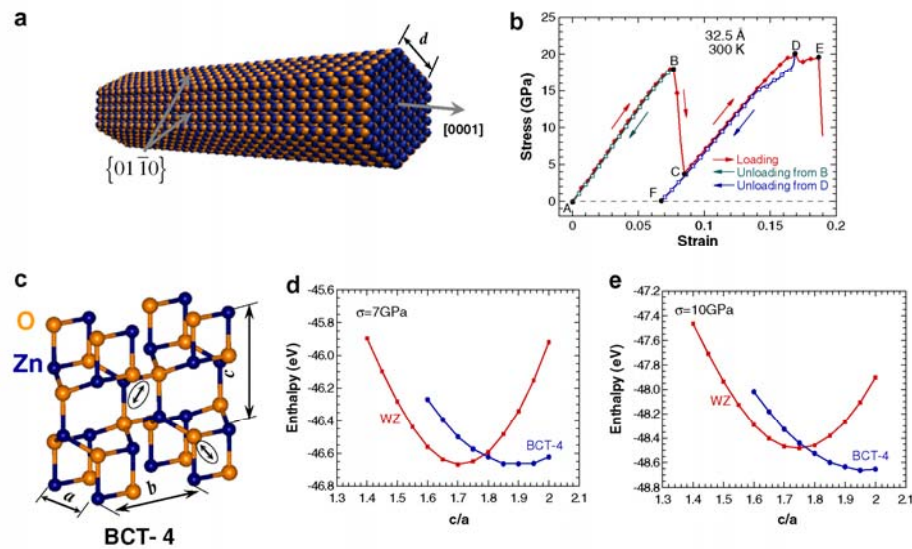


Fig. 3. (a) Configuration of a [0001] nanorod with $d = 32.5 \text{ \AA}$, (b) stress–strain curve of this nanorod at 300 K during loading and unloading, (c) newly discovered body-centered-tetragonal with four atom rings (BCT-4) structure, (d) enthalpy (per 4 Zn–O pairs) as a function of c/a obtained from DFT calculations for $b/a = 1.73$ at a tensile stresses of $\sigma_c = 7 \text{ GPa}$, and (e) enthalpy map at $\sigma_c = 10 \text{ GPa}$.

retains the BCT-4 structure when the stress is reduced to zero [F in Fig. 3b]. The residual strain at F in Fig. 3b is 6.8% according to both MD and DFT. It reflects the dimensional difference between the unstressed WZ and BCT-4 structures in the [0001] direction. This unstressed BCT-4 structure corresponds to the “ideal” BCT-4 structure predicted by the DFT calculations with $b/a = c/a = 1.73$.

Fig. 3d and e show the enthalpy values (eV per 4 Zn–O pairs) for both WZ and BCT-4 with $b/a = 1.73$ at $\sigma = 7$ and 10 GPa. At any stress level, each structure has its own enthalpy minimum. The first minimum (H_{\min}^{WZ}) is in the vicinity of $c/a \approx 1.6$ which corresponds to a WZ structure with lattice parameters slightly different from those at zero stress and the second minimum ($H_{\min}^{\text{BCT-4}}$) is in the vicinity of $c/a \approx 1.7$ – 1.9 which corresponds to the BCT-4 structure. At a stress of 7 GPa, H_{\min}^{WZ} and $H_{\min}^{\text{BCT-4}}$ become comparable, indicating that WZ and BCT-4 are equally favored. This value of stress corresponds to the equilibrium transition stress for the two phases. At 10 GPa [Fig. 3c], $H_{\min}^{\text{BCT-4}}$ is lower than H_{\min}^{WZ} and BCT-4 is clearly favored. Further increases in stress result in a higher driving force for and the eventual initiation of the phase transformation into the BCT-4 structure as $H_{\min}^{\text{BCT-4}}$ becomes progressively lower than H_{\min}^{WZ} . The gradual evolution of the local enthalpy minimum for the BCT-4 at $\sigma = 0$ into a global minimum as stress increases confirms that the phase transformation is indeed favorable.

3.4. Hydrostatic compression

Fig. 4a and b show the initial WZ and transformed RS structures for ZnO. The corresponding pressure–dilatation relation is shown in Fig. 4c. Three distinctive stages of response during loading (A → B, B → C and C → D) and unloading (D → E, E → F and F → G) are observed. During loading, the first stage (A → B) corresponds to the elastic deformation of the WZ structure. The precipitous drop in pressure at $p = 9.4$ GPa is associated with the transformation of the initial WZ structure to the RS structure. Crystallographically, the

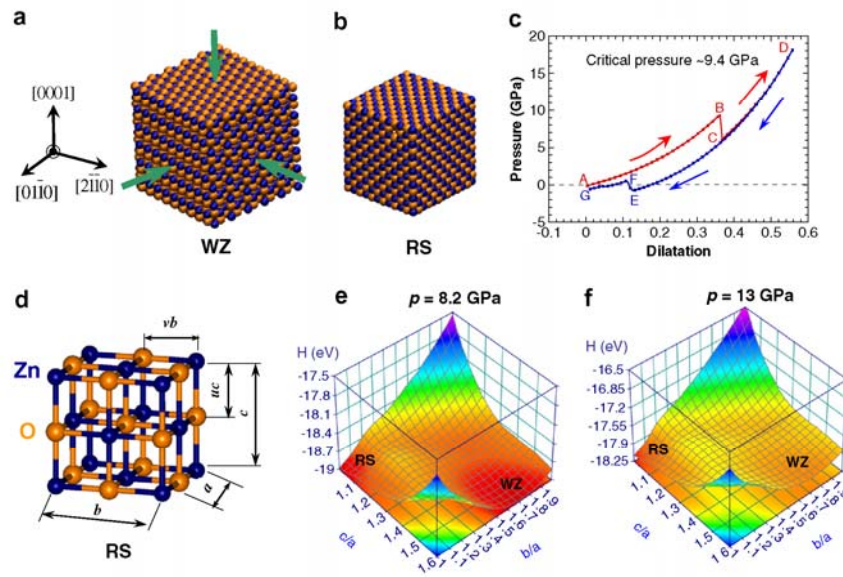


Fig. 4. (a) Bulk ZnO with the WZ structure under hydrostatic compression, (b) the RS structure as a result of the WZ-to-RS transformation, (c) pressure–dilatation relation of bulk ZnO during loading and unloading at 300 K, (d) lattice structure of the RS phase, (e) enthalpy surface obtained from DFT calculations for a hydrostatic pressure of $p = 8.22$ GPa, and (f) enthalpy surface for $p = 13$ GPa.

Author's personal copy

A.J. Kulkarni et al. / Mechanics Research Communications 35 (2008) 73–80

79

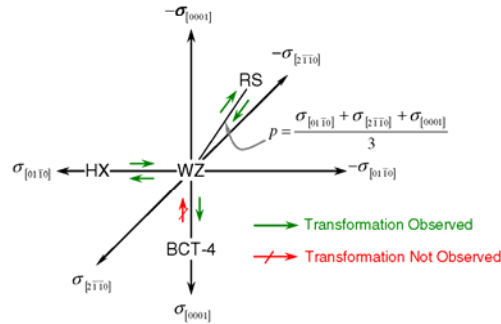


Fig. 5. Crystalline structure-load triaxiality map showing the relationship between applied loading and the resulting polymorphs of ZnO.

transformation proceeds such that both u and v change to 0.5 and the b/a and c/a ratios become unity [Fig. 4d]. Consequently, the RS structure has a six-fold coordination and belongs to the $Fm\bar{3}m$ space group. The transformation pressure observed here is consistent with experimental measurements in the range of 8.7–9.1 GPa (Desgreniers, 1998; Karzel et al., 1996). These values are higher than the phase equilibrium stress predicted by first-principles calculations (6.6–8.5 GPa) (Jaffe and Hess, 1993; Jaffe et al., 2000; Limpijumnong and Jungthawan, 2004). The difference is that, while the MD and experimental values are actual transformation stresses which reflect the effect of the energy barrier between the WZ and RS phases, the DFT phase equilibrium stress only indicates the level of stress at which the two phases are equally favored but does not relate to the stress required to overcome the energy barrier and activate the transformation.

Upon transformation completion, further increase in pressure results in the elastic deformation of the RS phase. Unloading is carried out from various stages of deformation of the RS phase to analyze the reversibility of the transformation. Specifically, unloading from point D along the loading path results in the recovery of the elastic deformation of the RS phase. Decrease in pressure beyond the transformation initiation point (B) does not result in the reverse transformation. Instead, the RS structure remains upon complete unloading. This retention of the RS structure upon full unloading has been reported in experiments (Recio et al., 1998). However, a spontaneous reverse transformation has also been observed in experiments (Mujica et al., 2003). Both sets of experimental results are reasonable because in experiments temperature is controlled only in an average sense and different experiments are carried out at different temperatures. Excess thermal energy in high temperature regions can allow the energy barrier between the RS and WZ structures to be overcome, resulting in the reverse RS-to-WZ transformation upon unloading. Furthermore, in experiments, defects such as grain boundaries in polycrystalline ZnO samples can act as potential nucleation sites for the reverse transformation and this effect is not considered in the calculations. In the simulations, the RS structure can easily revert to the WZ structure upon the application of a small negative hydrostatic pressure (E → F), leading to full elastic recovery of the volumetric strain (F → G).

Fig. 4e and f show the enthalpy landscapes for $p = 8.22$ and 13 GPa, respectively. Similar to what is seen for the HX and BCT-4 transformations, there are two minima; one corresponds to WZ (H_{\min}^{WZ} , $c/a \approx 1.6$ and $b/a \approx 1.6$) and the other corresponds to RS (H_{\min}^{RS} , $c/a \approx 1.0$ and $b/a \approx 1.0$). At $p = 8.22$ GPa, $H_{\min}^{\text{WZ}} = H_{\min}^{\text{RS}}$ and WZ and RS are equally favored. This value of pressure is the phase equilibrium pressure for ZnO. As the pressure is increased to 13 GPa, H_{\min}^{RS} becomes much lower than H_{\min}^{WZ} and the transformation to RS is energetically favored.

4. Summary

The identification of the novel HX and BCT-4 crystalline structures and the characterization of the WZ-to-HX and WZ-to-BCT-4 phase transformations lead to a more complete understanding of the nature of

polymorphism in ZnO and its dependence on load triaxiality. Obviously, polymorphism is much more pronounced in ZnO than previously understood and load triaxiality plays a very significant role in determining the structures. Fundamentally, this complexity is a reflection of the anisotropy and tension–compression asymmetry embedded in the atomic bonding and crystalline structures. It is possible to construct a crystalline structure–load triaxiality map for ZnO, as shown in Fig. 5. Among the previously well known phases, WZ is the most stable and naturally occurring phase and RS is observed under hydrostatic compressive conditions. Both BCT-4 and HX are stabilized under uniaxial loading, with HX occurring under tension along the $[01\bar{1}0]$ and BCT-4 occurring under tension along the $[0001]$ direction.

Acknowledgement

Support from NSF (CMS9984298) and NSFC (10772012, 10432050, and 10528205) is acknowledged. SL and KS are supported by TRF (BRG4880015 and PHD/0264/2545) and CHE (CHE-RES-RG “Theoretical Physics”). Computations are carried out at the NAVO, ARL, AHPCRC & ASC MSRCs.

References

- Binks, D.J., Grimes, R.W., 1993. Incorporation of monovalent ions in ZnO and their influence on varistor degradation. *J. Amer. Cer. Soc.* 76, 2370–2372.
- Desgreniers, S., 1998. High-density phases of ZnO: Structural and compressive parameters. *Phys. Rev. B* 58, 14102–14105.
- Diao, J. et al., 2004. Surface stress driven reorientation of gold nanowires. *Phys. Rev. B* 70, 075413.
- Haile, J.M., 1997. *Molecular Dynamics Simulation*. Wiley Interscience, New York.
- Jaffe, J.E., Hess, A.C., 1993. Hartree-Fock study of phase changes in ZnO at high pressure. *Phys. Rev. B* 48, 7903–7909.
- Jaffe, J.E. et al., 2000. LDA and CGA calculations for high-pressure phase transition in ZnO and MgO. *Phys. Rev. B* 62, 1660–1665.
- Karzel, H. et al., 1996. Lattice dynamics and hyperfine interactions in ZnO and ZnSe at high external pressures. *Phys. Rev. B* 53, 11425–11438.
- Kresse, G., Furthmüller, J., 1996. Efficiency of ab initio total energy calculations for metals and semiconductors using a plane-wave basis set. *Comp. Mat. Sci.* 6, 15–50.
- Kulkarni, A.J. et al., 2005. Orientation and size dependence of the elastic properties of ZnO nanobelts. *Nanotechnology* 16, 2749–2756.
- Kulkarni, A.J. et al., 2006. Novel phase transformation in ZnO nanowires under tensile loading. *Phys. Rev. Lett.* 97, 105501–105504, 105502.
- Liang, W., Zhou, M., 2006. Atomistic simulations reveal shape memory of fcc metal nanowires. *Phys. Rev. B* 73, 115401–115411, 115409.
- Limpijumnong, S., Jungthawan, S., 2004. First-principles study of the wurtzite-to-rocksalt homogeneous transformation in ZnO: A case of a low-transformation barrier. *Phys. Rev. B* 70, 054101–054104, 054104.
- Melchionna, S. et al., 1993. Hoover NPT dynamics for systems varying in shape and size. *Mol. Phys.* 78, 533–544.
- Mujica, A. et al., 2003. High-pressure phases of group-IV, III-V, and II-VI compounds. *Rev. Mod. Phys.* 75, 863.
- Ozgur, U. et al., 2005. A comprehensive review of ZnO materials and devices. *J. Appl. Phys.* 98, 041301.
- Recio, J.M. et al., 1998. Compressibility of the high-pressure rocksalt phase of ZnO. *Phys. Rev. B* 58, 8949–8954.
- Spearot, D. et al., 2005. Nucleation of dislocations from $[001]$ bicrystal interfaces in aluminum. *Acta Mat.* 53, 3579–3589.
- Vanderbilt, D., 1990. Soft self-consistent pseudopotentials in a generalized eigenvalue formalism. *Phys. Rev. B* 41, 7892.
- Wang, J. et al., accepted for publication. Molecular dynamics and density functional studies of a body-centered-tetragonal polymorph of ZnO. *Phys. Rev. B*.
- Wang, Z.L., 2004. Zinc oxide nanostructures: growth, properties and applications. *J. Phys.:Cond. Matt.* 16, R829–R858.
- Wolf, D. et al., 1999. Exact method for the simulation of Coulombic systems by spherically truncated, pairwise r^{-1} summation. *J. Chem. Phys.* 110, 8254–8282.
- Zhou, M., 2003. A new look at the atomic level virial stress: on continuum-molecular system equivalence. In: *Proceedings of the Royal Society of London* 459, 2347–2392.

Abstract submitted for the Siam Physics Congress 2007, Nakhon Pathom (2007)

SPC2007
NAKHON PATHOM, THAILAND

Oral Presentation

Novel phase of ZnO nanowires under tension

K. Sarasamak^{1*}, ***A. J. Kulkarni***², ***M. Zhou***², and ***S. Limpijumnong***¹

¹School of Physics, Suranaree University of Technology and Synchrotron Light
Research Institute, Nakhon Ratchasima 30000, Thailand

²School of Mechanical Engineering, Georgia Institute of Technology, Atlanta, GA
30332-0405, USA

Abstract

A phase transformation of ZnO nanowires from the natural wurtzite phase (WZ) to a novel graphite-like hexagonal structure (HX) is predicted for the first time, based on first-principle calculations and molecular dynamic simulations. We found that a $[01\bar{1}0]$ nanowire, i.e. a nanowire with its principal axis oriented along the WZ $[01\bar{1}0]$ direction, has a special property under tension. Under a large tension, the wire can have the WZ-HX phase transformation which effectively allows the wire to stretch by almost 20% before breaking. This property is very unusual for ZnO which normally can stretch by less than 7% before fracture. We have recently published this work in Physical Review Letters. [1].

Keyword: first-principle calculations, nanowires, phase transformation

* Corresponding author, Email: kanoknans@hotmail.com

Abstract submitted for the APS March Meeting 2008, New Orleans, Louisiana,
USA (2008)

Abstract Submitted
for the MAR08 Meeting of
The American Physical Society

Sorting Category: 19.1 (C)

High-stress phases of SiC, GaN, InN, ZnO, and CdSe
KANOKNAN SARASAMAK¹, AMBARISH J. KULKARNI, MIN
ZHOU, SUKIT LIMPIJUMNONG, Suranaree University of Technology,
Thailand — Phase transformations of SiC, GaN, InN, ZnO, and CdSe
from wurtzite (WZ) to three other different crystalline structures under
loading of different stress tensors are studied using first-principle calcu-
lations. The first transformation studied is well known and occurs under
hydrostatic compression and leads to a six-fold coordinated *rocksalt* (RS)
structure. The equilibrium pressures for this transformation of the mate-
rials are calculated and found to be proportional to the energy difference
between the phases at zero stress and vary monotonically with the mate-
rials' ionicity. The second and third transformations studied occur under
uniaxial stresses and lead to two new crystal structures previously un-
known for these materials. Specifically, uniaxial compression along the
[0001] direction or uniaxial tension along the $[01\bar{1}0]$ direction, causes a
transformation to a five-fold coordinated *unbuckled wurtzite* structure
which we named HX. On the other hand, uniaxial tension along the
[0001] direction causes the materials to transform into a body-centered-
tetragonal structure which we named BCT-4. The critical equilibrium
transformation stresses for these transformations are obtained and their
correlation with the ionicity of the materials is analyzed.

¹currently at CWRU, Cleveland, OH 44106

Prefer Oral Session
 Prefer Poster Session

Kanoknan Sarasamak
kanoknans@hotmail.com
Suranaree University of Technology, Thailand

Date submitted: 22 Nov 2007

Electronic form version 1.4

Abstract submitted for the RGJ-Ph.D. Congress X, Chonburi (2009)

Stability of wurtzite, unbuckled wurtzite, rocksalt, and BCT-4 phases of ZnO under different loading conditions

K. Sarasamak,¹ A. J. Kulkani,² M. Zhou,² F. J. Ke,^{3,4} J. Wang³, and S. Limpijumnong¹

¹*School of Physics, Suranaree University of Technology and Synchrotron Light Research Institute, Nakhon Ratchasima 30000, Thailand*

²*School of Mechanical Engineering, Georgia Institute of Technology, Atlanta, GA 30332-0405, USA*

³*Department of Physics, Beihang University, Beijing 100083, China*

⁴*Institute of Mechanics, Chinese Academy of Sciences, Beijing 100080, China*

Introduction

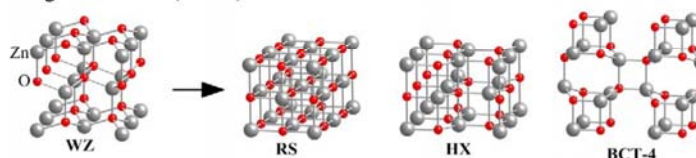
Phase transformations of crystals under high pressure or uniaxial stress have been physical phenomena of great interest for a long time. In this work, homogeneous phase transformations of ZnO from wurtzite (WZ) to three other different crystalline structures; unbuckled wurtzite (HX), rocksalt (RS), and BCT-4 under different loading conditions are studied by using first-principle calculations.

Methods

First principles calculations are used to calculate the total energy of each ZnO crystal structure. The calculations are based on the density functional theory (DFT) with local density approximation (LDA) and ultrasoft pseudopotentials, as implemented in the VASP code. The stability of each crystal structure is determined by analyzing enthalpy of the structures under distortions. For each distorted configuration, an equation of state (energy-volume relation) is obtained by a third-degree polynomial fit through the series of calculations with varied volume. Under different loading conditions (hydrostatic pressure or uniaxial stress along certain crystal axes), the lowest enthalpy configuration is identified. By gradually increase the pressure (or stress) the homogeneous transformation path can be described.

Results

To ensure that our computation scheme is valid, we studied the well known hydrostatic case. Under hydrostatic pressure (~ 8 GPa), wurtzite ZnO can transform into a six-fold coordinated rocksalt (RS) structure. This is consistent with available experimental and theoretical results in the literatures. For the uniaxial stress conditions, we found that (1) the uniaxial compression along the [0001] direction or uniaxial tension along the $[01\bar{1}0]$ direction can lead to a transformation into a five-fold coordinated unbuckled wurtzite structure (HX); (2) the uniaxial tension along the [0001] direction can lead to a transformation into a body-centered-tetragonal structure (BCT-4).



Conclusions

Based on first principles calculations, we predicted the new polymorphs of ZnO that are stable under uniaxial stresses. Our results show that the unbuckled wurtzite structure (HX) can be stabilized by either the tension along $[01\bar{1}0]$ or the compression along [0001], while the BCT-4 structure by tension along [0001] direction.

Keywords: phase transformation. Zinc Oxide, First principles

References

1. Sarasamak K, Kulkani A. J, Zhou M, and Limpijumnong, S. Phys. Rev. B 2008;77:024104-12.
2. Kulkani A. J, Sarasamak K, Wang J, Ke F. J, Limpijumnong, S, Zhou M. Mech. Research Commun. 2008;35:73-80.

Abstract submitted for the Siam Physics Congress 2009. Phetchburi (2009)

SPC2009
CHA-AM, PHETCHBURI, THAILAND

Poster Presentation

Crystal structures of SiC, GaN, InN, ZnO, and CdSe under different stress directions

K. Sarasamak^{1*}, A. J. Kulkarni², M. Zhou², and S. Limpijumnong¹

¹School of Physics, Suranaree University of Technology and Synchrotron Light Research Institute, Nakhon Ratchasima 30000, Thailand

²School of Mechanical Engineering, Georgia Institute of Technology, Atlanta, GA 30332-0405, USA

Abstract

Under ambient pressures, SiC, GaN, InN, ZnO, and CdSe have a four-fold coordinated wurtzite (WZ) structure. It is well known that under sufficiently high hydrostatic compressive stress, the transformation of these materials into a six-fold coordinated *rocksalt* (RS) structure takes place. Based on first principles calculations, the critical pressures of transformation are calculated and found to be in good agreement with available experimental results. Further calculations of the transformations driven by uniaxial stresses suggest that the crystal can transform into a five-fold coordinated *unbuckled wurtzite* phase (HX) under uniaxial compression along the [0001] direction or uniaxial tension along the [0110] crystalline direction. The critical equilibrium transformation stresses for these transformations are predicted and their correlation with the ionicity of the materials is analyzed.

Keyword: phase transformation, wurtzite, rocksalt, uniaxial stress

* Corresponding author. Email: kanoknans@hotmail.com

CURRICULUM VITAE

Kanoknan Sarasamak was born on October 26, 1980 in Ubon Ratchathani, Thailand. She received her Bachelor degree of science with second class honor in 2002 from Department of Physics, Faculty of Science, Khon Kaen University. In 2003, she was granted the scholarship from the Thailand Research Fund under the Royal Golden Jubilee Program to study in Ph. D. program in the School of Physics, Suranaree University of Technology under the supervision of Prof. Dr. Sukit Limpijumnong. She has contributed to several national/international conferences (listed in APPENDIX). Her publications are also listed in APPENDIX.